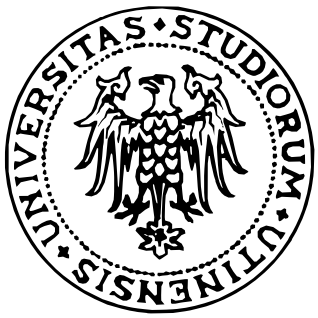

UNIVERSITÁ DEGLI STUDI DI UDINE

Ph.D. Thesis

For the title of

Dottore di Ricerca dell'Università degli Studi di Udine

Dipartimento Politecnico di Ingegneria e Architettura
Corso di dottorato in Ingegneria Industriale e dell'Informazione
XXIX ciclo

Paolo SCARBOLO

Electrical characterization and modeling of pH and microparticle nanoelectronic sensors

Advisor:

Prof. Luca SELMI

Co-advisor

Prof. Pierpaolo PALESTRI

External reviewers:

Prof. Marco SAMPIETRO
Prof. Andreas OFFENHÄUSSER

2014-2016

Contents

Summary

By 2050, the world's population will have risen to 9.7 billion, with 2 billion over the age of 60. To face this situation the actual healthcare system must be improved and innovated. One way to achieve this is to invest in technology.

Already today, advancements in biology, chemistry and medicine are being enabled by devices, tools and instrumentation powered by existing micro- and nanoelectronics; nevertheless the potential of these technologies is still far from being fully developed. In fact, recent years have seen a growing attention toward novel and interdisciplinary research fields at the frontier between life sciences and engineering. One clear example is the area of bioelectronics, which holds the potential to revolutionize, among others, our approach to healthcare.

Electronics and the semiconductor industry are sufficiently mature to offer and support a huge variety of solutions, going from the enormous data centers to collect the clinical data of the patients and perform accurate analysis, the ability to provide portable systems equipped with biosensors for point-of-care diagnosis and treatments, and the nanotechnologies and nanobiosensors enabling the so-called personalized medicine and the next-generation of devices for research purposes.

Technology innovation and the development of the next-generation bioelectronic sensors require deep understanding of new phenomena and must necessarily pass through a phase of research, design, optimization, and characterization. Accurate numerical and analytical models to predict the transduction performances and the reliability of a new biosensor concept play a role of utmost importance in supporting all of the above.

My thesis falls in this realm.

In particular, I focused on the modeling and characterization of ion-sensitive field-effect-transistors (ISFETs) made of silicon nanoribbons. The concept of ISFET, developed in the early 1970's, has re-gained increasing attention in the last decade thanks to its flexibility in sensing different types of analytes and due to its compatibility with the CMOS fabrication process. The research activity was focused in two directions: (i) ISFET characterization with experiments performed in dry and liquid electrolyte environments, and (ii) simulations performed with commercial (Sentaurus TCAD) and in-house developed tools (ENBIOS). Existing simulation tools have been extended and improved to account for surface reactions. We modeled and characterized the pH-sensitivity in DC conditions, and we developed a quasi-3D model for the AC response of nanoribbons to dielectric microbeads in liquid environment. The measurements were performed during a

stage at the CLSE laboratory at EPFL (Lausanne, CH), whereas the measurements of the nanoribbons in dry were performed at the University of Udine. Original contributions in this area regard the characterization of signal-to-noise ratio (SNR) in nanoribbon ISFETs and the study of the SNR scaling with the nanoribbon architecture and dimensions.

Besides ISFETs, we studied the AC response of electrolyte/insulator/semiconductor samples. The insulator surface was functionalized with a self-assembled-monolayer for the detection of specific molecules. We developed a compact model that is extremely useful to analyze the electrical properties of each part composing the sample and gives useful indications for the realization of a full sensor for the detection of DNA/PNA at the insulator/electrolyte surface. Original contributions in this area regard the development of a compact model capable of detecting different PNA orientations attached on the sensor surface.

As a last activity, the thesis describes the publication of two simulation tools on the nanohub.org portal. The tools are based on ENBIOS, include DC and AC the surface reaction models developed during the PhD and represent a useful reference for researchers and scholars interested to explore the potential of the ISFET sensing concept.

Sommario

Si stima che nel 2050 la popolazione mondiale sará di 9.7 miliardi, di cui 2 miliardi sopra i sessant'anni. Per sostenere questa situazione è necessaria un'innovazione e un miglioramento del sistema sanitario attuale. Una possbilitá concreta per raggiungere questo obbiettivo è investire nell'innovazione tecnologica.

Giá oggi i progressi in biologia, chimica e medicina sono resi possibili da dispositivi, metodi e strumentazioni basati sulla micro e nanoelettronica; tuttavia il potenziale di queste tecnologie é lungi dall'essere completamente sfruttato. Infatti, gli ultimi anni sono stati testimoni di un interesse crescente verso campi di ricerca nuovi e interdisciplinari che si trovano alla frontiera tra le scienze della vita e l'ingegneria. Un esempio chiaro é l'area della bioelettronica, la quale ha in se il potenziale per rivoluzionare l'approccio alla sanitá.

L'elettronica e l'industria dei semiconduttori sono sufficientemente mature per offrire e supportare un'immensa varietá di soluzioni, partendo da grandi data center per raccogliere i dati clinici dei pazienti ed effettuare analisi, fornendo sistemi portatili equipaggiati con biosensori per diagnosi e trattamenti decentrati (cosiddette point-of-care) e offrendo nanotecnologie e nanobiosensori per la medicina personalizzata e per le nuove generazioni di dispositivi per la ricerca.

L'innovazione e lo sviluppo tecnologico della prossima generazione di sensori bioelettronici richiede una profonda conoscenza di nuovi fenomeni a deve necessariamente attraversare una fase di ricerca, progettazione, ottimizzazione e caratterizzazione. Accurati modelli numerici ed analitici per prevedere le prestazioni e l'affidabilitá di un nuovo concetto di biosensore giocano un ruolo di supporto estremamente importante.

La mia tesi ricade proprio negli ambiti sopra elencati.

In particolare mi sono focalizzato sulla modellazione e caratterizzazione di dispositivi ad effetto di campo sensibili agli ioni (ISFET) basati su nanoribbon di silicio. Il concetto di ISFET, sviluppato nei primi anni '70, ha riacquistato un crescente interesse negli ultimi decenni grazie alla sua flessibilitá nel poter rilevare diversi tipi di analiti a grazie anche alla sua compatibilitá con il processo di fabbricazione CMOS. L'attivitá di ricerca si è focalizzata su due fronti: (i) la caratterizzazione degli ISFET con esperimenti a secco e in liquido e (ii) le simulazioni eseguite con strumenti commerciali (Sentaurus TCAD) e altri sviluppati in-house (ENBIOS). Gli strumenti di simulazione esistenti sono stati estesi e migliorati per poter includere reazioni superficiali. Abbiamo modellato e caratterizzato la sensitivitá al pH in condizioni DC e abbiamo sviluppato un modello quasi-3D

per la risposta AC dei nanoribbon in ambiente liquido ed in presenza di microparticelle dielettriche. Le misure in liquido sono state eseguite durante uno stage presso il laboratorio CLSE all'EPFL (Losanna, CH), mentre le misure sui nanoribbon a secco sono state eseguite all'Universitá di Udine. Contributi originali in questo campo riguardano la caratterizzazione del rapporto segnale-rumore (SNR) negli ISFET a nanoribbon e lo studio dello scaling dell'SNR con le dimensioni dei nanoribbon.

Oltre ai dispositivi ISFET, abbiamo studiato la risposta AC di strutture elettrolita/isolante/semiconduttore. La superficie dell'isolante a contatto con l'elettrolita é stata funzionalizzata con un self-assembled monolayer per la rilevazione di specifiche molecole. Abbiamo sviluppato un modello compatto che é estremamente utile per analizzare le proprietá dielettriche di ciascuna parte costituente la struttura e fornisce utili indicazioni per la realizzazione di un sensore completo per la rilevazione di DNA/PNA all'interfaccia elettrolita/isolante. Contributi originali in questo campo riguardano lo sviluppo di un modello compatto capace di distinguere molecole di PNA legate alla superficie del sensore con una diversa orientazione.

Come ultima attivitá, la tesi descrive due strumenti di simulazione che abbiamo pubblicato sul portale nanohub.org. Gli strumenti sono basati su ENBIOS, includono reazioni superficiali in DC e AC sviluppate durante il dottorato e rappresentano un'utile referenza per ricercatori e studenti interessati ad esplorare le potenzialitá del concetto di sensing offerte dall'ISFET.

Chapter 1

Introduction

The healthcare access and its financing is becoming extremely challenging due to various factors; the increase of the worldwide population and its life expectancy; the rise of chronic diseases and complex medical conditions; the lack of human resources and infrastructures; the air pollution combined with the use of tobacco; and the growing sedentary lifestyle associated with unhealthy diets. These health-related problems are even more accentuated in emerging economies, where health costs are growing faster than the national income. The life expectancy in developed countries has increased of about 10 years in the last two decades and is leading to a rapid ageing of the population. This process puts under stress the availability of healthcare resources, because aged people require additional costly medical attention. For these and many other reasons, the healthcare industry is an extremely active and growing sector, as shown in fig. 1.1.

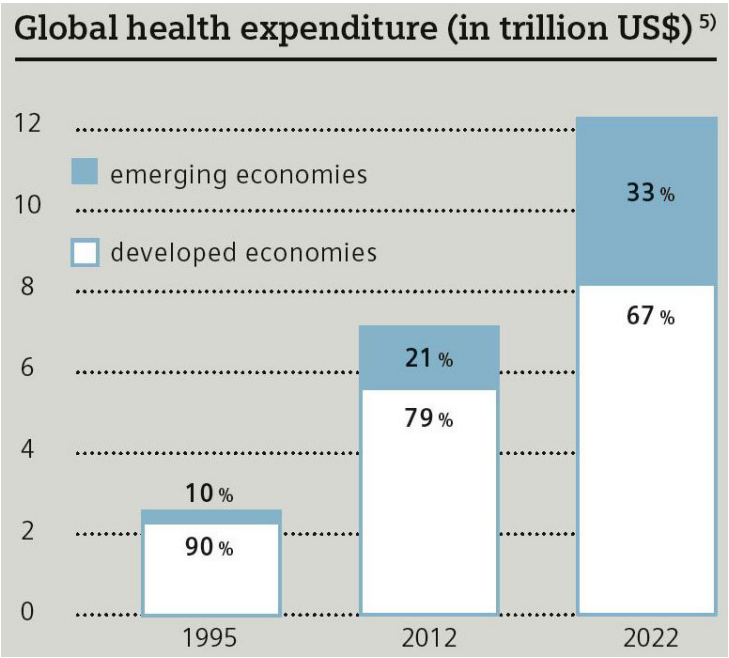

Figure 1.1: *Spending on healthcare will continue to grow and one-third of all global health expenditure will occur in emerging economies by 2022 [1].*

Among different players, technology is at present and will continue to be a factor of outmost importance for the development of new sustainable healthcare models. In fact, technology can provide better and more accessible treatments, by increasing the level of care and its efficiency and by providing instruments for tracking, storing, retrieving and using valuable data for a better control of patients and diseases.

Technology is pushing in essentially two directions: (i) the innovation and improvement of the existing medical and analysis tools available for known diseases and known medical conditions, and (ii) the design and development of new concepts and more effective tools for complex pathologies and instruments suitable for research and study of rare diseases. From this differentiation we can identify two application macro-areas for the next generation of devices and tools. The first category comprises the devices that can be used easily by the patient itself, such as implantable and portable systems for point-of-care diagnosis, monitoring and treatments; devices that can be used on bedside, ambulance or during a clinic visit. Low-cost, low-power and ease-of-use should be the main features of these devices. The second category, instead, regards devices for microanalysis research purposes, such as lab-on-chip solutions for diagnostic and personalized medicine. In this case the devices are developed to meet high performances, such as high sensitivity and high parallelism, with less constraints on power consumption and costs. There is also a need of huge amounts of data per sample in an adequate time, short time response, low detection limits, and especially the possibility for multi-parameter analysis. These are the key features for the next generation of lab-on-chip devices, that are currently becoming superior to classical biochemical analysis instruments.

The advancement in the technology should provide devices and tools for the diagnosis and treatment of primary medical conditions without the necessity to go to hospitals or medical centers. In this way the workload of hospitals and medical centers can be reduced by moving devices and instrumentation for monitoring, diagnostic and treatment from public/private infrastructures directly to the patient, as portable or implantable devices. In particular, point-of-care solutions have a large impact especially in resource-limited settings where healthcare infrastructure is weak and access to quality and timely medical care is a challenge. Such devices should be as much as possible autonomous, disposable and, most important, interconnected to the internet and the cloud for easy remote access by analysts and physicians.

When thinking about technologies that can be at the same time low-cost, mature enough for massive development and enablers of interconnected sensing capability, CMOS appears a natural choice. The steady scaling of CMOS electronic device dimension have reached a point where the dimension of a single device is with the order of tens of nanometers. A clear illustration of this concept is the so-called biological meter reported in fig. 1.2, that shows how the size of devices currently in production have reached the size of a single protein, $\sim$10 nanometers. The advantages of such nanometric dimensions are enormous, one over all is the possibility to detect single molecules of incredibly small size [2]. Interfacing with individual molecules offers unique opportunities to understand the

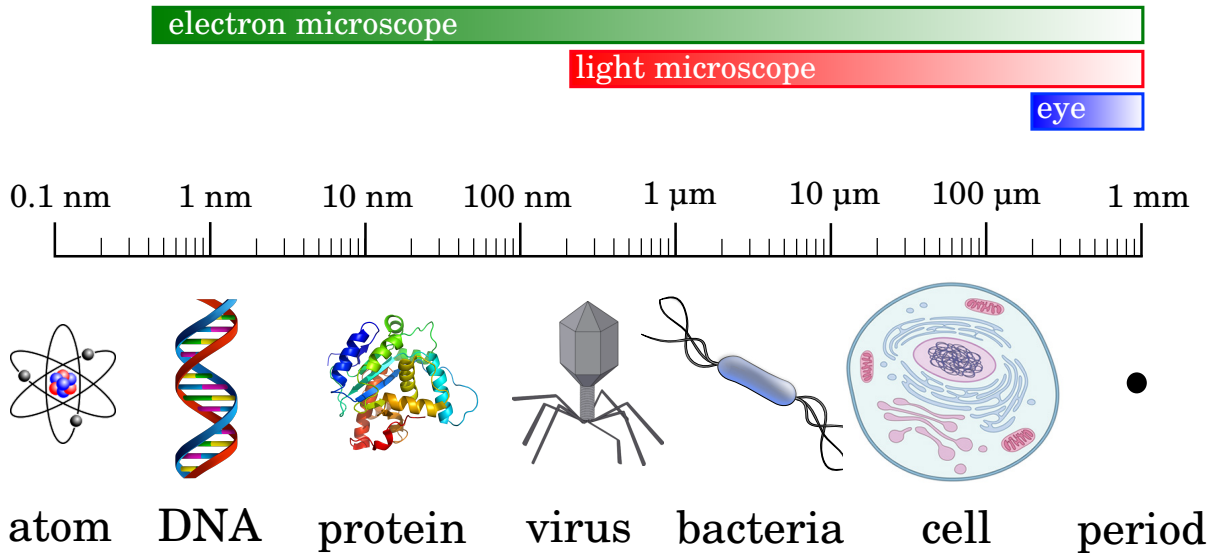

Figure 1.2: *The biological meter.*

basis of larger living systems, as well as to take advantage of the inherent spatial localization and heterogeneity that single-molecule data can offer. This can lead to molecular assays using extremely small volumes of analytes at low concentration. Applications such as DNA sequencing have led the innovation in this field till now, but new possibilities are now attracting increasing interest for nongenomic analytes for which no straightforward amplification protocol exists [2].

It is now clear that many advancements in biology, chemistry, medicine can be enabled by the devices, tools and instruments provided by existing and future micro- and nanotechnologies. The combination and constant merge of the different disciplines necessary to design and develop such devices has led to the birth of a stable, innovative, interdisciplinary and challenging field, that is *bioelectronics*.

Bioelectronics is a frontier discipline that combines synergically different fields and in the last two decades, have led to a large amount of new sensor systems for biological, medical and environmental purposes. These sensors, enabled by the great advances in micro- and nanotechnologies, are called *biosensors*. A biosensor can be defined as an analytical tool that combines a biological element (biosensing component, for recognition/detection) with a physicochemical element (transducer component) to generate a measurable signal (typically electrical) for the detection of a specific analyte. A biosensor device consist typically of three components: a detector, a transducer and eventually a signal processing unit. Once the analyte is detected, the transducer converts the signal in a measurable form and finally this signal is amplified, part of the noise rejected and presented in an appropriate form.

Before analyzing the different types of biosensing elements and transducers, it is necessary to introduce a first broad classification of biosensors. Depending on the detection/recognition process, biosensors can be:

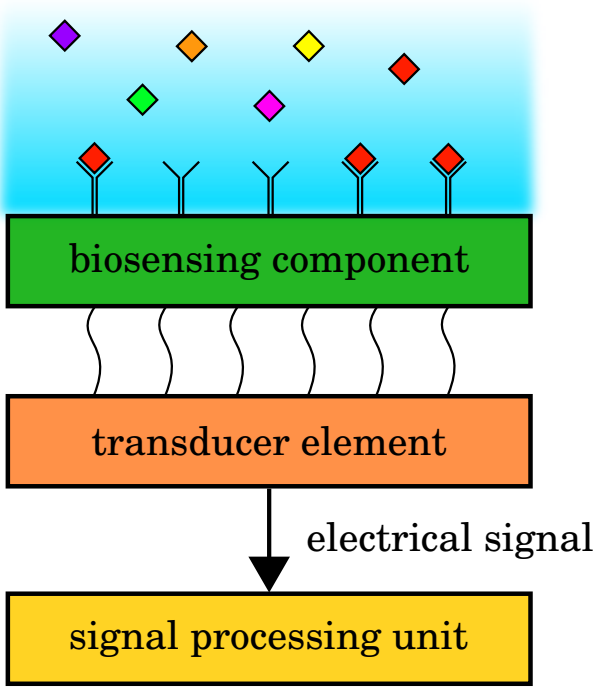

Figure 1.3: *Biosensor schematic representation.*

- *Biocatalytic sensors*: Biocatalytic devices incorporate enzymes, whole cells or tissue slices that recognize the target analyte and produce electroactive species. Biocatalytic sensors can also be easily adapted to automatic clinical lab and industrial analysis. Blood glucose monitoring devices are the most successful commercial application of biocatalytic sensors;

- *Affinity sensors*: Affinity-based biosensors rely on a selective binding interaction between the analyte and a biological component such as antibodies, nucleic acids, or receptors. The molecular recognition is mainly determined by the complementarity, in size and shape, of the binding site to a specific analyte.

A second broad biosensor classification regards the technique of transducing the biological events. The main techniques are:

- *Labeled*: a label is an additional molecule that is chemically or temporarily attached to the analyte that needs to be detected. With this technique it is possible to detect concentration and activity. The labeling process requires a preparation step that is usually low yield, combined with synthesis and purification. Examples of labeled biosensors approaches are: fluorescence, radioactive and chemiluminescence;

- *Label-free*: in a label-free biosensing process, the signal is transduced by mechanical, electrical or optical mechanisms, without the need of any label. The main advantage

for label-free detection is that more direct information can be acquired, such as real-time data and tracking of molecular events. Furthermore, label-free biosensor can probe the analytes in their unperturbed states, and as a result, they are faster, simpler, and more physiological than their labeled counterparts. Examples of label-free approaches are: surface plasmon resonance (SPR), electrical techniques (field-effect based biosensors such as ISFET, ENFET, ImmunoFET, CNFET), surface stress (piezoelectric and optical), mass spectrometry and acoustic wave techniques.

These preliminary definitions allow us to describe more easily what are the different components of a biosensors.

The biosensing element is a set of biological entities that is capable of generating a biological signal, readable by the transducer. Examples of biosensing elements are:

- *Enzymes*: enzyme based biosensors utilize the principle of enzyme catalytic reactions, that release or consume detectable ions (H^+) or compounds (O_2, CO_2, H_2O_2 and NH_3), or differently, enzymes are inhibited or activated by specific and detectable analytes. In fact, the major advantage of enzymes is their aptness to be genetically engineered to detect a wide range of analytes;

- *Microbes*: microbes (e.g., algae, bacteria, and yeast) offer an attractive alternative to enzymes since they are cheper and less time-consuming to purify. Furtheremore they can simplify the fabrication of biosensors because they can be massively produced through cellculturing. They can also easily adapt to undesirable environments, they can metabolize a wide range of molecules, both aerobically and anaerobically, releasing various molecules (NH_3 and CO_2) or ions (H^+), that can be monitored by different transducers [3];

- *Cells or tissue*: cells and tissues are used as bioreceptors because they have high sensitivity to adjacent environment. Cells and tissues can be easily attached and immobilized on the surface. They are frequently used to detect global parameter like stress condition, toxicity, organic derivatives and the release of specific ions and to monitor the treatment effect of drugs;

- *Antibodies*: antibodies are used for immunosensors, based on the principle of antigen-antibody reaction. They are attached on the biosensor surface and they react with the analytes producing modification at the functional groups allowing the detection of the reaction;

- *Nucleic acids*: DNA is a perfect candidate as detector due to its specificity of base pairing with its complementary sequence. Nucleic acids, such as DNA, RNA or PNA, are attached at the sensor surface through short synthetic single-stranded oligonucleotide probes. DNA and RNA have a deoxyribose and ribose sugar backbone, respectively, while PNA is artificially synthesized, with a backbone composed by repeated N-(2-aminoethyl)-glycine units;

- *Novel receptors*: aptamers. These receptors are attracting great interest since they are artificially built by using DNA, RNA or PNA strands that can be easily synthesized and functionalized. Furthermore they can be synthesized to have an high affinity in order to efficiently discriminate between two or more similar targets.

The transducer transforms the biological signal into a detectable signal. Most common used transducers are of three categories:

- *Optical*: optical biosensors are analytical devices composed by a biosensing element integrated with an optical transducer, typically an optical fiber. The basic principle of an optical biosensor is to produce a signal which is proportionate to the concentration of a measured substance or analyte. In label-free sensors, the optical signal is generated directly by the interaction between the analyte and the transducer; while in label-based sensing there is the need of a label to generate the optical signal by a colorimetric, fluorescent or luminescent method. Simple molecules such as glucose can be detected by enzymatic oxidation using label-assisted sensing. The glucose analysis of blood is one of the most successful application of a biosensor, i.e. the handheld glucose meter used by diabetics;

- *Mass-sensitive*: mass-sensitive biosensors such as piezoelectric are typically used to measure the amount of analyte in solution. Usually, the surface of a piezoelectric resonator is suitably functionalized with probes to capture specific analytes. The binding of the analytes on the resonator surface changes its resonating frequency and/or oscillation amplitude and the amount of analyte can be measured;

- *Thermal*: thermal or calorimetric biosensors are based on reactions that generate heat after the adsorption of a specific analyte. The temperature is monitored and compared with an analyte-free sensor for a differential measurement;

- *Electrochemical*: electrochemical and electrical techniques are based on the measurement of electrical properties, such as current, voltage drop or impedance between electrodes that are placed in contact with a solution. Electrochemistry is a surface technique and consequently, electrochemical biosensors are sensitive to what happens at the surface of working electrodes. The reaction being monitored electrochemically typically generates a measurable current, a measurable change of charge or potential, or alters the conductive properties of the medium between electrodes.

Electrochemical biosensors are the main topic of the thesis and they will be analyzed extensively in the following section. Before that, due to the large variety of biosensors, it is necessary and important to define a few common *metrics* to evaluate biosensor performance.

- *Sensitivity*: it is defined as the amount of change of the output signal corresponding to a unitary change in the input signal. It is sometimes normalized to the surface area or volume;

- *Resolution*: it is the smallest detectable change distinguishable from the noise in the measurement. A signal is theoretically detectable if it has a signal-to-noise ratio (SNR) of 1. The resolution is also indicated as limit of detection (LOD) or limit of determination;

- *Selectivity*: it is the ability to discriminate among different analytes or, in other words, the ability to respond only to the target analyte and not to similar targets. A closely related concept is that of nonspecific binding, that happens when unwanted molecules stick on the probe layer, preventing true target binding or generating false target binding. To alleviate this problem, the samples can be pre-exposed to a solution containing bovine serum albumin (BSA), that nonspecifically adsorbs on the sensor surface, preventing subsequent nonspecific binding from the sample to be analyzed;

- *Dynamic range (DR)*: it is the ratio between the maximum and minimum analyte quantity that can be measured;

- *Response time*: it is the time elapsed since the analyte is added to an analyte-free solution, to the moment when the sensor response attains a practically constant value.

These primary figures of merit qualify the output of the biosensors, but there are also secondary metrics, that are more useful to evaluate the commercial impact of a biosensor. Examples of secondary metrics are: ease of use, cost, detection instrumentation and throughput.

1.1 Electrochemical biosensors

Given the classifications above, in the following we will outline the main electrochemical measurement techniques. Electrochemical measurements are possible with the system analyzed in fig. 1.4. It comprises a minimum of two electrodes in solution, the *working* and the *counter* electrodes, but usually it is preferred to use a three-electrodes configuration, with an additional *reference* electrode. The current flowing from counter to working electrodes is measured at the working electrode, that is typically functionalized with probes (affinity sensor) or biocatalytic material. The electrostatic potential of the solution is stabilized through the counter and monitored by the reference.

In electrochemistry its customary to discriminate between two types of electrodes:

- *Faradaic*: faradaic electrodes allow charge transfer between the solution and the electrode itself. When using faradaic electrodes, it is necessary to provide redox species (in solution) to sustain the electron transfer to and from the metal electrode, otherwise a depletion condition will arise and consequently the solution potential will not be stable. Reference electrodes are faradaic;

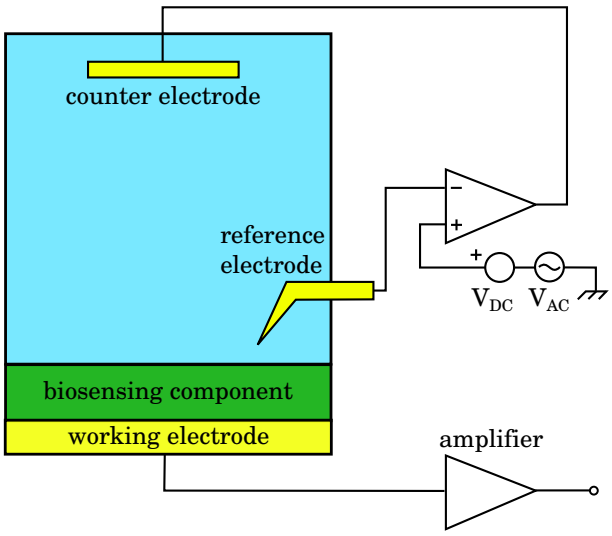

Figure 1.4: *Schematic representation of a three-electrodes configuration.*

- *non-Faradaic*: DC current are not sustained by non-faradaic electrodes, however transient currents are possible without charge transfer (AC operation). Typical applications of non-faradaic electrodes are the capacitive biosensors; in this case, working and counter electrodes are non-faradaic. If necessary, one reference (faradaic) electrode is used to stabilize the solution potential.

Typical three-electrode configuration is made by placing the reference electrode to monitor the electrostatic potential in the proximity of the working electrode; while the counter electrode is placed far away, sometimes even in different microfluidic chambers. The voltage of counter and reference electrodes are stabilized by an electronic feedback.

Depending on the measurement method, electrochemical biosensors can be classified as follows:

- *Amperometric/Voltammetric*: amperometric and voltammetric biosensors apply a potential between counter and working electrodes and measure the current at the working electrode. The current arises from oxidation-reduction at the working electrode, and it is limited by mass transport of the reactant molecules from the bulk of the solution to the electrode interface. Amperometric techniques apply a constant potential at the working electrode (with respect to counter and reference electrodes) and by monitoring the current it is possible to detect analytes. Voltammetric techniques, instead, measure the current at the working electrode while the potential is ramped at a constant rate. The measured current shows peaks and plateaus that can be related to the concentration of analyte in solution;

- *Potentiometric*: potentiometric biosensors are usually composed by an electrochemical cell with two reference electrodes capable of measuring the potential across an ion-selective membrane; membrane that reacts with charged ion of interest in solution. Biological elements such as enzymes are commonly integrated into potentio-

metric sensors to catalyze the reaction that forms the ions, which can be detected by the underlying electrode. For example, a pH electrode, that detects H^+ ions, can be transformed in a biosensor by coating the surface with penicillinase that produces H^+ when reacting with penicillin in solution;

- *Conductometric and capacitive*: most reactions involve a change in the composition of the solution that normally results in a change in the electrical conductivity of the solution. Conductometric biosensors monitors these changes in the electrical conductivity of a sample solution as the composition of the solution or medium changes during a chemical reaction. Conductometric biosensors often include enzymes whose charged products cause changes in the ionic strength of the sample solution. This category comprises also the capacitive biosensors [4], which measure the changes of permittivity and conductivity properties of systems characterized by an interface between liquid (electrolyte) and solid (metals, insulators or semiconductors) materials. Examples are electrolyte/insulator/semiconductor (EIS) capacitors [5, 6, 7, 8, 9], arrays of nanoelectrodes [10, 11] and interdigitated electrodes [12, 13, 14].

- *Charge-effect (or field-effect)*: the first attempt to use a Field-Effect-Transistor (FET) as biosensors, was reported by P. Bergveld in 1970 [15]. Bergveld proposed an Ion Sensitive Field-Effect Transistor (ISFET) for neurophysiological measurements, in which the gate metallization of the FET was removed, leaving the bare oxide in contact with the liquid environment. Gate insulators such as SiO_2, Al_2O_3 and HfO_2 have surface sites that in solution can capture and release H^+ ions, developing a pH-dependent surface charge. This surface charge, modifies the conductivity of the field-effect device underneath and the pH-dependent charge can be detected. This is the principle on which pH sensor are based on. After the development of the ISFET, different kind of FET-based biosensors were developed, such as EnzymeFETs (ENFETs), ImmunoFETs (IMFETs), etc. More recently, in the late 1990's, ISFETs made from semiconducting nanowires (NWs) [16], nanoribbons (NRs)[17, 18, 19] or FinFETs [20] have attracted great attention as electronic biochemical sensors due to their capability to be integrated as an array in a CMOS-compatible architecture together with microfluidics and interface electronics.

- *Impedimetric*: impedimetric biosensors measure the electrical impedance between two electrodes in AC steady state with constant DC bias conditions [21, 22, 23, 24, 25, 26]. This is accomplished by imposing a small sinusoidal voltage at a particular frequency and measuring the resulting current at the electrode. This is typically done by sweeping the frequency of the applied small signal voltage, and recording the spectrum response of the system under test. The AC current-voltage ratio gives the impedance. This approach, known as electrochemical impedance spectroscopy, has been used to study a variety of electrochemical phenomena over a wide frequency range. In fact, changes in the dielectric or conductive properties, that can arise from the binding of molecules on electrode surface or from antibody-antigen reactions,

can be detected as changes in the impedance spectrum. An advantage is that the applied voltage can be much smaller compared to the other electrochemical techniques, and it does not damage the probe-functionalized layer. In conclusion, impedance spectroscopy is a powerful technique mainly due to its operation as label-free biosensor.

As anticipated before the signal-to-noise ratio is a fundamental metric that defines the limit of detection of a biosensor. There are two ways to increase the SNR, and consequently the LOD: one is obtained by increasing the output signal and the other by decreasing the output noise. Let's analyze these two options with reference to the affinity-based label-free electrochemical biosensors, objects of this thesis, by looking firstly at the characteristics of the transduced signal and secondly at the noise sources.

1.1.1 Transduced signal

Fig. 1.5 illustrates typical conditions in proximity of the working electrode which acts as sensing element. The region near the interface, on the electrolyte side, is called Electrical Double Layer (EDL) and it is composed by charged ionic species and solvated ions. The EDL theory was developed by Gouy, Chapman and Stern [27]. The double layer forms an electrical screen that prevents the electrode from being sensitive to analytes that are $2 \div 3$ times the Debye length far from the interface. For a physiological solution the Debye length is $\sim$1 nm, meaning that the device can sense in a very narrow spatial range from the interface. In other words, in order to sense analytes in solution, they need to be attached to the interface or at least very close to it. This fact, in turn, creates a need for a capturing layer (that can also provide selectivity).

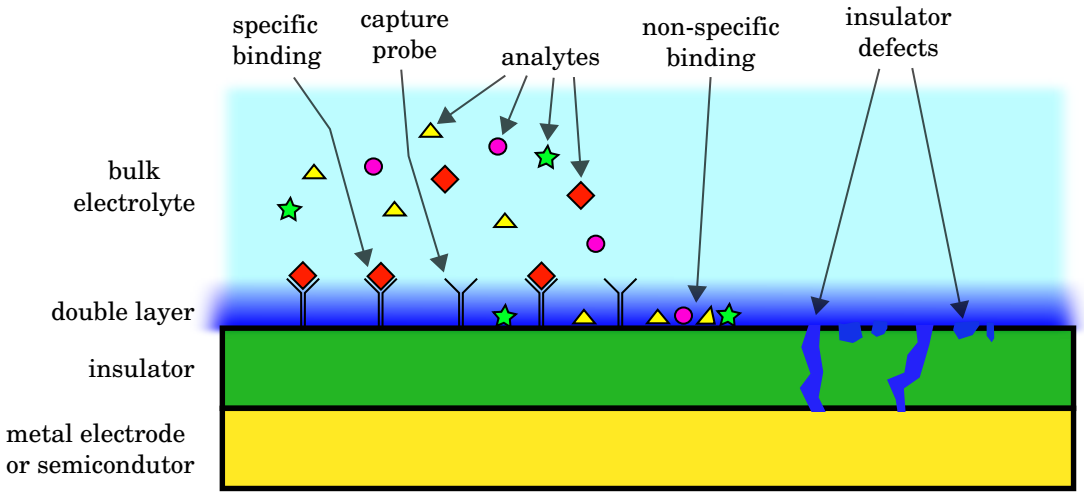

Figure 1.5: *The electrical double layer limits the visibility of the biosensors.*

Being sensitive only next to the surface, it is thus necessary to wait enough time for the analytes to diffuse on the sensing surface. Once they are close to the surface, they can

be captured and immobilized by specific probes placed on the sensor surface with ad-hoc functionalization processes. Neutral and charged particles inside the double layer affect the interface surface potential. The potential changes is then detected and transformed in an useful electrical signal. As an example, in the case of an ISFET, the changes in the surface potential affects the current flowing from drain to source in the channel of the FET device located in the semiconductor or underneath the sensing surface. Typical application are: pH sensing [28, 29, 30, 31, 32, 33, 34, 35, 36, 20, 19, 37], ion sensing [38, 39, 40, 41, 42], and label-free biosensing [43, 44, 45, 7, 46, 47, 48, 49, 24].

One way to overcome the sensitivity limitation of the double layer screening is to operate in AC conditions [23, 50], at frequencies comparable or larger than the electrolyte cut-off frequency. This frequency is independent of the electrode's geometry and is given by the ratio between the electrolyte permittivity and conductivity ($f_2 = \sigma_e/(2\pi\varepsilon_e)$). An additional cut-off frequency $f_1 \approx f_2/\alpha$, determines the impedance response of the electrode, where $\alpha > 1$ depends on the electrolyte composition and concentration and on the electrode's geometry. In AC operation we can thus distinguish three regions split by the two cut off frequencies (low, medium and high frequencies) and two type of sensitivities (surface and bulk), as reported in fig. 1.6. The surface sensitivity is high at low frequencies

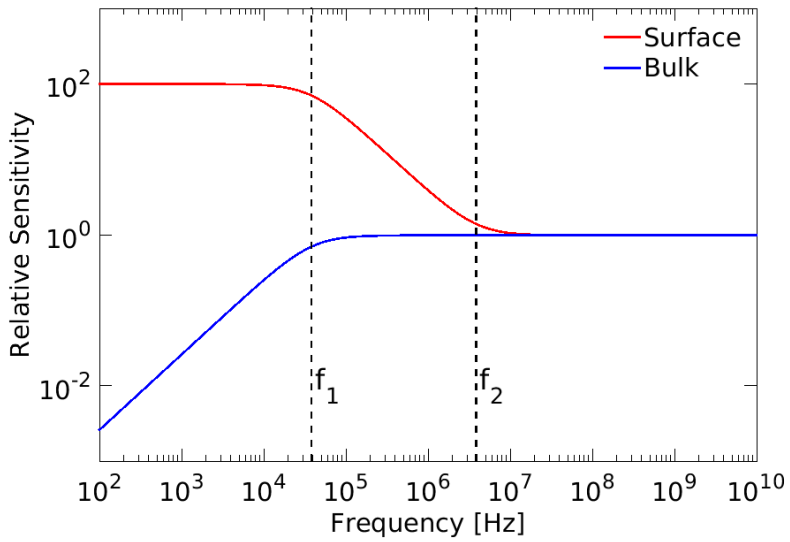

Figure 1.6: *Typical relative sensitivities of surface and bulk regions versus frequency.*

because analytes perturb the EDL and are al the minimum distance from the electrode. Bulk sensitivity instead is very low due to the presence of the double layer that screens analytes located beyond 2÷3 times the Debye length. The bulk sensitivity increases at higher frequencies, reaching its nominal value in between the two cut off frequencies. Finally, for frequencies above the electrolyte cut off (dielectric relaxation), where the electrical double layer has completely vanished, the sensitivity, both the surface and bulk, only weakly depends on distance from the electrode and therefore AC sensitivity are equal. At such high frequencies the sensor is thus able to detect particles that are placed very

far from the interface.

Working in AC at low or high frequencies has its own pros and cons. At frequency below the electrolyte cut-off (f_2) the read out circuits are simpler (commercial instrumentation) and parasitics play less of a role, but the response is dominated by the screening effect of the electrical double layer. On the other hand, working at very high frequencies is favourable in terms of sensitivity to particles and biomolecules located far from the interface and reduced dependence on surface charges and spurious effects, but it is necessary to design specific read out circuits to pre-amplify the signal and to reduce the otherwise detrimental effect of noise and parasitics. In fact it is of paramount importance to reduce the parasitics (small parasitic capacitance) in between the sensor and the readout and signal processing stages to reach single molecule detection capabilities. Therefore it is important to establish what (dielectric, charge) and where (interface or bulk) to sense, in order to optimize the design of a biosensor device.

Due to the devices and instrumentation available, the research activity was mainly focused on measurements and experiments at medium and low frequencies.

1.1.2 Noise

Noise in biosensors is an important factor that must be taken into account and minimized as much as possible to increase the SNR and increase the resolution.

The majority of the biosensors have intrinsic noise that comes from the interaction between the probes and target analyte at molecular level. To generate target-specific signal, the target analytes in solution first need to collide with the detection layer, interact with the probes, take part in a transduction process, and ultimately pass through the read out circuitry. All these steps introduce noise, that may cover the useful signal produced by the true binding events. In all practical biosensors, different species coexist with the target in the sample, and they may or may not bind to the probes. We call such species interferers. Effects of interference (competing with different analytes in solution), non-specific binding (binding of interferes on probes or sensor's active surface) fall in the category of mechanisms that generate the so-called biological noise. The signal generated by the transducer which originates from non-specific bindings is called non-specific signal or background signal.

At low frequencies, the noise in MOSFET devices is dominated by the flicker noise [51, 17], which is characterized by a power spectral density that is proportional to $f^{-\alpha}$, where $0.7< \alpha <1.3$ [52]. The $1/f$ noise can be originated from different mechanisms: (i) fluctuations in the gate due to the trapping and de-trapping of carriers, (ii) dielectric polarization fluctuations, or (iii) the noise is generated inside the conducting channel in the form of either carrier density or mobility fluctuations. The 1/f noise is dominating in application such as pH sensing, because the device respond with high time constant, meaning low frequency domain, where the noise is larger.

An other noise component is associated with the connection between the biosensor and

the instrumentation. Cables and interconnections are one of the most relevant sources of noise, that impact the high frequency response. While the devices have scaled in dimensions over the years, the detection instrumentation has remained almost of the same size (i.e. semiconductor parameter analyzers, LCR meters, etc.). For this reason it is usually preferable to have an integrated read out circuit to reduce at minimum the interconnections, the stray capacitances and all the instrumentation-related parasitics components. As an example, in impedance measurements the noise spectrum of the signal, $S_{i,i}$, is:

$$S_{i,i} \propto \omega^2 \sum_i C_p^i \tag{1.1}$$

where C_p^i are all the parasitic capacitances on the signal path, i.e. capacitance of the device under test (DUT), cables, interconnections, instrumentation and so on. In other words, by reducing the area of the device and by moving the read out circuit close to the sensor, adopting integrated solutions, is one of the key characteristics in developing new biosensor devices with lower LOD. Alternative and widely used solutions are the lock-in amplifiers [53, 54] that avoid the use of complex high-frequency filters with a narrow band. To do so, the lock-in firstly uses a modulator to shift the signal from high frequency to base band and secondly uses a low-pass filter to remove noise and undesired harmonics generated by the modulation step.

1.2 Summary and scope

In the last decades the world of research has seen the birth of various hybrid fields combining together different communities as, for example, bioelectronics. Fields such as biology and medicine are historically based exclusively on experiments and empirical facts, while electronic engineers are more suited to develop models and rely on the results of accurate physically-based simulation tools. For this reason, two extremely different ways of doing research are merging together. For example, equivalent electrical models and simulation tools that were typically considered with scepticism by biologists and doctors, are now starting to get more visibility and receive higher attention.

It is the purpose of this thesis to develop new analytical and numerical models to analyze and interpret the experimental findings. The scope is also to develop compact equivalent models to get a simplified view of a complex real system composed by the device under test (the electronic part) and its surrounding environment (the biological part). At the same time we aim to extend and optimize currently available simulation tools, with existing or newly developed models, in order to design new and optimized devices with biosensing capabilities.

In this thesis we analyze ISFETs made of NRs working in DC and AC conditions and impedance spectroscopy data on EIS samples. Chapter 3 is essential, since it presents the simulation tools (commercial TCAD and ad-hoc simulators) and the analytical and numerical models (models of surface reactions, i.e. the site-binding model) that will be

used as additional tools to analyze and interpret the experimental data on ISFETs and EIS devices.

Chapter 4 is dedicated to the NRs working in DC conditions. We started with a thorough characterization of the NR devices working in dry and liquid environments and we compared the features of each working condition. Then, we characterized the pH-sensitivity of the NRs in liquid, analyzing different working regions (subthreshold and triode regions) and using both p-MOS and n-MOS devices. Finally, we completed the DC analysis with an accurate analysis of the signal-to-noise ratio, from which we extracted the minimum detectable pH change with the considered technology.

Chapter 5 is dedicated to NRs and EIS working in AC conditions. We started presenting experiments in AC with bare NRs, on which we calibrated a quasi-3D model made of a combination of finite element simulations and lumped elements. The model was then used to study the capabilities of NRs to detect dielectric microparticles in solution. Lastly, we analyzed impedance spectroscopy data on EIS devices functionalized with PNA molecules on top of a self-assembled monolayer. We built a physically-based equivalent circuit model to study the effect of different PNA molecule orientations.

Chapter 2

Devices

The purpose of this chapter is to present the devices that have been used throughout this thesis. Section 2.1 is focused on the fabrication process, layout and measurement set-up of a silicon chip of nanoribbon (NR) devices explicitly designed and fabricated for measurements in liquid environment. The devices were fabricated at CEA-LETI and afterwards they were measured at the University of Udine (concerning the characterization in air, sec. 4.1) and at the École Polytechnique Fédérale de Lausanne, CLSE laboratory (concerning the characterization in liquid, sec. 4.2 and sec. 4.4, and the measurements with microparticles, sec. 5.1). In section 2.2 we present the Electrolyte-Insulator-Semiconductor (EIS) capacitors, used for the electrochemical measurements discussed in chapter 5. This is essentially a one dimensional system which serves as case study for the electrical processes occurring in AC small signal operation at functionalized surfaces. The EIS samples were characterized by the group at the Technische Universität München (TUM, Munich) following the measurements procedures we suggested and abundant data was available for our analysis. Section 2.3 reports the fabrication process and the gate-oxide characterization of FinFET nanodevices with high-k dielectric developed for measurements in liquid. These devices were fabricated at CMI-EPFL and the electrical characterization was performed at NANOLAB (EPFL).

2.1 Nanoribbons

We start presenting the nanoribbon (NR) devices used extensively in this work, chapters 4 and 5. Fig. 2.1 (right) is an optical image of the silicon chip on which the NRs are fabricated. The position of the NRs are indicated by the white circles in the picture. The devices can be addressed by connecting needle probes on the square contacts positioned on the sides of the chip. The chips were designed and fabricated at CEA-LETI. Thanks to the collaboration with Dr. Thomas Ernst of this institution we could receive samples for research activities. Fig. 2.1 (right) reproduces the 2×2 cm^2 chip.

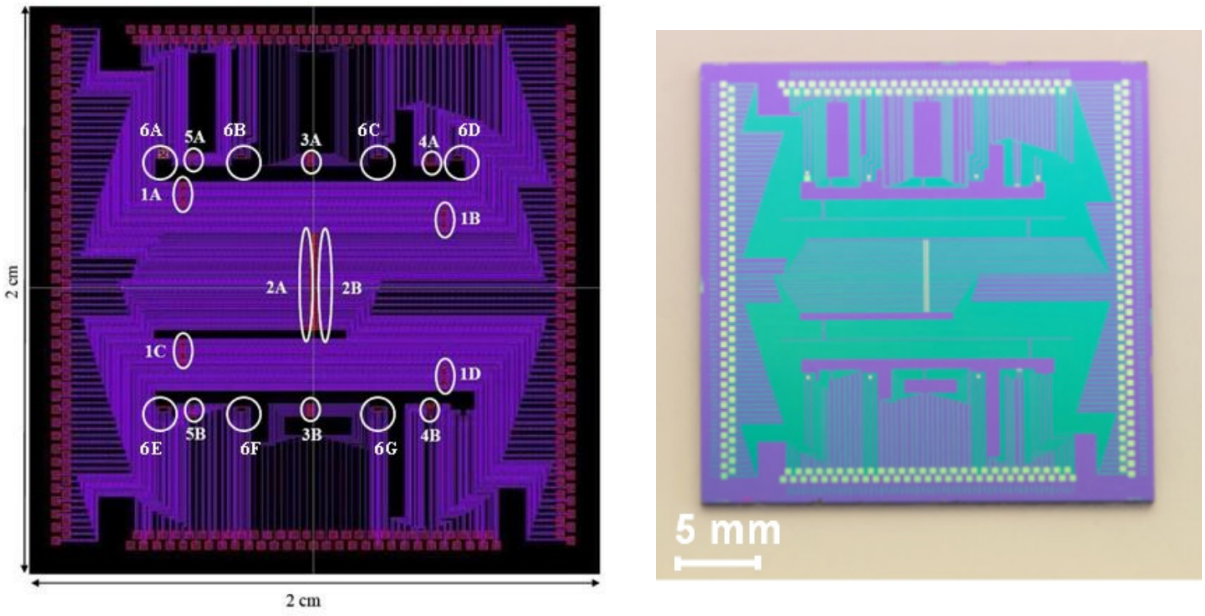

Figure 2.1: *Chip of silicon nanoribbon devices fabricated at CEA-LETI. Left: optical image with indications of the devices positions. Right: picture of one chip, taken after standard surface cleaning procedure [37].*

2.1.1 Technology and Fabrication Process

The fabrication starts from an SOI wafer that is patterned by means of a top-down hybrid deep ultraviolet (DUV) and e-beam lithography followed by a reactive ion etching (RIE). A summary of the main fabrication steps is reported in fig. 2.2. The wafers feature a 200 nm thick silicon layer on top of a 400 nm thick SiO_2 buried oxide layer (BOX). The first operation is to thin down the top layer by chemical mechanical polishing (CMP) and then by using several steps of thermal oxidation/deoxidation to obtain the desired silicon thickness, nominally 50 nm. Devices are then patterned by using DUV, if their feature sizes are above 300 nm, or e-beam lithography for smaller devices, down to widths of 50 nm. Once the NRs are patterned the RIE is performed. An high quality SiO_2 is then grown by using dry thermal oxidation. This will be the gate oxide of the NRs, and the thicknesses available are 3 or 8.5 nm, depending on the wafer (see tab. 2.1). Drain,

source and channel regions are doped with boron or phosphorous to obtain n-type or p-type dopings. A sacrificial polysilicon gate is used as an hard mask to dope the source and drain terminals, thus effectively defining the NR channel length. The entire chip surface, with the exceptions of the contact pads and the NR channel, is passivated by a multi-layer insulator composed of 50 nm of Si_3N_4, 300 nm of tetraethyl orthosilicate (TEOS) and 200 nm phosphosilicate glass (PSG). This is a thick large-area of passivation that prevents short-circuits and failures due to the exposure to liquid solution, moisture and humidity. The multilayer structure is favourable compared to a single-layer one to avoid the propagation of pin-holes in the passivation, that could short-circuit the electrolyte solution with the contact lines [55].

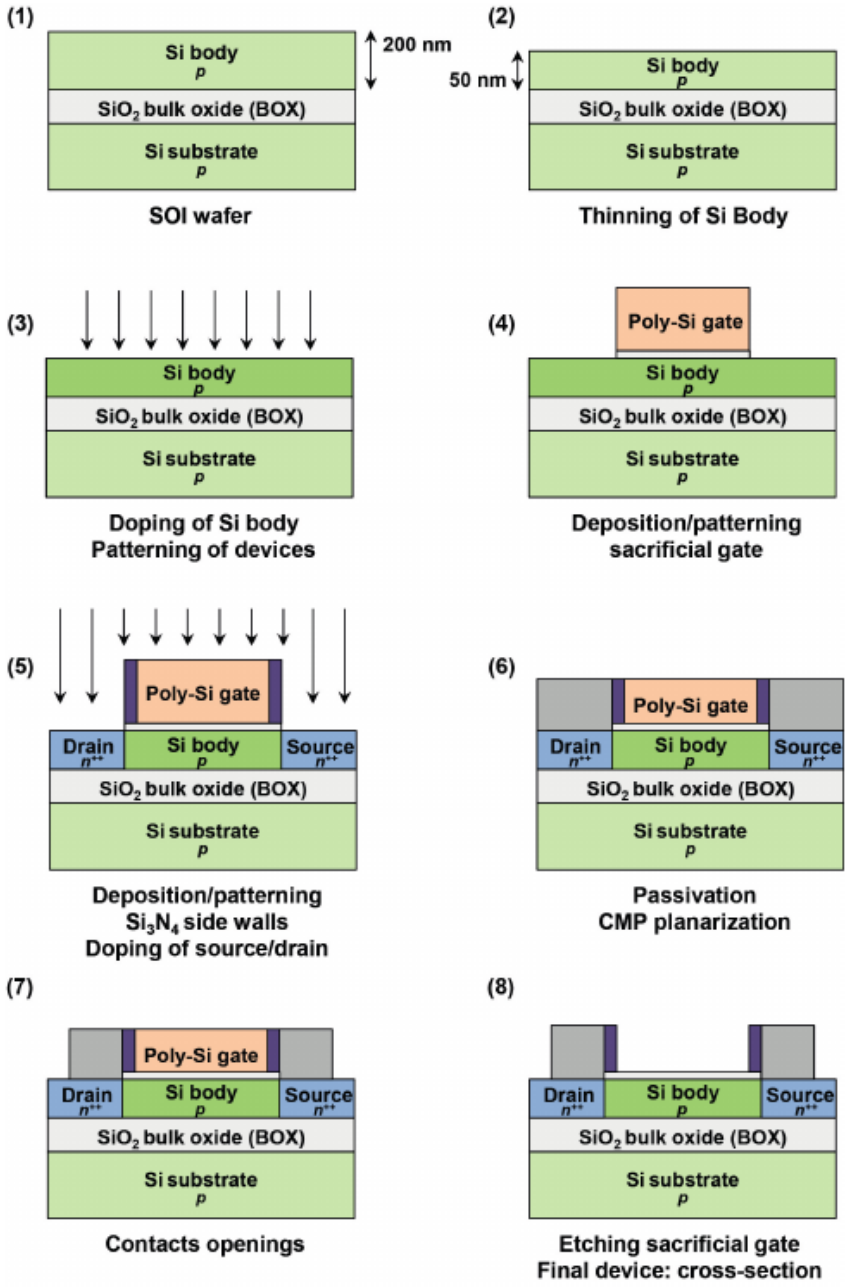

Figure 2.2: *Summary of the main fabrication process steps for the silicon NR [56].*

The SEM image in fig. 2.3 shows the top-view of a NR at the end of the fabrication process. The light grey part all around the NR and covering the source and drain leads is the multi-layer insulator that passivates the whole chip surface. Only small openings, like the one in dark grey in the figure, are made to expose the NR top oxide to the liquid environment.

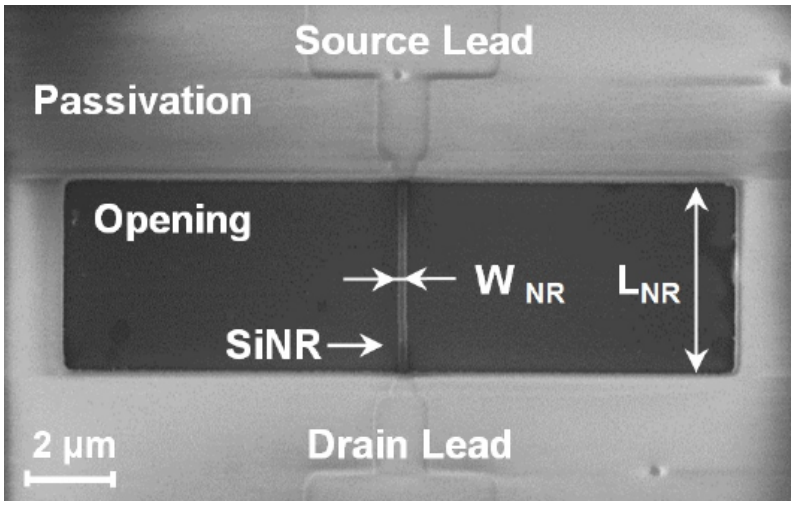

Figure 2.3: *SEM image of a nanoribbon.*

CEA-LETI fabricated a batch of wafers with different characteristics. Tab. 2.1 summarizes the parameters of the wafers that we have measured and characterized. On each wafer there are 38 identical chips, as the one reported in fig. 2.1. Each chip has approximately 140 devices, with a broad range of different geometries: widths ranging from 30 nm to 300 μm and lengths ranging from 500 nm to 300 μm. On the corners of the chip, the designers arranged also a few useful test structures for series resistance extraction (see sec. 4.1.1).

Parameters [Units]	wafer p24	wafer p05	wafer p07	wafer p11/p12
Doping S/D [cm^{-3}]	n^{++}, $>10^{20}$	n^{++}, $>10^{20}$	p^{++}, $>10^{20}$	n^{++}, $>10^{20}$
Doping channel [cm^{-3}]	p^{+}, $5{\cdot}10^{18}$	n, 10^{16}	n, 10^{16}	p, 10^{16}
Channel thickness [nm]	50	25	25	25
Gate Oxide Thickness [nm]	3	3	8.5	3
Silicide Contacts [PtSi]	No	Yes	Yes	Yes
Silicide S/D [PtSi]	No	Yes	Yes	No

Table 2.1: Parameters of the wafers fabricated at CEA-LETI.

In general, the top-silicon layer, defining source, drain and channel regions, is 50 nm thick over the whole wafer. In some wafers, such has the p12, the thickness of the nanoribbon channel has been reduced to 25 nm, while maintaining source and drain regions at 50 nm. Wafer batches can also be distinguished by the different types of

contact pads and source/drain interconnections. As reported in fig. 2.5 there are 3 different possibilities: 1) contacts and S/D regions of doped silicon; 2) silicided contacts and 3) silicidation along the entire path from the S/D to the contacts. This latter option results in a large difference in terms of series resistances. By looking at fig 2.1 we see that the contact pads are placed on the edges of the silicon chip while the devices are placed in the inner part; thus, the interconnection is very long and adds non negligible series resistance. This is nevertheless inevitable, because there must be room to install microfluidic pipes onto the chip, as we will see more in detail in the next section.

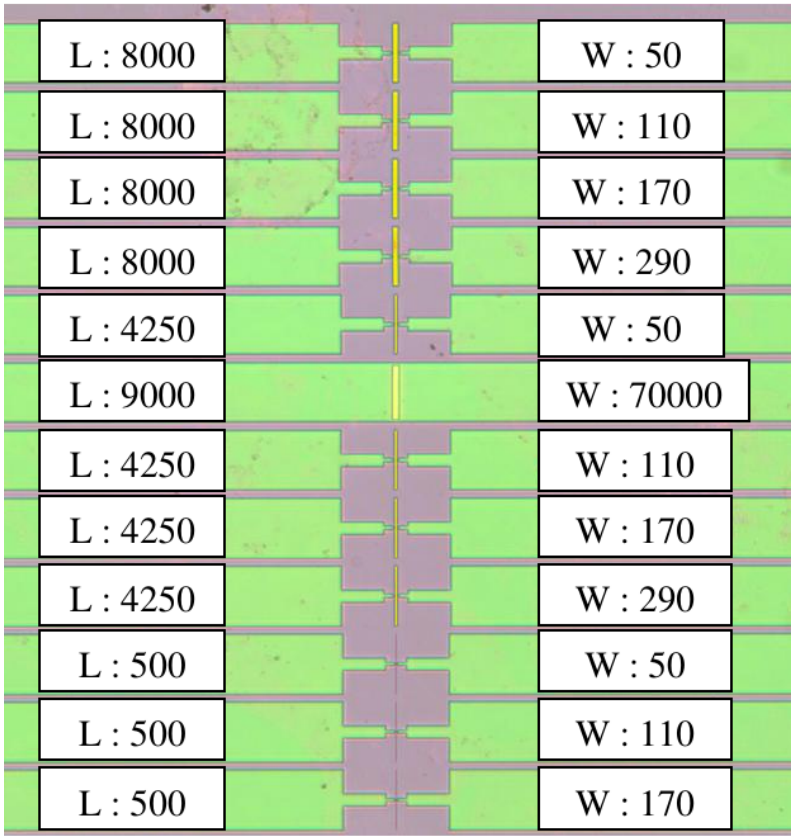

Figure 2.4: *Optical image of an array of nanoribbons with indication of the device dimensions.*

2.1.2 Microfluidics and Ag/AgCl Reference Electrode

Thanks to a collaboration with prof. Carlotta Guiducci we had the opportunity to perform experiments in liquid environment by using the facilities an the measurement instrumentation of the CLSE Laboratory at EPFL (Lausanne), as a part of a long term stage at the laboratory. In order to measure the devices in liquid, microfluidics and reference electrodes are necessary [37], fig. 2.7. The micro-channels are obtained with a chemical-resistant double-coated tape (3M 9086), patterned by laser micro-machining. The height of the channels is thereby defined by the thickness of the tape ($\sim$190 μm). A poly(methyl methacrylate) (PMMA) cap with 6 holes drilled in the locations of inlets and outlets is

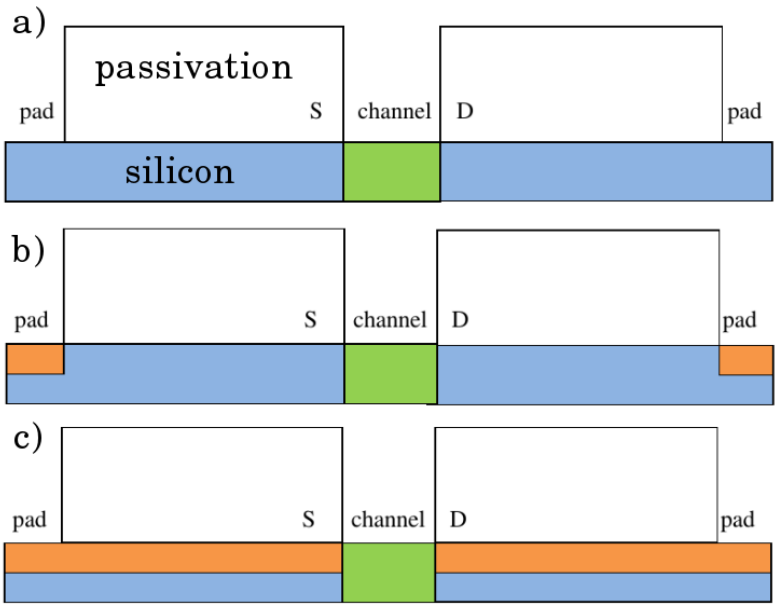

Figure 2.5: *Sketch of nanoribbon contacts. The orange area represent the silicide. See tab. 2.1 for indications on the available samples. a) unsilicided; b) silicided pads; c) fully silicided.*

placed on top of the tape to seal the channels. The inlet and outlet tubes are then inserted. A syringe pump (Harvard Apparatus) is used to flux the solution of interest into the microfluidics. Due to the double-coated tape system, the microfluidics can easily be removed by incubating the chip in 2-Propanol alcohol overnight. The chip can, therefore, be cleaned thoroughly and re-used.

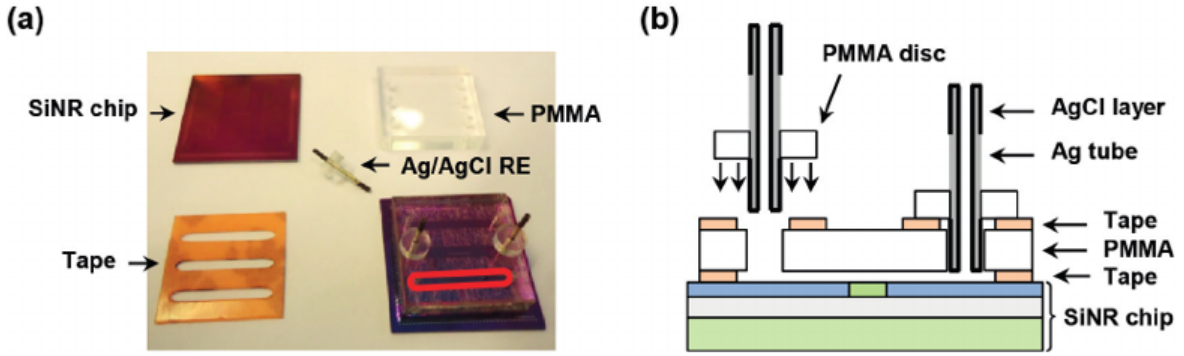

Figure 2.6: *Left: silicon chip, PMMA microfluidics, double-coated tape and Ag/AgCl reference electrode (disassembled and assembled). Right: cross-section of a micro-channel (chip and microfluidic mounted on top), illustrating the insertion of the Ag/AgCl reference electrodes. Figure taken from [37].*

The Ag/AgCl electrodes are obtained by a galvanostatic oxidation on silver tubes. The silver tubes are dipped in 100 mM HNO_3 for about 1 min, in order to clean and activate the surface, and then rinsed with deionized water. After the surface activation,

the silver wire is connected to a working electrode (anode); a platinum wire is connected to a counter electrode (cathode) and both of them are dipped into a solution of 100 mM KCl. A current density of 2.5 mA/cm^2 is applied at the anode for a time that depends on the desired thickness of the AgCl layer (5 μm in this work). At the end of the oxidation, the Ag/AgCl tubes are dipped into a solution of 100 mM KCl for at least 4 hours prior to use.

2.1.3 Measurement Set-up

Fig. 2.7 shows a typical measurement set-up used for the characterizations described in sections 4.2 and 4.4. Once the microfluidics is mounted the chip can be placed and blocked on the chuck of a probe station to set-up the external connections. The reference electrodes are contacted by two crocodile connectors. The tubing are connected on one end to a syringe pump and on the other end to an Eppendorf. The Eppendorf acts as a reservoir or tank for the liquid, depending if the syringe is pumping or sucking. The devices are individually accessible by contacting the probes to the contact pads on the border of the chip. The chuck can be used to bias the back gate, since the back side of the chip is metallized. By using 4 probes, it is possible to measure at the same time up to 3 different devices; in fact, some of the devices on the chip share a common source contact. The probe station has an external Faraday cage that protects the devices from external electrical noise sources and light. The probes are accessible from outside instrumentation by triaxial connectors placed on the faraday cage. This measurement set-up is highly flexible because it is easy to mount and unmount the microfluidics, and to change the reference electrodes or switch from one NR to the other. It provides direct access to each single device on the chip, with low resistance probes and shielded triaxial cables for low current measurements, without the necessity of a read out circuit.

In the following sections we present results of three different kind of measurements with such system. Current-voltage (or I-V) and current-sampling (or I-t) measurements in DC conditions and impedance spectroscopy measurements. The former two, were performed with a semiconductor parameter analyzer (SPA, Agilent 4156C) controlled by Matlab scripts through a GPIB interface, while the latter were performed with a lock-in amplifier (Zurich Instruments, HF2LI Lock-in Amplifier) controlled by a PC with proprietary software.

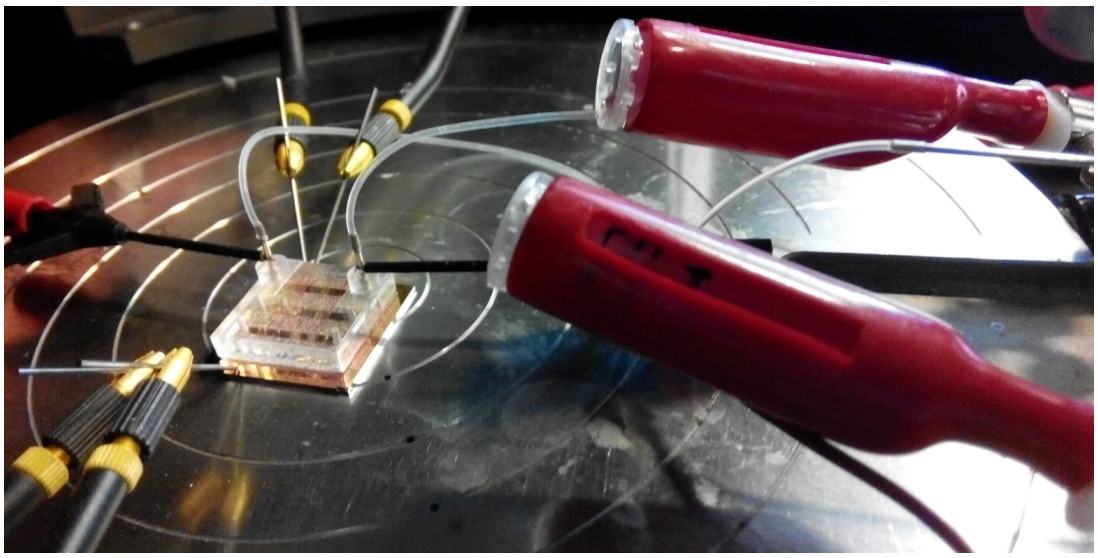

Figure 2.7: *Picture of a typical measurement set-up. Silicon chip with PMMA microfluidics, two reference electrodes contacted by crocodile connectors, four needle probes of the probe station contacting the devices pads and 2 Eppendorf positioned inside a red holder. On the top right side of the picture the needle of the syringe can be glimpsed.*

2.2 Electrolyte/Insulator/Semicondutor Capacitors

Electrolyte-Insulator-Semiconductor (EIS) capacitors are widely used test structures in biosensor development. Due to their simple 1-D structure they represent a testing workbench for a wide variety of application related to the sensing at the solid/liquid interface. In our case the interface is made of semiconductor native oxide in contact with an electrolyte (usually a buffered solution). As we have anticipated in the introduction, with such a device it is possible to sense charges and particles positioned at the interface or at least at a distance of a few Debye lengths from the interface. Thanks to a collaboration with prof. Anna Cattani-Scholtz (TUM, Walter Schottky Institut) we had the possibility to access electrochemical impedance spectroscopy data performed on EIS capacitors samples, as the one reported in fig. 2.8. The capacitor sample is a stack of metal (Cr/Au), Boron-doped silicon ($\sim 4 \cdot 10^1 8$ cm^{-3}, 360 µm thick) and native silicon dioxide (SiO_2 thickness expected to be $\approx$1 nm). The back metal contact is used as *working* electrode to bias the device. The sample is positioned inside a teflon chamber, closed by a teflon cap on top, that ensures complete darkness and electrical insulation from the external environment. The chamber is filled by an electrolyte solution, in which are immersed an Ag/AgCl *reference* electrode and a self-made platinized wire platinum *counter* electrode. This is a typical three-electrode configuration, widely used for electrochemistry experiments. The sample surface area of 0.189 cm^2 is defined by the Teflon chamber and it is the only portion of the substrate wetted by the solution.

Impedance measurements were made using a Metrohm Autolab PGSTAT 12 potentiostat in a single-sine recorded as a function of frequency between 0.1 Hz and 100 kHz,

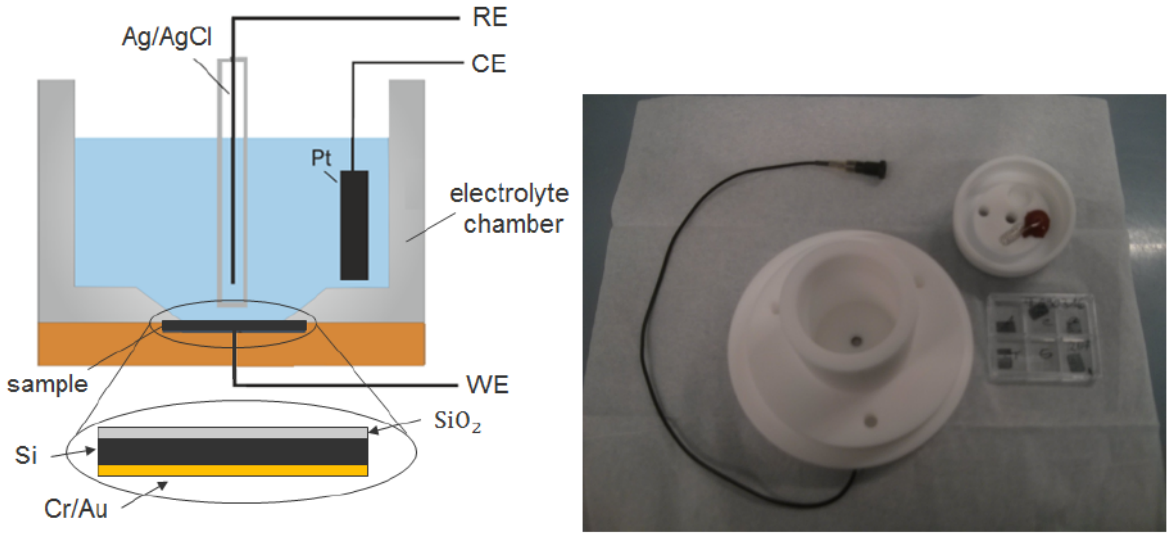

(a) Chamber schematic **(b)** Measurement cell

Figure 2.8: *Left: chamber cross-section schematic, with a zoom on the sample device. Right: measurement cell made of teflon (chamber and cap disassembled).*

with an AC signal amplitude of 50 mV.

To be able to sense specific molecules (e.g. DNA), the interface between the silicon-based sensor and the electrolyte has to be duly functionalized. Fig. 2.9 summarizes different surface conditions considered in this work. Fig. 2.9a is a sketch of the reference system, that is just native silicon dioxide in contact with the electrolyte. The first step is to functionalize the surface with a self assembled monlayer (SAM), fig 2.9b. In our case a self-assembled monolayer of phosphonates (SAMPs) have been used. SAMPs have been reported to be an attractive alternative to the commonly used organo-silicon-based coating SAMs [57, 58]. After that, a maleimdo-linker is deposited onto the SAMP to immobilize PNA molecules, fig 2.9c. PNA molecules are artificially synthesized polymer that also show greater specificity in binding to complementary DNAs. The main reason is that the PNA backbone has no charged phosphate groups, thus there is no electrostatic repulsion with a DNA strand (taht is negatively charged). In chapter 5 we analyze the response for two type of PNA. PNA1, that has 3 anchor points for binding to the malmeido-linker, and PNA2 that has only one anchor point at one end of the strand. We expect to see a different response due to the fact that the PNA1 is forced in an horizontal position, while PNA2 is anchored on one end and the other is free to bend. As a last step, fig 2.9d, DNA strands are injected in the solution and hybridization (PNA/DNA biding) can occur at the surface, eventually affecting the EIS response. By performing impedance measurements we aim to electrically characterize and extract characteristic special features that can be a signature of each individual stage.

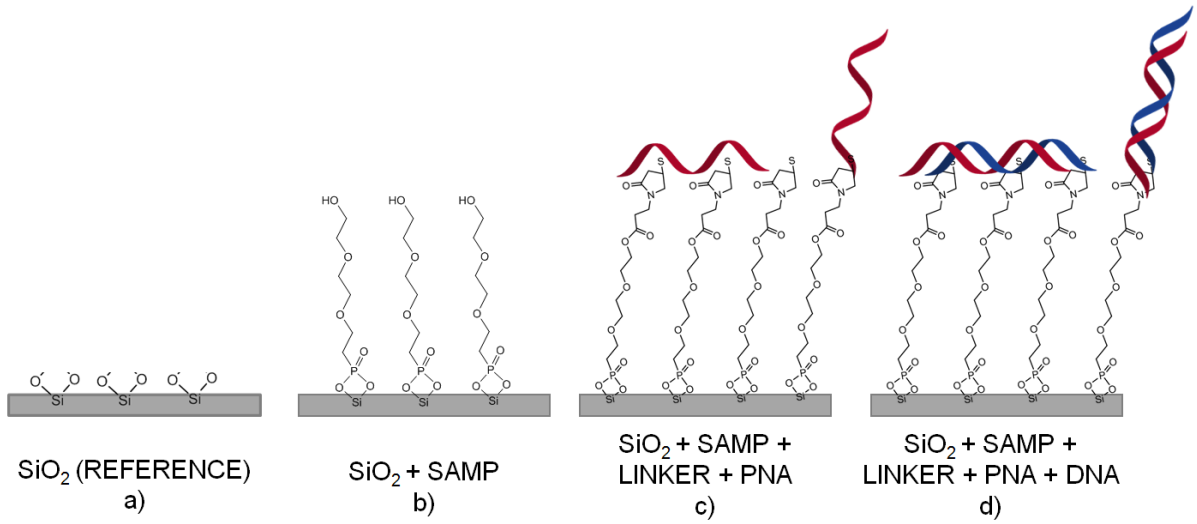

Figure 2.9: *Sketch of the EIS system at different stages of the surface modification process. Note the two different arrangements of PNA+DNA.*

2.3 FinFETs

The FinFETs were fabricated according to a top-down approach on a bulk silicon substrate. The fabrication aimed at a specific and reproducible geometry of the FinFETs, with the body of the devices isolated from the substrate similarly to what is expected on SOI wafers, and a high-k dielectric (HfO_2) as the sensing gate insulator. The whole fabrication process can be simplified as shown in fig. 2.10. A well-controlled wet oxidation of the etched silicon fins protected by the Si_3N_4 spacers is used to provide a local SOI structure for every fin device. The final dimensions of the fabricated device are 16 nm $\leq$ T_{Fin} $\leq$ 40 nm and 50 nm $\leq$ H_{Fin} $\leq$ 120 nm, with H_{Fin}/T_{Fin} always greater than 3.

The quality and uniformity of the FinFETs have been first tested on the metal gate devices. Subthreshold slope (SS) values are in the range of 70 mV/dec and 81 mV/dec with the steepest value achieved for the smallest T_{Fin} = 16 nm. The ratio between ON and OFF currents is I_{on}/I_{off} ~100, with the highest value $I_{on}/I_{off} = 2{\cdot}10^6$ obtained for T_{Fin} = 40 nm. Such excellent results imply that there is no parasitic leakage current through the bulk Si, and the local SOI on bulk offers equivalent performance to a fully depleted FinFET on SOI.

The FinFET sensors have been tested in liquid gate configuration, and long-term stability measurements have been performed over 4.5 days [20]. All devices feature a HfO_2 oxide with a thickness of $t_{HfO_2} \sim 8$ nm. The wafers have been treated with a full RCA cleaning[1] followed by a Piranha[2] step, thus the presence of a chemical oxide (also

[1]RCA is a standard process to clean a semiconductor substrate before any other fabrication step, e.g. thermal oxidation, diffusion or chemical deposition. The RCA cleaning process consists in three steps: 1) cleaning of organic contaminations, 2) removal of the native oxide layer, typically formed in the during the previous step)and 3) removal of the metallic contaminations.

[2]The piranha etching consist in cleaning the surface with a chemical mixture that removes completely

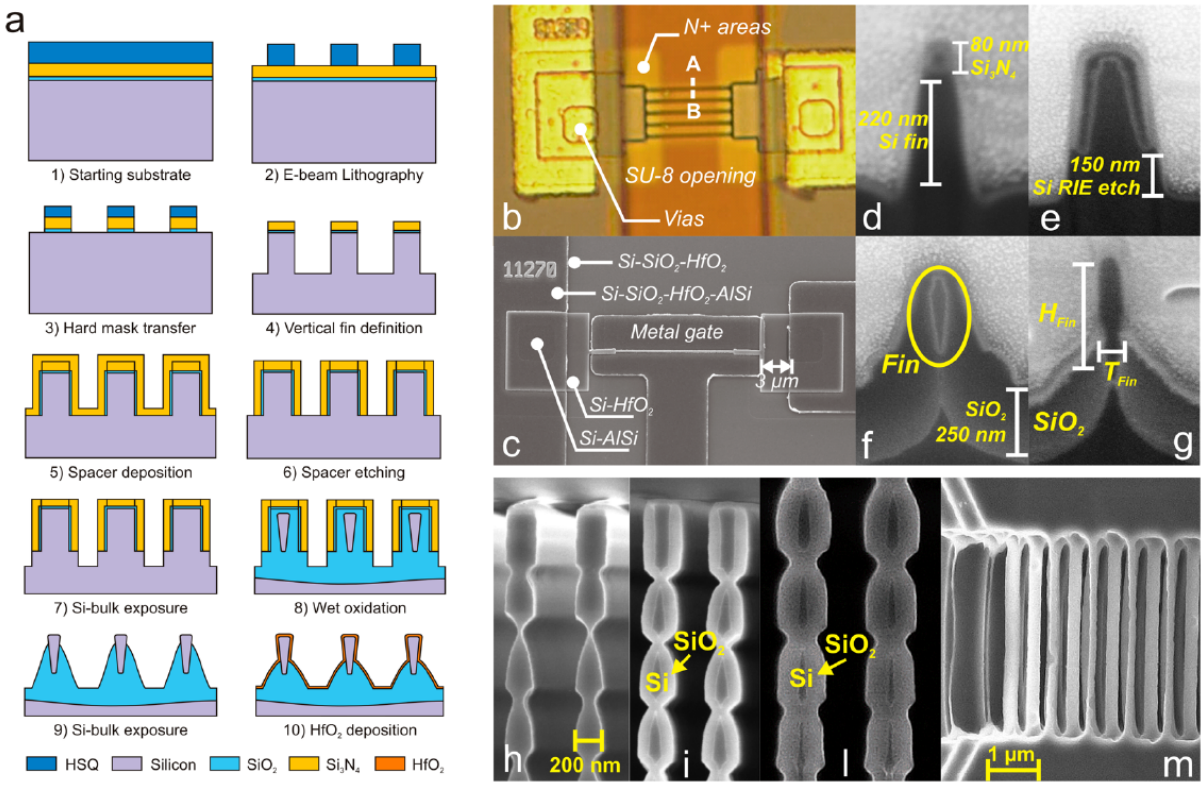

Figure 2.10: *a) Simplified process flow for two-dimensional FinFETs. b) Optical image of a FinFET array for sensing application with SU-8 next to the FET channels. c) SEM top image of a single FinFET with a metal gate. d) SEM cross sections obtained by focused ion beam during the fabrication process: definition of the vertical Si fin with top Si_3N_4 hard mask. e) Deposition of the Si_3N_4 spacers. f) Si fin after wet oxidation and growth of a 250 nm thick SiO_2 layer. g) Si fin after Si_3N_4/SiO_2 etching and exposure of the fin surface. h) Here we show a version of the process that can provide 3D fins formed with a combination of anisotropic and isotropic etches before oxidation to vertically stack multiple fin channels. (i) Nonsharp scallop 3D fins after oxidation. (l) Sharp scallop with O_2 step included after oxidation and (m) top side of 3D fin channel view after Buffered Oxide Etching (BOE) release. Note that the electrical and sensing characteristics reported in this work correspond to devices in panels b-g. Figure taken from [20].*

called Interface Layer, IL) between Si and HfO_2 of around 1 nm is highly probable. On this particular aspect an extensive characterization of different insulators has been made. In fact, for application such as pH-sensing, it is important to use a gate insulator that has a linear and high sensitivity over the whole range of pH values. Of course one should also consider a good-quality insulator, meaning low hysteresis (low concentration of traps), high dielectric constant and compatibility with the CMOS fabrication process.

any organic contaminations, and due to its strong oxidizing properties, it will also hydroxylate the semiconductor surface, making it highly hydrophilic.

2.3.1 Gate Insulator Characterization

The hafnium dioxide was deposited using a technique called Atomic Layer Deposition (ALD). This is a complex and recently developed technique for the deposition of thin oxide films on semiconductor substrates. For this reason, simple metal-oxide-semiconductor capacitors (MOSCAP) have been fabricated in order to characterize the electrical properties of the insulator. We started by depositing the hafnium dioxide directly on the semiconductor substrate after different cleaning processes, as summarized by the TEM images in fig. 2.11. After that, we also tried to deposit the HfO_2 on a thin layer of thermally grown SiO_2. Some of the wafers were finally subjected to thermal treatments, such as Post Deposition Annealing (PDA) or Post Metallization Annealing (PMA). Each wafer was then electrically characterized by means of capacitance-voltage and current-voltage measurements, as reported in fig. 2.12.

We start by considering the different cleaning processes reported in fig. 2.11. These procedures not only result in a different thickness of the interface layer (IL), but its chemical nature is different [59], meaning that each IL has different electrical properties as demonstrated by the results presented in [60]. A simple RCA and an RCA followed by a Piranha step exhibit two main differences. Firstly, Piranha treatment leads to a smaller hysteresis with respect to the standard RCA. Secondly, a higher dielectric constant is observed for the Piranha cleaning for wafer with no annealing. In agreement with the presented results, Green et al. [61] have reported that the use of a chemical oxide as the one produced by a Piranha cleaning results in almost no barrier to film nucleation, enabling linear and predictable growth at constant film density, and the most two-dimensionally continuous HfO_2 film. By adopting HF cleaning lousy results were achieved, thus it is not recommended.

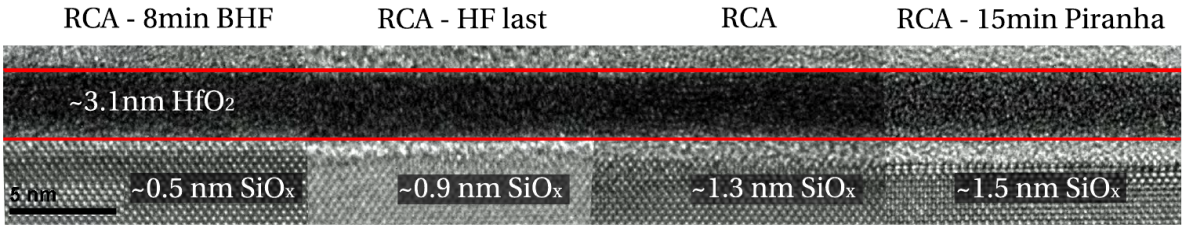

Figure 2.11: *TEM image of HfO_2 deposited on silicon substrate treated with four different cleaning processes (courtesy of M. Zervas, LSM, EPFL). Picture taken from [60].*

Hysteresis in C-V curves has been calculated by linear interpolation of the measurements as the voltage difference (ΔV_H) between forward and backward curves, correspondent to $y = (C_{max} + C_{min})/2$. C_{max} and C_{min} are the maximum and minimum capacitance values recorded during one measurement.

When HfO_2 is directly deposited on Si substrates, an IL layer seems to be inevitably formed at the Si interface, as clearly visible in fig. 2.12b. Annealing performed at different process step and cleaning procedures have resulted in small changes in the oxide electrical

properties. Satisfactory results have been reported in terms of dielectric constant, low level of leakage current and high breakdown voltages [62, 20], but, hysteresis values are still quite pronounced with the lowest value of $\Delta V_H = 0.27$ V obtained for a RCA followed by Piranha cleaning and PDA. Considering pH sensing the main application of the FinFETs, ΔV_H is still five times higher than $\Delta V_{TH} = 56$ mV/pH, which is the maximum threshold voltage shift expected for $\Delta pH = 1$. A solution to avoid the formation of the IL and consequently reducing the hysteresis consist in the integration of a thermally grown thin layers of SiO_2 before the hafnium dioxide deposition, as illustrated by the TEM image in fig. 2.12d. Of course there is a trade off between the thickness of the SiO_2 layer, the maximum tolerated hysteresis and the minimum affordable dielectric constant. The oxide capacitance, $C_{OX} = \varepsilon_0 \varepsilon_{OX}/t_{OX}$, is an important parameter that defines the performances of a MOSFET device. Materials with a high dielectric constant, e.g. HfO_2, enables thicker oxide thickness, meaning better insulation properties (especially when operating in liquid environments) and typically lower complexity of the fabrication process. By the results of our study, the hysteresis in the C-V curves decreases as the SiO_2 layer thickness increases, resulting in more reliable devices. However, increasing the SiO_2 layer leads to a lower overall dielectric constant.

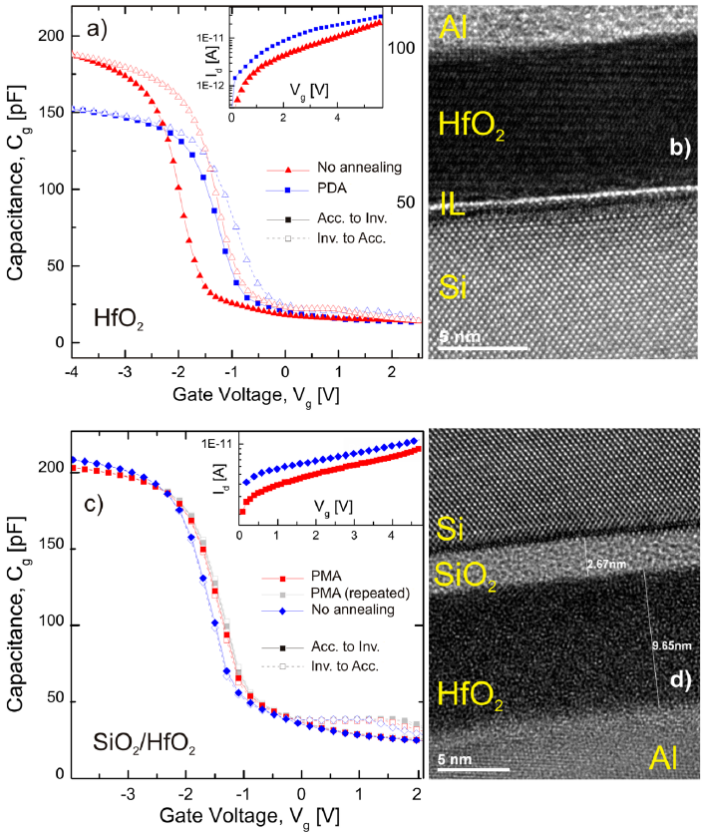

Figure 2.12: *Left graphs: C-V and I-V (inset) measurements of the (a) $Si/HfO_2/Al$ and (c) $Si/SiO_2/HfO_2/Al$ FinFET gate stack. Right: TEM images of the respective gate stack. Figure taken from [20].*

2.4 Summary

- Three type of devices have been considered and characterized in this thesis for possible use as nanoelectronic sensing elements: 1) nanoribbon devices with SiO_2 gate oxide, operated in DC as pH meters and in AC as microparticle detection elements; 2) nanoscale FinFET transistors with high-k gate dielectric (HfO_2), and 3) Electrolyte/Insulator/Semiconductor (EIS) capacitors with SiO_2 dielectric and functionalized surfaces for DNA/PNA detection and hybridization sensing.

- HfO_2 dielectrics stacked on top of moderately thick SiO_2, hold the promise for improved pH sensitivity as will be shown in sec. 3.2.3 but suffer from high level of traps and defects, and complex deposition processes. SiO_2 dielectrics exhibit reduced sensitivity at low pH values but yield stable trap-free interfaces at least when the oxide thickness is large enough.

- We exploit the variety of available nanoribbon geometrical dimensions to study the impact of the device geometry and scaling on the performance (e.g. sensitivity and signal-to-noise ratio, see sec. 4.5).

- Available FinFETs have less variety of device dimensions compared to the planar NR devices. The width is essentially set to multiple integers of $(2 \cdot W_{Fin} + H_{Fin})$. However, since they feature HfO_2 as gate-oxide, the pH differential sensitivity as predicted by the models in chapter 3 is expected to be higher, less pH dependent and closer to the Nernst limit than for the available NR counterparts. Very thin nanoribbons with the same high-k gate dielectric, however, are expected to exhibit performance similar to the FinFETs.

Chapter 3

Models and Simulation Tools

This chapter presents the models and the simulation tools that were developed and used in this thesis to investigate the devices described in chapter 2 and to interpret the experiments in chapters 4 and 5. We start by illustrating the mathematical framework on which the simulation tools and the models that we present in the following sections are based on. Section 3.1 starts by presenting the DC and AC modeling framework, based on the Poisson-Boltzmann and Poisson-Nernst-Plank equations, respectively. Section 3.2 starts by introducing the theoretical concepts necessary to understand the models, such as the physics that governs the solid/liquid interface.

Next, we discuss the surface electrochemistry models that have been additionally implemented into the existing simulation tools. Section 3.3 presents the three simulation tools that have been partially developed and used throughout the thesis, and the implementation of the surface electrochemistry models. Furthermore, we dedicate an additional section to present the simulation platform implemented on nanoHUB.org that we used to open to the general public worldwide two different tools for the simulation of biosensors. Section 3.4 is devoted to a compact analytical model for the AC response of nanoelectrode-based impedimetric biosensors to dielectric nanoparticles in electrolyte solution.

3.1 The PB-PNP model framework

In this work we assume that the biosensors are fabricated by micro/nanotechnologies combining together three different types of materials (semiconductors, insulators and electrolytes) to form a complete device for biological measurements.

The mathematical framework, to describe such a sennsor system, is set by the Poisson-Boltzmann (PB) equation (at equilibrium) and the Poisson-Nernst-Plank equations (PNP, also known as Poisson drift-diffusion equations) for transport in the AC small signal regime. This set of equations has been widely used in literature for biosensor modelling. [25, 63, 64, 65, 66, 67, 68, 69, 70, 71]. Results prove it serves as a valuable framework to interpret impedance spectrum experiments and steer sensor device design.

As anticipated in the introduction the activity addresses both DC and AC operating conditions, and characterizations were carried out in both regimes. For this reason we will present models and simulation tools covering both DC and small signal frequency dependent domains.

3.1.1 Numerical models for DC operation

The electrostatics of the system under study is described by the Poisson equation

$$\nabla \cdot (\varepsilon \nabla V_0) = -\rho_0 = -(\rho_{0,f} + \rho_{0,nl}) \tag{3.1}$$

Here, the subscript 0 indicates the steady state DC variables. ρ_0 is the total volume charge density in the system, that is given by the sum of a component independent of bias voltages $\rho_{0,f}$ (e.g. the semiconductor doping) and a non-linear term $\rho_{0,nl}$ (i.e. the ionic charge in the electrolyte or the free carriers charge in the semiconductor), that is a non-linear function of the potential, V. In fact, both for semiconductors and electrolytes we can express the mobile charge as:

$$\rho_{0,nl} = \sum_{m=1}^{N} Z_m q n_{0m} \tag{3.2}$$

where Z_m is the signed valence and n_{0m} is the steady state value of the ion/carrier concentration n_m. The latter is always (both DC and AC cases) given by

$$n_m = n_m^{\infty} exp\left(\frac{Z_m q}{k_B T}(\phi_m - V)\right) \tag{3.3}$$

where the ϕ_m are the ion/carriers pseudo-potentials. For the case of semiconductor, n_m is either the electron or the hole concentration (Z_m =-1 for electrons, +1 for holes) and it is possible to choose for the pseudo-potentials such that $n_m^{\infty} = n_i$, where n_i is the intrinsic carrier concentration.

By combining eq. 3.1, 3.2 and 3.3 we obtain the Poisson-Boltzmann equation

$$\nabla \cdot (\varepsilon \nabla V_0) = -\left(\rho_f + \sum_{m=1}^{N} Z_m q n_{0m}^{\infty} exp\left(\frac{Z_m q}{k_B T}(\phi_{0m} - V_0)\right)\right). \tag{3.4}$$

Together with a suitable set of boundary conditions eq. 3.4 describes both the electrolyte and semiconductor. As for the dielectrics the voltage dependent charge term is null.

Since we are mostly interested to the AC operating regime, in our models we assume zero DC current flow in the electrolyte. The condition is approximately achieved with the use of ideally polarizable electrodes in noble metals and it implies that the current equations need to be written for the semiconductor only. To this end, we consider the drift-diffusion model equations

$$\frac{\partial n_m}{\partial t} + U_{gr} = -\frac{\nabla \cdot \vec{J_m}}{Z_m q} \tag{3.5}$$

where $U_{gr} = R - G$ is the generation-recombination rate (in units of $[1/\mathrm{m}^3\mathrm{s}]$) and $\vec{J_m}$ is the drift-diffusion current density, that can be written as

$$\vec{J_m} = -Z_m q \left[Z_m q \mu_m n_m \nabla V + D_m \nabla n_m \right] \tag{3.6}$$

where the Einstein relation

$$D_m = \mu_m k_B T \tag{3.7}$$

relates the mobility, expressed in $[m/N/s]$, and the diffusivity expressed in $[m^2/s]$. This form of the equation and the corresponding units stems from the definition of mobility as the ratio of the velocity to the force, and not to the electric field as routinely done in semiconductor physics. It can be used to describe both the semiconductor and the electrolyte materials provided the q term is correctly introduced at the right point of the equation.

Substitution of eq. 3.3 and eq. 3.7 in eq. 3.6 leads to a compact expression for the drift-diffusion current density

$$\vec{J_m} = -Z_m^2 q^2 \mu_m n_m \nabla \phi_m \tag{3.8}$$

Finally, by choosing the pseudo-potentials such that $n_m^{\infty} = n_i$, we can rearrange eq. 3.5 to obtain

$$U_{gr}(\phi_m, V) + n_i \frac{Z_m q}{k_B T}\left(\frac{\partial \phi_m}{\partial t} - \frac{\partial V}{\partial t}\right) exp\left(\frac{Z_m q}{k_B T}(\phi_m - V)\right) = Z_m q \mu_m \nabla \cdot \left(n_i exp\left(\frac{Z_m q}{k_B T}(\phi_m - V)\right)\right) \tag{3.9}$$

Eq. 3.9 and the associated boundary conditions define the pseudo-potentials, hence the current density via eq. 3.8. Jointly with Poisson equation 3.4 they describe the sensor system in DC conditions.

3.1.2 Numerical models for AC operation

The AC model framework stems from the same set of Poisson-Nernst-Plank equations as in the DC case. For the AC case however we embrace the so-called small-signal approximation, meaning that all the physical quantities, such as the potential, the pseudo-potentials and the concentrations are expressed as the sum of a DC and a time-harmonic AC component; namely:

$$\begin{aligned} \phi_m &= \phi_{0m} + Re\Big\{\tilde{\phi_m} \cdot exp(j\omega t)\Big\} \\ V &= V_0 + Re\Big\{\tilde{V} \cdot exp(j\omega t)\Big\} \end{aligned} \tag{3.10}$$

where $\tilde{V}$, $\tilde{\phi}_m$ are the complex phasors of the potential and the quasi-potentials. By assuming that $|\tilde{\phi}_m|, |\tilde{V}| < k_B T/q$ it is legitimate to linearize eq. 3.3, and neglecting the higher order terms, we obtain a linear relation between the small-signal concentrations and the difference between the potential and the pseudo-potential phasors

$$\tilde{n}_m = n_{0m} \frac{Z_m q}{k_B T} (\tilde{\phi}_m - \tilde{V}) \tag{3.11}$$

In the same fashion, upon linearization of the PB equation we get

$$\begin{aligned} \nabla \cdot \left[\varepsilon \nabla \left(V_0 + Re\{\tilde{V} exp(j\omega t\}\right)\right] + \\ \left[\rho_{0,f} + \sum_{m=1}^{N} Z_m q n_{0m}^{\infty} exp\left(\frac{Z_m q}{k_B T}(\phi_{0m} - V_0)\right)\left(1 + \frac{Z_m q}{k_B T} Re\Big\{(\tilde{\phi}_m - \tilde{V}) exp(j\omega t)\Big\}\right)\right] = 0 \end{aligned} \tag{3.12}$$

Since V_0 and ϕ_0 satisfy the PB equations in DC, we can rearrange and simplify equation 3.12 to obtain a compact version of the PB equation valid in the AC small-signal regime

$$\nabla \cdot \left(\varepsilon \nabla \tilde{V}\right) + \sum_{m=1}^{N} \frac{Z_m^2 q^2}{k_B T} \left(\tilde{\phi}_m - \tilde{V}\right) = 0 \tag{3.13}$$

As regards the PNP equations, we follow the same procedure outlined above. Linearization of eq. 3.9 yields

$$Z_m q \mu_m \nabla \cdot \left(n_{0m} \left(\frac{Z_m q}{k_B T} (\tilde{\phi}_m - \tilde{V}) \nabla \phi_{0m} + \nabla \tilde{\phi}_m\right)\right) - j\omega n_{0m} \frac{Z_m q}{k_B T} (\tilde{\phi}_m - \tilde{V}) = 0 \tag{3.14}$$

This equation can be further simplified in the case that $\nabla \phi_{0m} = 0$, which is valid if the electrolyte is in equilibrium and no DC current flows in it because of at most one electrode being faradaic and all others ideally polarizable. It follows that

$$Z_m q \mu_m \nabla \cdot (n_{0m} \nabla \tilde{\phi}_m) - j\omega n_{0m} \frac{Z_m q}{k_B T} (\tilde{\phi}_m - \tilde{V}) = 0 \tag{3.15}$$

In the time-harmonic AC regime the total current density is the sum of the displacement and of the ionic current densities

$$\vec{\tilde{J}} = \vec{\tilde{J}}_D + \sum_{m=1}^{N} \vec{\tilde{J}}_m \tag{3.16}$$

where the displacement ionic current density is

$$\vec{\tilde{J}}_D = -j\omega\varepsilon\nabla\tilde{V} \tag{3.17}$$

and the ionic current are

$$\vec{\tilde{J}}_m = -Z_m^2 q^2 \mu_m n_{0m} \left(\frac{Z_m q}{k_B T} (\tilde{\phi}_m - \tilde{V}) \nabla\phi_{0m} + \nabla\tilde{\phi}_m \right) \tag{3.18}$$

The AC current density at the electrodes is necessary to extract important parameters from the simulation results; e.g. the admittance Y (impedance Z) at the contacts

$$Y = \frac{\tilde{I}}{\tilde{V}} \tag{3.19}$$

where $\tilde{I} = \int\int \tilde{J} dA$ is the total current at the contacts (A is the contact area) and $\tilde{V}$ is the applied voltage.

Eqs. 3.13, 3.15 and 3.16 form the AC set of equation that have been implemented in our simulation tools (described in section 3.3) regarding the solution of the AC system.

3.2 Surface electrochemistry models

For the calculation of the DC and AC sensor response to ionic species and analytes in the electrolyte it is important to consider the surface charge possibly generated by surface reactions. The most fundamental ones have been identified in the early 1970s [72, 73, 74, 75], when the concept of Ion Sensitive Field Effect Transistor, ISFET, was presented and demonstrated for the first time [15]. The present work is particularly focused on the electrolyte-gated field-effect transistor or in more specific terms on the concept of ISFET, where the metal gate is replaced by an electrolyte solution. This kind of devices are used as pH and ion sensors operating in liquid environment. ISFET-based devices are nowadays considered for a wide variety of new applications. In particular, they have gained remarkable attention as building blocks for new generation DNA sequencing platforms [76, 77]. In these platforms ISFETs are employed in massively parallel pH-sensors due to their capability to sense the concentration of H^+ ions in solution. In the following, we start by presenting the theory for the electrical modelling of the solid/liquid interface (sec. 3.2.1). Thereafter, we present briefly the theory that lies behind the pH-sensing principle (sec. 3.2.2) and we show how such theory can be rearranged to consider a larger set of surface reactions (sec. 3.2.3). We then conclude the section by presenting a compact model for the surface potential sensitivity to pH (sec. 3.2.4) which we extensively verified.

3.2.1 Double layer theory

Let's start by considering a generic metal/electrolyte interface. Since the metal does not sustain an electric field, the excess of charge in the metal will be concentrated in a very thin layer at the interface with the electrolyte. On the liquid side of the interface, instead, there will be an opposite amount of charge. The first attempt to model the interface was developed by Helmholtz, in the second half of 1800 [78], that suggested the existence of two sheets of charge, with opposite signs, on the metal and electrolyte sides, represented by a constant interface capacitance, C_{dl}. From there, the name of *electrical double layer* was generally adopted.

This zero-th order model, was then replaced by a more sophisticated one, independently proposed by Gouy and Chapman in the early years of 1900 [79, 80]. They suggested the use of the Boltzmann factor to express the concentration of the ion species in the electrolyte as follows

$$n_m = n_m^{\infty} exp\left(-\frac{qZ_m\psi}{k_BT}\right) \tag{3.20}$$

where Z_m is the ion valence and ψ is the solution potential measured with respect to the bulk solution. In this section we use ψ to indicate the electrostatic potential (instead of V as we have used in the previous section). Eq. 3.20 coincides with eq. 3.3 when there is no current in the elecrolyte and ϕ_{0m} is constant. Gouy and Chapman, considered the solution divided in laminae of infinitesimal thickness. Although each laminae is in thermal equilibrium with each other, the energy of the ions in each laminae is different, because it depends on the electrostatic potential ψ. The laminae is regarded as a system of non-interacting energy states in thermal equilibrium, allowing the use of the Maxwell-Boltzmann statistics [81].

The charge on the electrolyte side of the interface is then modelled as a *diffuse layer* of charge, concentrated at the interface and decreasing exponentially when going towards the bulk solution.

The total charge per unit volume in each laminae is then:

$$\rho(x) = \sum_{m=1}^{N_{sp}} qZ_m n_m \tag{3.21}$$

where N_{sp} is the number of ion species in the solution. By applying Poisson equation

$$\varepsilon_{el}\varepsilon_0 \frac{d^2\psi}{dx^2} = -\rho(x) \tag{3.22}$$

where we assume the electrolyte permittivity ε_{el} constant [1]. With the condition that far from the electrode $d\psi/dx = 0$ and considering a symmetric 1:1 electrolyte ($|Z| = 1$), we can reduce Poisson equation to the following

[1] The electrolyte permittivity is not always constant but depends on ionic strength, field intensity, temperature and frequency of the AC signal, if any [82, 83, 84].

$$\frac{d\psi}{dx} = -\sqrt{\frac{8k_BTn^{\infty}}{\varepsilon_{el}\varepsilon_0}}sinh\left(\frac{qZ\psi}{2k_BT}\right) \tag{3.23}$$

where n^{∞} is the bulk ion concentrations assumed all equal because we are considering a 1:1 symmetric electrolyte.

Let's consider a volume that starts from the surface interface and extends in the solution, sufficiently far from the interface such that $d\psi/dx = 0$.

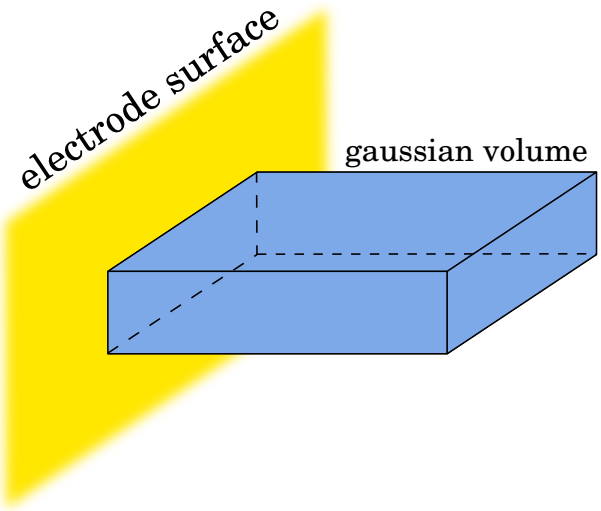

Figure 3.1: *Sketch of the Gauss volume. The volume starts from the surface and extends in the solution, where* $d\psi/dx = 0$.

By applying Gauss law to the surface S of this volume we get

$$Q = \varepsilon_{el}\varepsilon_0 \oiint_S \mathbf{E}\cdot \mathrm{d}S = \varepsilon_{el}\varepsilon_0 \oiint_S \frac{d\psi}{dx}\,\mathrm{d}S = \varepsilon_{el}\varepsilon_0 S\left(\frac{d\psi}{dx}\right)_{x=x_0} \tag{3.24}$$

The solution phase charge density σ is then given by Q/S, and by using eq. 3.23 in eq. 3.24 we get

$$\sigma = \sqrt{8k_BT\varepsilon_{el}\varepsilon_0 n^{\infty}}sinh\left(\frac{qZ_m\psi_0}{2k_BT}\right) \tag{3.25}$$

where ψ_0 is the interface potential at the coordinate $x = x_0$ as indicated in fig. [XX]. One important feature, that will be recalled many times in the following sections, is the so called double layer capacitance, that is given by

$$C_{dl} = \frac{d\sigma}{d\psi_0} = \sqrt{\frac{2q^2Z^2\varepsilon_{el}\varepsilon_0 n^{\infty}}{k_BT}}cosh\left(\frac{qZ\psi_0}{2k_BT}\right) \tag{3.26}$$

C_{dl} is a differential capacitance and represents the ability of the electrolyte close to the interface to store charge in response to a change of the interface potential ψ_0. It depends on to electrolyte quantities, such as the ionic strength and the dielectric permittivity. Fig.

3.2 shows the Gouy-Chapman prediction for the double layer capacitance as a function of the interface potential, for three values of ionic strength.

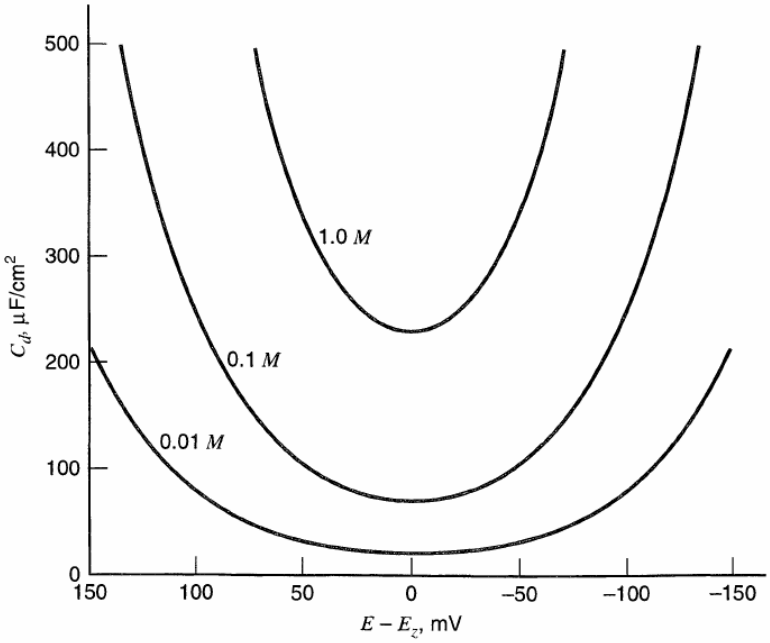

Figure 3.2: *Double layer capacitance as a function of the potential ($E - E_z$) predicted by the Gouy-Chapman model. Picture taken from [81].*

Fig. 3.3 shows experimental data for the differential capacitance of two categories of interfaces:

- *Ideally polarizable*: allowing DC and AC current flow (Hg/NaF in fig. 3.3);
- *Faradaic*: where both DC and AC current flow is possible (AgI/$NaClO_4$ and Ag_2S/$NaNO_3$ in fig. 3.3).

In fact, the Gouy-Chapman model refers to ideally polarizable electrodes, and in fact, by comparing fig. 3.2 with the experiments shown in the central picture of fig. 3.3, there are some common features. However, the model fails to reproduce the differential capacitance for relatively high potentials and high ionic strengths.

The Gouy-Chapman model treats the ions as point charges, so that they can approach the interface arbitrarily close. Stern, in 1924, proposed a more realistic model[86], that sets a limit for the minimum distance that the first layer of ions can reach from the solid/liquid interface. This distance, indicated as x_2 in fig. 3.4 called *outher Helmholtz plane* (OHP) is given by the ionic radius of the ions in solution, plus an additional term if the ions approaching the surface are solvated. In other words, Stern, introduced the concept of plane of closest approach, that is fundamental for critical cases where the interface potential is high compared to the bulk electrolyte or for the cases of high ionic strengths, where the Gouy-Chapman model fails. For the purpose of our simulations the Stern layer will be approximated with a thin dielectric layer, as explained in sec. 3.4.

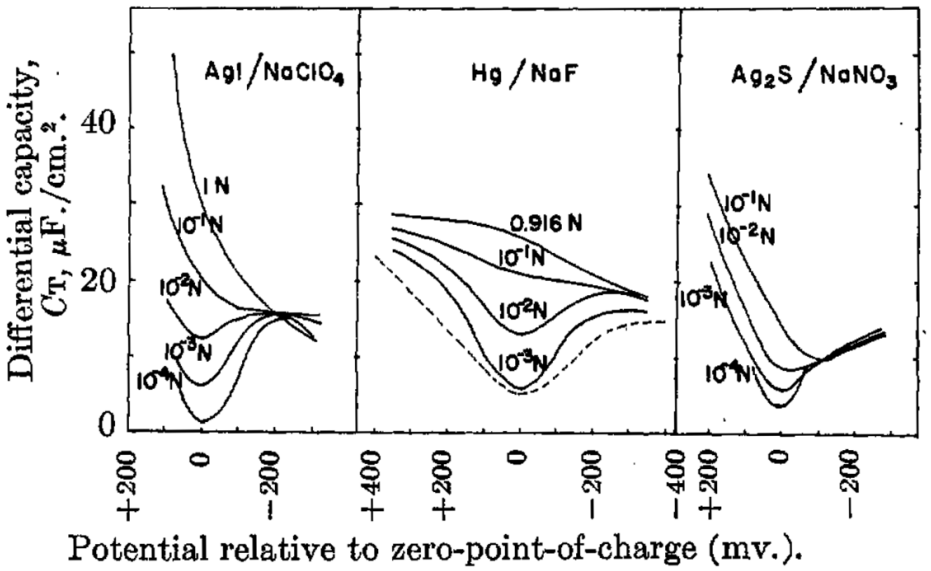

Figure 3.3: *Double layer capacitance of mercury (Hg) polarizable electrode, and silver iodide (AgI) and silver sulfide (Ag_2S) non polarizable electrodes. Picture taken from [85], where N, in the graphs, is the so-called normality or equivalent concentration.*

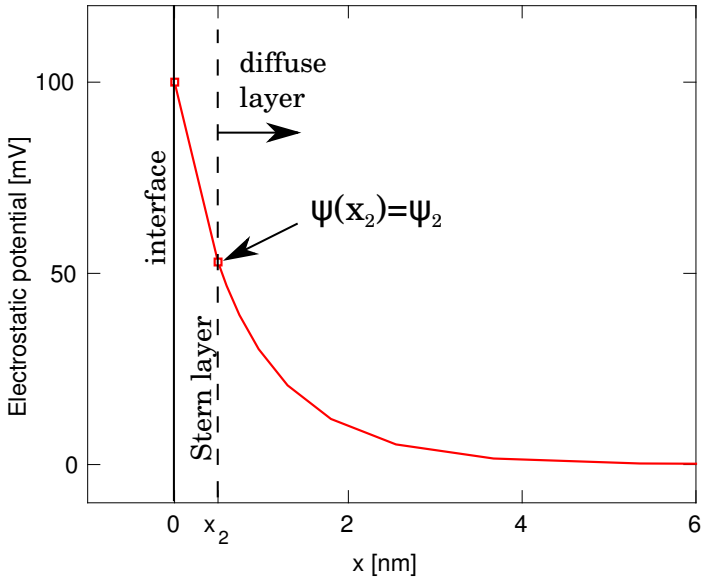

Figure 3.4: *Simulation of the Gouy-Chapman-Stern model. The Stern layer is modeled as a thin dielectric. The electrostatic potential is linear in the Stern layer and decays exponentially in the diffuse layer region. Data obtained with the 1-D simulator presented in 3.3.1.*

3.2.2 Site-binding charge model

In the double-layer theory we have considered metal/electrolyte interfaces, where the charge in the system is given by the charge on the metal side and the charge on the electrolyte side. What if we consider a material such as a dielectric in contact with the

electrolyte?

The gate dielectrics most commonly used in CMOS devices (SiO_2, HfO_2, TiO_2, Al_2O_3 [87, 88]) when operated in liquid environment (meaning that they are in contact with an electrolyte solution) exhibit a surface charge dependent on pH and ionic strength. This is because the surface of these oxides exposes amphoteric ionizable groups, e.g. MOH groups (where M can be a metal or a semiconductor), that can capture or release an hydrogen ion, this taking the form MOH_2^+ or MO^- respectively. The ability of reacting with the hydrogen ions in solution produces an additional charge in the system, located in a specific section, namely the solid/liquid interface.

These surface reactions can be written as follows

$$MOH_2^+ \overset{K_b}{\rightleftharpoons} MOH + H_s^+ \tag{3.27a}$$

$$MOH \overset{K_a}{\rightleftharpoons} MO^- + H_s^+ \tag{3.27b}$$

where we used the subscript s to emphasize the fact that we are considering the surface concentration of H^+ ions. Here K_b and K_a are the equilibrium, acid (a) and basic (b), reaction constants. The result of the ionization of the surface sites is the formation of a net surface charge at the solid/liquid interface. The reaction constants can be derived reminding the definition of chemical potential μ_m of a species m, that is, of the potential energy, expressed in units of J/mol, that can be absorbed or released during a chemical reaction

$$\mu_m = \mu_m^0 + RT \cdot ln(a_m) \tag{3.28}$$

where μ^0 is the standard chemical potential and, a is the activity that describes how active is a chemical species when it is not in standard state conditions (defined by μ^0). The activity can be defined as

$$a_m = exp\left(\frac{\mu_m - \mu_m^0}{RT}\right) \tag{3.29}$$

and it is often expressed as an activity coefficient γ multiplied by a measured amount of concentration, as follows

$$a_m = \gamma_m \cdot \frac{n_m}{n_m^0} \tag{3.30}$$

where the concentration n_m is normalized to a standard concentration ${n_m^0}^2$. In the present work we will always consider activity coefficients = 1, which is a widely adopted approximation for dilute solutions (ionic concentrations $\leq$ 100 mM). Hence: $a_m = n_m/n_m^0$.

The electrochemical potential of a species i, also takes into account the contribution of electrostatics to the total energy

[2]The standard amount of concentration (typically 1 M) ensures that both activity (a_m) and activity coefficient (γ_m) are dimensionless.

$$\bar{\mu}_i = \mu_i^0 + RT \cdot ln(a_i) + z_i q N_A \psi \tag{3.31}$$

where ψ is the inner potential or Galvanic potential. An example of electrochemical potential in solid-state electronics is the Fermi energy level, that is expressed in energy per unit particle charge, eV, instead of energy per mole. In electrochemistry, an ion will always move from higher to lower electrochemical potentials.

We can now write the electrochemical potentials for the species involved in the surface reactions (MOH, MOH_2^+, MO^- and H_s^+)

$$\bar{\mu}_{MOH_2^+} = \mu^0_{MOH_2^+} + RT \cdot ln(a_{MOH_2^+}) + qN_A\psi_0 \tag{3.32a}$$
$$\bar{\mu}_{MO^-} = \mu^0_{MO^-} + RT \cdot ln(a_{MO^-}) - qN_A\psi_0 \tag{3.32b}$$
$$\bar{\mu}_{MOH} = \mu^0_{MOH} + RT \cdot ln(a_{MOH}) \tag{3.32c}$$
$$\bar{\mu}_{H_s^+} = \mu^0_{H_s^+} + RT \cdot ln(a_{H_s^+}) + qN_A\psi_0 \tag{3.32d}$$

where $a_{H_s^+}$ is the activity of the hydrogen ion at the surface, that is related to the activity of the bulk solution by the Nernst equation [81]

$$a_m^s = a_m^b exp\left(-\frac{qZ_m\psi_0}{k_BT}\right) \tag{3.33}$$

where m is a generic ion species, Z_m is the ionic valence and ψ_0 is the electrostatic potential at the solid/liquid interface with respect to the bulk of the solution. Equilibrium requires that the sum of the electrochemical potentials of reactants equals the sum of the electrochemical potentials of the products,

$$\bar{\mu}_{MOH_2^+} = \mu_{MOH} + \bar{\mu}_{H_s^+} \tag{3.34a}$$
$$\mu_{MOH} = \bar{\mu}_{MO^-} + \bar{\mu}_{H_s^+} \tag{3.34b}$$

where $\bar{\mu}_{MOH} = \mu_{MOH}$ for the neutral MOH site.

By substituting eq. 3.32a in eq. 3.34a and rearranging, we obtain the described expression for the reaction constants

$$\frac{a_{MOH}a_{H_s^+}}{a_{MOH_2^+}} = exp\left(-\frac{\mu^0_{MOH} + \mu^0_{H_s^+} - \mu^0_{MOH_2^+}}{RT}\right) = K_b \tag{3.35a}$$
$$\frac{a_{MO^-}a_{H_s^+}}{a_{MOH}} = exp\left(-\frac{\mu^0_{MO^-} + \mu^0_{H_s^+} - \mu^0_{MOH}}{RT}\right) = K_a \tag{3.35b}$$

It has been proven [89] that the activity of any surface sites a_m is simply given by the surface concentration of that site, ν_m in units of m^{-2}. The previous equations can then be re-written to obtain what are called *effective dissociation constants*

$$\frac{\nu_{MOH}a_{H_s^+}}{\nu_{MOH_2^+}} = K_b \ , \quad \frac{\nu_{MO^-}a_{H_s^+}}{\nu_{MOH}} = K_a \tag{3.36}$$

For simplicity of notation we will omit the symbols + and − when considering ions and the charged surface sites.

Having described the reaction constants, in the following, we present the essential elements of the site-binding charge model as developed in [90] for equilibrium conditions. Such model will be extended in transient and AC small signal conditions in the next sections.

Given the total number surface sites per unit area

$$N_S = \nu_{MOH} + \nu_{MOH_2} + \nu_{MO} \tag{3.37}$$

we can derive the neutral and charged surface site concentrations

$$\nu_{MOH} = N_S \frac{a_{H_s}K_a}{a_{H_s}^2 + a_{H_s}K_b + K_bK_a} \tag{3.38a}$$

$$\nu_{MOH_2} = N_S \frac{a_{H_s}^2}{a_{H_s}^2 + a_{H_s}K_b + K_bK_a} \tag{3.38b}$$

$$\nu_{MO} = N_S \frac{K_aK_b}{a_{H_s}^2 + a_{H_s}K_b + K_bK_a} \tag{3.38c}$$

By knowing the dissociation constants, the surface hydrogen ion concentration and the total number of surface sites, it is possible to calculate the surface concentration of each site. As a direct consequence, we can calculate the net surface charge at the interface as the difference between the positive and the negative charged surface sites

$$\sigma_{sb} = q(\nu_{MOH_2} - \nu_{MO}) = qN_S \frac{a_{H_s}^2 - K_bK_a}{a_{H_s}^2 + a_{H_s}K_b + K_bK_a} \tag{3.39}$$

where σ_{sb} is the site-binding surface charge in [C/m^2].

By recalling the definition of $pH = -log_{10}(a_H)$, we can cast eq. 3.39 into the classical expression for the site-binding charge

$$\sigma_{sb} = qN_S \frac{10^{-2pH_s} - K_bK_a}{10^{-2pH_s} + 10^{-pH_s}K_b + K_bK_a} \tag{3.40}$$

where pH_s is the pH at the surface.

By looking at eq. 3.40, it is apparent that the site-binding charge becomes 0 at the so-called pH of zero charge

$$pH_{zc} = -\frac{1}{2}\Big(log_{10}(K_b) + log_{10}(K_a)\Big) = \frac{1}{2}\Big(pK_b + pK_a\Big) \tag{3.41}$$

Dissociation constants for silicon and metal oxides can be found in literature [91, 38, 92, 90, 93]. Table 3.1 lists the main properties of the most common dielectrics in nanoelectronics.

Insulator	N_S	K_a	K_b	pH_{zc}	ε_r	E_G	CB_{offset}	I_b[a]	C.N.[b]
	sites/cm^2					eV	eV	%	
SiO_2[90, 91]	$5{\cdot}10^{14}$	10^{-6}	10^{2}	2	3.9	9	3.2	0.45	4
Al_2O_3[90, 91]	$8{\cdot}10^{14}$	10^{-10}	10^{-6}	8	14	8.8	2.8	0.57	4-6
Ta_2O_5[90]	$1{\cdot}10^{15}$	10^{-4}	10^{-2}	3	22	4.4	0.35	0.61	6-8
HfO_2[93]	$1{\cdot}10^{15}$	10^{-7}	10^{-7}	7	25	5.8	1.4	0.68	8

Table 3.1: Dissociation constants of typical CMOS-compatible insulators.

[a]Ionicity, calculated as $100 \cdot \left(1 - exp\left(-0.25(\chi_A - \chi_B)^2\right)\right)$, where $\chi_{A,B}$ are the electronegativities of the two considered atoms.

[b]The coordination number (CN) of a central atom in a molecule or crystal is the number of its near neighbours.

As we will see in the following sections, in order to treat electrolyte and semiconductor with the same set of equations, both concentration of anions/cations (in the electrolyte) and electrons/holes (in the semiconductor) are expressed in m^{-3} for consistency. Furthermore, we will also approximate the activity, a_m of a species with its concentration n_m, normalized to a reference concentration of 1 M, that is a good approximation when dealing with dilute solutions. We can then write the site-binding charge as

$$\sigma_{sb} = qN_S \frac{n_{0H_s}^2 - K_b' K_a'}{n_{0H_s}^2 + n_{0H_s} K_b' + K_b' K_a'} \tag{3.42}$$

where $K'_{a/b} = K_{a/b} \cdot 10^{-3} N_A$. We defined K' in units of m^{-3} exclusively for simulations purposes; in fact, this equation will be useful when implementing the site-binding charge in the simulator described in section 3.3.

Fig. 3.5 shows the relation between the site-binding surface charge (σ_{sb}) and the surface potential (ψ_0) for different pH values and for the four insulators reported in tab. 3.1.

Transient site-binding model

In this section we present a dynamic version of the site-binding model, based on the individual surface reaction rates. It creates the basis for a dynamic site-binding charge model useful to incorporate transient site-binding charge effects in AC simulations. The model takes into account the kinetics of the individual forward and backward surface reactions, determining the surface sites occupation.

To start with, we remind that, a generic reaction equation is expressed as

$$A^\alpha + B^\beta \rightleftharpoons S^\sigma + T^\tau \tag{3.43}$$

For this reaction equation, we can write the reaction rate as

$$r = -k^f [A]^\alpha [B]^\beta + k^b [S]^\sigma [T]^\tau \tag{3.44}$$

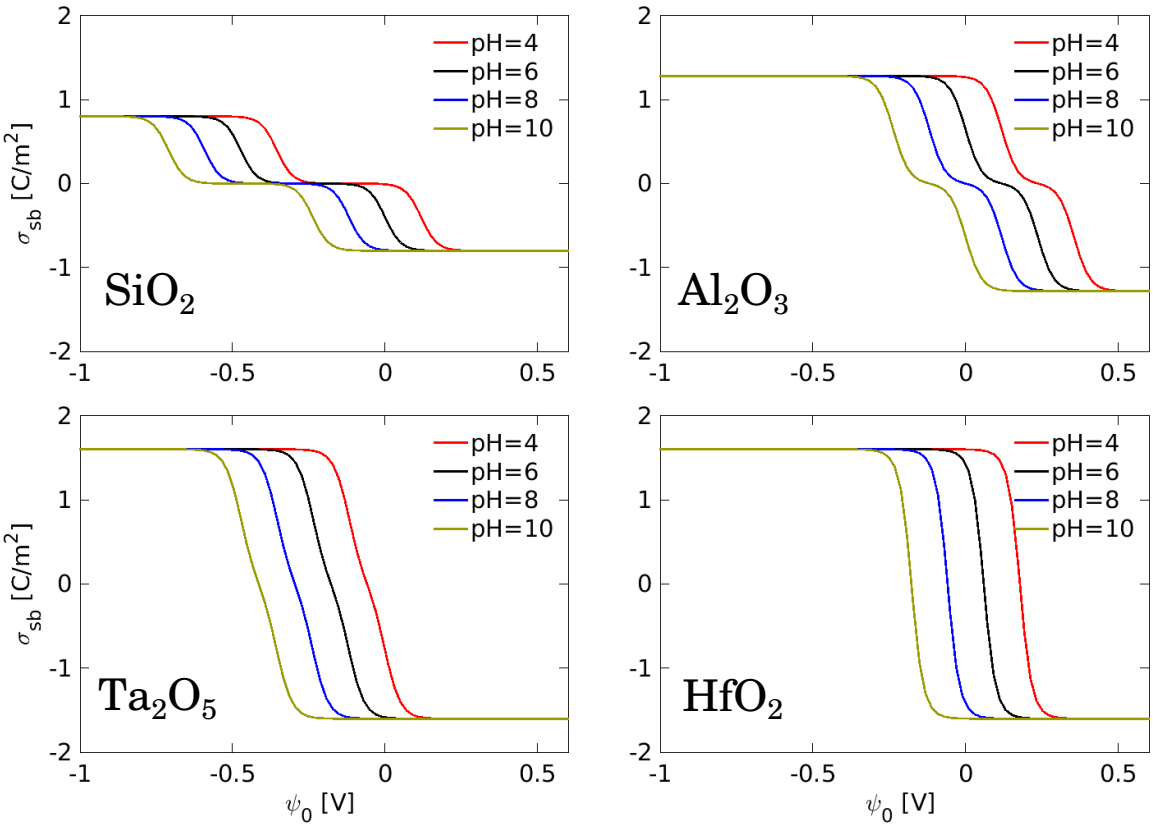

Figure 3.5: *σ_{sb} vs. ψ_0 for pH values ranging from 4 to 10 and for four different insulators.*

where r is the reaction rate, that represent the variation of molecules' number per unit time and volume $[nmolecules/s/m^3]$ and k^f and k^b are respectively the forward and backward reaction constants. From the equilibrium condition, $r = 0$, the ratio of the forward and backward reaction constants gives the dissociation constant K

$$\frac{[S]^\sigma[T]^\tau}{[A]^\alpha[B]^\beta} = \frac{k^f}{k^b} = K \tag{3.45}$$

The site-binding model reaction equations in eq. 3.27a can be written in terms of reaction rates as follows

$$r_+ = -k_b^f \nu_{MOH_2} + k_b^b \nu_{MOH} n_{H_s} \tag{3.46a}$$

$$r_- = -k_a^f \nu_{MOH} + k_a^b \nu_{MO} n_{H_s} \tag{3.46b}$$

From the equilibrium condition, $r_+ = r_- = 0$, we can express the dissociation constants as a function of the reaction constants

$$K_b' = \frac{k_b^f}{k_b^b}, \qquad K_a' = \frac{k_a^f}{k_a^b} \tag{3.47}$$

Equations 3.46a can also be written as

$$\begin{cases} \dfrac{d\nu_{MOH_2}}{dt} = -k_a^f \nu_{MOH_2} + k_a^b \nu_{MOH} n_{H_s} \\ \dfrac{d\nu_{MOH}}{dt} = -\dfrac{d\nu_{MO}}{dt} = -k_b^f \nu_{MOH} + k_b^b \nu_{MO} n_{H_s} \end{cases} \tag{3.48}$$

We omit from now on the superscripts + and − of the surface sites concentration for simplicity of notation. For numerical implementation we discretized eq. 3.48 following a simple forward Euler scheme

$$\begin{cases} \dfrac{\nu_{MOH_2}(t+\Delta T) - \nu_{MOH_2}(t)}{\Delta T} = -k_a^f \nu_{MOH_2}(t) + k_a^b \nu_{MO}(t) n_{H_s} \\ \dfrac{\nu_{MO}(t+\Delta T) - \nu_{MO}(t)}{\Delta T} = k_b^f \nu_{MOH}(t) - k_b^b \nu_{MO}(t) n_{H_s} \\ N_S = \nu_{MOH}(t+\Delta T) + \nu_{MOH_2}(t+\Delta T) + \nu_{MO}(t+\Delta T) \end{cases} \tag{3.49}$$

Eq. 3.49 allows us to compute the neutral and charged sites densities at $t + \Delta T$

$$\begin{cases} \nu_{MOH_2}(t+\Delta T) = \nu_{MOH_2}(t) - k_a^f \nu_{MOH_2}(t)\Delta T + k_a^b \nu_{MO}(t) n_{H_s} \Delta T \\ \nu_{MO}(t+\Delta T) = \nu_{MO}(t) + k_b^f \nu_{MOH}(t)\Delta T - k_b^b \nu_{MO}(t) n_{H_s} \Delta T \\ \nu_{MOH}(t+\Delta T) = N_S - \nu_{MOH_2}(t+\Delta T) - \nu_{MO}(t+\Delta T) \end{cases} \tag{3.50}$$

where ΔT is the time step and n_{H_s} is the volume concentration of hydrogen ions at the interface. The initial conditions for the surface sites concentrations are given by eq. 3.38a for a specific initial pH value. The only unknowns in the system are the forward and backward reaction constants, respectively k^f and k^b, whose ratio is the dissociation constant, K'. This means that for each reaction equation we have only one unknown, because the other is straightforwardly calculated from the dissociation constant, eq. 3.47.

Experimental data on ISFETs reported by Woias in 1995 [94], enabled us to extract the forward and backward reaction constants of SiO_2 separately (unfortunately, we didn't find similar experiments carried out on different oxides). The ISFETs were subject to pH-steps starting at different pH initial values and step amplitude. Fig. 3.6 compares the measurements and the transient model, obtained with the following values of reaction constants: $k_b^b \approx 10^{-23}$ and $k_a^b \approx 10^{-20}$ both measured in m^3/s. Consequently the forward reaction constants are $k_b^f = K_b' k_b^b$ and $k_a^f = K_a' k_a^b$ both measured in s^{-1}.

The forward and backward reaction constant are parameters of key relevance for the AC site-binding model. In principle, by fitting pH-step response of ISFETs with different gate-oxide, it is possible to characterize and extract their forward and backward reaction constants. These constants are very difficult to find in literature, and a parametrization of their values based on measurements is necessary. In this work, we will use only the reaction constants that we have extracted from the experimental data in [94].

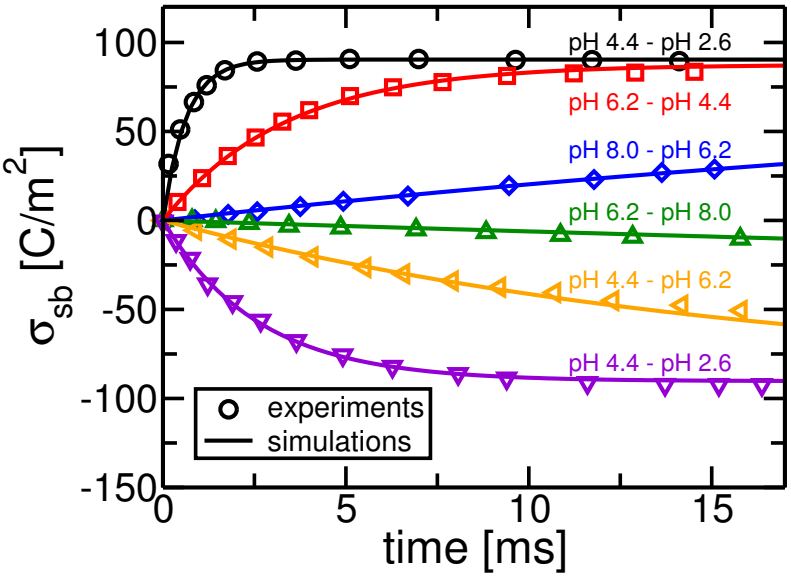

Figure 3.6: *Comparison between the model and the experimental data [94]. Fitting of the curves yields forward and backward reaction constants,* $k_b^b \approx 10^{-23}$ *and* $k_a^b \approx 10^{-20}$.

AC site-binding model

Applying the time harmonic small signal approximation to eq. 3.48 we obtain

$$j\omega\tilde{\nu}_{MO} = k_a^f\left(\nu_{0,MOH} + \tilde{\nu}_{MOH}\right) - k_a^b\left(\nu_{0,M} + \tilde{\nu}_{MO}\right)\left(n_{0,H} + \tilde{n}_H\right) \tag{3.51a}$$

$$j\omega\tilde{\nu}_{MOH_2} = -k_b^f\left(\nu_{0,MOH_2} + \tilde{\nu}_{MOH_2}\right) + k_b^b\left(\nu_{0,MOH} + \tilde{\nu}_{MOH}\right)\left(n_{0,H} + \tilde{n}_H\right) \tag{3.51b}$$

The equations above refer to surface reactions but for the sake of a lean notation we omit the subscript "s" (i.e. $n_{0,H}$ and $\tilde{n}_H$ are surface concentration in m^{-2}). We know that for the first equation $k_a^f\nu_{0,MOH} - k_a^b\nu_{0,M}n_{0,H} = 0$ and for the second equation $-k_b^f\nu_{0,MOH_2} + k_b^b\nu_{0,MOH}n_{0,H} = 0$. Furthermore by neglecting the second order terms, i.e. $\tilde{\nu}_{MO}\cdot\tilde{n}_H$, we obtain

$$j\omega\tilde{\nu}_{MO} = k_a^f\tilde{\nu}_{MOH} - k_a^b\left(\nu_{0,M}\tilde{n}_H + \tilde{\nu}_{MO}n_{0,H}\right) \tag{3.52a}$$

$$j\omega\tilde{\nu}_{MOH_2} = -k_b^f\tilde{\nu}_{MOH_2} + k_b^b\left(\nu_{0,MOH}\tilde{n}_H + \tilde{\nu}_{MOH}n_{0,H}\right) \tag{3.52b}$$

Substitution $\tilde{\nu}_{MOH} = -\tilde{\nu}_{MOH_2} - \tilde{\nu}_{MO}$ in eq. 3.52 yields

$$\tilde{\nu}_{MO} = \frac{-k_a^f\tilde{\nu}_{MOH_2} - k_a^b\left(\nu_{0,M}\tilde{n}_H\right)}{j\omega + k_a^b n_{0,H} + k_a^f} \tag{3.53a}$$

$$\tilde{\nu}_{MOH_2} = \frac{k_b^b(\nu_{0,MOH}\tilde{n}_H - n_{0,H}\tilde{\nu}_{MO})}{j\omega + k_b^b n_{0,H} + k_b^f} \tag{3.53b}$$

we denote D_- and D_+ the denominators of equations 3.53a and 3.53b, $j\omega+k_a^b n_{0,H}+k_a^f$ and $j\omega+k_b^b n_{0,H}+k_b^f$, respectively. Now we need two more relations for $\nu_{0,MOH}$ and $\nu_{0,MO}$ to complete the system of equations. Combining eq. 3.37 with eq. 3.36 we obtain

$$N_S = \nu_{0,MO} + \frac{\nu_{0,MO} n_{0,H}}{K'_a} + \frac{\nu_{0,MOH} n_{0,H}}{K'_b} \tag{3.54a}$$

$$N_S = \nu_{0,MO} + \frac{\nu_{0,MO} n_{0,H}}{K'_a} + \frac{\nu_{0,MO} n_{0,H}^2}{K'_a K'_b} \tag{3.54b}$$

from which we can write:

$$\nu_{0,M} = \frac{N_S K'_a K'_b}{K'_a K'_b + n_{0,H} K_b + n_{0,H}^2} \tag{3.55}$$

and

$$\nu_{0,MOH} = \frac{N_S n_{0,H} K'_b}{K'_a K'_b + n_{0,H} K'_b + n_{0,H}^2} \tag{3.56}$$

To simplify the equations we substitute: $D_0 = K_a^{'} K_b^{'} + n_{0,H} K_b^{'} + n_{0,H}^2$ inside equations 3.53a and 3.53b. We thus obtain the expression for the two AC charges which contribute to the site-binding AC charge

$$\tilde{\nu}_{MO} = -\frac{N_S \tilde{n}_H K'_b (k_a^f k_b^b n_{0,H} + k_a^b D_+ K'_a)}{D_0 (D_+ D_- - k_a^f k_b^b n_{0,H})} \tag{3.57a}$$

$$\tilde{\nu}_{MOH_2} = \frac{N_S \tilde{n}_H K'_b k_b^b n_{0,H} (D_- + K'_a k_a^b)}{D_0 (D_+ D_- - k_a^f k_b^b n_{0,H})} \tag{3.57b}$$

The site-binding AC surface charge then is:

$$\tilde{\sigma}_{sb} = q N_S \left(\tilde{\nu}_{MOH_2} - \tilde{\nu}_{MO} \right) \tag{3.58}$$

which be rearranged by using eq. 3.53 as follows

$$\tilde{\sigma}_{sb} = q N_S \tilde{n}_H K'_b \frac{n_{0,H} k_b^b (D_- + 2K'_a k_a^b) + k_a^b K'_a D_+}{D_0 (D_+ D_- - k_a^f k_b^b n_{0,H})} \tag{3.59}$$

expanding all the terms we get

$$\tilde{\sigma}_{sb} = q N_S \tilde{n}_H K'_b \frac{k_b^b n_{0,H} (k_a^b n_{0,H} + j\omega) + K'_a k_a^b (K'_b k_b^b + 4 k_b^b n_{0,H} + j\omega)}{(K'_a K'_b + n_{0,H}(n_{0,H} + K'_b))((j\omega + k_b^b n_{0,H} + k_b^f)(j\omega + k_a^b n_{0,H} + k_a^f) - k_a^f k_b^b n_{0,H})} \tag{3.60}$$

where $n_{0,H}$ is the concentration in m^{-3} of the hydrogen ion calculated from the solution of the DC problem. $\tilde{n}_H$ is given from eq. 3.11

$$\tilde{n}_H = n_{0,H} \left(\frac{\tilde{\psi}_H^{(0)} - \tilde{V}^{(0)}}{v_{th}} \right) \tag{3.61}$$

where the superscript "(0)" indicates the values at the interface between the oxide and the Stern layer (see fig. 3.4).

This is valid in theory, but since the pseudo potentials ($\tilde{\phi}_m$) are defined only in the electrolyte, 3.61 has to be modified using the pseudo potentials at the stern/electrolyte interface. Thus the equation has to be rewritten as follows

$$\tilde{n}_H = n_{0,H} \left(\frac{\tilde{\psi}_H^{(2)} - \tilde{V}^{(2)}}{v_{th}} \right) \tag{3.62}$$

where the superscript "(2)" indicates the interface stern/electrolyte, see again fig. 3.4.

Equations 3.42, 3.60 represent a complete model of the dominant surface reactions involving the hydrogen ions and the amphoteric surface sites in DC, transient and AC conditions. Once implemented, the model expands the ability of the ISFET simulator and constitutes a useful tool for interpretation of experiments. As a matter of fact, this derivation is a general approach applicable to a generic insulator and it can be extended to a broader range of surface reactions. An example that we will present in the next section 3.2.3, is the adsorption of chlorine ions at the surface, in addition to the surface reaction with the hydrogen ions.

3.2.3 Counter ion adsorption

In this section we present an additional surface effect that becomes important when dealing with high salt concentrations. *Tarasov et. al* [93] found that the surface potential at the insulator/electrolyte interface is affected by the chlorine ions, in electrolytes such as KCl and NaCl. This effect is particularly relevant for salt concentrations larger than 100 mM, which is the range of physiological salt conditions of most interest for applications. To account for this effect, they proposed an additional surface chemical reaction, to the already affirmed site-binding model in DC [74, 95]. The surface reaction is

$$MOH_2^+ + Cl_s^- \overset{K_c}{\rightleftharpoons} MOHCl^- + H_b^+ \tag{3.63}$$

Fig. 3.7 reports the measurements (filled square symbols) and compares them to the 2-reactions model (dashed line) and the 3-reactions model (solid line with triangles). The measurements clearly shows a concentration dependent behaviour for salt concentrations larger than ∼100 mM. The addition of this third reaction to the classical site-binding model (eq. 3.27a) entails a salt concentration dependent response. This reaction equation shows no pH dependence in the considered pH range and therefore does not affect the pH differential sensitivity per se.

$$\sigma_{sb} = q(\nu_{0,MOH_2^+} - \nu_{0,MO^-} - \nu_{0,MOHCl^-}) \tag{3.64}$$

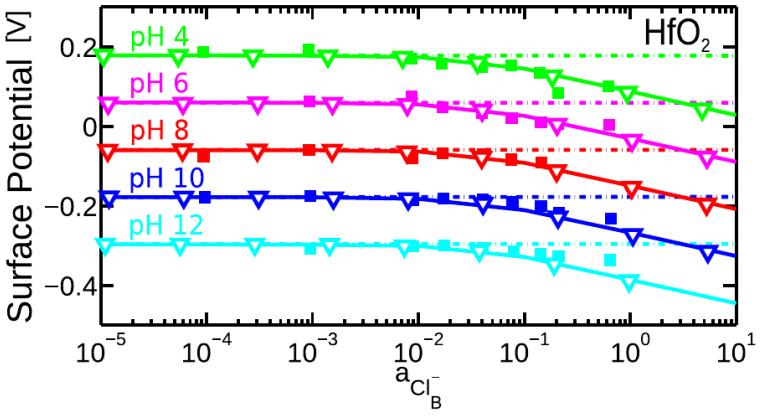

Figure 3.7: *Surface potential as a function of the chlorine ion activity. Dashed: classic site-binding model. Solid and triangles: modified site-binding model. Filled squares: measurements data. Figure reworked from [96].*

By following the same procedure as in section 3.2.2, we write the reaction rates

$$r_c = -k_c^f \nu_{0,MOH_2} n_{0,Cl_s} + k_c^b \nu_{0,MOHCl} n_{0,H_b} \tag{3.65}$$

Thus, by imposing equilibrium, the dissociation constant is

$$\frac{k_c^f}{k_c^b} = \frac{\nu_{0,MOHCl} n_{0,H_b}}{\nu_{0,MOH_2} n_{0,Cl_s}} = K_c \tag{3.66}$$

In this case, the total amount of surface sites N_S is expressed as

$$N_S = \nu_{0,MOH_2^+} + \nu_{0,MOH} + \nu_{0,MO^-} + \nu_{0,MOHCl^-} \tag{3.67}$$

and by substituting eq. 3.36 and eq. 3.66 into 3.67 we can write a new expression for the DC site-binding charge (hereafter denoted SBT model as opposed to the conventional site-binding model, SB)

$$\sigma_{sb} = qN_S \left(\frac{n_{0,H_s}^2 n_{0,H_b} - K_a K_b n_{0,H_b} - K_c n_{0,Cl_s} n_{0,H_s}^2}{n_{0,H_s}^2 n_{0,H_b} + K_a K_b n_{0,H_b} + K_c n_{0,Cl_s} n_{0,H_s}^2 + K_b n_{0,H_s} n_{0,H_b}} \right) \tag{3.68}$$

Surface and bulk quantities (indicated with the subscripts s and b respectively) are related by the interface potential ψ_0 by eq. 3.33.

Figures 3.8, 3.9 and 3.10 compare the classical site-binding model (eq. 3.42, SB) to the site-binding model with the additional reaction equation for the chlorine ion (eq. 3.68, SBT). With the aid of the 1-D simulator presented in section 3.3, which implements the site-binding equations 3.42 and 3.68, we performed an extensive set of simulations. The simulated structure is composed by 3 nm of insulator in contact with 2 µm of electrolyte, with non DC bias voltage applied at the external contact.

From a comparison of the results on left and on the right, we clearly see that the SiO_2 response is not affected by the presence of the chlorine ion in solution, for any of the

considered molar concentrations. On the other hand, by analyzing the results obtained simulating the hafnium dioxide, we see that it its response is largely affected by the presence of the chlorine ion.

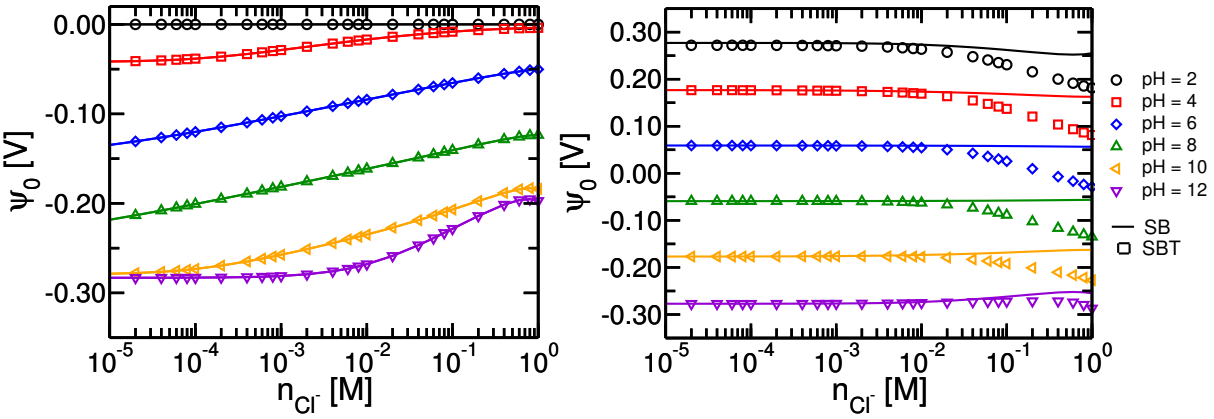

Figure 3.8: *ψ_0 as a function of the chlorine concentration, for pH values ranging from 2 to 12. Left: SiO_2, right: HfO_2.*

The effect of the chlorine ion is evident on hafnium dioxide for salt concentrations $\geq$ 10 mM. In particular, the symmetry in the hafnium response with respect to pH = 7 is compromised when the concentration of Cl^- increases over 10 mM.

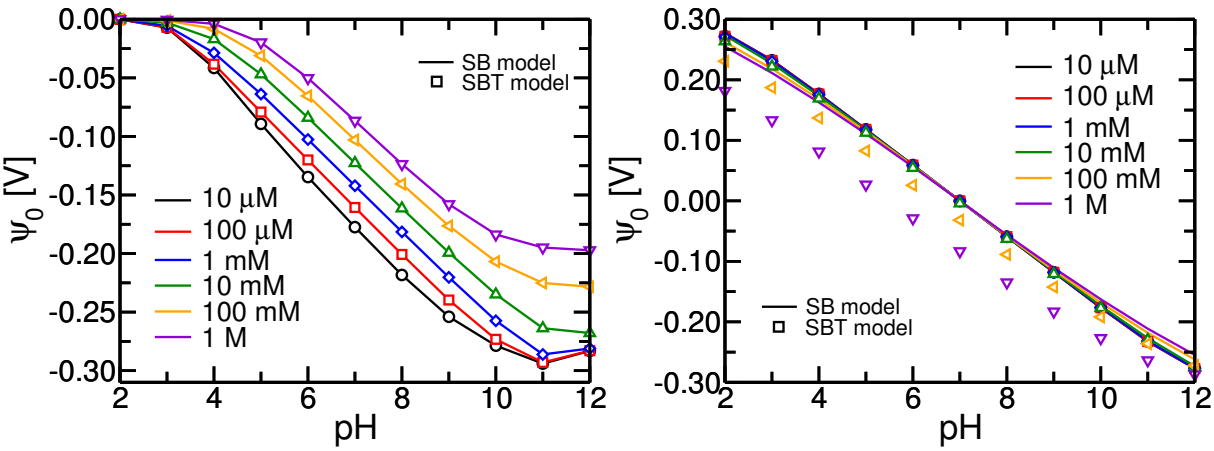

Figure 3.9: *ψ_0 as a function of pH, for chlorine concentrations ranging from 10 µM to 1 M. Left: SiO_2, right: HfO_2.*

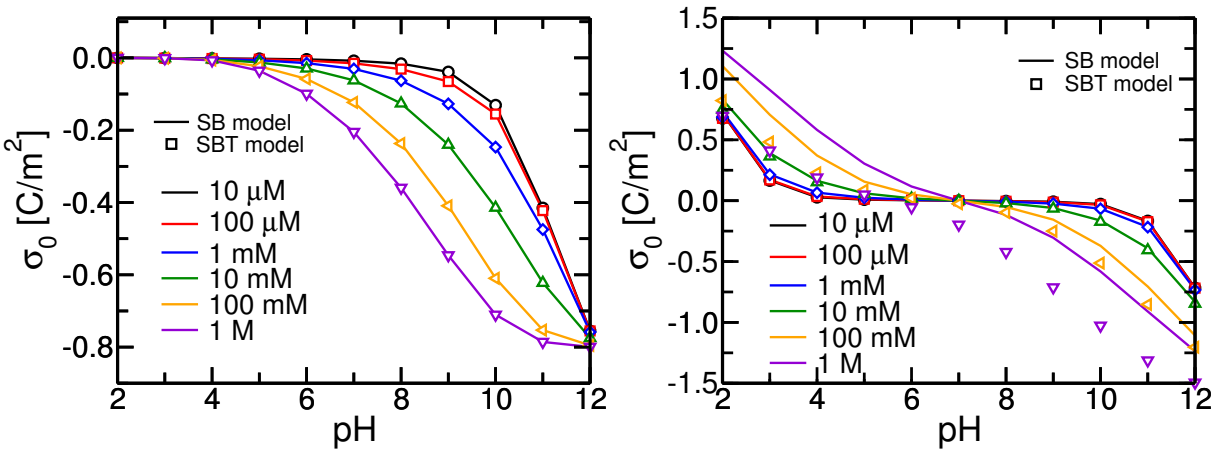

Figure 3.10: *σ_{sb} as a function of pH, for chlorine concentrations ranging from 10 µM to 1 M. Left: SiO_2, right: HfO_2.*

AC site-binding model with Cl^-

As we have done for the classical site-binding model, we calculated an equation also for the AC site-binding charge taking into account the additional effect of the chlorine ion. The three reaction constant are:

$$K_a = \frac{\nu_{MO} n_{H_s}}{\nu_{MOH}} = \frac{k_a^f}{k_a^b}, \quad K_b = \frac{\nu_{MOH} n_{H_s}}{\nu_{MOH_2}} = \frac{k_b^f}{k_b^b}, \quad K_c = \frac{\nu_{MOHCl} n_{H_s}}{\nu_{MOH_2} n_{Cl_s}} = \frac{k_c^f}{k_c^b}, \tag{3.69}$$

By following the same procedure adopted before (see eq. 3.48), the reaction rates of the three reactions considered in the model can be expressed as follows:

$$\begin{cases} \dfrac{d\nu_{SiOH}}{dt} = -k_a^f \nu_{SiOH} + k_a^b \nu_{SiO} n_{H_s} \\ \dfrac{d\nu_{SiOH_2}}{dt} = -k_b^f \nu_{SiOH_2} + k_b^b \nu_{SiOH} n_{H_s} \\ \dfrac{d\nu_{SiOHCl}}{dt} = k_c^f \nu_{SiOH_2} n_{Cl_s} - k_c^b \nu_{SiOHCl} n_{H_b} \end{cases} \tag{3.70}$$

Applying the AC small-signal approximation we obtain:

$$\begin{cases} j\omega\tilde{\nu}_{MO} = k_a^f \left(\nu_{0,MOH} + \tilde{\nu}_{MOH}\right) - k_a^b \left(\nu_{0,MO} + \tilde{\nu}_{MO}\right)\left(n_{0,H_s} + \tilde{n}_{H_s}\right) \\ j\omega\tilde{\nu}_{MOH_2} = -k_b^f \left(\nu_{0,MOH_2} + \tilde{\nu}_{MOH_2}\right) + k_b^b \left(\nu_{0,MOH} + \tilde{\nu}_{MOH}\right)\left(n_{0,H_s} + \tilde{n}_{H_s}\right) \\ j\omega\tilde{\nu}_{MOHCl} = k_c^f \left(\nu_{0,MOH_2} + \tilde{\nu}_{MOH_2}\right)\left(\nu_{0,MOHCl} + \tilde{\nu}_{MOHCl}\right) \\ \qquad\qquad -k_c^b \left(\nu_{0,MOHCl} + \tilde{\nu}_{MOHCl}\right)\left(n_{0,H_b} + \tilde{n}_{H_b}\right) \end{cases} \tag{3.71}$$

We recall the DC reaction equation, that are:

$$\begin{cases} k_a^f \nu_{0,MOH} - k_a^b \nu_{0,MO} n_{0,H_s} = 0 \\ k_b^f \nu_{0,MOH_2} - k_b^b \nu_{0,MOH} n_{0,H_s} = 0 \\ k_c^f \nu_{0,MOH_2} n_{0,Cl_s} - k_c^b \nu_{0,MOHCl} n_{0,H_b} = 0 \end{cases} \tag{3.72}$$

The DC reaction equations (eq. 3.72) must be satisfied and by neglecting the second order terms, i.e. $\tilde{\nu}_{MOH} \cdot \tilde{\nu}_{MO}$, we obtain:

$$\begin{cases} j\omega\tilde{\nu}_{MO} = k_a^f \tilde{\nu}_{MOH} - k_a^b \left(\nu_{0,MO}\tilde{n}_{H_s} + \tilde{\nu}_{MO} n_{0,H_s}\right) \\ j\omega\tilde{\nu}_{MOH_2} = -k_b^f \tilde{\nu}_{MOH_2} + k_b^b \left(\nu_{0,MOH}\tilde{n}_{H_s} + \tilde{\nu}_{MOH} n_{0,H_s}\right) \\ j\omega\tilde{\nu}_{MOHCl} = k_c^f \left(\nu_{0,MOH_2}\tilde{n}_{Cl_s} + \tilde{\nu}_{MOH_2} n_{0,Cl_s}\right) - k_c^b \left(\tilde{\nu}_{MOHCl} n_{0,H_b}\right) \end{cases} \tag{3.73}$$

rearranging the equations:

$$\begin{cases} \tilde{\nu}_{MO} = \dfrac{k_a^f \tilde{\nu}_{MOH} - k_a^b \nu_{0,MO}\tilde{n}_{H_s}}{j\omega + k_a^b n_{0,H_s}} \\ \tilde{\nu}_{MOH_2} = \dfrac{k_b^b (\nu_{0,MOH}\tilde{n}_{H_s} + \tilde{\nu}_{MOH} n_{0,H_s})}{j\omega + k_b^f} \\ \tilde{\nu}_{MOHCl} = \dfrac{k_c^f (\nu_{0,MOH_2}\tilde{n}_{Cl_s} + \tilde{\nu}_{MOH_2} n_{0,Cl_s})}{j\omega + k_c^b n_{0,H_b}} \end{cases} \tag{3.74}$$

knowing that arithmetic sum of the AC surface charges is zero, $\tilde{\nu}_{MOH} + \tilde{\nu}_{MOH_2} + \tilde{\nu}_{MO} + \tilde{\nu}_{MOHCl} = 0$, we can rewrite eq. 3.74 as follows:

$$\begin{cases} \tilde{\nu}_{MO} = -\dfrac{k_a^f (\tilde{\nu}_{MOH_2} + \tilde{\nu}_{MOHCl}) + k_a^b \nu_{0,MO}\tilde{n}_{H_s}}{j\omega + k_a^f + k_a^b n_{0,H_s}} \\ \tilde{\nu}_{MOH_2} = \dfrac{k_b^b (\nu_{0,MOH}\tilde{n}_{H_s} - n_{0,H_s}(\tilde{\nu}_{MO} + \tilde{\nu}_{MOHCl}))}{j\omega + k_b^f + k_b^b n_{0,H_s}} \\ \tilde{\nu}_{MOHCl} = \dfrac{k_c^f (\nu_{0,MOH_2}\tilde{n}_{Cl_s} + \tilde{\nu}_{MOH_2} n_{0,Cl_s})}{j\omega + k_c^b n_{0,H_b}} \end{cases} \tag{3.75}$$

we call D_{SiO} and D_{SiOH_2} the denominators of equations 3.75. By using the following relation:

$$\nu_{0,MOH} + \nu_{0,MOH_2} + \nu_{0,MO} + \nu_{0,MOHCl} = N_S \tag{3.76}$$

and after long but straightforward calculations, we can write the three expressions for the AC surface charge concentrations:

$$\begin{aligned} \tilde{\nu}_{MO} = -\frac{1}{D}(&k_a^f k_b^f k_c^f \tilde{n}_{Cl_s}\nu_{0,MOH_2} - k_a^b \tilde{n}_{H_s}\nu_{0,MO}\omega^2 + j\omega k_a^f k_c^f \tilde{n}_{Cl_s}\nu_{0,MOH_2} + j\omega k_a^b k_b^f \tilde{n}_{H_s}\nu_{0,MO} \\ &+ j\omega k_a^f k_b^b \tilde{n}_{H_s}\nu_{0,MOH} + k_a^f k_b^b k_c^f n_{0,Cl_s}\tilde{n}_{H_s}\nu_{0,MOH} + k_a^b k_b^f k_c^b n_{0,H_b}\tilde{n}_{H_s}\nu_{0,MO} + k_a^f k_b^b k_c^b n_{0,H_b}\tilde{n}_{H_s}\nu_{0,MOH} \\ &+ j\omega k_a^b k_b^b \tilde{n}_{H_s} n_{0,H_s}\nu_{0,MO} + j\omega k_a^b k_c^b n_{0,H_b}\tilde{n}_{H_s}\nu_{0,MO} + k_a^b k_b^b k_c^f n_{0,Cl_s}\tilde{n}_{H_s}\nu_{0,MO} \\ &+ k_a^b k_b^b k_c^b n_{0,H_b}\tilde{n}_{H_s} n_{0,H_s}\nu_{0,MO}) \end{aligned} \tag{3.77}$$

$$\begin{aligned} \tilde{\nu}_{MOH_2} = -\frac{k_b^b}{D}(&k_a^f k_c^b n_{0,H_b}\tilde{n}_{H_s} + j\omega k_a^f \tilde{n}_{H_s}\nu_{0,MOH} - \tilde{n}_{H_s}\nu_{0,MOH}\omega^2 - j\omega k_c^f \tilde{n}_{Cl_s} n_{0,H_s}\nu_{0,MOH_2} \\ &+ j\omega k_a^b \tilde{n}_{H_s} n_{0,H_s}\nu_{0,MO} + j\omega k_a^b \tilde{n}_{H_s} n_{0,H_s}\nu_{0,MOH} + j\omega k_c^b n_{0,H_b}\tilde{n}_{H_s}\nu_{MOH} - k_a^b k_c^f \tilde{n}_{H_s} {n_{0,H_s}}^2 \nu_{0,MOH_2} \\ &+ k_a^b k_c^b n_{0,H_b}\tilde{n}_{H_s} n_{0,H_s}\nu_{0,MO} + k_a^b k_c^b n_{0,H_b}\tilde{n}_{H_s} n_{0,H_s}\nu_{0,MOH}) \end{aligned} \tag{3.78}$$

$$\tilde{n}_{SiOHCl} = -\frac{k_c^f}{D}(k_a^f k_b^f k_c^f \tilde{n}_{Cl_s}\nu_{0,MOH_2} - \tilde{n}_{Cl_s}\nu_{0,MOH_2}\omega^2 + j\omega k_a^f \tilde{n}_{Cl_s}\nu_{0,MOH_2} + j\omega k_b^f \tilde{n}_{Cl_s}\nu_{0,MOH_2}$$
$$k_a^f k_b^b n_{0,Cl_s}\tilde{n}_{H_s}\nu_{0,MOH} + k_a^b k_b^f \tilde{n}_{Cl_s} n_{0,H_s}\nu_{0,MOH_2} + j\omega k_a^b \tilde{n}_{Cl_s} n_{0,H_s}\nu_{0,MOH_2} + j\omega k_b^b n_{0,Cl_s}\tilde{n}_H^S \nu_{0,MOH}$$
$$+ j\omega k_b^b \tilde{n}_{Cl_s} n_{0,H_s}\nu_{0,MOH_2} + k_a^b k_b^b \tilde{n}_{Cl_s} {n_{0,H_s}}^2 \nu_{0,MOH_2} + k_a^b k_b^b n_{0,Cl_s}\tilde{n}_H^S n_{0,H_s}\nu_{0,MO}$$
$$+ k_a^b k_b^b n_{0,Cl_s}\tilde{n}_H^S n_{0,H_s}\nu_{0,MOH}) \quad (3.79)$$

and the denominator is:

$$D = j\omega^3 + \omega^2(k_a^f k_b^b + k_a^b n_{0,H_s} + k_b^b n_{0,H_s} + k_c^b n_{0,H_b}) - j\omega(k_a^f k_b^f + k_a^b k_b^f n_{0,H_s} + k_a^f k_c^b n_{0,H_b} + k_b^f k_c^b n_{0,H_b}$$
$$k_a^b k_b^b {n_{0,H_s}}^2 + k_b^b k_c^f n_{0,Cl_s} n_{0,H_s} + k_a^b k_c^b n_{0,H_b} n_{0,H_s} + k_b^b k_c^b n_{0,H_b} n_{0,H_s}) - (k_a^f k_b^f k_c^b n_{0,H_b} + k_a^b k_b^f k_c^b n_{0,H_b} n_{0,H_s}$$
$$+ k_a^b k_b^b k_c^f {n_{0,H_s}}^2 + k_a^b k_b^b k_c^b n_{0,H_b} {n_{0,H_s}}^2) \quad (3.80)$$

by using eq. 3.76 we can write the expression for the AC small signal site-binding surface charge with the chlorine ion contribution. The surface charge is defined as:

$$\tilde{\sigma}_{sbt} = q(\tilde{n}_{SiOH_2} - \tilde{n}_{SiO} - \tilde{n}_{SiOHCl}) \quad (3.81)$$

and rearranging the equation we obtain the formula for the AC site-binding charge accounting for the chlorine ion:

$$\tilde{\sigma}_{sbt} = qN_S \frac{n_{0,H_b}}{D_\sigma}[\tilde{\mathbf{n}}_{\mathbf{H_s}} K_b(-\omega^2(K_a k_a^b + k_b^b n_{0,H_s}) + j\omega k_a^b k_b^b(K_a K_b + {n_{0,H_s}}^2 + 4K_a n_{0,H_s})$$
$$+ j\omega k_c^b(K_a k_a^b n_{0,H_b} + k_b^b n_{0,H_b} n_{0,H_s} - K_c k_b^b n_{0,Cl_s} n_{0,H_s}) + k_a^b k_b^b k_c^b(K_a K_b n_{0,H_b} + n_{0,H_b} {n_{0,H_s}}^2 + 4K_a n_{0,H_b} n_{0,H_s}$$
$$- K_c n_{0,Cl_s} {n_{0,H_s}}^2)) + \tilde{\mathbf{n}}_{\mathbf{Cl_s}} {n_{0,H_s}}^2 K_c k_c^b(\omega^2 - j\omega(k_a^b n_{0,H_s} + 2k_b^b n_{0,H_s} - K_b k_b^b) - k_a^b k_b^b n_{0,H_s}(2n_{0,H_s} + K_b))] \quad (3.82)$$

where:

$$\tilde{D}_\sigma = \left(n_{0,H_b}{n_{0,H_s}}^2 + K_a K_b n_{0,H_b} + K_b n_{0,H_b} n_{0,H_s} + K_c n_{0,Cl_s}{n_{0,H_s}}^2\right) \cdot$$
$$[-j\omega^3 - \omega^2(k_a^b n_{0,H_s} + k_b^b n_{0,H_s} + k_c^b n_{0,H_b} + K_a k_a^b + K_b k_b^b) + j\omega(k_a^b k_b^b n_{0,H_s} + K_a K_b k_a^b k_b^b$$
$$+ K_a k_a^b k_c^b n_{0,H_b} + K_b k_a^b k_b^b n_{0,H_s} + K_b k_b^b k_c^b n_{0,H_b} + k_a^b k_c^b n_{0,H_b} n_{0,H_s} + k_b^b k_c^b n_{0,H_b} n_{0,H_s} + K_c k_b^b k_c^b n_{0,Cl_s} n_{0,H_s})$$
$$+ K_c k_a^b k_b^b k_c^b n_{0,Cl_s} {n_{0,H_s}}^2 + k_a^b k_b^b k_c^b n_{0,H_b} {n_{0,H_s}}^2 + K_a K_b k_a^b k_b^b k_c^b n_{0,H_b} + K_b k_a^b k_b^b k_c^b n_{0,H_b} n_{0,H_s}] \quad (3.83)$$

and where $\tilde{n}_{H_s}$ and $\tilde{n}_{Cl_s}$, similarly to eqs. 3.61 and 3.62, are the AC surface concentrations of hydrogen and chlorine ions, respectively.

3.2.4 Surface potential sensitivity to pH

One common application of ISFET devices is the sensing of the pH of a solution. pH is one of the most frequently measured characteristics since it controls or monitors many physics/physilogical processes of interest in applications. In the following we recapitulate the main derivation of pH sensing theory as originally developed by Bergveld in [15] in view of its implementation in ad-hoc numerical models and TCAD simulation tools described in sec. 3.3. We will start from Nernst equation (eq. 3.33) that relates the surface potential to the solution's pH.

$$pH_s = pH_b + \frac{\psi_0}{\frac{k_B T}{q} ln(10)} \tag{3.84}$$

A small quasi-static variation of the surface potential due to a change in pH in the bulk of the solution

$$\frac{\partial \psi_0}{\partial pH_b} = \frac{\partial \psi_0}{\partial pH_s} \cdot \frac{\partial pH_s}{\partial pH_b} = \frac{\partial \psi_0}{\partial \sigma_0} \cdot \frac{\partial \sigma_0}{\partial pH_s} \cdot \frac{\partial pH_s}{\partial pH_b} \tag{3.85}$$

Let's analyze each one of the three partial derivatives in eq. 3.85. The first partial derivative is directly connected to the double layer theory, in fact it is just the inverse of the double layer capacitance

$$\frac{\partial \sigma_0}{\partial \psi_0} = C_{dl} \tag{3.86}$$

The second partial derivative is directly connected to the site-binding model. From eq. 3.39 and eq. 3.40 we get [90]

$$\frac{\partial \sigma_0}{\partial pH_s} = -q \frac{\partial [B]}{\partial pH_s} = -q \beta_{int} \tag{3.87}$$

where $[B]$ is, by definition, the net (negative) surface charged groups per unit area (see eq. 3.40). β_{int} is the so-called intrinsic buffer capacity, a property of the insulator, that represents the variation of surface charged groups due to a local (surface) variation of the pH.

The third partial derivative can be calculated from eq. 3.84 as follows

$$\frac{\partial pH_s}{\partial pH_b} = 1 + \frac{\partial \psi_0}{\partial pH_b} \frac{1}{\frac{k_B T}{q} ln(10)} \tag{3.88}$$

Combining all the three partial derivatives together we get

$$\frac{\partial \psi_0}{\partial pH_b} = -\frac{q \beta_{int}}{C_{dl}} \left(1 + \frac{\partial \psi_0}{\partial pH_b} \frac{1}{\frac{k_B T}{q} ln(10)} \right) \tag{3.89}$$

By rearranging the equation we obtain

$$\frac{\partial \psi_0}{\partial pH_b} = -\frac{k_B T ln(10)}{q} \frac{1}{1 + \frac{C_{dl} k_B T ln(10)}{q^2 \beta_{int}}} = -2.3 \frac{k_B T}{q} \alpha \tag{3.90}$$

Eq. 3.90 shows how the double layer theory ($\partial\sigma_0/\partial\psi_0$) and the site-binding theory ($\partial\sigma_0/\partial pH_s$) combine together with the Nernst equation. α is a material dependent parameter that ranges between 0 and 1. Consequently, the pH voltage sensitivity, as defined here, has a limit called *Nernst limit* (-59.2 mV/pH, at room temperature 298 K). Secondly, α is a multiplicative factor that depends on the insulator surface properties (β_{int}), and on the electrolyte characteristics (C_{dl}). Depending on these two parameters, there are typically three conditions according to the quantity $\frac{C_{dl} k_B T ln(10)}{q^2 \beta_{int}}$ being:

- $>> 1$: ψ_0 is insensitive to pH
- ~ 1: ψ_0 is sensitive to both pH and ionic strength (e.g. SiO_2, left graph in fig. 3.9)
- $<< 1$: ψ_0 is only pH sensitive (e.g. HfO_2, right graph in fig. 3.9)

These dependencies can be seen by looking at fig. 3.9, where we compared SiO_2 (on the left) and HfO_2 (on the right). The site-binding charge (SB model in fig. 3.9) of SiO_2 insulator, is both sensitive to pH and concentration, while the interface potential in the case of HfO_2 is sensitive to the pH and almost insensitive to the electrolyte concentration (NaCl in this particular case).

To conclude, depending on the application, it is possible to look for materials with the desired value of α, or to optimize α by modifying the surface, for example by functionalization process, while maintaining the properties of the material below the functionalization.

3.3 Model implementations

In this section we describe how the model equations have been discretized for implementation in ad-hoc numerical models and how commercial TCAD simulator featuring an open physical model interface has been adjusted to incorporate the site-binding charge into self-consistent simulations.

3.3.1 1-D finite difference simulator

The domain is discretized as follows:

To calculate the solution of the DC model, we start considering the Poisson-Boltzmann equation 3.4 in the integral form

$$\int_\nu \nabla \cdot (\varepsilon \nabla V) d\nu + \int_\nu \left(q \sum_{m=1}^{N_{sp}} Z_m n_{0m} \exp\left(-\frac{q Z_m (V - V_{ref})}{k_B T} \right) \right) d\nu = 0 \tag{3.91}$$

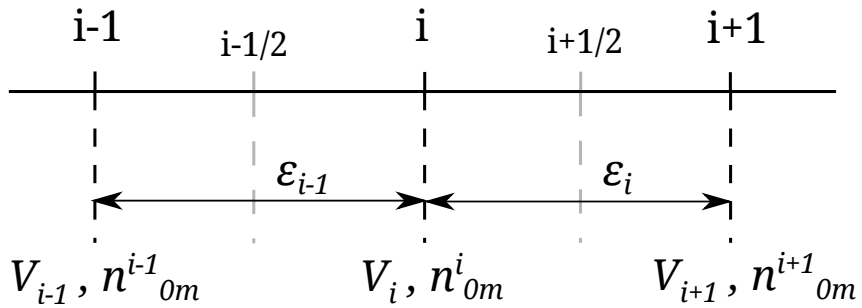

Figure 3.11: *Mesh and DC quantities. The mesh is composed by the points i and by the mid-points $i \pm 1/2$. V_i and n^i_{0m} are the unknowns, while ε_i is the dielectric constant parameter.*

where ν is the domain volume. We discretize the equation after applying the divergence theorem

$$\int_S \varepsilon \nabla V \cdot n \; dS + q\nu \sum_{m=1}^{N_{sp}} Z_m n_{0m} \exp\left(-\frac{qZ_m(V - V_{ref})}{k_B T}\right) = 0 \tag{3.92}$$

where S is the surface of the domain volume ν. The second term in eq. 3.92 has been taken out of the volume integral, because we assume a constant charge distribution inside that volume ν. The equation can then be discretized as follows

$$\begin{aligned} V_{i-1}\left(\frac{\varepsilon_{i-1}}{x_L}\right) - V_i\left(\frac{\varepsilon_{i-1}}{x_L} + \frac{\varepsilon_i}{x_R}\right) + V_{i+1}\left(\frac{\varepsilon_i}{x_R}\right) + \\ q\Delta_x \sum_{m=1}^{N_{sp}} Z_m n_{0m} \exp\left(-\frac{qZ_m(V_i - V_{ref})}{k_B T}\right) = 0 \end{aligned} \tag{3.93}$$

where:

$$x_L = x_i - x_{i-1}, \qquad x_R = x_{i+1} - x_i, \qquad \Delta_x = x_{i+1/2} - x_{i-1/2} \tag{3.94}$$

where x is the vector of mesh points.

Eq. 3.93 can be written as a non linear system of equations, where the potential at each node of the grid yields the vector of unknowns

$$\mathbf{A} \cdot \mathbf{V} + \mathbf{B} + \mathbf{C} = 0 \tag{3.95}$$

where $\boldsymbol{A}$ is an $N \times N$ matrix containing the coefficients the multiply the potential $\boldsymbol{V}$ in eq. 3.93, $\boldsymbol{V}$ is the $N-$lines vector of unknowns, $\boldsymbol{B}$ is an $N-$lines vector of known terms ($V_1 = V_T$ and $V_N = V_B$, bottom and top voltages) and $\boldsymbol{C}$ is an $N-$lines vector that contains the non linear terms (essentially the charge in eq. 3.93). It is now clear that the DC site-binding charge can be easily included in the vector $\boldsymbol{C}$ of non-linear terms, at the position corresponding to the oxide/electrolyte interface.

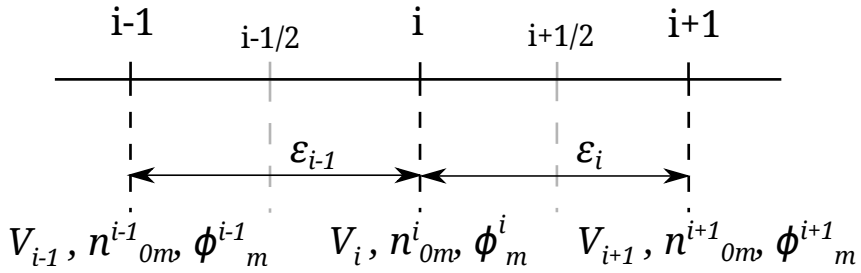

Figure 3.12: *Mesh and DC quantities.*

AC simulator

For the numerical solution of the AC model we consider eq. 3.12 and eq. 3.15. Similarity to the DC model, we consider the integral form of the PB equation

$$\int_S \varepsilon \nabla \tilde{V} \cdot n \; dS + q\nu \sum_{m=1}^{N_{sp}} Z_m n_{0m} \frac{Z_m q}{k_B T} (\tilde{\phi}_m - \tilde{V}) = 0 \tag{3.96}$$

that we discretize as follows

$$\tilde{V}_{i-1} \left(\frac{\varepsilon_{i-1}}{x_L} \right) + \tilde{V}_i \left[- \left(\frac{\varepsilon_{i-1}}{x_L} + \frac{\varepsilon_i}{x_R} \right) - q\Delta_x \sum_{m=1}^{N_{sp}} Z_m n^i_{0m} \frac{Z_m q}{k_B T} \right] + \tilde{V}_{i+1} \left(\frac{\varepsilon_i}{x_R} \right) + q\Delta_x \sum_{m=1}^{N_{sp}} Z_m n^i_{0m} \frac{Z_m q}{k_B T} \tilde{\phi}^i_m = 0 \tag{3.97}$$

The discretization mesh is the same as for the DC problem. The coefficients of eq. 3.97 are in F/m^2. Eq. 3.97 can be re-written in a more compact form as follows

$$b_i \tilde{V}_{i-1} + a_i \tilde{V}_i + c_i \tilde{V}_{i+1} + \sum_{m=1}^{N_{ions}} d^m_i \tilde{\phi}^i_m = 0 \tag{3.98}$$

$$\begin{cases} a_1 \tilde{V}_1 = \tilde{V}_B \\ a_2 \tilde{V}_2 + c_2 \tilde{V}_3 + \sum\limits_{m=1}^{N_{sp}} d^m_2 \tilde{\phi}_m = -b_2 \tilde{V}_B \\ b_3 \tilde{V}_2 + a_3 \tilde{V}_3 + c_3 \tilde{V}_4 + \sum\limits_{m=1}^{N_{sp}} d^m_3 \tilde{\phi}_m = 0 \\ \ldots \\ b_{N-1} \tilde{V}_{N-2} + a_{N-1} \tilde{V}_{N-1} + \sum\limits_{m=1}^{N_{sp}} d^m_{N-1} \tilde{\phi}_m = -c_{N-1} \tilde{V}_T \\ a_N \tilde{V}_N = \tilde{V}_T \end{cases} \tag{3.99}$$

Since the goal is to compute the AC admittance of the one-dimensional device, we have to include in the system the AC current equations, that were presented before, in section 3.1. Equation 3.15 can be written in the integral form:

$$Z_m q \mu_m \int_S n_{0m} \nabla \tilde{\phi}_m \cdot n \; dS - j\omega\nu n_{0m} \frac{Z_m q}{k_B T} (\tilde{\phi}_m - \tilde{V}) = 0 \tag{3.100}$$

this equation can be discretized as we have done before

$$\tilde{\phi}_m^{i-1}\left(Z_m q\mu_m \frac{n_{0m}^{iL}}{x_L}\right) + \tilde{\phi}_m^{i}\left[-Z_m q\mu_m\left(\frac{n_{0m}^{iL}}{x_L}+\frac{n_{0m}^{iR}}{x_R}\right) - j\omega\Delta_x n_{0m}^{i}\frac{Z_m q}{k_B T}\right] + \tilde{\phi}_m^{i+1}\left(Z_m q\mu_m \frac{n_{0m}^{iR}}{x_R}\right) + \tilde{V}_i\left(j\omega\Delta_x n_{0m}^{i}\frac{Z_m q}{k_B T}\right) = 0 \tag{3.101}$$

where

$$n_{0m}^{iL} = \frac{n_{0m}^{i} + n_{0m}^{i-1}}{2} \qquad n_{0m}^{iR} = \frac{n_{0m}^{i} + n_{0m}^{i+1}}{2} \tag{3.102}$$

The coefficients of eq. 3.101 are in $1/(sVm^2)$, thus we have to multiply these coefficients by q/ω in order to be consistent with the coefficients of the PB equation and reduce the risk of ill-conditioned problems.

Eq. 3.101 can be written in a more compact form as follows

$$e_i\tilde{\phi}_m^{i-1} + f_i\tilde{\phi}_m^{i} + g_i\tilde{\phi}_m^{i+1} + h_i\tilde{V}_i = 0 \tag{3.103}$$

$$\begin{cases} f_1\tilde{\phi}_m^{1} + g_1\tilde{\phi}_m^{2} = -h_1\tilde{V_B} \\ e_2\tilde{\phi}_m^{1} + f_2\tilde{\phi}_m^{2} + g_2\tilde{\phi}_m^{3} + h_2^m\tilde{V}_2 = 0 \\ ... \\ e_N\tilde{\phi}_m^{N-1} + f_N\tilde{\phi}_m^{N} = -h_N\tilde{V_T} \end{cases} \tag{3.104}$$

where the coefficients are: $e_i = Z_m q\mu_m \frac{n_{0m}^{iL}}{x_L}$, $f_i = -Z_m q\mu_m\left(\frac{n_{0m}^{iL}}{x_L}+\frac{n_{0m}^{iR}}{x_R}\right) - j\omega\Delta_x n_{0m}^{i}\frac{Z_m q}{k_B T}$, $g_i = Z_m q\mu_m \frac{n_{0m}^{iR}}{x_R}$ and $h_i = j\omega\Delta_x n_{0m}^{i}\frac{Z_m q}{k_B T}$.

Equations 3.97 and 3.101 can be written as a linear system of equations

$$\mathbf{A}\cdot\mathbf{X} + \mathbf{B} = 0 \tag{3.105}$$

where $\boldsymbol{A}$ is a square matrix that contains the system coefficients (a,..,h), $\boldsymbol{X}$ is the vector of variables ($\tilde{V}$ and $\tilde{\phi}_m$) and $\boldsymbol{B}$ is the vector of known terms (such as the applied voltages at the boundaries). We solve this system with the aid of a Matlab script, by using the function *fsolve* that implements different iterative methods to solve the non-linear system.

The solution of the system in eq. 3.105 returns the potentials and the pseudo-potentials at all grid nodes. We then have to calculate the admittance, that is, the current, $\tilde{I}$, or the current density $\vec{\tilde{J}}$. There are two contributions to the current density, the displacement current density $\vec{\tilde{J}}_D$ and the ionic current density $\vec{\tilde{J}}_m$

$$\vec{\tilde{J}} = \vec{\tilde{J}}_D + \sum_{m=1}^{N_{sp}}\vec{\tilde{J}}_m = j\omega\varepsilon\nabla\tilde{V} + \sum_{m=1}^{N_{sp}}\vec{\tilde{J}}_m \tag{3.106}$$

where

$$\vec{\tilde{J}}_m = -Z_m^2 q^2 \mu_m n_{0m} \left(\frac{Z_m q}{k_B T} (\tilde{\phi}_m - \tilde{V}) \nabla \phi_{0m} + \nabla \tilde{\phi}_m \right) \tag{3.107}$$

Implementation of the surface reactions models

In section 3.2 we have presented different type of surface reaction models that describe the generation of a surface net charge at the solid/liquid interface, due to the capture and release of ions to and from the surface. For each model, we have shown the surface charge as a function of physical parameters (i.e. reaction constants) and physical quantities of the system (i.e. potential, concentration). The surface charge is typically a non linear function of, e.g., the potential. For this reason, its contribution is included in the system of eq. 3.95, if it is a DC charge, or in the system of eq. 3.105, if it is a frequency dependent charge. In particular the non linear surface charge goes in the **C** vector, in the positions corresponding to the insulator/electrolyte interface mesh points.

3.3.2 3-D finite element simulator

The analysis of the measurement performed on the NRs was carried out with the aid of ENBIOS, a fully 3-D simulator developed by Dr. F. Pittino at the University of Udine, and extensively described in [65, 50].

ENBIOS implements the Control Volume Finite Elements Method (CVFEM) to solve numerically and self-consistently the system of equation composed by the Poisson-Boltzmann and Poisson-Nernst-Plank set of equation, that we presented in section 3.1. ENBIOS solves the equation on unstructured 3D meshes describing electronic micro- and nano-biosensors, such as the NRs, either in DC and AC conditions [97, 98, 25, 99].

As part of this thesis, the existing simulator has been further developed and extended to include the effect of the site-binding charge, in order to asses their impact on the impedance, especially at low frequency were measures could be made with existing commercial equipment.

In the following section we present the implementation of the AC site-binding charge in ENBIOS. The methodology is general and it can be applied to any other non linear surface charge.

Implementation of the surface reactions models

The implementation of the non linear surface charge, in our particular case the AC site-binding charge, is less trivial compared to the case of the 1D simulator described in section 3.3.1. For a 1D simulator the interface region between insulator and electrolyte is just a single mesh point, while in a 3D domain as the one solved by ENBIOS, is a 2D surface. Before starting a simulation, the user can decide to activate the AC site-binding model and he/she can specify the interface region on which the AC non linear charge has to

be computed. For our purposes we activate the AC site-binding charge on the interfaces between insulators and electrolytes (e.g. gate-oxide and passivations).

The mesh of the simulated 3D domain is generated by the use of an automatic 3D tetrahedral mesh generator, *Netgen* [100]. The mesh is thus made of tetrahedrons only, as reported in detail in fig. 3.13. The non linear surface charge is a mathematical function that depends on physical parameters and quantities that are known or calculated during the solving process. To implement this new feature in ENBIOS, we need to calculate the surface integral of the non linear surface charge in the faces of the tetrahedrons that belong to the user specified interfaces. Firstly, each tetrahedron is normalized, by a linear transformation, to a unitary reference tetrahedron, as depicted in fig. 3.13. Consequently, the surface on which we need to calculate the integral, will be a series of unitary reference triangles, as the one in fig. 3.14.

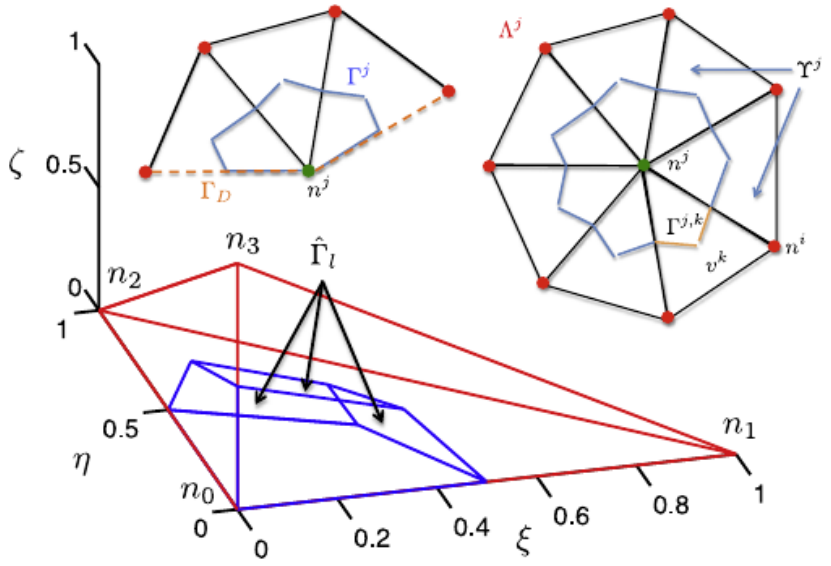

Figure 3.13: *Unitary reference tetrahedron (red) and control volume Ω_c around the node n_0 (blue). In addition, 2D cuts (for clarity) with node n^j and its neighborou volumes and nodes are shown. The control volume is highlighted and the surfaces Γ^j, Γ_D and $\Gamma^{j,k}$ are marked. Picture take from [65].*

ENBIOS implements the finite element method based on control volumes. A control volume Ω_c^j is associated to each node n^j of the mesh. $\Gamma^j = \partial\Omega_c^j$ is the border of the control volume, defined by connecting the baricenters of volumes, faces and edges, as depicted in fig. 3.13. By denoting $\Gamma_{j,k}$ the portion of Γ^j that lies inside the volume ν^k (as shown in fig. 3.13), the additional contribution of the AC site-binding charge ($\tilde{\sigma}_{sb}$) to the Poisson equation is

$$\tilde{Q}_{sb} = q^2 \int_{\Gamma^{j,k}} N_S \alpha_{sb} \frac{\tilde{\phi}_H - \tilde{V}}{k_B T} d\Gamma \tag{3.108}$$

where α_{sb} is calculated from eq. 3.60

$$\alpha_{sb} = K'_b n_{0,H} \frac{k^b_b n_{0,H}(k^b_a n_{0,H} + j\omega) + K'_a k^b_a (K'_b k^b_b + 4k^b_b n_{0,H} + j\omega)}{(K'_a K'_b + n_{0,H}(n_{0,H} + K'_b))((j\omega + k^b_b n_{0,H} + k^f_b)(j\omega + k^b_a n_{0,H} + k^f_a) - k^f_a k^b_b n_{0,H})} \tag{3.109}$$

The non linearity is introduced by the presence of $\tilde{\phi}_H$ and $\tilde{V}$ in the AC site-binding charge formula. The integral of the surface charge is then given by

$$I = \sum_{i \in \Lambda} \tilde{V}^i \int_{\Lambda} N^i \alpha_{sb} \left(\sum_{i=1}^{\Lambda} N^i V_0^i \right) d\Lambda \tag{3.110}$$

where N_i are coefficients defined as

$$N^0 = \eta, \quad N^1 = 1 - \eta - \xi, \quad N^2 = \xi \tag{3.111}$$

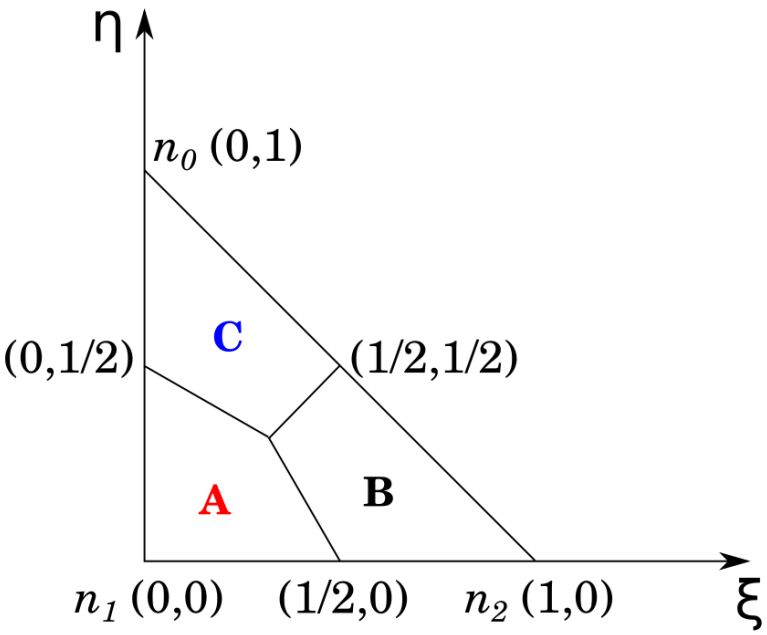

Figure 3.14: *Normalized triangle.*

while η and ξ are the coordinates for the reference system where the unitary triangle is defined.

Each unitary reference triangle is divided into three quadrilateral entities (A, B and C), as shown in fig. 3.15. Furthermore each quadrilateral is divided in triangles (e.g. A1 and A2 in fig. 3.15) and each triangle is normalized into a unitary reference triangle by a linear transformation, $\eta \to \eta'$ and $\xi \to \xi'$.

At this point we calculate the surface integral on the normalized triangles by numerical integration using Gaussian quadrature formulas. In order to reduce the computational effort, we decided to use only three points to compute the surface integral (i.e. second order approximation). The integral on the unitary triangle of a function $\mathbf{f}$ can be approximated as

$$I = \frac{1}{3}\left(f\left(\frac{1}{6},\frac{1}{6}\right) + f\left(\frac{1}{6},\frac{2}{3}\right) + f\left(\frac{2}{3},\frac{1}{6}\right)\right) \tag{3.112}$$

Since we are working on the unitary reference triangles, our integrating function is $N^i\alpha_{sb}$. A powerful property of the unitary reference triangles is that the integral of a function f on A_2 is two times the area of A_2 times the integral of f calculated on the unitary reference triangle. Further details can be found in [101].

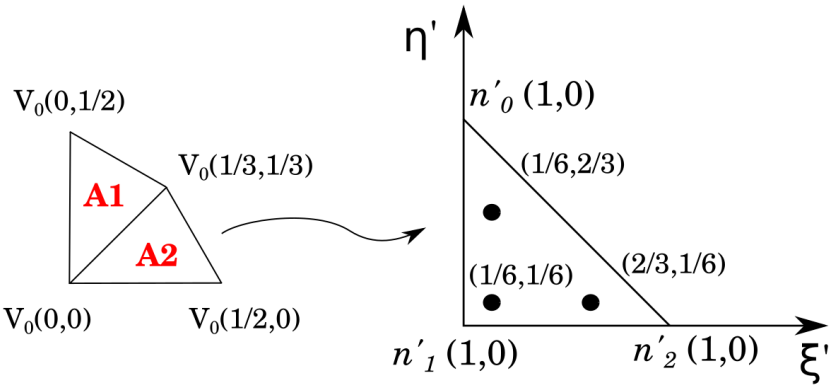

Figure 3.15: *Normalized triangle.*

By using this property, we can easily calculate the total integral on each triangle surface in coordinates η and ξ as the sum of the integrals

$$\begin{aligned} I_{sb}(2,2) = 2A_{A_1}\left(\frac{1}{3}\left(N^1(\frac{1}{6},\frac{1}{6})\alpha_{sb}^{A_1}(\frac{1}{6},\frac{1}{6}) + N^1(\frac{1}{6},\frac{2}{3})\alpha_{sb}^{A_1}(\frac{1}{6},\frac{2}{3}) + N^1(\frac{1}{6},\frac{2}{3})\alpha_{sb}^{A_1}(\frac{2}{3},\frac{1}{6})\right)\right) + \\ 2A_{A_2}\left(\frac{1}{3}\left(N^1(\frac{1}{6},\frac{1}{6})\alpha_{sb}^{A_2}(\frac{1}{6},\frac{1}{6}) + N^1(\frac{1}{6},\frac{2}{3})\alpha_{sb}^{A_2}(\frac{1}{6},\frac{2}{3}) + N^1(\frac{1}{6},\frac{2}{3})\alpha_{sb}^{A_2}(\frac{2}{3},\frac{1}{6})\right)\right) \end{aligned} \tag{3.113}$$

where α_{sb} has the superscript A_x to remind that it is computed considering the V_0^i of the triangle A_x. For example, the triangle A_2, has the following potentials at the vertices

$$V_0^1 = V_0(0,0), \quad V_0^2 = V_0(\frac{1}{2},0), \quad V_0^0 = V_0(\frac{1}{3},\frac{1}{3}) \tag{3.114}$$

meaning that the voltage V_0^0 is mapped to the node n_0', the voltage V_0^1 is mapped to the node n_1' and the voltage V_0^2 is mapped to the node n_2'. The voltage at the vertices of triangle A_x and its unitary reference are the same by construction.

The integrals I_{sb} have to be calculated for each node ($n_{0,0}$, $n_{1,1}$, $n_{2,2}$) and for each node an its adjacent ($n_{0,1}$, $n_{0,2}$, $n_{1,0}$, $n_{1,2}$, $n_{2,0}$, $n_{2,1}$), in order to build a 3×3 square matrix of integrals.

$$
\begin{aligned}
I_{sb}(2,1) = 2A_{A_1}\left(\frac{1}{3}\left(N^0(\frac{1}{6})\alpha_{sb}^{A_1}(\frac{1}{6},\frac{1}{6}) + N^0(\frac{2}{3})\alpha_{sb}^{A_1}(\frac{1}{6},\frac{2}{3}) + N^0(\frac{2}{3})\alpha_{sb}^{A_1}(\frac{2}{3},\frac{1}{6})\right)\right) + \\
2A_{A_2}\left(\frac{1}{3}\left(N^0(\frac{1}{6})\alpha_{sb}^{A_2}(\frac{1}{6},\frac{1}{6}) + N^0(\frac{2}{3})\alpha_{sb}^{A_2}(\frac{1}{6},\frac{2}{3}) + N^0(\frac{2}{3})\alpha_{sb}^{A_2}(\frac{2}{3},\frac{1}{6})\right)\right) \\
I_{sb}(2,3) = 2A_{A_1}\left(\frac{1}{3}\left(N^2(\frac{1}{6})\alpha_{sb}^{A_1}(\frac{1}{6},\frac{1}{6}) + N^2(\frac{1}{6})\alpha_{sb}^{A_1}(\frac{1}{6},\frac{2}{3}) + N^2(\frac{1}{6})\alpha_{sb}^{A_1}(\frac{2}{3},\frac{1}{6})\right)\right) + \\
2A_{A_2}\left(\frac{1}{3}\left(N^2(\frac{1}{6})\alpha_{sb}^{A_2}(\frac{1}{6},\frac{1}{6}) + N^2(\frac{1}{6})\alpha_{sb}^{A_2}(\frac{1}{6},\frac{2}{3}) + N^2(\frac{1}{6})\alpha_{sb}^{A_2}(\frac{2}{3},\frac{1}{6})\right)\right)
\end{aligned}
\tag{3.115}
$$

Each triangle that composes the surface interface has its matrix I_{sb}, that is used by ENBIOS to compute the overall surface integral.

3.3.3 Commercial TCAD

In this section we present an alternative approach to the simulation of biosensors devices by using commercial Technology Computer Aided Design (TCAD) tools for semiconductor devices [102, 96]. Simulation tools, such as Sentaurus Device [103], are developed with the aim of simulation and optimization of semiconductor processing technologies and devices. Sentaurus Device is an advanced multidimensional (1D/2D/3D) environment for electrical, thermal and optical characterization of silicon-based and compound semiconductor devices. It is a golden standard in semiconductor industry and adapting it to nanosensors would substantially reduce the entrance barrier to the adoption of modeling in the field of electronic biosensors. It supports a broad range of applications such as CMOS, power, memory, image sensors, solar cells, and analog/RF devices, but it is not dedicated to the simulation of devices in liquid environment. In other words, the "electrolyte material" is not available for simulations. However, adding such "material" would pave the way to an integrated approach to the simulation of semiconductor nanosensors [104, 105]. This observation sets the stage and motivation for the work described in the following which is complementary to the development of the ENBIOS tool.

Modeling of the electrolyte

In order to model the electrolyte material in Sentaurus Device, we exploit the similarity between the equations describing positive and negative ions in the electrolyte (Poisson-Nernst-Plank) and those for holes and electrons in a semiconductor (Poisson drift-diffusion). 1:1 electrolyte can be described in Sentaurus Device as a semiconductor with zero gap, a constant permittivity and an effective density of states in conduction and valence band

$$pH \leq 7: \quad N_C = N_V = N_A 10^{-3}\left(n_0 + n_{0,H_b^+}\right)$$
$$pH > 7: \quad N_C = N_V = N_A 10^{-3}\left(n_0 + \frac{10^{-14}}{n_{0,H_b^+}}\right) \tag{3.116}$$

where n_0 is the ion molar concentration in [M] (equivalently [mol/l]) in the bulk of the solution, defined as a region with the same concentration of positive and negative ions, hence overall charge neutrality. n_{0,H_b^+} is the hydrogen concentration in the bulk solution, normalized to 1 M. As an example, to model a buffer solution with 10 mM of NaCl and pH = 4, we set

$$N_C = N_V = N_A 10^{-3}(10 \cdot 10^{-3} + 1 \cdot 10^{-4}) = 6.082410^{18}\ cm^{-3} \tag{3.117}$$

The bulk electrolyte is defined as the region with constant potential and a zero net charge density as a result of equal total concentrations of positive and negative ions, respectively, represented by p and n; hence, for a zero bandgap material $n_b = p_b = N_C = N_V$. Note that $E_G = 0\ eV$ is not a necessary condition, provided that N_C and N_V are duly adapted in case that $E_G \neq 0$.

The electron and hole mobilities in this electrolyte material are adjusted to the corresponding values of the ions [106]. Care should be paid to disable the default temperature dependence of the model parameters and to avoid the build-up of unphysical offsets in N_C, N_V, E_G and mobility whenever the temperature is different from the model reference value.

The TCAD provides calibrated mobility models for silicon, DC, AC and transient analysis, meshing of arbitrary geometries in 2D and in 3D [96, 67]. Clearly, there are limitations as well. First of all, only a single 1:1 ionic solution can be included, whereas electrolytes with many types of ions and diversified valence are used in experiments; this point will be discussed later in this section. In addition, it is possible to add some simple surface reactions [96], but only idealized interfaces without steric effects [107] can be treated. The control on the numerical error is also quite limited with respect to the one achievable with ad-hoc codes. At the time that this approach was firstly developed and presented [102] a similar technique has been reported in [67], but independently developed.

Implementation of the surface reactions models

Even with the TCAD, as we have done in sections 3.3.1 and 3.3.2, it is possible to implement the site-binding charge defining the pH dependent response of insulators. The scope of this section is to present the implementation of a bias dependent surface charge able to replicate models such as the site-binding one described in 3.2. Details of this implementation were published in [96]. Sentaurus Device allows the users to insert a surface charge that has the form of interface donor or acceptor traps [103], which occupation functions are expressed as

$$f^a = \frac{c_C^a + c_V^a}{c_C^a + c_V^a + e_C^a + e_V^a}, \quad f^d = \frac{c_C^d + c_V^d}{c_C^d + c_V^d + e_C^d + e_V^d} \tag{3.118}$$

respectively for acceptor a and for donor d. c_C and c_V are the capture rates from the conduction and the valence band, respectively, and e_C and e_V are the emission rates to the conduction and valence band, respectively. Fig. 3.16 summarizes the capture and emission rates to and from the conduction and valence bands.

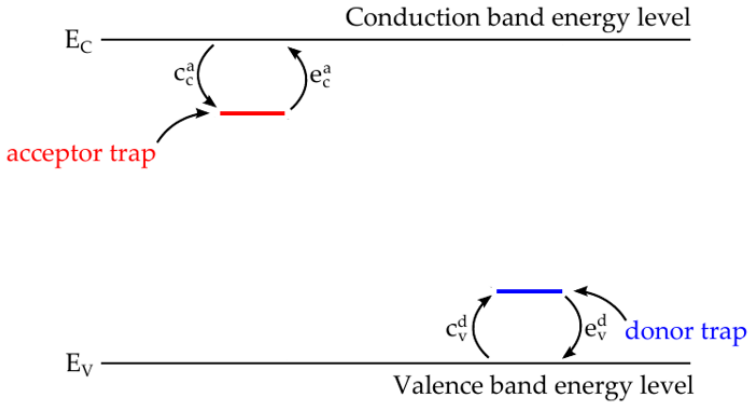

Figure 3.16: *Picture of the capture and emission rates to and from the conduction and valence bands.*

The surface charge is

$$\sigma_{sb} = q\left(N_S^d f^d - N_S^a f^a\right) \tag{3.119}$$

where N_S^d and N_S^a are the surface densities per unit area for donor and acceptor traps, respectively. Since we are using both donor and acceptor traps we are able to implement amphoteric sites, that can capture and emit charges (i.e. the difference between terms in eq. 3.119). Sentaurus Device provides a physical model interface (PMI) that allows the user to rewrite the emission and capture rates as arbitrary function of the main local physical parameters, such as electric field, temperature and electrons/holes concentrations. With eq. 3.119 we are able to map bias dependent surface charges such as the site-binding charge of eq. 3.42.

Reminding that surface and bulk concentrations are related by

$$n_s = n_b exp\left(\frac{q\psi_0}{k_B T}\right), \quad p_s = p_b exp\left(-\frac{q\psi_0}{k_B T}\right) \tag{3.120}$$

where $n_s p_s = n_b p_b$ and $n_b = p_b = N_C = N_V$, we can then express the exponential of the interface potential as

$$exp\left(-\frac{q\psi_0}{k_B T}\right) = \frac{p_s}{\sqrt{n_s p_s}} = \frac{p_s}{\sqrt{N_C N_V}} \tag{3.121}$$

The site-binding charge is finally implemented, as σ_{sb} in eq. 3.119, by choosing suitable expressions for the capture and emission rates (fig. 3.17) and assigning them by means of the PMI interface of Sentaurus Device.

$$
\begin{aligned}
c_V^d &= cH_B^2 p_S \\
e_V^d &= K_a K_b n_S + K_b c H_B \sqrt{n_S p_S} \\
c_C^a &= K_a K_b n_S \\
e_C^a &= K_b c H_B \sqrt{n_S p_S} + cH_B^2 p_S
\end{aligned}
$$

Figure 3.17: *Capture and emission rate equations [96] expressed in terms of local n and p concentrations of the surface.*

The site-binding model implemented in the TCAD was initially validated by a comparison with the theoretical models with the simple 1D simulator described in sec. 3.3.1. TCAD simulation and theoretical model show a perfect agreement in terms of site-binding surface charge as a function of the applied potential to the semiconductor on the back of the insulator (V_B in fig. 3.18), thus confirming the correctness of the approach.

Once the implemented model was validated, we have extensively used the modified version of the TCAD to simulate complex geometries, such as nanoribbon and FinFETs. As an example, fig. 3.19 shows on the left a picture of the simulated system with the SOI silicon NR with passivation over the source/drain connections included. On the right we reported the simulated $I_D - V_{FG}$ characteristics for different pH values. We see that the threshold voltage shift is small for high acidic pH values (around 3). This indeed confirms the validity of the model as expected from NRs featuring SiO_2 as gate oxide.

As a second example, we propose the simulation of a nanoribbon device, like the ones described in 2.1, by varying the pH of the electrolyte solution. The simulation results are in line with the experimental finding on SiO_2. In fact, as reported by the 1D simulations in fig. 3.9, the voltage shift tends to zero for very acidic pH values. This is also confirmed by the measurements performed on NRs and the corresponding voltage sensitivities that we have reported in sec. 4.4, fig. 4.21.

In the same way as for the DC site-binding model, also the model described in section 3.2.3 that accounts for the case of high salt concentration, has been implemented in the TCAD [96].

Extension to multi-ion electrolytes

One of the basic assumptions behind the proposed TCAD approach is that the electrolyte is symmetric with ion species of unit valence. In real world, however, most biosensors operate with multi-ion electrolytes featuring several ion species of diverse valence. For instance, a commonly used Phosphate Buffered Saline (PBS) in biosensor research is composed of four salts: potassium dihydrogen phosphate (KH_2PO_4), disodium hydrogen phosphate (Na_2HPO_4), sodium chloride (NaCl) and potassium chloride (KCl). At the

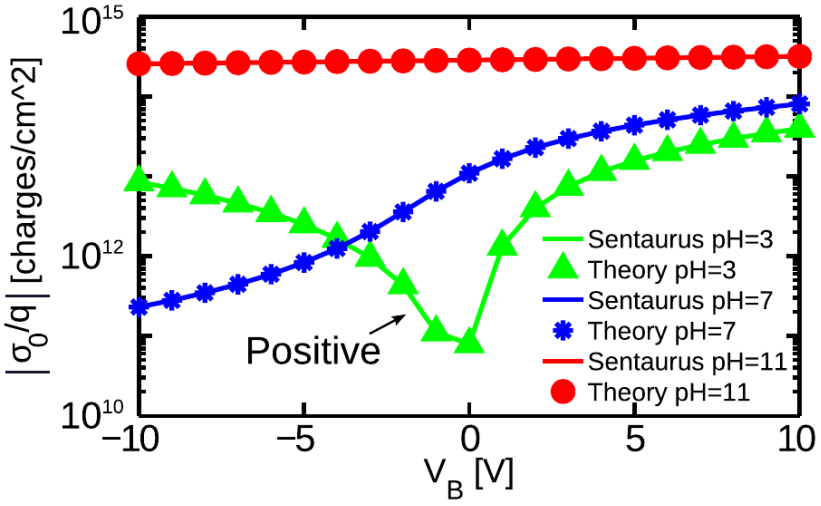

Figure 3.18: *Site-binding charge implementation verification by comparison with theoretical models (picture taken from [96]). Comparison between the PMI model (solid lines) and eq. 3.40 (symbols) for different values of V_B and pH. $N_S = 5 \cdot 10^{14}$ cm^{-2}, $n^{\infty} = 1$ mM, and SiO_2 gate dielectric.*

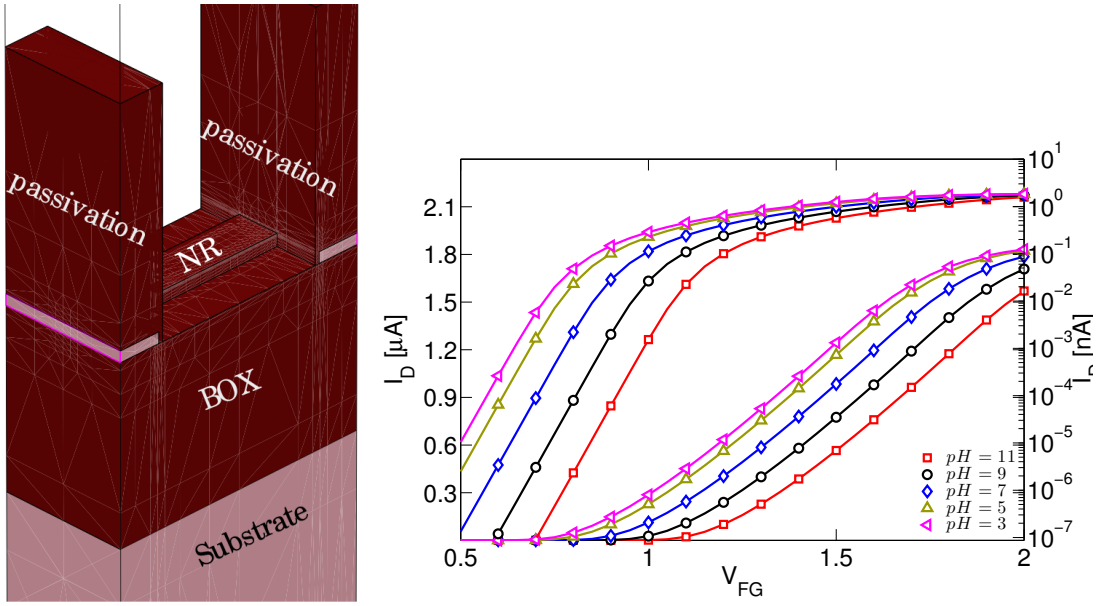

Figure 3.19: *Left: simulated nanoribbon structure, with passivations covering the source/drain regions. Right: TCAD simulated $I_D - V_{FG}$ characteristics for different pH values. The threshold voltage shift is clearly small for low pH values, as expected with NRs featuring SiO_2 as gate oxide.*

bulk concentration n_0 = 248.4 mM and the temperature T = 300 K, the dissociation leads to the following distribution of ion concentrations: K^+ = 45 mM, $H_2PO_4^-$ = 18 mM, Na^+ = 202 mM, HPO_4^{2-} = 101 mM, Na^+ = 1.4 mM, Cl^- = 28.4 mM. The description of such a complex electrolyte would be very complicated in ad-hoc simulators and actually impossible in state of the art TCAD tools, but it could be greatly simplified if we could introduce an *equivalent electrolyte* composed only of two ion species, one cation and one anion.

To see if such a simplification is possible, we firstly note that in DC conditions, under the assumption of a dilute electrolyte with non-interacting ion species, the Gouy-Chapman theory predicts that the potential profile decays according to a Debye length given by [108]

$$\lambda_D = \sqrt{\frac{\varepsilon_0 \varepsilon_r k_B T}{\sum_{M_a} (qZ_m)^2 n_{0m} + \sum_{M_c} (qZ_m)^2 n_{0m}}} \tag{3.122}$$

where we have separated the contributions of anions, in number of M_a, from that of the cations, in number M_c. The screening properties of the electrolyte are defined by the Debye length. Since the biosensor response is determined by the screening properties of the electrolyte, then it makes sense to define the ion concentration of the equivalent electrolyte in such a way that its Debye length is the same as the one of the actual electrolyte. We will assume, in general, that the equivalent electrolyte has a valence Z_a for the anions and Z_c for the cations. Imposing the equivalence of the Debye lengths and the bulk charge neutrality for the equivalent electrolyte, we have the following system of equations

$$\begin{cases} \sum_{M_a} Z_m^2 n_{0m} = Z_a^2 n_{0a} \\ \sum_{M_c} Z_m^2 n_{0m} = Z_c^2 n_{0c} \\ Z_a n_{0a} = Z_c n_{0c} \end{cases} \implies \begin{cases} F_a = Z_a^2 n_{0a} \\ F_a = Z_c^2 n_{0c} \\ F_a Z_c = F_c Z_a \end{cases} \tag{3.123}$$

where $F_a = \sum_{M_A} Z_m^2 n_{0m}$ and $F_c = \sum_{M_c} Z_m^2 n_{0m}$. As expected the system is underdetermined and the free parameter Z_c remains. We note that Z_a may not be an integer number. We also note that if $F_a = F_c$ then the equivalent electrolyte has symmetric valence Z:Z and concentrations $n_{0a} = n_{0c}$. Consequently, it is possible to assume unit valence and then exactly represent the actual electrolyte with an equivalent one having $n_{0a} = F_a$ and $n_{0c} = F_c$ by setting the corresponding effective density of states according to 3.123. The PBS solution we introduced before fulfils the charge neutrality condition but it does not fulfil the condition Fa = Fc. Therefore, it cannot be modeled exactly with an equivalent electrolyte of unit valence. In this case we have decided to use F_a and F_c, namely $F_M = (F_a + F_c)/2$.

To appreciate the quantitative impact of the error induced in the solution we report in the left plot of fig. 3.20 the mean field electrostatic potential profiles for two values of n_0 and two values of V_{DC}. The right plot shows the corresponding charge density profiles due to anions and cations at $V_{DC} = 100$ mV and $n_0 = 200$ mM. All the simulations were made using ENBIOS. As expected the symmetric 1:1 electrolyte does not exactly mimic the real PBS, but in this case the maximum error on the potential is at most a fraction of $k_B T/q$. We also note that the charge profile of the real electrolyte is squeezed toward the interface more than that of the equivalent electrolyte. This is because the solution has a large component, both in cations and in anions, of ions with valence modulus 2, hence it has a shorter Debye length.

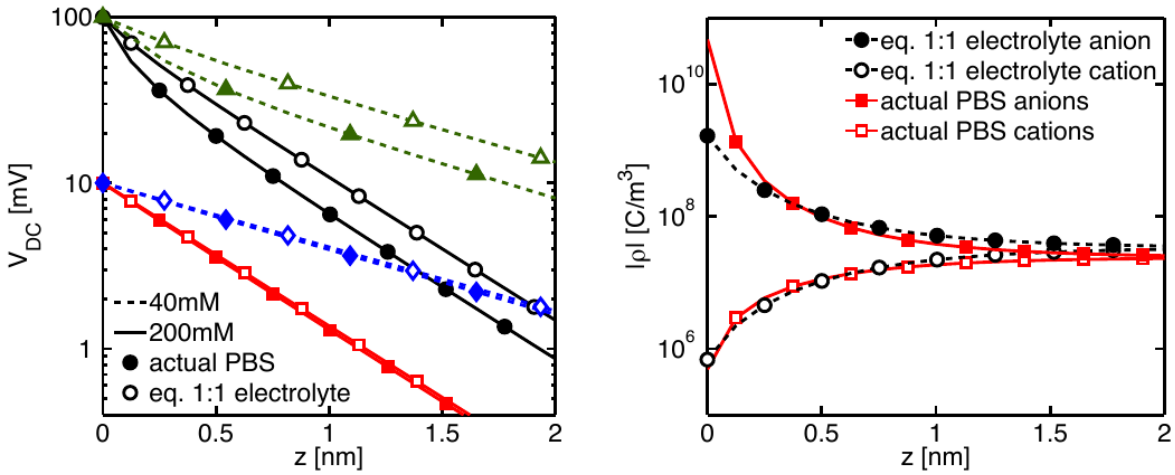

Figure 3.20: *Comparison of potential profiles (left) and absolute charge density profiles of anions and cations (right) between the PBS solution with $F_a \neq F_c$ (filled symbols) and the equivalent electrolyte with unit valence (open symbols). The curves in the left plot correspond to $n_0 = 40$ mM (dashed lines) and 200 mM (solid lines) and $V_{DC} = 10$ and 100 mV, while in the right plot $V_{DC} = 100$ mV and $n_0 = 200$ mM. We verified explicitly that the mutual agreement at high V_{DC} is much improved if an equivalent electrolyte with $Z = 2$ is chosen (not shown). Unfortunately this is not possible in commercial TCAD.*

To understand in detail the derivations above, we simulated an hypothetical buffer solution with composition: K^+ 45 mM, $H_2PO_4^-$ = 18 mM, Be^{2+} = 101.4 mM, HPO_4^{2-} = 101.4 mM, Na^+ = 1.4 mM, Cl^- = 28.4 mM, where we have replaced some Na^+ with Be^{2+} in order satisfy the condition $F_a = F_c$. The equivalent electrolyte was chosen to be 1:1 symmetric, as the one simulated by the TCAD. In this case the agreement between simulations with the actual and the equivalent electrolyte is improved but there is still a small error. If we then use a valence of 2 instead of 1 in the equivalent electrolyte, in particular if the valence of the symmetric species of the equivalent electrolyte is chosen to be equal to the one of the ion species dominating the composition of the buffer, we can obtain an almost perfect agreement between simulations with the actual and the equivalent electrolyte. Unfortunately, it is not possible in TCAD to change the electron and hole charges so as to mimic valence values different from 1. Therefore the accuracy of TCAD simulations is inherently limited by the errors exemplified in fig. 3.20. Such errors are modest unless very high potentials and very high concentrations are achieved in the system.

3.3.4 Porting on the nanoHUB platform

This section describes the effort made as part of this thesis to make available to a larger community of researchers the extended PB and PNP modeling tools including surface reactions that were developed in our work. Such an effort is synergetic with that on development of TCAD models for nanobiosensors with Sentaurus Device. It has been

modeled by the nanoHUB platform.

nanoHUB is a community web site dedicated to education and research through online simulation tools and online tutorials. Online simulation on nanoHUB is a free service, it comprises more than 400 tools in various fields of the nanotechnologies an it is currently used by 1.4 million users. The simulation tools and the tutorials are powerful educational means for students and professors. The resources available on nanoHUB can be used for research purposes but it is also possible, by using the nanoHUB workspace, to develop an interface for a new tool. It is indeed possible for a user, or a group of users, to upload, compile, test and debug their own code, written in different programming languages (e.g. C, C++, Fortran ad Matlab). The developers can work on the code in a private area of nanoHUB. Once the code of the new tool is stable, the users can share it with the other users of nanoHUB by making it public, if necessary with some restrictions.

This is the framework and modality that we exported to make available impedance spectroscopy and ISFET simulations based on ENBIOS to the general community. nanoHUB offers a unique opportunity to participate to a community of researchers, contribute and get visibility worldwide. For these many reasons we decided to use the nanoHUB platform to publish two different tools, ENBIOS-1D Lab and ENBIOS-2D Lab, that are based on ENBIOS, the 3D-CVFEM simulator that we presented in sec. 3.3.2.

ENBIOS-1D Lab

ENBIOS-1D Lab [109] has been created to simulate simple 1D structures that can help researchers gaining an intuitive insight on the DC and AC operation of parts of electronic biosensors. The GUI (Graphical User Interface) interface of the tool is reported in fig. 3.21. It is possible to simulate three different structures, as depicted in fig. 3.22:

- E: electrolyte;
- EI: electrolyte/insulator;
- EIS: electrolyte/insulator/semiconductor;

The structures have two contacts, $E1$ and $E2$, that can be set (according to the user needs) as either *ideally polarizable* or *faradaic* (if in contact with the electrolyte) or *ohmic* (if in contact with the semiconductor). Faradaic (or ohmic) contacts mimic contacts that support electrochemical reactions (generation-recombination processes, respectively); therefore, non-zero ionic (electron and hole) DC currents can flow through these electrodes. Faradaic contacts do not allow the formation of the double layer, regardless of the bias voltage applied. Ideally-polarizable contacts behave as blocking contacts; DC ionic currents (electron/hole currents) are not implemented while displacement currents are possible. Ideally-polarizable contacts, in contrast to Faradaic electrodes, generate an electrical double layer in the electrolyte. As described in sec. 3.3.2, the simulator solves initially the DC problem and consequently the AC problem. The user can set and tune

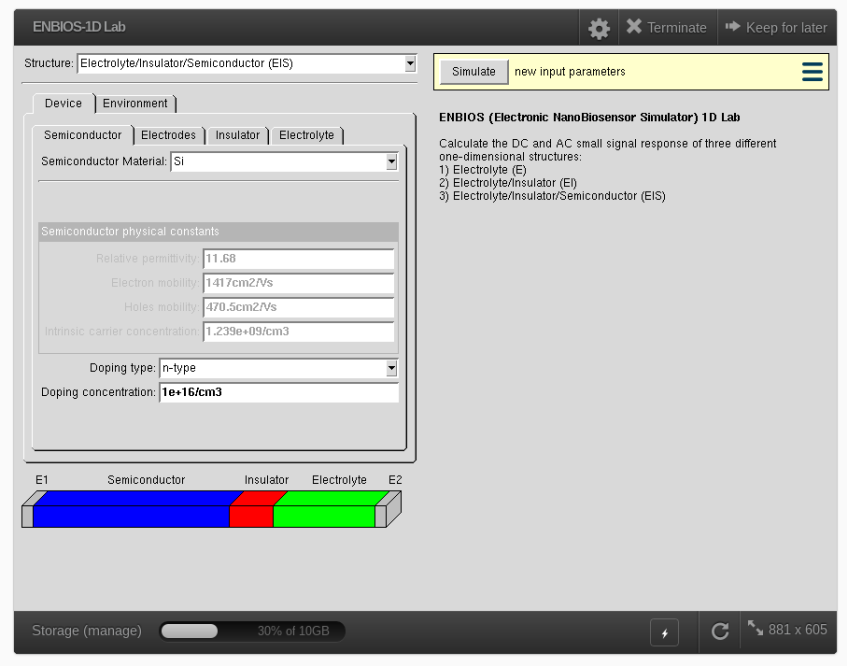

Figure 3.21: *ENBIOS-1D Lab graphical interface.*

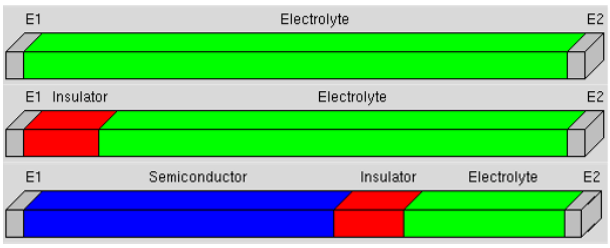

Figure 3.22: *Sketch of the three structures available for simulations in ENBIOS-1D Lab.*

many different options, as we can see from fig. 3.23: (a) semiconductor parameters, (b) electrodes types, (c) insulator properties (insulator type, site-binding DC and AC and their corresponding parameters), (d) electrolyte parameters (solvent, ion composition, concentration, pH, frequency dependent dielectric constant, etc.) and (e) environment parameters (DC voltage applied at the electrodes, temperature, type of AC sweep and tolerance of the solution).

Once the simulation is done, it is possible to analyze the results by plotting many different DC and AC quantities. Electrostatic potential, carrier concentrations and ion concentrations can be plotted either in DC or in AC, real-imaginary or magnitude-phase or cartesian, for each DC bias point or AC frequency point. 3.24a-c shows the DC electrostatic potential, the DC concentrations of charged particle and the real and imaginary part of the AC charged particle concentrations, respectively. Finally, it is also possible to plot the admittance (or impedance) of the simulated structure, as reported in 3.24d.

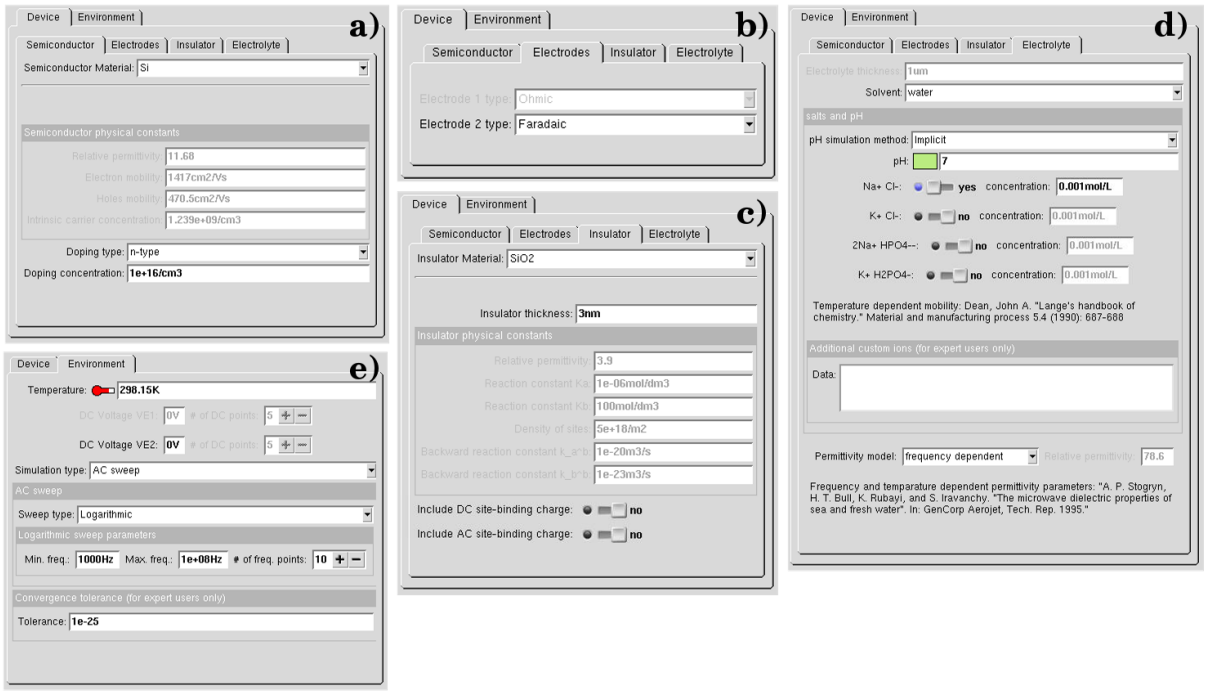

Figure 3.23: *a) Semiconductor, b) Electrodes, c) Insulator, d) Electrolyte and e) Environment folders of ENBIOS-1D interface.*

ENBIOS-2D Lab

ENBIOS-2D Lab [110] exploits all the features of the 1D version to simulate a 2D SOI ISFET. The GUI of ENBIOS-2D Lab is reported in fig. 3.25, that shows also a picture of the simulated device. As for the 1D version of the tool, the building blocks are semiconductor, insulator and electrolyte materials. The properties of each material can be modified, as shown in fig. 3.26. The folder "Semiconductor" allows to select the type of semiconductor and the doping parameters of source, drain and channel regions. In the "Insulator" folder is possible to select the physical parameters for the BOX, gate-oxide and passivations. It is also possible to enable/disable the DC and AC site-binding on the gate insulator. The "Electrolyte" folder offers the possibility to select the ionic composition of the electrolyte solution, the molar concentration and the pH. It is also possible to activate the frequency dependent permittivity model. The "Environment" folder, reported in fig. 3.27 has some interesting additional features with respect to ENBIOS-1D Lab. It is possible to simulate an $I_{DS} - V_{FG}$ characteristics, by setting the amplitude of the V_{FG} sweep and the values of V_{DS} and V_{BG}. The user can also specify either as voltage or as current multiple DC bias point at which the frequency analysis will be performed.

By selecting the "Plots" folder, the user can also specify multiple cut lines in x and z directions. For each cut line, the tool will generated the correspondent plots of the DC and AC quantities. ENBIOS-2D Lab provides also multiple plots of the admittance and impedance.

Additionally, the user can perform different simulations in sequence, by changing some

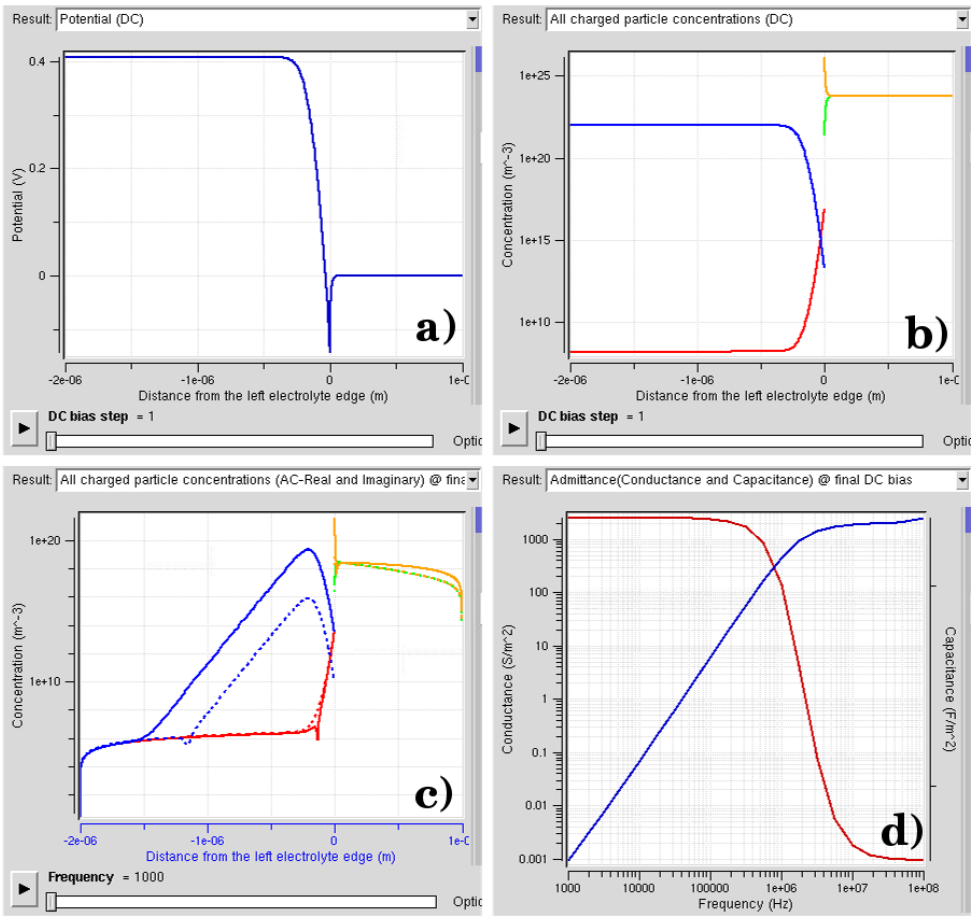

Figure 3.24: *Summary of the main plots generated by the tool at the end of a simulation. a) DC potential, b) DC concentrations of all the charged particles (electrons/holes and anions/cations), c) AC concentrations (real and imaginary part at a fixed frequency) of all the charged particles (electrons/holes and anions/cations) and d) admittance spectra in terms of capacitance and conductance.*

of the simulation parameters, and then compare the results. For example, in fig. 3.28a,c we have performed two simulations with an electrolyte solution at different pH value. Fig 3.28a shows the comparison between the $I_D - V_{FG}$ characteristics, simulated at pH=3 and pH=7. From the results it is easy to calculate the current and/or voltage shift between the two $I_D - V_{FG}$ curves hence the sensitivity. 3.28d shows an other example of curves comparison; it is indeed possible to compare the impedance, V_{FG}/I_{FG} (or admittance, I_{FG}/V_{FG}) simulated at the two pH values. This was just an example obtained by performing two simulations at different solution pH values, but the same comparison can be made by changing any other simulation parameter.

The flexibility, the large number of input parameters, the ease of use, make ENBIOS-1D Lab and ENBIOS-2D Lab two powerful tools. ENBIOS-1D Lab is the right starting point to understand and get practice on the basic concepts of nanoelectronics biosensing, such as the double layer theory and the site-binding surface charge. ENBIOS-2D Lab extends its 1D counterpart and allows users to practically observe and analyze both the

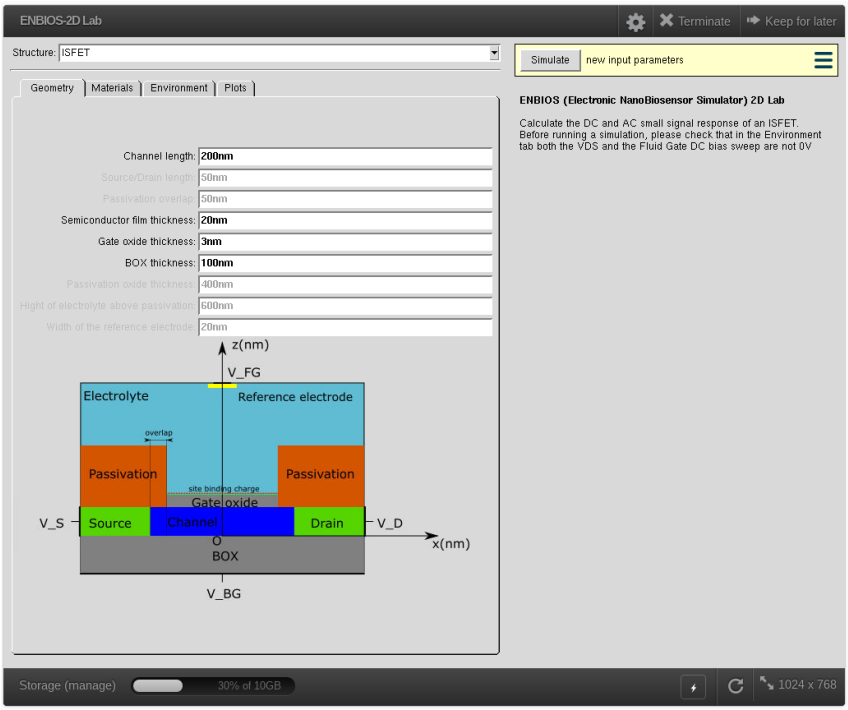

Figure 3.25: *ENBIOS-2D Lab graphical interface.*

Figure 3.26: *Left: semiconductor, center: insulator and right: electrolyte folders of the ENBIOS-2D interface.*

inner physical quantities (e.g. electrical potential, ions concentrations, etc.) and the outer electrical quantities (e.g. I_D-V_{FG}, impedance, admittance, etc.) of an ISFET.

Usage and results

Both tools are experiencing fair amount of success in terms of usage at the time of writing they collected more than 400 simulation runs for ENBIOS-1D Lab and more than 100 for ENBIOS-2D Lab, and the overall number of users is 50 and constantly growing.

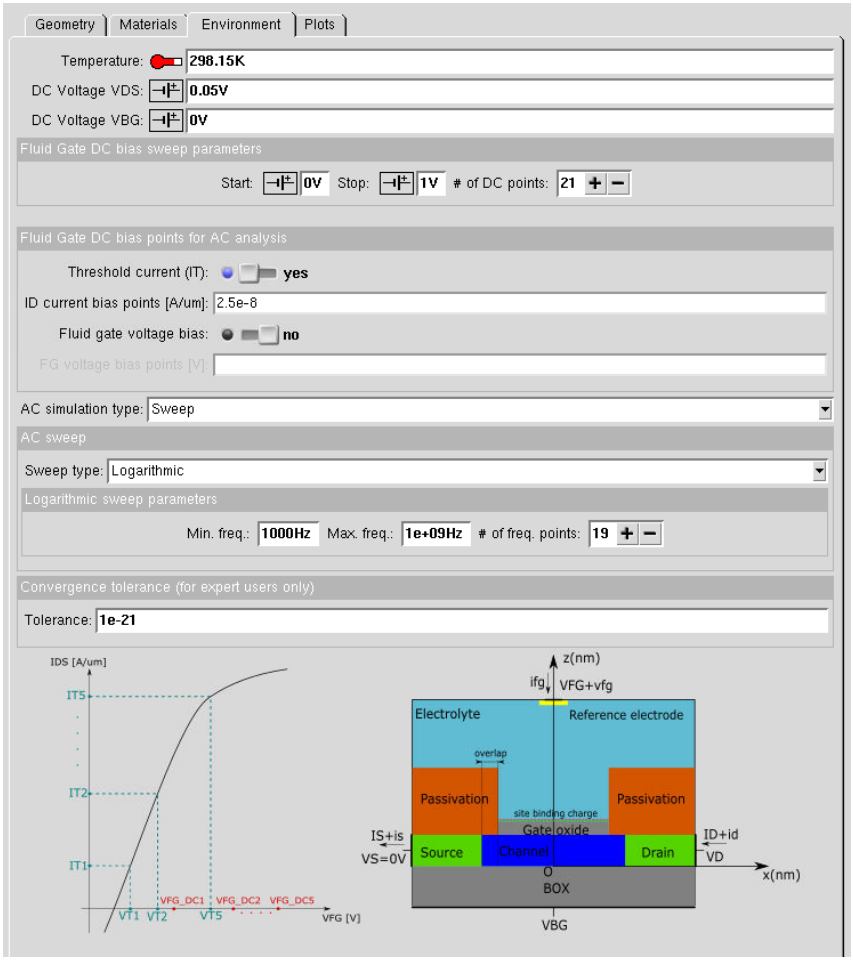

Figure 3.27: *Environment folder of the ENBIOS-2D interface.*

The feedbacks received after the publication of the 1D version were extremely useful and have led to relevant improvements, both regarding the features of the tool and the corresponding documentation.

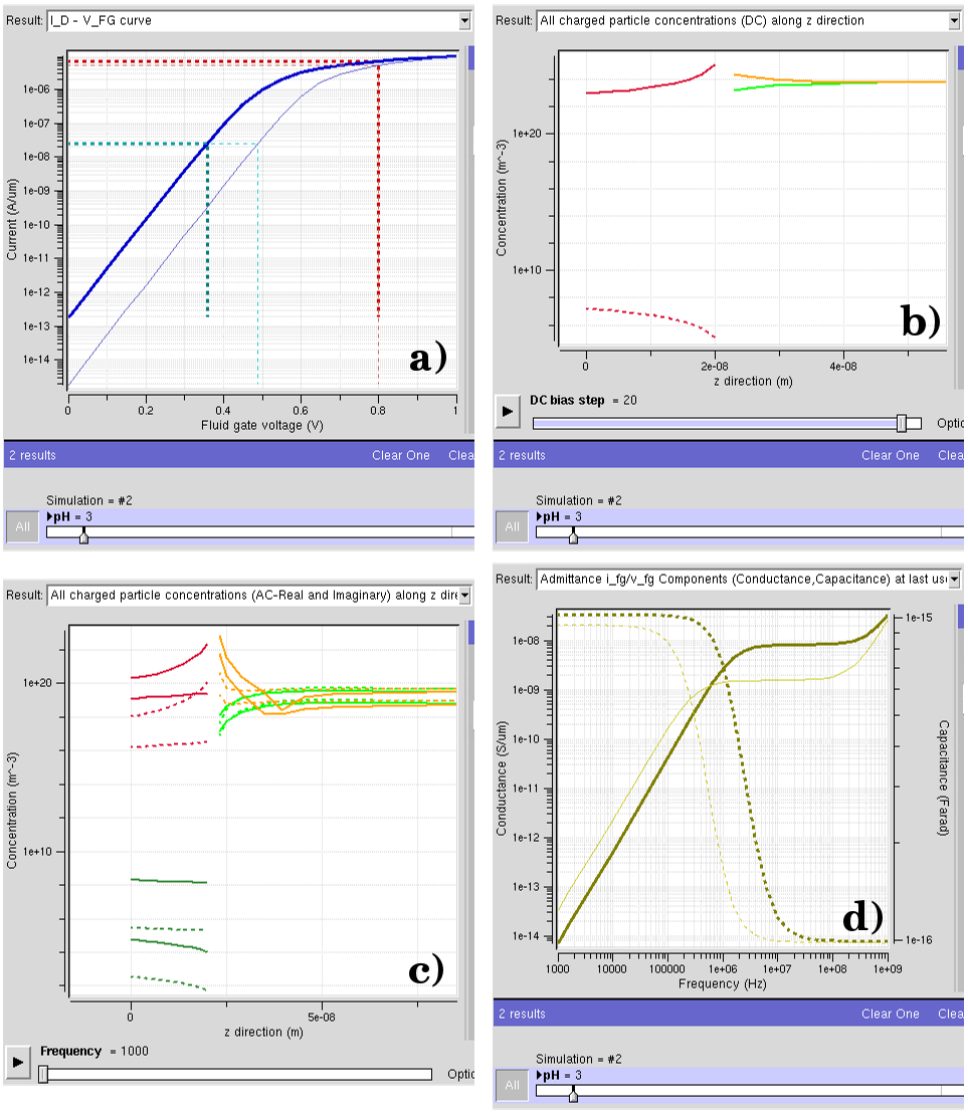

Figure 3.28: *Summary of the main plots generated by the tool at the end of a simulation. a) I_D-V_{FG} at pH=7 and pH=3, b) DC concentrations (at x=0) of all the charged particles (electrons/holes and anions/cations), c) real and imaginary part of the AC concentrations (at x=0 and at 1 kHz) of all the charged particles (electrons/holes and anions/cations) and d) admittance spectra in terms of capacitance and conductance at pH=7 and pH=3.*

3.4 Compact model for microparticles response

Besides numerical models as those presented in the previous paragraphs, compact analytical models are also extremely useful in all the fields of engineering to gain physical insight on the main physical dependencies that governs the sensing process. This is especially true for the microparticle sensing, where there is a lack of simple models. In this context an analytical theory consistent with the PB-PNP modeling framework of the analytical model for the admittance change (ΔY) induced by spherical neutral dielectric (colloidal) particles in nanoelectrode based biosensors at zero DC bias developed in [10, 101] and then extended to explicitly takes into account ionic diffusion currents. We have extensively val-

idated it by means of numerical simulations. The dielectric particles can represent a first order approximation of several types of biomolecules such as for instance proteins and viruses [111]. We demonstrate that, in spite of the approximations made, the proposed model nicely captures the dependence of the nanoelectrode admittance change upon frequency (f), particle volume (Ω_a) and permittivity of the media, over a wide range of sensor and particle physical and geometrical parameters. Our results support the possibility to use the analytical model as a mean to gain insight on the nanoelectrode response, especially in the high frequency limit. In particular we will compare the model to the microparticle data presented in chapter 5.

The analytical model presented in [112] asserts that the admittance variation due to the insertion of a nanoparticle in the electrolyte can be expressed as:

$$\Delta Y = \Delta G + \jmath\omega\Delta C = f(\omega)\,(\sigma_b + j\omega\varepsilon_b)\Omega_a \left(\frac{\tilde{E}_0}{\tilde{V}_0}\right)^2 \tag{3.124}$$

where $f(\omega)$ is a complex function that depends slightly on the particle radius a and the electrolyte and particle conductivities (σ_b and σ_a, respectively) and permittivities (ε_b and ε_a, respectively), Ω_a is the particle volume, $\tilde{V}_0$ is the AC potential applied at the electrodes and $\tilde{E}_0$ is the unperturbed electric field at the particle position (assumed constant over the particle volume).

Eq. 3.124 generalizes a similar expression presented in [10] but extends it considerably by accounting for the ionic diffusion currents, which were instead neglected in [10], and are especially important for conductive particles. Where a non negligible electrical double layer is formed at the surface. The model predicts that for small particles the nanoelectrode response should be proportional to the electrolyte complex conductivity, to the particle volume, and to the (in general complex and frequency dependent) squared unperturbed electric field at the particle location normalized to the corresponding applied voltage.

In order to validate the analytical model of eq. 3.124 we used as reference the two-dimensional numerical finite-difference solver for the Poisson-Boltzmann (eq. 3.4) and Poisson-Nernst-Planck equations (Eqs. 3.13-3.15) described in [50, 113]. We explicitly verified that the addition of more counter-electrodes would not change the results in the considered range of particle radii.

Therefore, differently from [50, 113] where electrodes were located one in front of the other (Fig.3.29a), the improved simulation code used in this work is suited to check if the assumption of field uniformity made in the derivation of eq. 3.124 has an appreciable impact on the accuracy of the results.

Unless otherwise stated, the DC bias on the electrodes and the net charge on the particle are both zero, consistently with the model assumptions. The particle permittivity is taken equal to $2.3\varepsilon_0$ and its radius ranges from 5 nm (which may represent a large protein [111]) to 500 nm (a virus or a colloidal particle [114]). A thin dielectric layer with

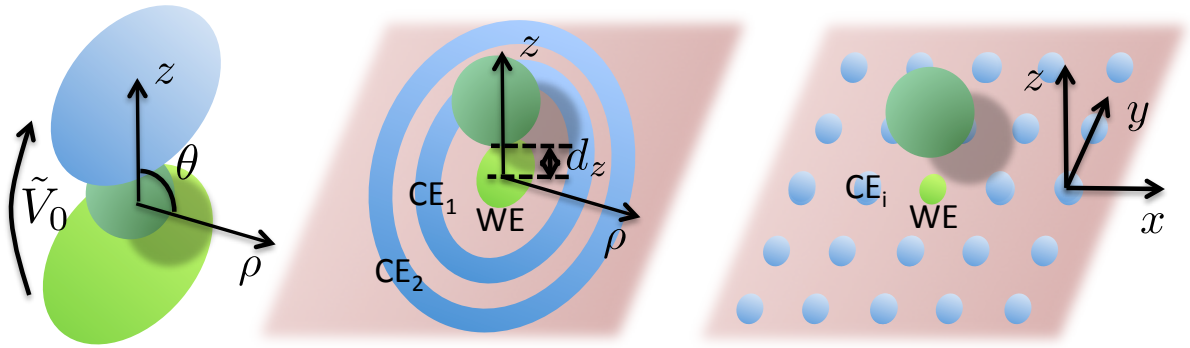

(**a**) uniform field (**b**) 2D approximation (**c**) real array

Figure 3.29: *(a) Sketch of the uniform field system used to derive the analytical model; (b) 2D approximation with cylindrical symmetry of the nanoelectrode array; (c) sketch of the real array presented in [10]. The AC potential (2 $\tilde{V}_0$) is applied to the working electrode (WE, green). The counter electrodes (CE_i, blue) are grounded. The inner ring (CE1) in (b)) mimics the 8 CEs nearest to WE in (c); CE2 is shorted to CE1 and mimics the next 16 nearest electrodes.*

Parameter	**Symbol**	**Value**	**Units**
System radius	ρ_{max}	1.5	μm
System height	z_{max}	2	μm
Electrode radius	r_{el}	75	nm
Electrode pitch	p_{el}	660	nm
Counter-electrode width	$2r_{el}$	150	nm
Stern layer thickness	h_S	0.25	nm
Mobility of Na^+	μ_1	$3.242{\cdot}10^{11}$	m/Ns
Mobility of Cl^-	μ_2	$4.937{\cdot}10^{11}$	m/Ns
Electrolyte permittivity	ε_b	$75\varepsilon_0$	F/m
Particle permittivity	ε_a	$2.3\varepsilon_0$	F/m
Temperature	T	298.16	K

Table 3.2: Parameters used in the simulations.

permittivity ε=$75\varepsilon_0$ and thickness 0.25 nm, mimicking the Stern compact layer [115] was considered on the bottom surface. Note that in the Stern layer the permittivity should be lower than in the electrolyte [115] but, because in all the simulations no DC bias is applied, the exact value of the compact layer permittivity has a modest quantitative impact on the results [102], thus justifying the assumptions made. For the sake of simplicity the electrolyte dielectric constant is independent of ion-concentration and frequency [84, 82]. This approximation has a small quantitative impact but no qualitative practical consequence on the results. Tab. 3.2 reports the simulation parameters (if not otherwise stated), where the pitch is defined as the distance between the electrodes centres.

Fig. 3.30 compares the change in conductance (ΔG, top) and capacitance (ΔC, bottom) obtained by means of 2D numerical simulations with the predictions of eq. 3.124 for particles of different radius (from 40 nm to 500 nm, left) suspended 200 nm above

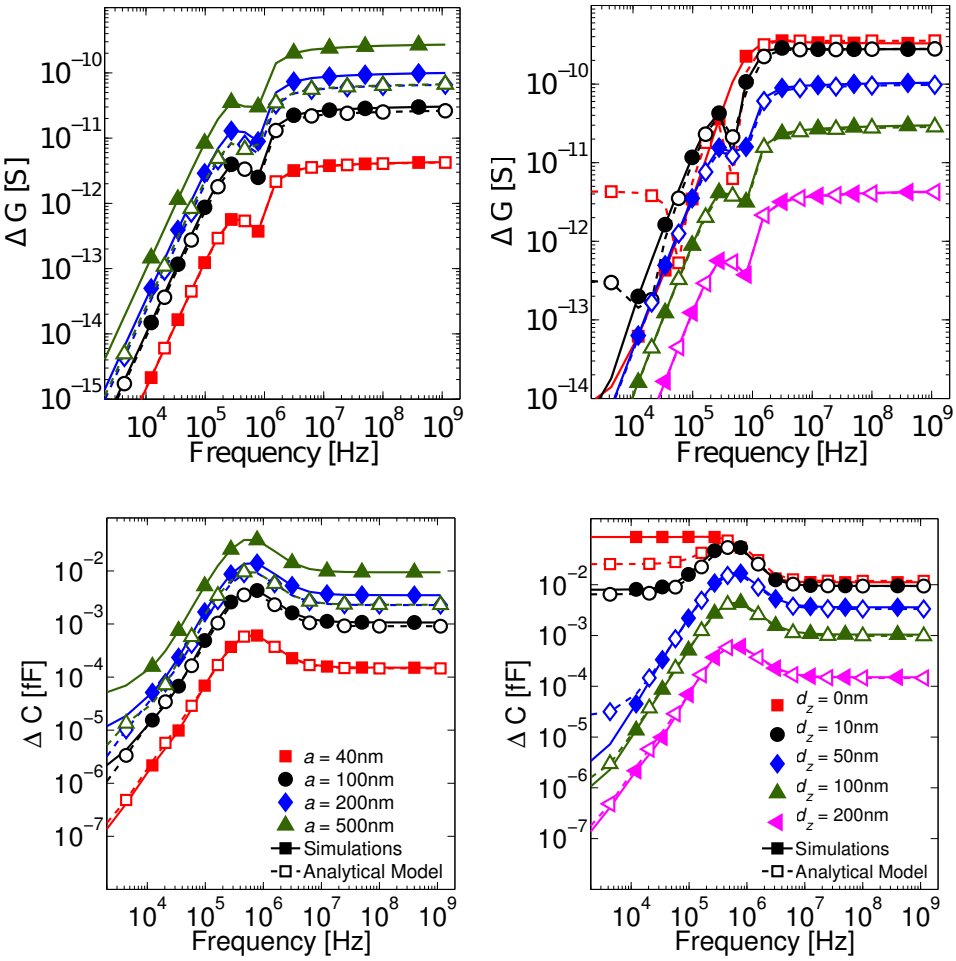

Figure 3.30: *Comparison between the change in conductance (ΔG, top) and capacitance (ΔC, bottom) obtained by means of 2D numerical simulations and the predictions of the proposed analytical model for neutral particles of different radius suspended 200 nm above the bottom electrode (left) and for a particle with fixed $a = 40$ nm suspended at different height above the electrode (right). The glitch on ΔG at about 1MHz is due to a sign change. Bulk electrolyte ion concentration n_0=1.5 mM.*

the bottom electrode and for a particle with fixed 40 nm radius suspended at different height above the electrode (right). The analytical model (open symbols) nicely reproduces all features in the simulated nanoelectrode admittance response, and shows very good quantitative agreement for particles smaller than the electrode radius placed at least a few Debye lengths above the electrode surface. In most cases, ΔG and ΔC increase for increasing frequency and tend to a constant value for $f \gg f_c = \sigma_b/(2\pi\varepsilon_b)$. A peak in ΔC is sometimes observed, which is discussed in more detail in [112]. It is essentially due to not too large particles in proximity of the working electrode. The dips in ΔG are caused by sign changes. It can be shown analytically that these sign-changes appear in multi-domain media with spatially dependent complex conductivity that entail sign changes of the frequency dependent real part of $(\tilde{E}_0/\tilde{V}_0)^2$. The cut-off frequency f_c is in very good quantitative agreement with the one derived from the results in [116], thus

supporting the validity of our models.

Quantitative understanding of dielectric spectroscopy experiments and nanoelectrode response to small particles and biomolecules is important to advance the analytic power of modern impedimetric biosensors. The analytical model of eq. 3.124 is derived under the assumption of constant AC field, zero DC bias, and non interacting electrode and particle double layers. Furthermore, the model predicts the frequency dependence of the sensor response and suggests the existence of an optimum detection frequency in proximity of the electrolyte cut-off frequency where the ΔC is maximum.

The model has been carefully verified by means of extensive numerical simulations [112], and found to be accurate provided the particle is not too large with respect to the electrode dimensions or too close to the electrode itself.

As a final remark, we have verified that the model can be improved for the case of large particles by acting on the value of $\tilde{E}_0$. The analytical model results reported in fig. 3.30 were obtained by using as $\tilde{E}_0$ the electric unperturbed field exactly at the center of the particle position. The accuracy of the model is much improved by averaging the field term over the entire particle volume, as demonstrated by the results in figs 3.31 and 3.32.

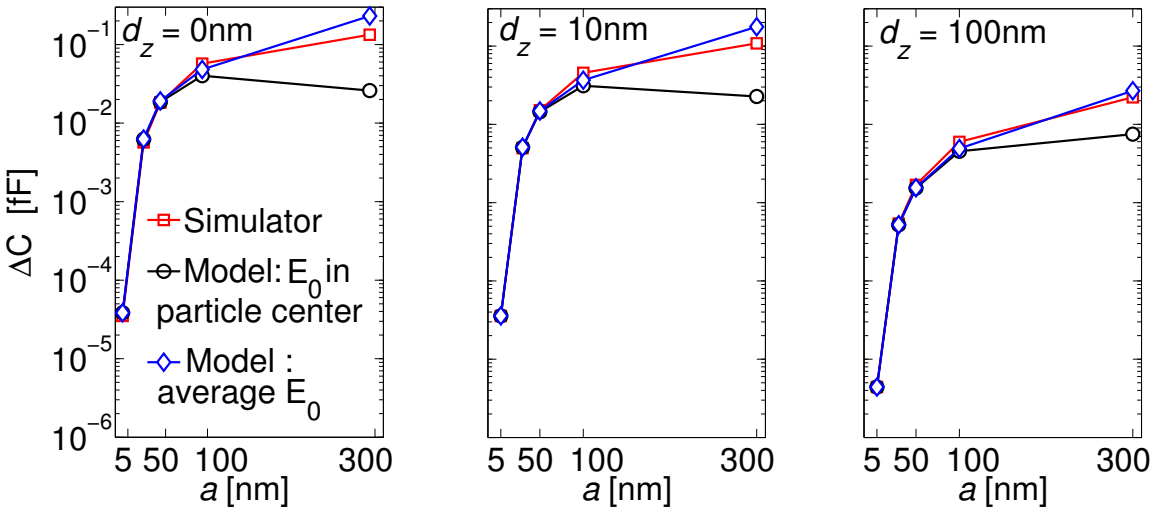

Figure 3.31: *High frequency capacitance change ΔC due to biomolecules of 5 different radii (5, 30, 50, 100 and 300 nm). Biomolecule attached on the electrode (left), biomolecule detached by 10 nm (center) and biomolecule detached by 100 nm (right). Ion concentration 1.5 mM, $\lambda_D \simeq 1$ nm.*

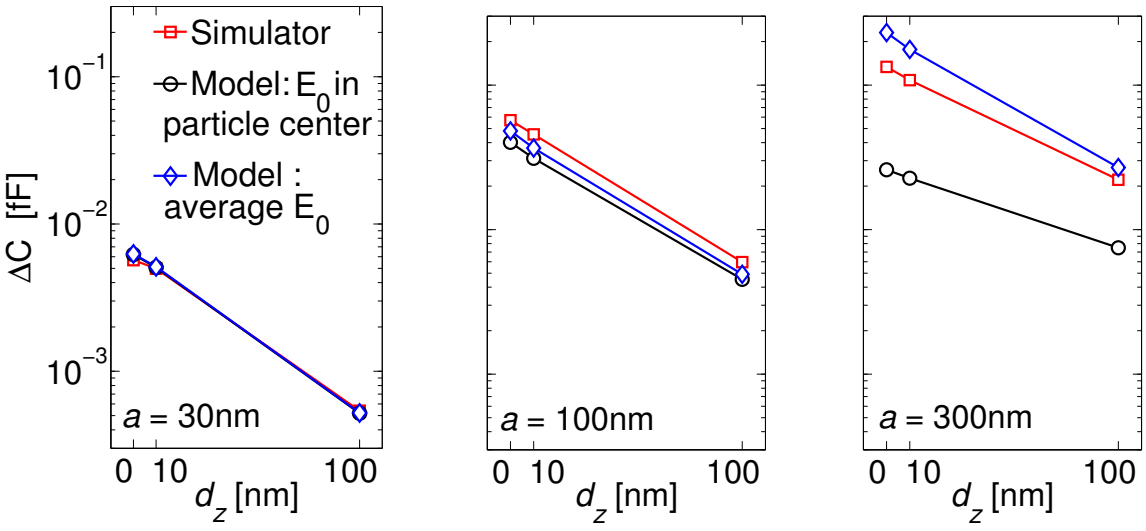

Figure 3.32: *High frequency capacitance change ΔC due to biomolecules with 3 different positions (0, 10 and 100 nm from the electrode surface). Biomolecule radius $a = 30$ nm (left), 100 nm (center) and 300 nm (right). Ion concentration 1.5 mM.*

3.5 Summary

Most of the modeling work presented in the thesis is based on the Poisson-Boltzmann (PB) and Poisson-Nernst-Plank (PNP) equations, that is a consolidated framework used to describe biosensors based on electrolytes/electronics interfaces.

The simulators presented in this chapter have been extended or developed *ex-novo* to describe electronic devices, such as nanoribbon and FinFETs, in electrolyte environment, both in DC and AC regimes.

The TCAD tool was used to validate the already implemented models for the pH-dependent surface charge, by comparison with literature data and measurements performed on NRs and FinFETs, in both dry and wet environments. An analytical model, based on the PB-PNP framework, for the admittance change induced by dielectric particles in nanoelectrode sensors, has been extensively validated by comparison with fully-3D simulation performed with ENBIOS.

A 1-D simulator was developed *ex-novo* for the simulation of insulator/electrolyte and semiconductor/insulator/electrolyte structures. Both DC and AC pH-dependent surface charges have been implemented. The key parameters of the newly developed AC site-binding model have been extracted from literature data on fast pH transient response of ISFETs. This model was secondly implemented in ENBIOS.

Lastly, we published two simulation tools and accompanying documentation on the nanoHUB.org website, by using the Rappture GUI provided by the nanoHUB platform. The tools offer the possibility to simulate simple 1-D structures, such as semiconductor/insulator/electrolyte, but also more complex devices such as ISFETs. The tools are based on ENBIOS and include both the surface reaction models in both DC and AC operating regimes. Documentation and working examples for teaching are available.

Chapter 4

pH-sensing

This chapter presents a comprehensive study of the NR devices in DC conditions. We introduce the topic of pH-sensing by presenting an accurate characterization of the NR devices that we have used as pH sensors. We start by presenting the characterization of the devices in dry (sec. 4.1). We discuss the main features of the DC response in dry environment by focusing our attention on the series resistance extraction, their impact on the $I-V$ and comparison with simulations including extraction of surface trap densities. We then characterized the NR device in liquid (sec. 4.2) environment, with a special care regarding the series resistances. Sec. 4.3 summarizes the key results of the operations in dry and liquid environments by comparison between measurements and TCAD simulations. The second part of this chapter is devoted to the pH-sensitivity and signal-to-noise ratio (SNR) analysis in liquid environment. Firstly, we present the voltage and current sensitivities to pH, obtained from the measurements of pH ladders (sec. 4.4). Lastly, we present noise measurements on NRs (sec. 4.5) and we conclude the chapter examining the performances of the NRs in terms of SNR.

4.1 Characterization in dry environment

Since the beginning of the electrical characterization of the devices in dry environment we noticed long transients, high instability of the threshold voltage (V_T) and very large series resistance limiting the ON current of the devices. For these many reasons, we decided to perform an accurate characterization of these features before using the devices for the experiments in liquid environment.

The devices were measured in dry air (without microfluidics) meaning that the front gate is floating (in air) and the biasing voltage is always performed through the back gate, V_G. We started by measuring the $I_D - V_G$ characteristics by using two different techniques: linear sweeps and pulsed measurements. Linear sweeps are the classical way of measuring the current-voltage characteristic of a device. The voltage is swept linearly (or in some cases logarithmically) while measuring the current, typically with medium or long integration times to obtain accurate measurements. Pulsed measurements instead, are adopted when the devices is affected by long transients, that can be generated by slow trapping/de-trapping mechanisms (e.g. at the oxide-semiconductor interface) or in this particular case by dust particles in air electrically attracted by the devices. In this measurement technique, instead of a slow linear sweep, the voltage applied to the device is pulsed, with a duration that ranges from a few hundred of microseconds to a few hundred of milliseconds. Time dependent mechanisms with time constants larger than the impulse will not respond and consequently we can record the unperturbed current-voltage characteristic.

Figure 4.1 shows the main parameters of the pulsed and sweep voltage signals.

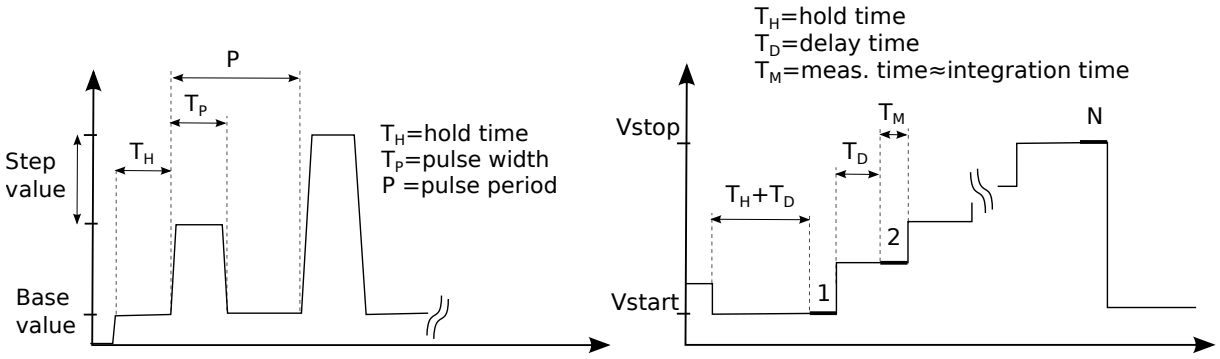

Figure 4.1: *Pulsed (left) and sweep (right) waveforms and timings.*

Due to the large dependence of the device's characteristics on the measurement parameters, we have tried three different setups for current-voltage (I-V) measurements:

- *SSW, Standard Sweep*: we sweep the back gate voltage and apply a constant V_{DS} voltage. With this setup it is possible to have more accurate measurements because we can set medium/long integration times.

- *PVG, Pulsing V_G*: we keep the V_{DS} at a fixed voltage, while we pulse the back gate voltage. An example of pulsed signal is depicted in the left picture of fig. 4.1. Due to

the large back gate capacitance, this method can depend on long charging transients at the back interface (due to the SOI structure of the devices), thus affecting the measurements as reported by the results in fig. 4.3 (left).

- *PVD, Pulsing V_D*: we sweep the back gate and we pulse a constant voltage at the drain (with a fixed base value), keeping the source grounded. With this method we can avoid the transients related to the back gate polarization, if the sweep time step size ($T_D + T_M$) is kept sufficiently long.

As a first task we examined the repeatability of the device characteristics to gain insight on the best operating conditions. We highlight that by using negative starting voltage and negative base value the measurements are more repeatable for all the measured devices and for different measurement setups. We obtained the best results in terms of repeatability with the PVD measurement technique. The accuracy of the results is lower compared to the SSW technique, but the measurements are repeatable and almost not dependent on the sweep starting voltage.

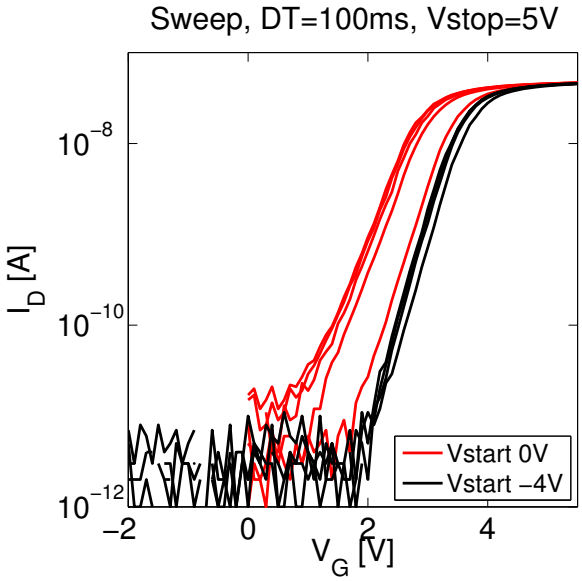

Figure 4.2: *$I_D - V_G$ measured using the SSW technique; sweep from 0 V to 5 V (red curves), sweep from -4 V to 5 V (black curves). The measurements are repeated on the same device (L = 2375 nm, W = 110 nm, wafer p11), without hold time between consecutive measurements.*

Dynamic response and transients

Figures 4.4 and 4.5 show the results of transient measurements performed on NRs by applying a step voltage at the back gate (left plots) and at the drain contact (right plots), always keeping the source contact grounded. We characterized device with different widths, ranging between 110 nm and 1 µm, belonging to wafers p11 and p05. The differences between wafers are essentially two: p11 devices have n-type channel doping

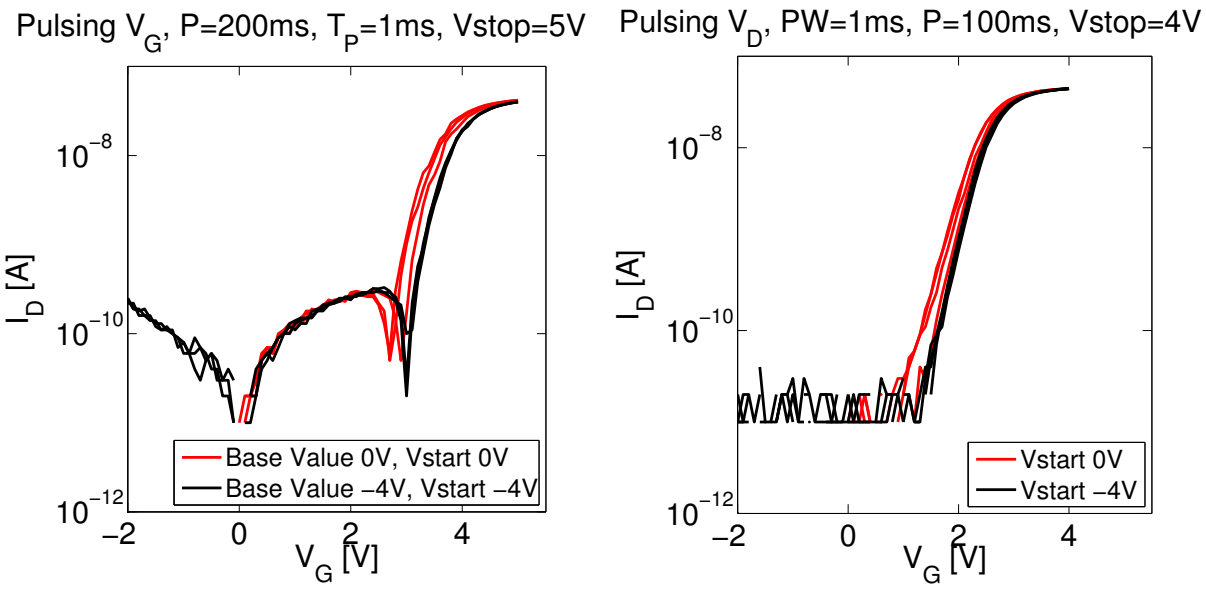

Figure 4.3: *Left: $I_D - V_G$ measured using the PVG technique, $V_{DS} = 100$ mV, starting voltage and base value for V_G is 0 V (red curves), starting voltage and base value for V_G is -4 V (black curves). Right: $I_D - V_G$ measured using the PVD technique; starting V_G is 0 V (red curves), starting V_G is -4 V (black curves). The measurements are repeated on the same device ($L = 2375$ nm, $W = 110$ nm, wafer p11), without hold time between consecutive measurements.*

(10^{16} cm^{-3}) and no silicidation on the S/D paths, while p05 devices have a p-type channel (10^{16} cm^{-3}) and silicided the S/D paths.

The results of the transient measurements show long transients in both the back gate and drain currents. Since we bias the devices from the back gate contact, the large back gate capacitance introduces long times to invert the BOX-substrate interface and consequently the drain current takes long time to saturate. Measurements on wafer p05 exhibits smaller transients compared to the wafer p11, probably due to the silicidation of the S/D paths.

After measuring the transient response to a voltage step signal, we studied the response of the NR devices by performing forward (from negative to positive back gate voltages) and backward (from positive to negative back gate voltages) $I_D - V_G$ measurements. Forward measurements where made without hold time, while backward measurements were made with an hold time of 5 s allowing the current to saturate. Fig. 4.6 and fig. 4.7 report the measurements performed on wafers p11 and p05, respectively. We remark that, for p11 devices, all the three different measurement setups (PVG, PVD and SSW) show a backward subthreshold slope lower than the forward one, as reported by the extracted values in tab. 4.1. Measurements on wafer p05, instead, do not show noticeable difference in the subthreshold slope between forward and backward measurements, confirmed by the extracted values reported in tab. 4.1. Concluding, measurements on device of wafer p05 are more stable and repeatable and also the hysteresis, between froward and backward measurements, is considerably smaller.

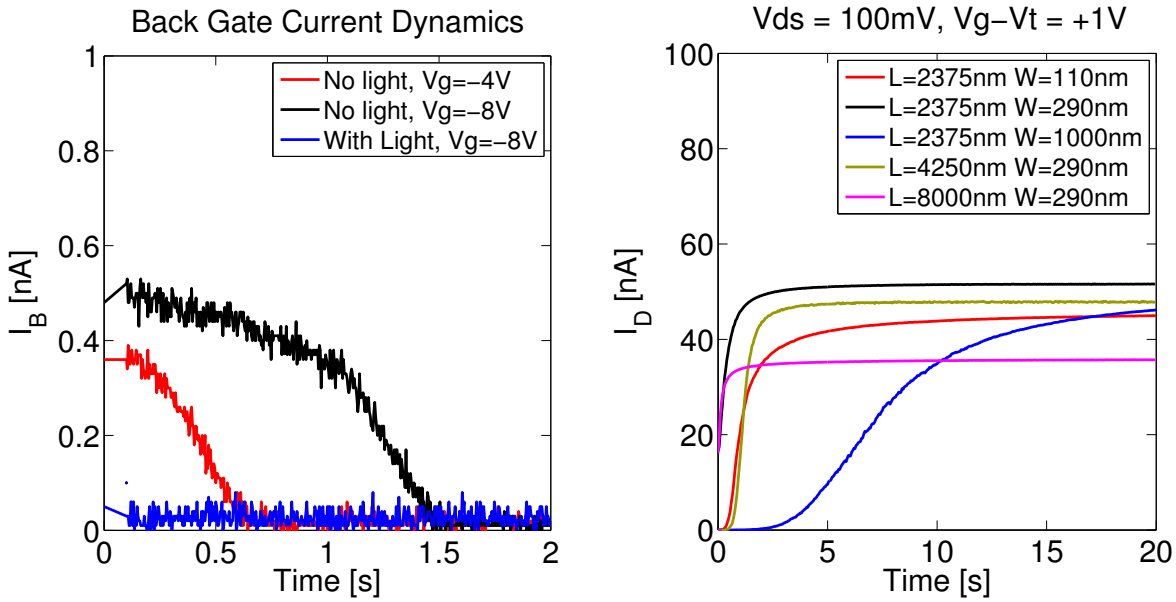

Figure 4.4: *Left: back gate current transient. Right: drain current transient, with a fixed* $V_G - V_T = +1$ *V. Devices widths ranging from 110 nm to 1 µm. Wafer p11.*

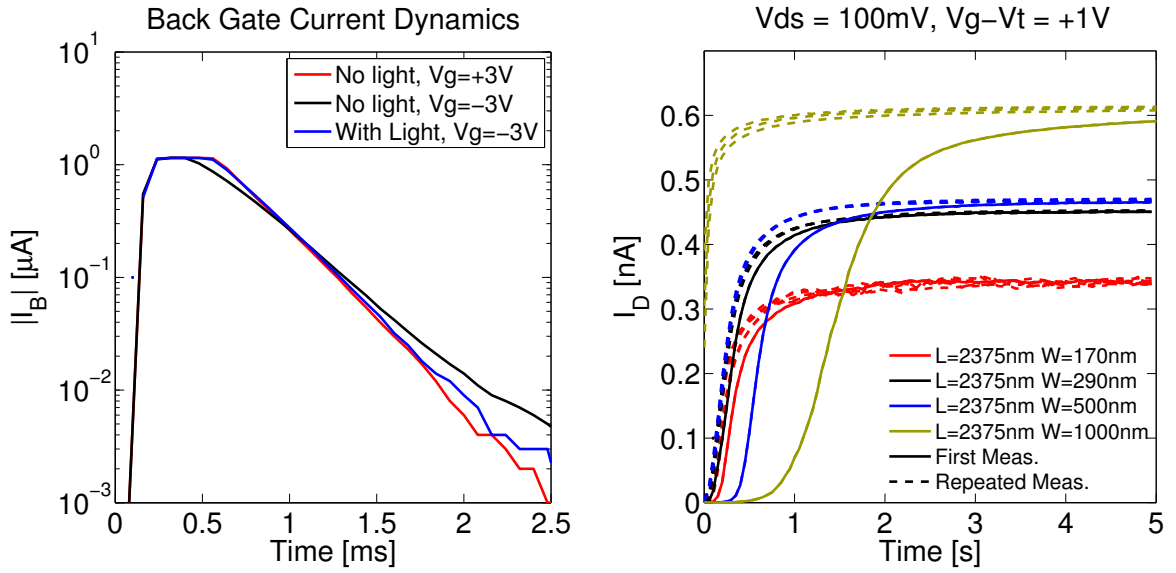

Figure 4.5: *Left: back gate current transient. Right: drain current transient, with a fixed* $V_G - V_T = +1$ *V. Devices widths ranging from 170 nm to 1 µm. Wafer p05.*

Type	Direction	V_T [V]	SS [mV/dec]
PVG	Forward	5.5	620
PVG	Backward	1.5	540
SSW	Forward	2.7	480
SSW	Backward	1.7	414
PVD	Forward	2.6	390
PVD	Backward	1.7	360

Table 4.1: Value extracted from figure 4.6, wafer p11.

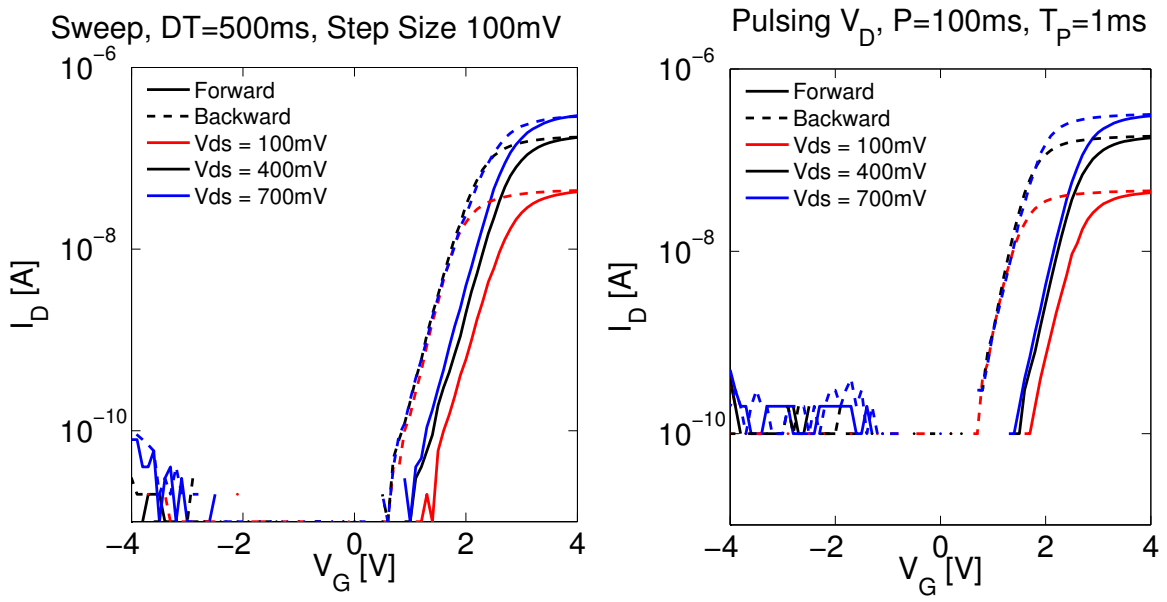

Figure 4.6: *Forward and backward measurements on device 2B06 (L = 2375 nm W = 110 nm), standard sweep (left) and pulsing V_D (right). Wafer p11.*

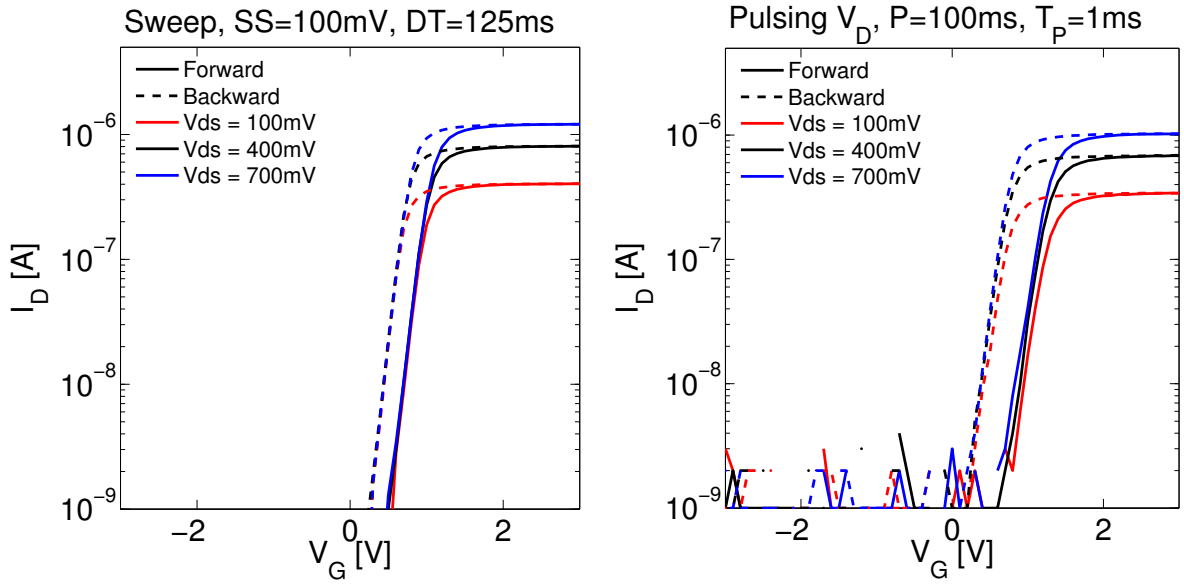

Figure 4.7: *Forward and backward measurements on device 3B01 (L = 1000 nm W = 1000 nm) of chip P05. Standard sweep (left) and pulsing V_D (right). Backward measurements were made with an hold time of 5 s allowing the current to saturate.*

The NRs measured in dry conditions show high instability probably due to contaminations, moisture and humidity. Measurements performed by pulsing the back gate contact have shown long transients, associated to the inversion of the BOX-substrate interface. PVD measurements are preferable, with respect to SSW and PVG, because less affected by mechanisms that generate slow transients dynamics. For these many reasons the NR devices can be characterized in dry to determine parameters such as the SS and ON

Type	Direction	V_T [V]	SS [mV/dec]
SSW	Forward	1.0	192
SSW	Backward	0.7	191
PVD	Forward	1.2	230
PVD	Backward	0.7	240

Table 4.2: Value extracted from figure 4.7, wafer p05.

current but not the threshold voltage.

4.1.1 Doping and series resistance characterization

Fig. 4.8 shows a device test structure fabricated on chip, that is useful to extract parameters such as the source/drain doping and resistance of the interconnections. The test structure has two additional terminals with respect to a standard device (T_2 and T_3 in fig. 4.8) with the same fabrication parameters as the source and drain leads (T_1 and T_4). This is a typical structure that is used for 4-terminal measurements to get rid of the series resistance by measuring the exact V_{DS} applied to the device.

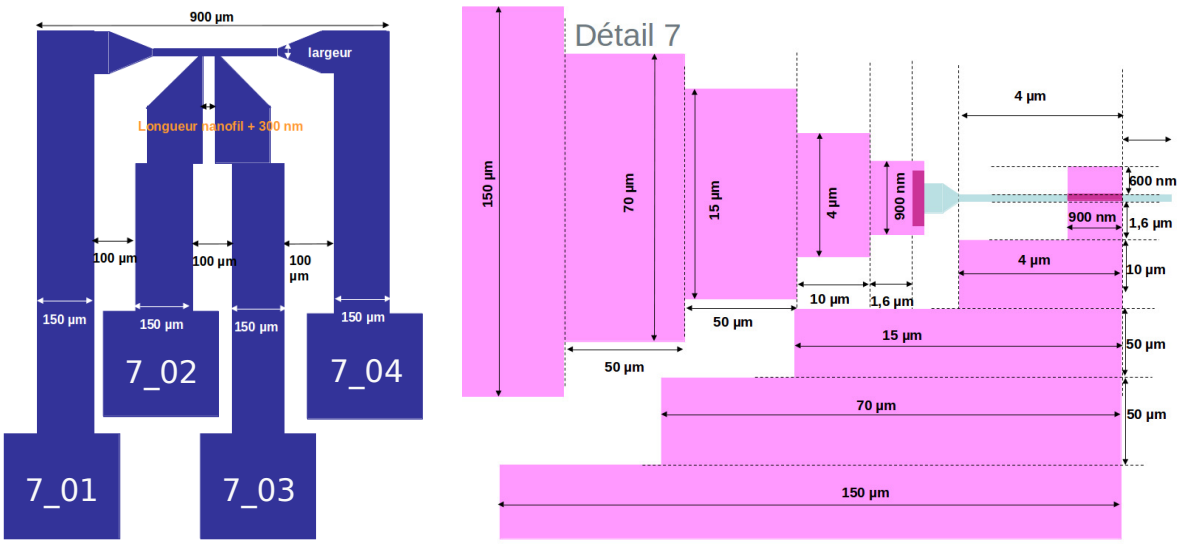

Figure 4.8: *4-terminals device (left). Layout of the 4-terminals device (right).*

Unfortunately, in all the chips that we have tested, the NR was not working. For this reason we decided to use the test structure by measuring the resistance between two adjacent terminals, $T_1 - T_2$ and $T_3 - T_4$. To extract the doping of the source and drain regions, we measured the voltage dependent resistance (by varying the back gate voltage) and from this equation, we can extract the resistivity as:

$$\rho = R_{meas}\left[\frac{1}{t}\left(\frac{L}{W}\right)_{\square}\right]^{-1} \tag{4.1}$$

In this section we present measurements carried out on devices of type p11, that have silicided contacts but they have no silicidation on the drain and source regions, thus we expect very high series resistances. Figure 4.9 (left) shows the measurements on the 4-terminals device. As we can see the resistance between two adjacent terminals is strongly dependent on the back gate bias. In fact, it decreases of about 100 KΩ from -4 V to 4 V of back gate bias.

With $R_{meas} \sim 1.4$ MΩ we obtain $\rho = 0.032$ Ω·cm, that correspond to an Arsenic doping concentration of $5 \cdot 10^{17}$ cm^{-3}, that is far from the nominal doping (>10^{20} cm^{-3}).

Right picture in figure 4.9 shows the simulated resistance with the same SOI structure of the measured device. As we can see, for the doping concentration of $5 \cdot 10^{17}$ cm^{-3} we obtain a variation of 100 KΩ of the resistance, as we have found in the measurements.

The very large resistance of the S/D connections and the large voltage dependence of the measured resistance (referred to these types of chips without complete silicidation) have a negative impact of the device characteristics.

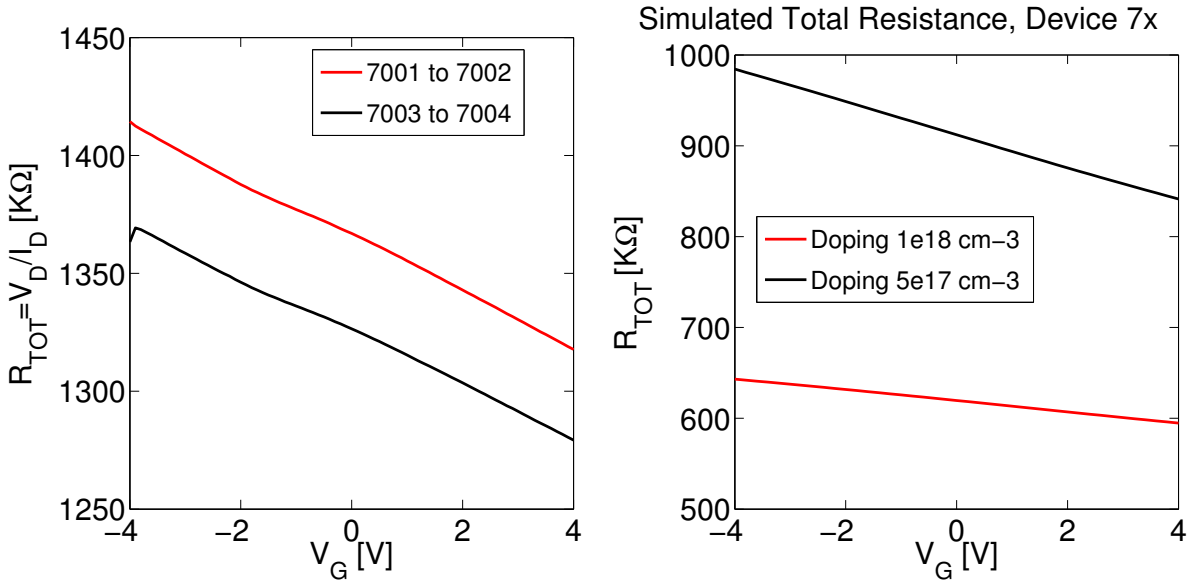

Figure 4.9: *Measured total resistance between two terminals of the device 7x (left). Simulated 3D resistance with the same SOI structure of the measured 7x device (right).*

R_{SD} extraction from I_D-V_G measurements in linear region

In order to determine the series resistance of our devices (which is presumably very large especially in non silicided devices and also asymmetric in many cases) we use the well known linear current equation (between source and drain)

$$I_D = \mu C_{ox} \frac{W}{L} (V'_{GS} - V_T - V'_{DS}/2) V'_{DS} \tag{4.2}$$

where μ is the mobility, C_{ox} is the gate oxide capacitance, V_T is the threshold voltage; $V'_{GS} = V_{GS} - \alpha R_D I_D$ and $V'_{DS} = V_{DS} - R_D(1+\alpha) I_D$ are the intrinsic voltages, R_D is

the drain series resistance and $\alpha = R_S/R_D$ is the ratio between the source and drain series resistances estimated from the layout of the source and drain lines. Assuming the mobility is constant in a V_{GS} range comparable to the voltage drop across the parasitic resistances (which is reasonable for our long-channel devices), we take the ratio between the linear I_D measured at two small V_{DS} (100 and 150 mV)

$$\frac{I_{D1}}{I_{D2}} = \frac{(V_{GS1} - \alpha R_D I_{D1} - V_{T1} - \frac{V_{DS1} - R_D(1+\alpha)I_{D1}}{2})(V_{DS1} - R_D(1+\alpha)I_{D1})}{(V_{GS2} - \alpha R_D I_{D2} - V_{T2} - \frac{V_{DS2} - R_D(1+\alpha)I_{D2}}{2})(V_{DS2} - R_D(1+\alpha)I_{D2})} \quad (4.3)$$

This is a second order equation in R_D where the combined dependence of the current on the mobility, oxide capacitance and device dimensions cancel out. Only one solution of the second order equation is a feasible R_D. The calculated R_D is a function of the gate bias V_G as reported in fig. 4.10. At sufficiently large gate bias values the R_D will converge. The series resistances extracted with this method are noisy in some cases. One possible reason is related to the extraction methodology; in fact, this method needs current measurements (I_{D1} and I_{D2}) at two different but close V_{DS} in the linear regime, where the series resistances are the dominant noise sources [117]. Nevertheless, this method is simple and gives very good results. Once the drain resistance, R_D, is calculated, the total series resistance is straightforwardly calculated as $R_{SD} = (1+\alpha)R_D$.

As a starting point we applied this methodology on two devices (2B06 and 4A04) with the same nanoribbon dimensions, with symmetric S/D leads, but located in different positions on the chip. Since the S/D paths are symmetric, we don't need to calculate α from the layout, but we know that the S/D paths of the two devices are approximately the double, as reported in tab. 4.3. By using the method described before, we extracted the series resistance and we found an aspect ration of $407/1029 \approx 0.4$, close to our expectations (see tab. 4.3).

Device	L [nm]	W [nm]	S/D length [cm]	R_{SD} [KΩ]
2B06	2375	110	≈0.9	1029
4A04	2375	110	≈0.45	407

Table 4.3: S/D connection lengths extracted from chip layout. R_{SD} extracted at the same $V_G - V_T$ in order to avoid the back gate polarization effect.

Given the encouragingly reasonable results we have used this method to extract the series resistance of different devices as shown in figure 4.10. The left graph reports the series resistance extracted from devices with silicide contacts (p11 wafer) while the right graph shows the series resistance extracted from devices with both contacts and S/D connection treated with the silicidation process (p05 wafer). As we can see there is a large difference between the two. Chips with silicide up to the nanowire have a much lower series resistance (≈70 KΩ instead of ≈1 MΩ). Note that devices in the left graph

show different series resistance, because of their different location on the chip and therefore different S/D connection lengths. Values are essentially independent of V_G except for the ones of the 1000 nm width NR.

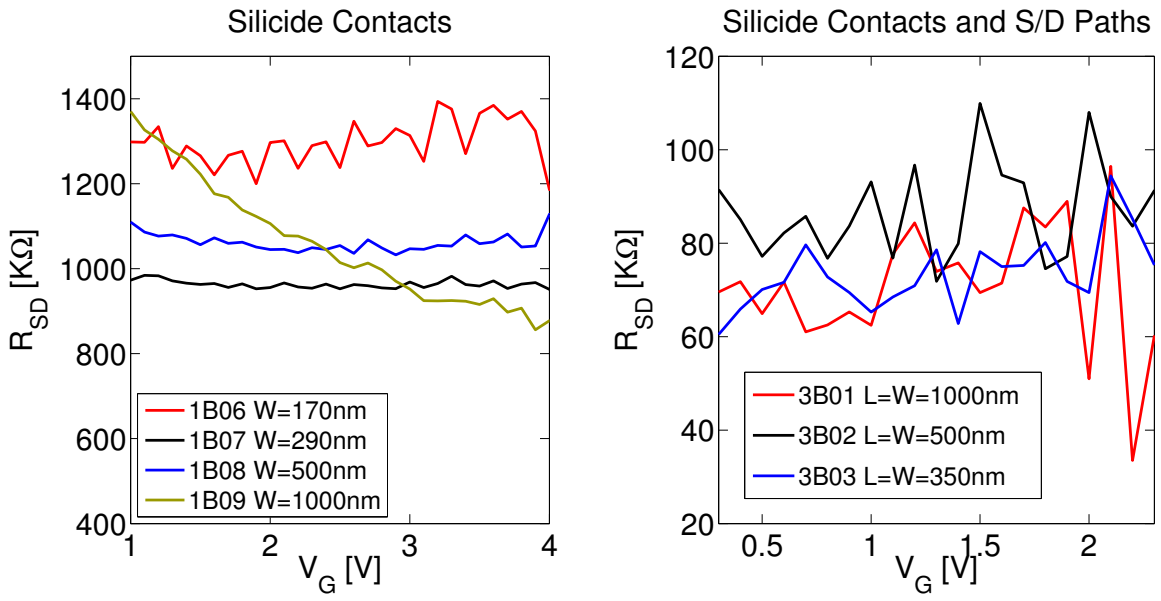

Figure 4.10: *Series resistance plotted as a function of the back gate bias, V_G. Left: chip p11 with only silicide contacts. Right: chip p05 with both silicided contacts and silicided source/drain paths.*

4.2 Characterization in liquid environment

This section is devoted to the characterization of the series resistances of the devices measured in wet environment. We start by considering fig. 4.11 that shows the series resistances of two devices with the same dimensions ($W = 170$ nm and $L = 500$ nm) but belonging to different wafers: p24 (without silicide contacts and S/D paths) and p05 (with both silicidations). The results confirm that the devices with silicided S/D paths and contact pads have a series resistance smaller by a factor of 3, approximately.

Fig. 4.12 shows how the current of the devices scales with the devices dimensions. In order to compare different devices, since they feature different threshold voltages V_T, we chose to plot the current I_D at a fixed $V_{FG} - V_T$ bias point. The current raw data in fig. 4.12 show almost no dependence on the $W_{eff} = W + 2 \cdot H$. We have then extracted the series resistances for the devices with different widths, by using the approach described in sec. 4.1. Consequently, we have de-embedded the series resistances from the raw data, in both linear and saturation regions. The de-embedded data show a good recover of the scaling with W_{eff}, especially at sufficiently large $V_{FG} - V_T$. This point will be analyzed in further detail in the next section, when comparing the current scaling of devices measured in dry and wet environments.

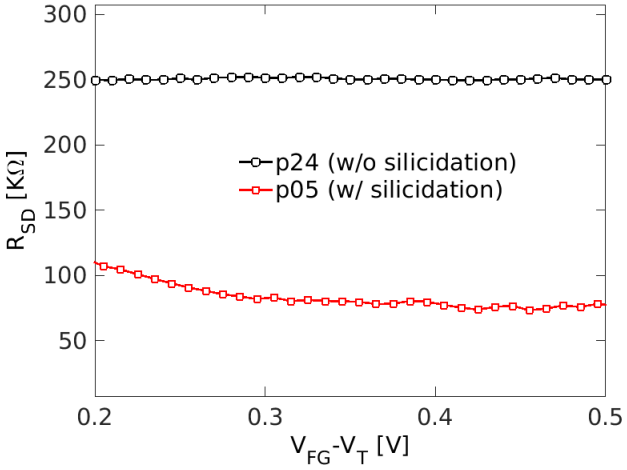

Figure 4.11: *Comparison between series resistance of wafer p24 (without silicidation) and p05 (with silicidations). Series resistance extracted on a device with dimensions L=500 nm and W=170 nm.*

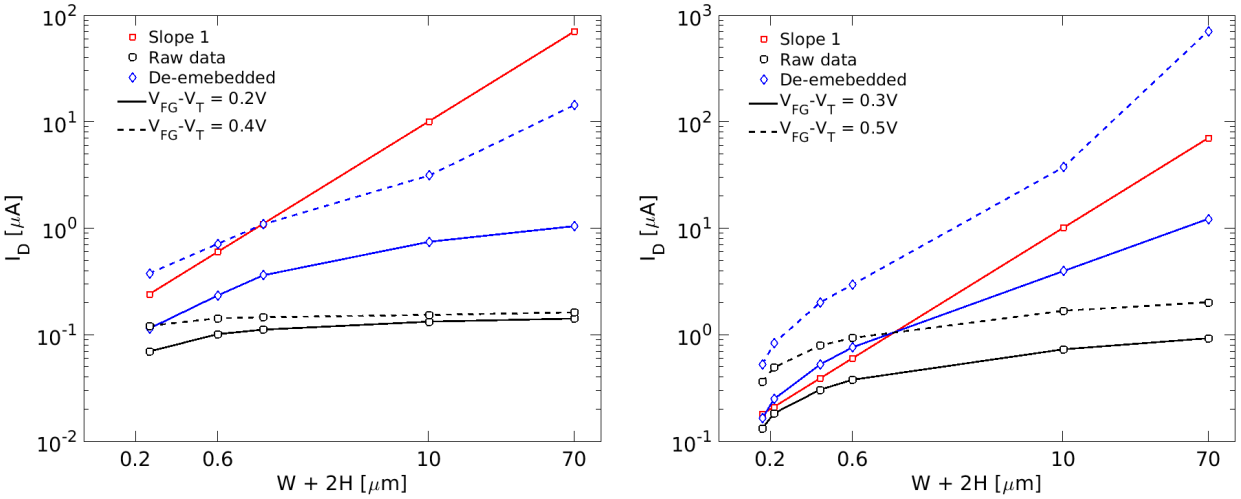

Figure 4.12: *I_D measured and I_D de-embedded of the series resistances plotted as a function of $W + 2 \cdot H$. Left: data extracted from measurements in linear region ($V_{DS} = 100$ mV). Right: data extracted from measurements in saturation ($V_{DS} = 1$ V). Wafer p24 (without silicidation)*

In the same way, we verified the scaling of the current I_D with the NR length. Fig. 4.13 shows the scaling of the current for devices without silicided S/D paths (left, wafer p24) and with silicided contacts and S/D paths (right, wafer p05). The results indicate that it is necessary to de-embed the series resistance from the raw data of the p24 devices to recover the true scaling with L. Instead, the raw data on p05 devices show an almost perfect scaling with L, meaning a lower impact of the series resistances, as expected from the series resistances reported in fig. 4.11.

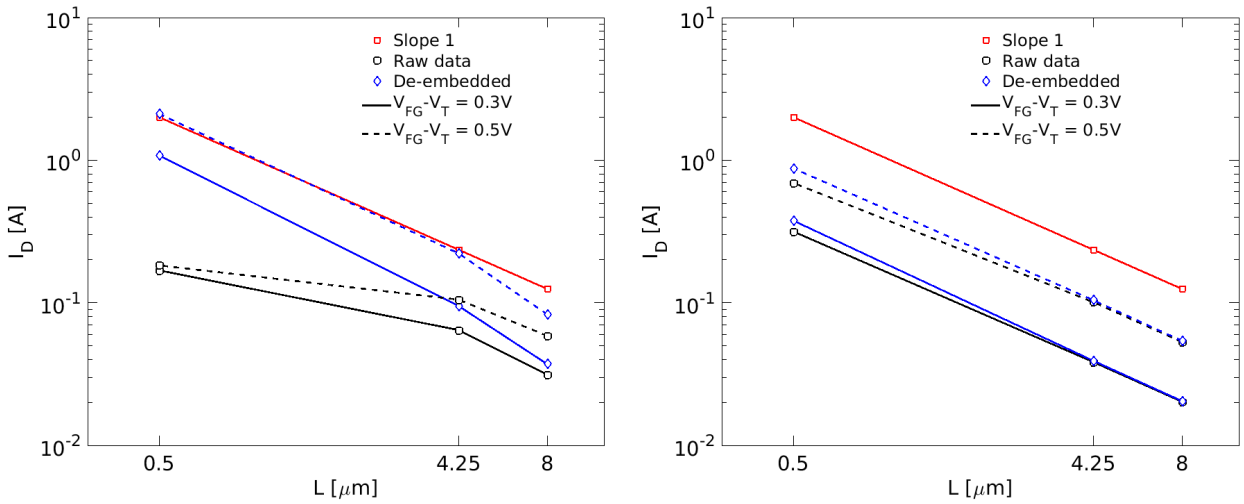

Figure 4.13: *I_D measured and I_D de-embedded of the series resistances plotted as a function of L. Left: wafer p24 (without silicidation), Right: wafer p05 (with silicidation on both contacts and S/D paths).*

4.3 A comparative study of dry and liquid environments

In the previous sections we have pointed out that the large and asymmetric parasitic series resistances of the devices is due to long and not-silicided source/drain access lines. To compare devices in dry and liquid environment we first reconstruct the current-voltage characteristics of the intrinsic devices and then investigate its geometrical scaling.

Following the method of series resistance extraction presented before, the series resistances of device with different widths were characterized and de-embedded from the raw data, both in dry and wet.

Fig. 4.14 shows that the de-embedded drain current, at constant gate overdrive, scales as $W_{eff} = W + \Delta W$ with $\Delta W < 0$ in air and $\Delta W > 0$ in electrolyte (wet) environment, respectively. The intercept with the x-axis ($W = -\Delta W$) suggests that the effective device width is larger (smaller) than the physical W in liquid (dry) environment, respectively. A possible interpretation is that current density has a non uniform distribution along the NR [118]. This interpretation has been verified by means of accurate 3D numerical simulations based on the TCAD model described in sec. 3.3.3 and calibrated to experiments as discussed in the following.

In particularly, fig.4.15 reports the electrostatic potential (top) and the current density (bottom) in dry (left) and in liquid (right) for the central cross section in the source/drain direction of a long channel device (wafer p07).

The electrostatic potential contour plots demonstrate that the electrolyte essentially behaves as a metal gate, meaning that the potential is uniform on all the gate oxide interface exposed to the solution. In air conditions, instead, the device is biased through

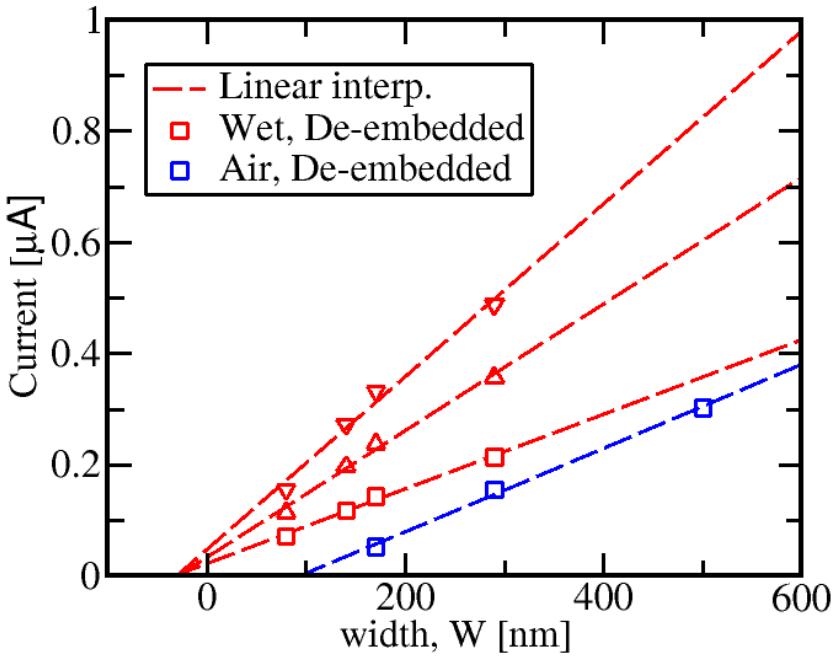

Figure 4.14: *Drain current at constant V'_{GS}-V_T in air and in electrolyte environment versus nanoribbon width de-embedded of the detrimental effect of series resistances. ΔW=30 nm in wet. V'_{GS}-V_T=0.3V (□), 0.5V (△) and 0.7V (▽). ΔW=-100 nm in dry*

the bottom gate, the electrostatic potential is not so uniform, and in fact higher in the top-center part of the nanoribbon, thus pushing the minority carriers on the bottom surface corners.

Consequently, the current density of the device operating in dry concentrates at the corners of the ribbon bottom surface, consistently with the applied bottom gate voltage; part of the bottom surface is inactive or less active than the corners in carrying the current and thus $W_{eff} < W$. In wet environment, instead, the current flows uniformly on the top and side walls ($W_{eff} > W$), consistently with the fluid gate wrapping the nanoribbon vertical edges.

These results suggest quite different conduction regimes in wet and dry, so that limited information can be extracted from the latter measurements to explain the former (notable exception being the series resistance values).

Fig. 4.16 reports the raw measured drain currents and the corresponding TCAD simulations in dry (left plot) and wet conditions (right plot) for a device of wafer type p07 with dimensions $L = 2375$ nm and $W = 170$ nm. A summary of the main simulation parameters are reported in tab. 4.4. We extracted the series resistances from measurements in liquid, obtaining a total series resistance of 279 kΩ. However, we used a value of 210 kΩ to fit the experiments in dry and wet, that we have implemented as lumped elements (R_S and R_D separately). Reasonably good mutual agreement was obtained for the nominal values of the source/drain doping (10^{20} cm^{-3}) and channel doping (10^{16} cm^{-3}) by intro-

[a]Extracted from measurements in liquid; no data for extraction from dry measurements.

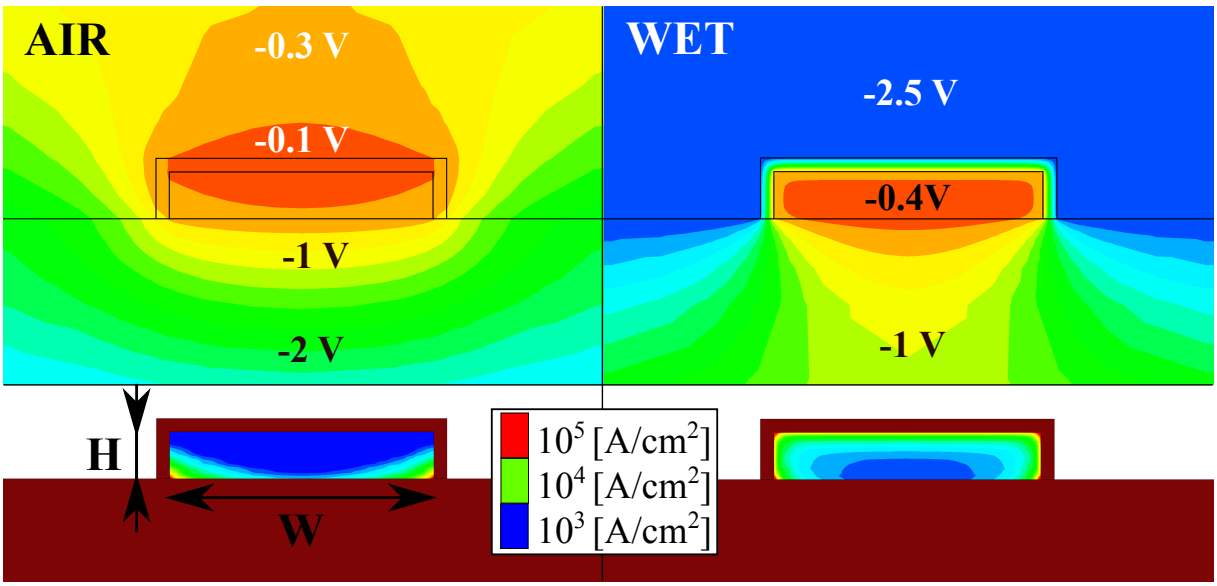

Figure 4.15: *Constant current density contours (bottom) and electrostatic potential contours (top) for air (left) and liquid (right) environment. V_{BG}=-6 V (air) and V_{FG}=-2.5 V, V_{BG}=0 V (liquid). Wafer p07.*

Parameters	Nominal Value	Sim. DRY	Sim. WET
S/D p-Doping [cm^{-3}]	$> 10^{20}$	10^{20}	10^{20}
Channel n-Doping [cm^{-3}]	10^{16}	10^{16}	10^{16}
Traps [cm^{-2}]		$1.2 \cdot 10^{11}$	$2.6 \cdot 10^{12}$
Fixed Charge [cm^{-2}]		$1 \cdot 10^{10}$	$7 \cdot 10^{11}$
R_S, R_D [KΩ]	191, 88[a]	140, 70	140, 70

Table 4.4: Summary of the main simulation parameters compared to the nominal values of wafer p07. Traps and fixed charges are placed at the nanoribbon channel/oxide interface. The simulation results are reported in 4.16.

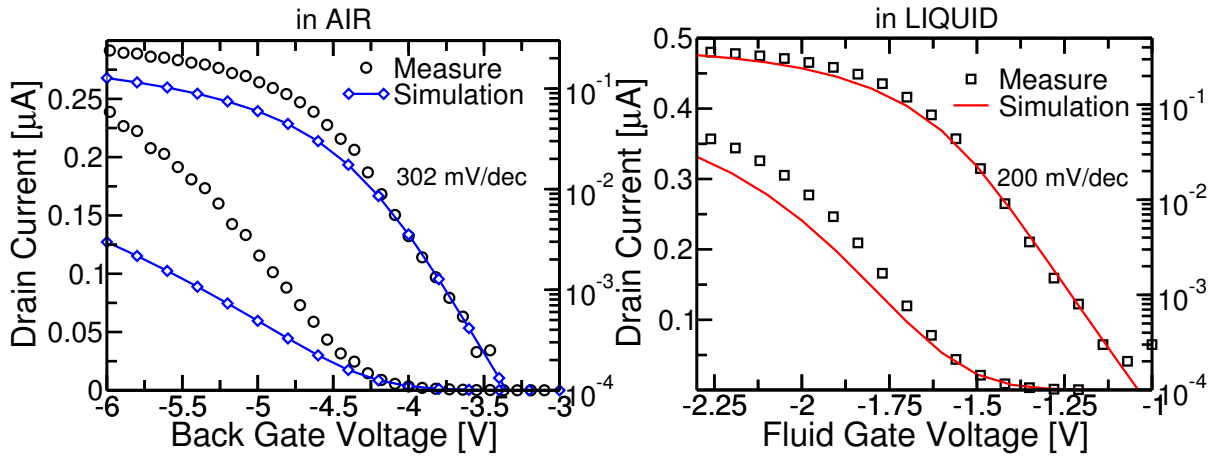

Figure 4.16: *Comparison between measurements and simulations in air (left) and in liquid (right). V_{DS}=100 mV. pMOS device, wafer p07, $W = 170$ nm, $L = 2375$ nm.*

ducing fixed charges (N_f) and interface states (D_{it}) at the gate-oxide/channel interface, with parameters independent of the pH. The interface states are acceptor (donor) type and have uniform energy distribution in the upper (lower) half of the bandgap, respectively. The flatband voltage has been adjusted to match the I-V curve at one pH value. Any other pH-dependence stems naturally from the implemented site binding and surface complexation model [96].

Parameters	Nominal Value	Sim. DRY	Sim. WET
S/D n-Doping [cm^{-3}]	$> 10^{20}$	10^{20}	10^{20}
Channel p-Doping [cm^{-3}]	$5 \cdot 10^{18}$	10^{17}	10^{18}
Traps [cm^{-2}]		$8 \cdot 10^{10}$	$3 \cdot 10^{12}$
Fixed Charge [cm^{-2}]		$1.3 \cdot 10^{11}$	$-8 \cdot 10^{11}$
R_S, R_D [KΩ]	545, 249[a]	410, 180	340, 170

Table 4.5: Summary of the main simulation parameters compared to the nominal values of wafer p24. Traps and fixed charges are placed at the nanoribbon channel/oxide interface. The simulation results are reported in 4.17.

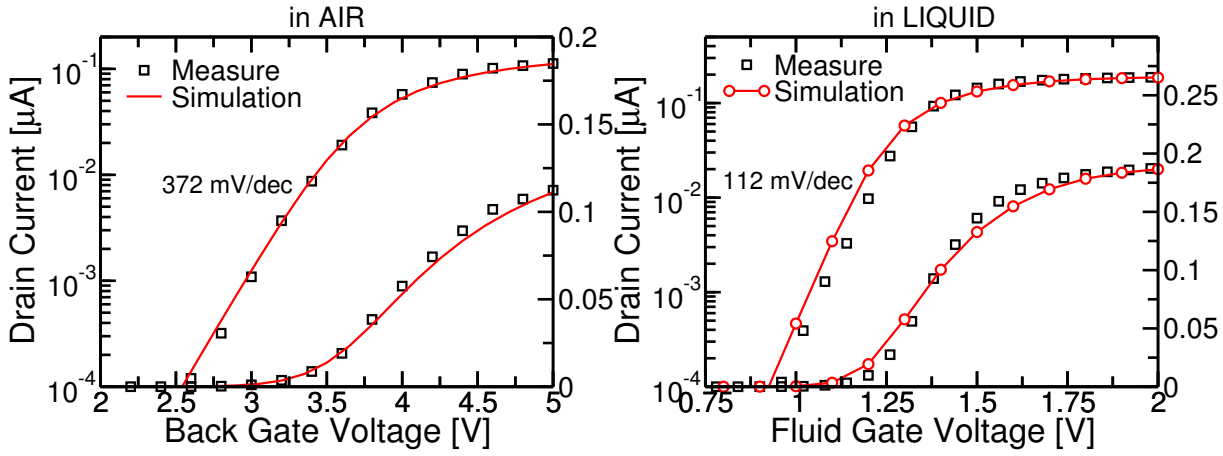

Figure 4.17: *Comparison between measurements and simulations in air (left) and in liquid (right). V_{DS}=100 mV. nMOS device, wafer p24, $W = 170$ nm, $L = 500$ nm.*

Fig. 4.17 reports the raw measured drain currents and the corresponding TCAD simulations in dry (left plot) and wet conditions (right plot) for a device of wafer type p24 with dimensions $L = 500$ nm and $W = 170$ nm. A summary of the main simulation parameters are reported in tab. 4.5. In this case, we have extracted the series resistances from measurements in dry, obtaining a total series resistance of 794 kΩ. However, as for the p07 wafer, this was an overestimation. In fact, total series resistance of 590 kΩ and 510 kΩ were used to fit the experiments in dry and wet, respectively. Reasonably good mutual agreement was obtained for the nominal values of the source/drain doping (10^{20} cm^{-3}) and channel doping ($5{\cdot}10^{18}$ cm^{-3}). Fixed charges (N_f) and interface states (D_{it})

[a]Extracted from measurements in dry (wafer p12).

at the gate-oxide/channel interface (implemented as before) are in line with the previous findings (tab. 4.4).

As already mentioned, measurements in air are partly affected by poorly controlled humidity and possibly by ambient contaminations; as a result the discrepancy with simulations is larger compared to the wet configuration in liquid environment. The measurement data in liquid environment are simpler to reproduce by the simulations, probably because the electrolyte acts as a metal gate. However, the concentration of interface states is higher for the simulation in liquid with respect to the dry environment. This is probably due to a degradation of the gate insulator in contact with the electrolyte and a penetration of ions such as Na^+ [119]. The data highlights that the introduction of the electrolyte not only rigidly shifts the characteristics but also increases the subthreshold swing, thus resulting in different D_{it} values. No evidence of the need to consider traps at the BOX-channel interface was found, underlying the good quality of the SOI film/BOX interface.

Comparative study performed on FinFETs

To corroborate the validity of the extended TCAD version to simulate FET devices operating in liquid environment, we present the same comparison study done on the NRs, but applied to the FinFETs presented in sec. 2.3. Fig. 4.18 shows the comparison between measurements and simulations of the FinFET devices in dry and liquid environments. The FinFETs that were used for the measurements in dry and wet were fabricated with different processes. The devices for the measurements in dry were fabricated with a front metal gate (as depicted in the inset of fig. 4.18a) while the devices for measurements in liquid did not have the metal gate so has to leave the gate-oxide exposed ($\approx$ 8 nm of HfO_2 deposited on top of a $\approx$ 1 nm of thermally grown SiO_2).

Fig. 4.18a shows the measurements and simulations in dry; figure b) instead shows the measurements and simulations in liquid enviroment. In the latter case, the measurements were performed with an electrolyte solution biased through an Ag/AgCl reference electrode. For simulation purposes, since the electrolyte ions cannot approach the surface arbitrarily closed, the hafnium gate oxide has been covered by a thin dielectric layer with 20 $\mu F/cm^2$ capacitance in order to replicate the Stern layer [95]. From the comparison of the metal and liquid gate FinFET characteristics, it is evident that the subthreshold slope is different between dry and wet conditions. The most probable origin of this phenomenon is the sensing surface modification, which occurs by charge trapping/detrapping at the interface states [120] and ion penetration through the gate insulator. This interpretation has been confirmed and replicated by the TCAD simulations introducing traps at the channel/gate-oxide interface. Acceptor traps from the midgap to the conduction band, and donor traps from the midgap to the valence band, both with a uniform distribution. In dry environment simulations, the trap concentration was $2{\cdot}10^{12}$ cm^2 eV^{-1}, while in the wet case, a concentration of $2{\cdot}10^{13}$ cm^2 eV^{-1} was used. All the other parameters, such as the doping concentrations and the device dimensions, have been kept at the nominal

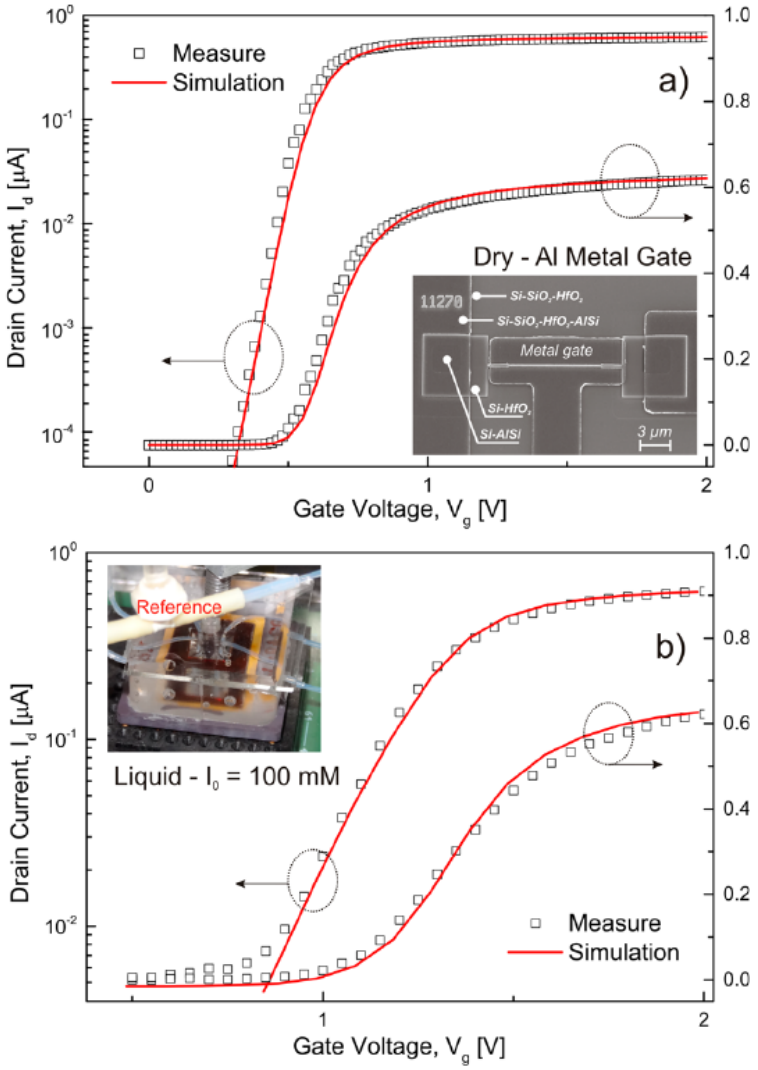

Figure 4.18: *Comparison between measurements and simulations performed with TCAD [20]. Top: dry (Al metal gate contact). Bottom: liquid (Ag/AgCl gate contact).*

values in both dry and wet environments, and they correspond to the ones mentioned in [20].

4.4 pH-sensitivity Analysis

To study the pH sensitivity of the NRs, we performed experiments in liquid by injecting in the microfluidics buffered solutions at different pH values. The solutions were prepared starting from 10 mM of phosphate buffered saline (PBS) and 100 mM of KCl (to stabilize the Ag/AgCl reference electrode) and H_2SO_4 or NaOH were added to obtain the desired pH values. The devices were biased sufficiently above threshold, in order to remain above V_T at all pH values.

The measurement protocol consists in injecting the solutions, approximately every 100 s, while continuously measuring the drain current I_D in time. Fig. 4.19 reports a summary

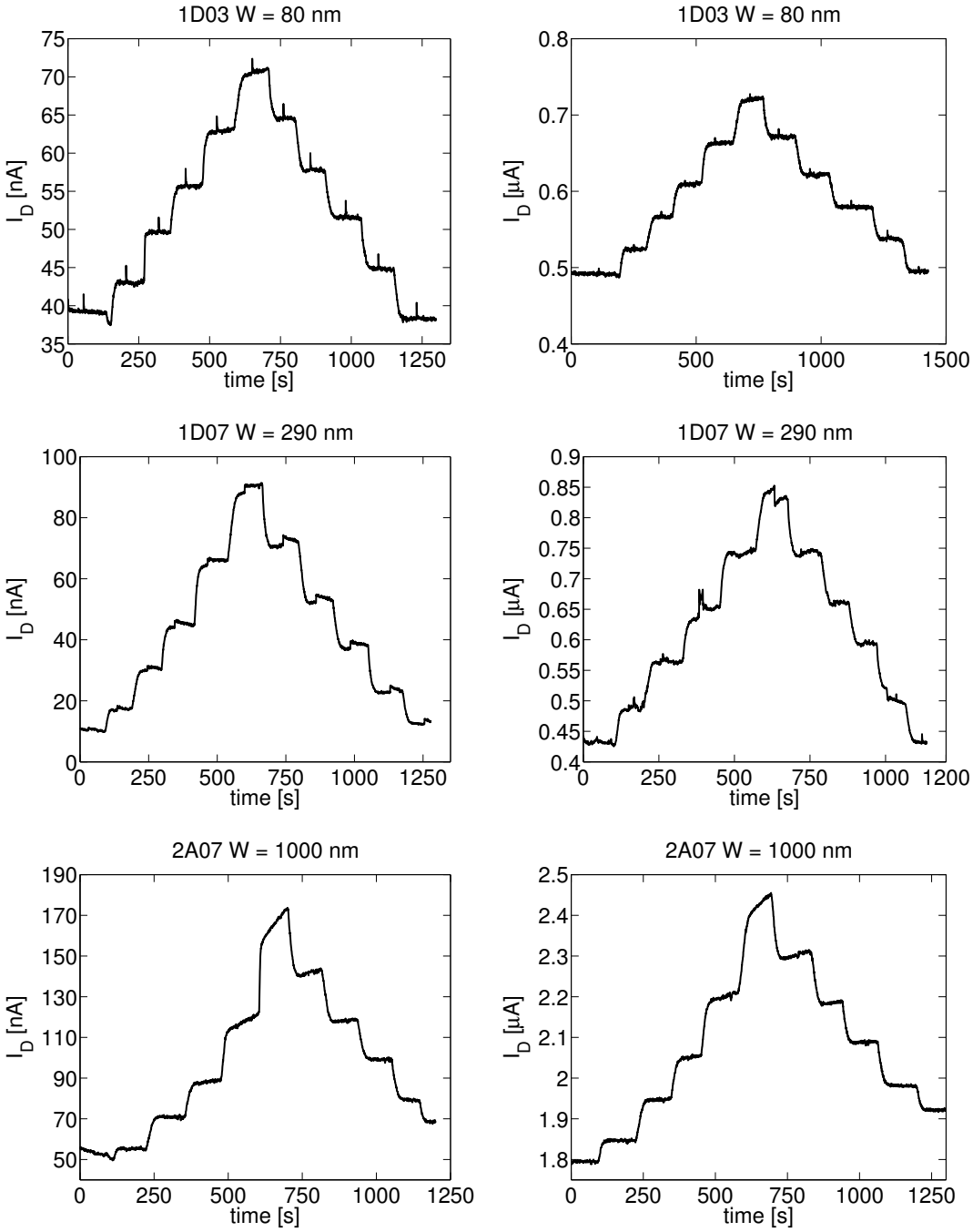

Figure 4.19: *Measured pH ladder on devices with $W = 80$ nm (top), $W = 290$ nm (center) and $W = 1$ μm (bottom), wafer p07, $t_{OX} = 8.5$. From pH=3 to pH=8 and back to pH=3. $V_{DS} = 100$ mV (left) and $V_{DS} = 1$ V (right). Devices are biased above V_T, such that $V_{DS} = 100$ mV is in the linear region and $V_{DS} = 1$ V is in the saturation region.*

of results. Furthermore, for each pH value we acquired an entire $I_D - V_{GS}$ characteristic. To do this, we suspend current sampling while performing the $I_D - V_{GS}$ and then restart measuring the I_D. The points in time when we performed the $I_D - V_{GS}$ sweep are clearly visible as small glitches in the top-left plot in fig. 4.19. From the $I_D - V_{GS}$ characteristic, we can extract the current and voltage sensitivities, S_V and S_I respectively, below and above threshold, as reported in figures 4.21, 4.22 and 4.23. S_V and S_I are defined as

$$S_V = \frac{\Delta V}{pH}, \qquad S_I = \frac{\Delta I/I}{pH} \tag{4.4}$$

where the voltage sensitivity, S_V, is calculated at a constant drain current in mV/pH, while the current sensitivity, S_I, is calculated at a constant gate voltage in A/(A·pH). Fig. 4.20 shows pH ladders performed on two devices with similar widths, $W = 140$ nm and $W = 170$ nm, belonging to wafers p24 (top figures) and p12 (bottom figures). We notice measurements less stable compared to those performed on p07 devices and more affected by current drift in time. The reason could be attributed to the thickness of the gate oxide, only 3 nm for p24 and p12 as opposed to 8.5 nm for the p07, suggesting the importance of having sufficiently thick oxide covering the nanoribbon channel.

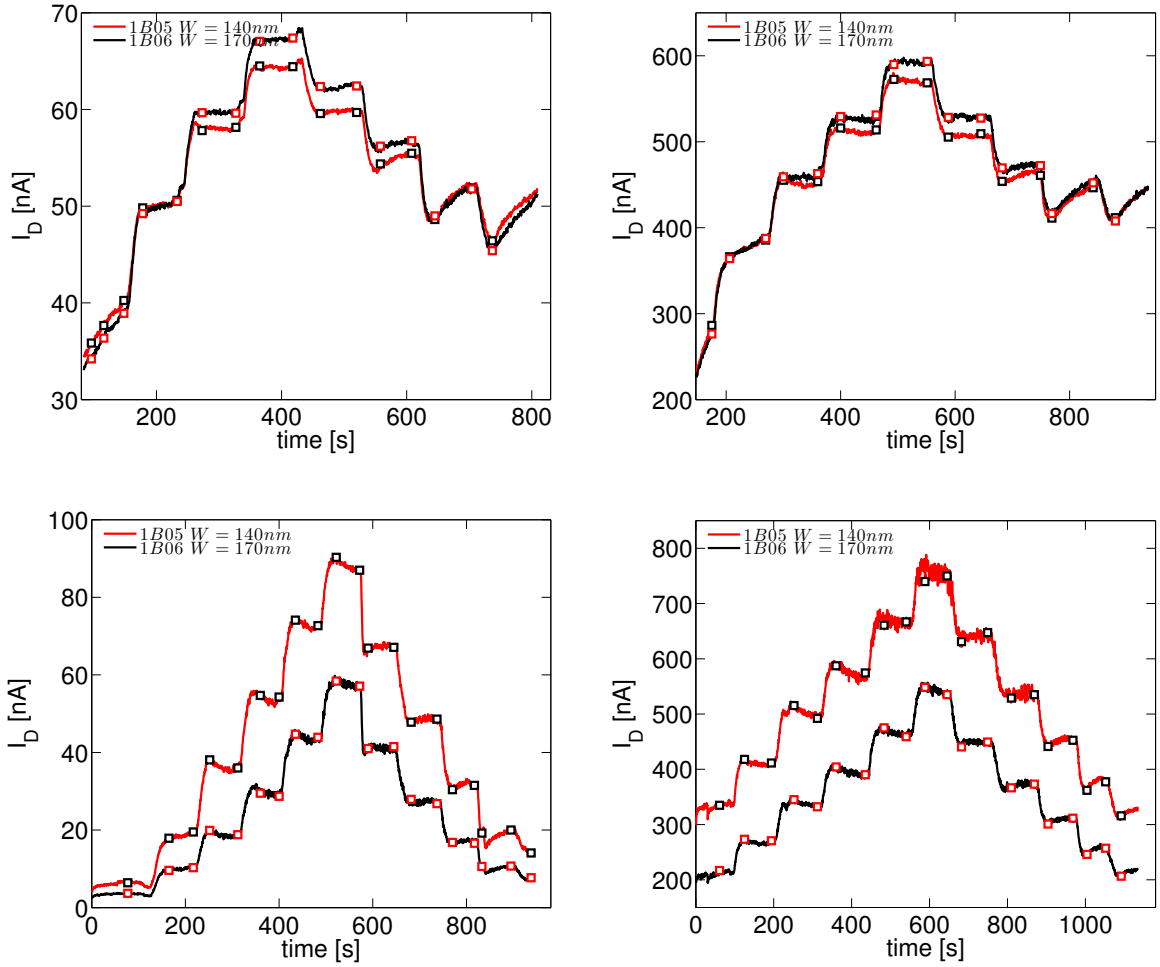

Figure 4.20: *Measured pH ladder on devices with $W = 140$ nm and $W = 170$ nm, wafer p24 nm (top) and wafer p12 (bottom). $t_{OX} = 3$ in both wafers. From pH=3 to pH=8 and back to pH=3. $V_{DS} = 100$ mV (left) and $V_{DS} = 1$ V (right). Devices biased above V_T, such that $V_{DS} = 100$ mV is in the linear region and $V_{DS} = 1$ V is in the saturation region.*

Fig. 4.21(symbols) shows the measured differential threshold voltage sensitivity for two devices ($W = 80$ nm and $W = 290$ nm) biased in the subthreshold and triode region (indicated as below V_T and above V_T, respectively). The threshold voltage sensitivity is

essentially independent of the operating region (subthreshold or inversion)[35], as demonstrated by both measurements and simulations. This entails that both measured and simulated I_D-V_{FG} characteristics shift rigidly as the pH is changed. The non-linearity of the site binding charge response to the pH shows up as an increased S_V for increasing pH, consistently with previously reported data for SiO_2 gate dielectric [74]. S_V approaches the Nernst limit at high pH but never reaches it, most likely because of electrolyte (e.g. C_{DL}) and insulator parameters (e.g. intrinsic buffer capacity, β_{int}). In addition, we note that the response for these low doped devices is essentially independent of W (compare graphs on the left and the right), consistently with recent literature on ISFETs with low channel doping and large device sizes [35, 121].

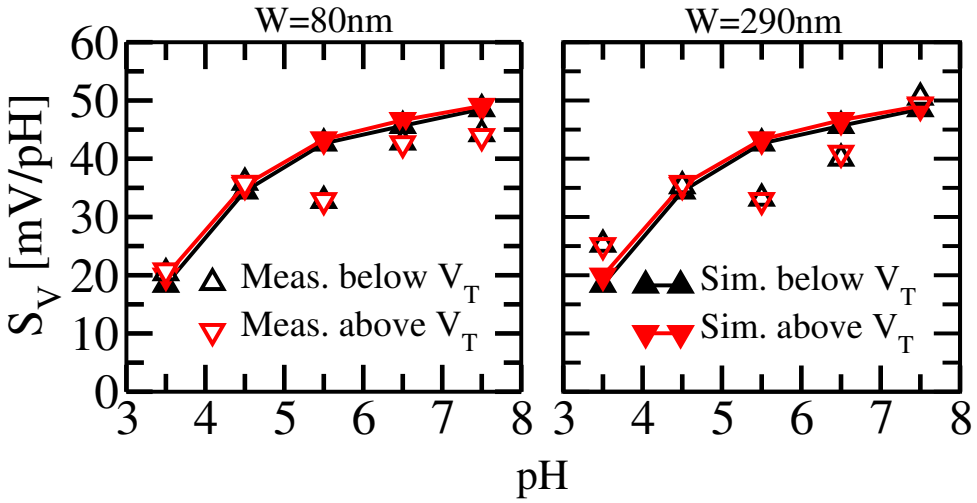

Figure 4.21: *Measured (open symbols) and simulated (filled symbols) voltage sensitivity S_V of devices biased in the subthreshold (triangles up) and in triode (triangles down) regions. V_{DS} = 100 mV. Wafer p07, t_{OX} = 8.5 nm and L = 2375 nm.*

Fig. 4.22 and 4.23 reports the differential current sensitivity (S_I=$\Delta I_D/[I_D \Delta pH]$, at a fixed V_{FG}) for the same devices of Fig. 4.21. Differently from the threshold voltage sensitivity, the current sensitivity exhibits a clear non-monotonic trend for increasing pH. The same behaviour is found in both the raw and the de-embedded data free of the effect of parasitic series resistances, suggesting the intrinsic nature of this effect.

The observed behaviour is explained by first noting that $S_I = S_V \cdot (g_m/I_D)$, where $g_m = (dI_D/V_{FG})$ is the device transconductance at the fluid gate terminal. The first term of this expression, S_V, increases for increasing pH (fig.4.21). The ratio g_m/I_D instead, decreases monotonically for increasing pH both above and below V_T (see left plot in fig. 4.24), essentially because for increasing pH the $I_D - V_{FG}$ curve shifts to the right; thus at constant V_{FG} the bias point of p07 devices (p-doped NR channel) moves toward the inversion region where g_m/I_D is smaller (fig. 4.24, right plot).

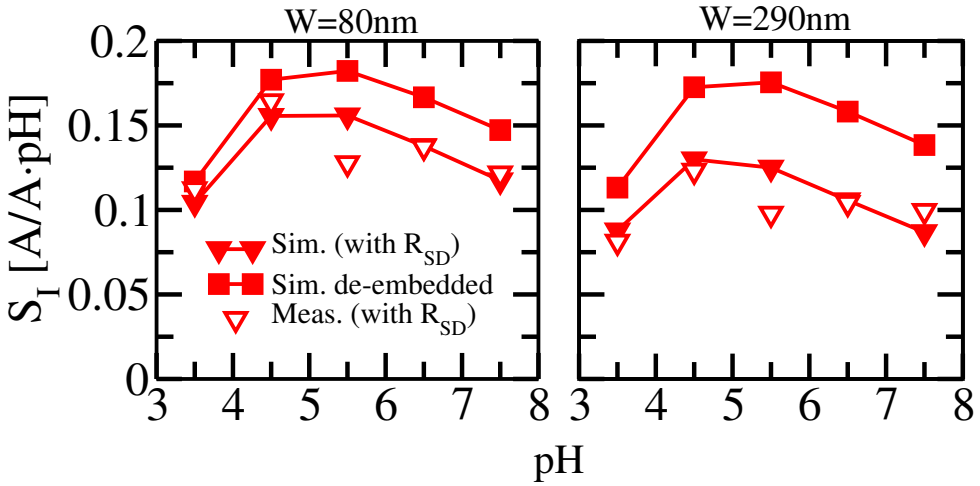

Figure 4.22: *Current sensitivity, S_I. Devices biased above threshold. Simulated sensitivities without series resistances (square symbols) are also shown. Wafer p07, t_{OX} = 8.5 nm and L = 2375 nm.*

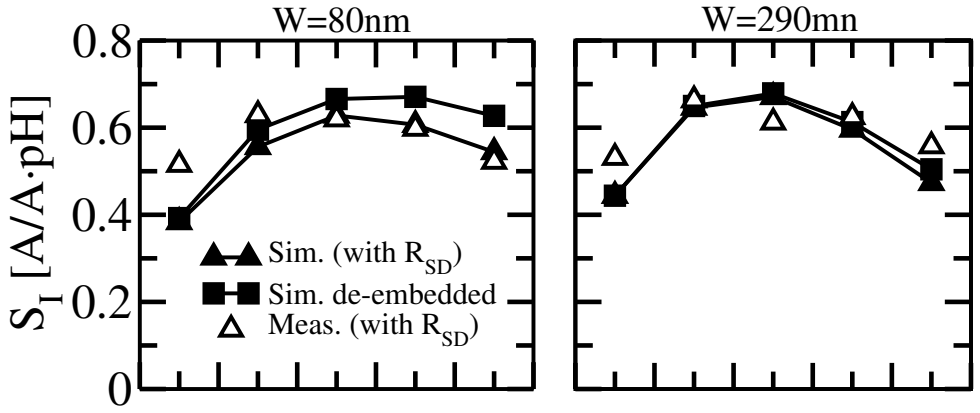

Figure 4.23: *Current sensitivity, S_I. Devices biased below threshold. Simulated sensitivities without series resistances (square symbols) are also shown. Wafer p07, t_{OX} = 8.5 nm and L = 2375 nm.*

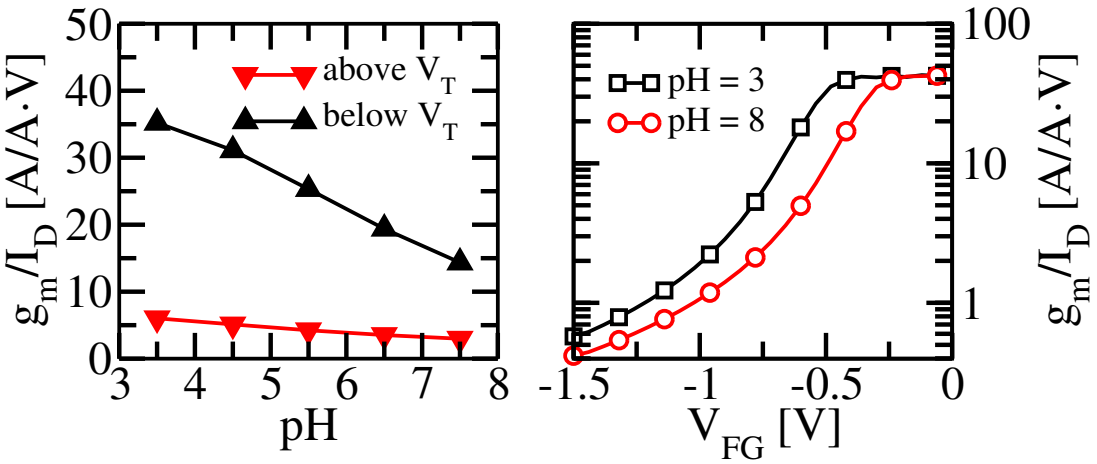

Figure 4.24: *Left: g_m/I_D in inversion (above V_T) and depletion (below V_T) versus pH. Right: g_m/I_D vs. V_{FG} at pH = 3 and pH = 8. Device with W = 80 nm. Wafer p07, t_{OX} = 8.5 nm and L = 2375 nm.*

4.5 Signal-to-Noise Ratio Analysis

The pH sensitivity shown in figs. 4.22, 4.23 and 4.23 is not sufficient to fully establish the ability of the NRs to detect pH changes. In fact, besides the long term drift also visible in the figures (which could be compensated by smart calibration strategies in an integrated realization) the NR current is affected by a number of random noise sources. Previous studies point out that at low frequencies, the noise of NRs is dominated by the flicker component [51, 17, 32, 122], which is characterized by a power spectral density that is proportional to $f^{-\gamma}$ where f is the frequency and $0.7 < \gamma < 1.3$ [52]. The flicker noise leads to a degradation of the NR gate oxide that is more important for devices having smaller gate areas [123]. It is thus relevant to assess it in view of integrated realizations of newly NR sensor arrays.

In what follows, we characterize the noise at different bias points for three NRs (wafer p24, $t_{OX} = 3$ nm), ranging from 110 nm to 10 μm in width, by performing the fast Fourier transform (FFT) [124] of I_D samples. The I_D current has been measured in time with a sampling frequency of $f_S = 10$ Hz (100 ms of sampling time). The current spectral density S_{I_D} has been calculated applying the FFT on the measured current samples, as:

$$S_{I_D}(f) = 2\frac{|X(k)|^2}{N_{FFT} \cdot f_S} \tag{4.5}$$

where N_{FFT} is the number of time samples, f_S is the sampling frequency and $X(k)$ is the discrete FFT of the sampled current, defined as:

$$X(k) = \sum_{n=1}^{N_{FFT}} I_D(n) \cdot exp\left(-j\frac{2\pi}{N_{FFT}}(k-1)(n-1)\right) \tag{4.6}$$

A spectral filtering technique, based on the work of [125], has been employed to compensate for the distortions caused by aliasing, which can impact the scaling exponents of $f^{-\gamma}$ noises [126, 127, 128]. The results obtained by the filtering techinque are reported in fig. 4.25. Further details on the employed filtering method can be found in [37] (supplementary material).

Fig. 4.26a shows the noise power spectral density (S_{I_D}) for a NR ($L = 2375$ nm, $W = 110$ nm) biased in subthreshold (V_{FG}=0.9 V), weak inversion ($V_{FG} = 1.0$ V and 1.1 V) and above threshold ($V_{FG} = 1.7$ V), respectively $V_T = 1.2$ V. The S_{ID} of the silicon nanoribbon follows the expected $1/f$ behaviour at low frequency, with larger noise at high V_{FG}. On the other hand, fig. 4.26 (right) shows that when considering the ratio between noise power and squared signal, working above threshold leads to higher signal-to-noise ratio (SNR). In support of this observation, fig. 4.27a reports S_{I_D}/I_D^2 vs. I_D for different sampling frequencies showing that working at larger currents lead to smaller noise-to-signal ratio. These results are consistent with previously reported works [129, 130], in which the SNR is maximized at the peak transconductance. Note that no signature is found of white thermal noise in the explored frequency range. Moreover, the plot shows that the quantity S_{I_D}/I_D^2 and (g_m/I_D^2) follow the same trend vs. I_D, thus supporting the

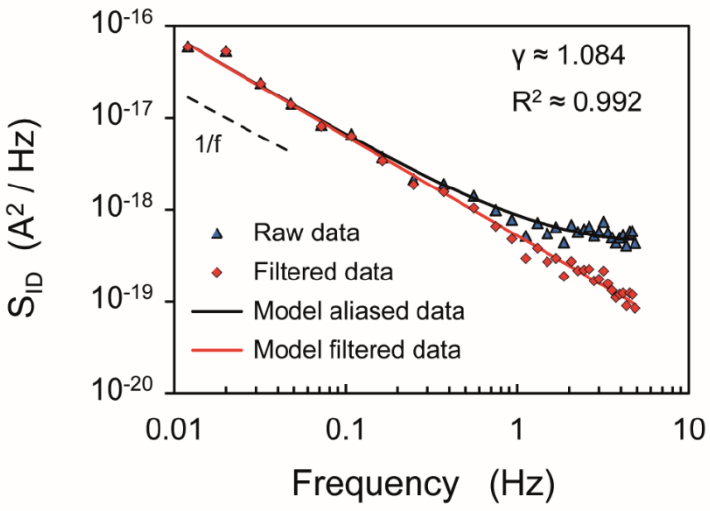

Figure 4.25: *Effect of the employed spectral filtering technique on a set of raw data. Figure taken from [37], supplementary materials.*

validity of the carrier-number fluctuation (ΔN) arising from the dynamic trapping and de-trapping of free carriers within the gate oxide as the dominating factor of the flicker noise [52, 123].

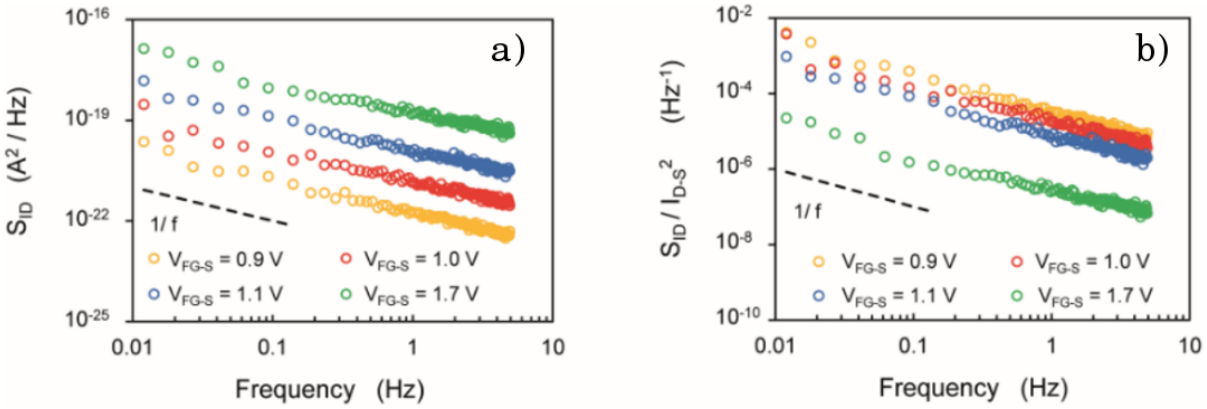

Figure 4.26: *Noise characteristics of a NR with $L = 2375$ nm, $W = 110$ nm, $t_{OX} = 3$ nm and biased at $V_{DS} = 1.5$ V. Left: Low-frequency drain current noise spectral density (S_{I_D}) spectrum. Right: S_{I_D}/I_D^2 as a function of frequency.*

Fig. 4.27b compares three NRs with different widths in terms of the S_{I_D}/I_D^2 factor. In the low current region, the SNR depends only weakly on the drain voltage. Instead, in strong inversion, the saturation regime ensures lower noise-to-signal ratio. In conclusion, since nano-sized transistors occupying smaller areas suffer more from intrinsic noise, those approaches aimed at increasing the array density of a chip by employing tinier pH sensors must take into account the degradation of the SNR, which would ultimately negatively affect the resolution in pH. In what follows, we show that multi-wire transistors can reduce this limit and thus allow smaller area per sensing pixel with improved resolution.

To conclude this section, we show that devices consisting of multiple NR connected in parallel exceed the performance of single devices occupying the same footprint area and we

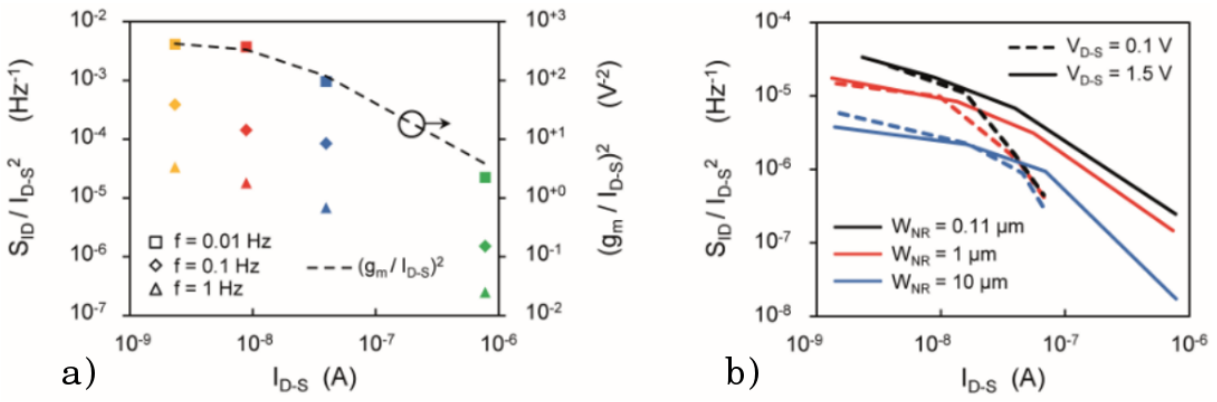

Figure 4.27: *Noise characteristics of a NR with $L = 2375$ nm, $W = 110$ nm and biased at $V_{DS} = 100$ mV and $V_{DS} = 1.5$ V. Left: S_{I_D}/I_D^2 plot for different frequencies ($f = 0.01$ Hz, $f = 0.1$ Hz and $f = 1$ Hz) as a function of I_D; Right: S_{I_D}/I_D^2 as a function of I_D for NRs with the same length ($L = 2375$ nm) and different widths ($W = 110$ nm, $W = 1$ µm and $W = 10$ µm) biased to work in saturation ($V_{DS} = 1.5$ V, solid lines) and triode regimes ($V_{DS} = 100$ mV), at a frequency $f = 1$ Hz.*

compare their performances with existing planar and tri-gate devices. In fact, multi-wires devices benefit, on one hand, from the enhanced sensitivity of narrower silicon structures and, on the other hand, from the lower noise provided by their larger interface area [131]. Moreover, previous works have shown the superior inter-device uniformity of multi-wire devices when compared to single NR [132]. As a consequence, multi-wire devices alleviate the variability of electrical parameters such as V_T, SS and g_m.

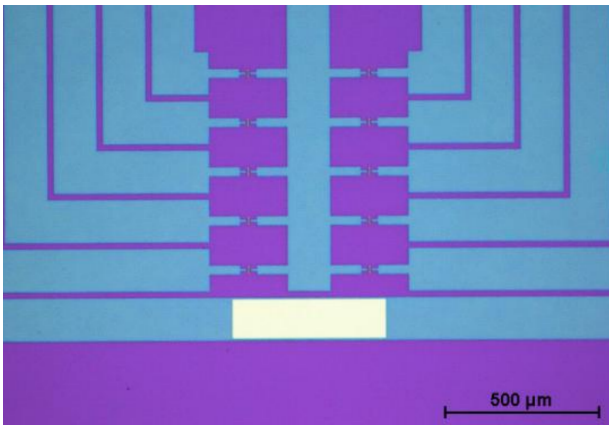

Figure 4.28: *Optical image of NR devices with common source connection.*

To start with, we consider four devices with common source connection and independent drain contacts for each finger, which allows us to compare the performance of the single-wire with that of 2-, 3- and 4-wires devices (fig. 4.30, cartoon A, B, C and D respectively). The devices were biased above threshold ($V_{FG} - V_T \sim 1$ V) and in saturation regime (V_{DS}=1.5 V). The results show an increase of the maximum transconductance with the number of NR fingers (fig. 4.30a). However, these values are smaller than the sum of the transconductances of individual wires, mainly due to the slightly different threshold

voltage of the considered four wires, which results in a degradation of the average g_m. As shown in fig. 4.29, the current sensitivity is directly linked to the transconductance of the device and, therefore, it also increases with the number of fingers.

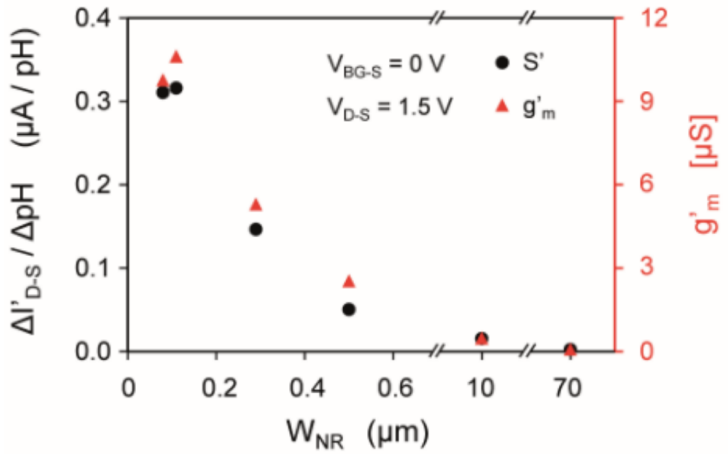

Figure 4.29: *pH current sensitivity ($\Delta I_{D-S}/\Delta pH$) and normalized transconductance (g'_m) as functions of the NR width (W_{NR}) for devices with constant length ($L = 2375$ nm).*

Fig. 4.30b reports the current noise as a function of the frequency for devices with increasing number of fingers showing an improvement for devices featuring larger area, as expected from S_{ID} scaling rules. As for fig. 4.26, the spectra have been compensated for aliasing distortions. Fig. 4.30a reports the Signal, Noise and SNR for devices of increasing occupied area featuring multiple nanowires (□). The Signal value corresponds to the measured g_m of the device multiplied by $\Delta V_T/\Delta$pH (assumed to be 30 mV/pH, average value for SiO_2) and the related error bars are defined based on the variability over the timescale of an experiment (a few hours). The Noise value of multi-wire devices is obtained by calculating the square root of the integral of the noise spectrum S_{I_D} in 1 Hz bandwidth centered at 1 Hz. The corresponding error bars are calculated from the prediction bounds of the interpolated spectrum.

The analysis of sensitivity and noise characteristics allows us to evaluate the resolution of the devices, i.e. the smallest detectable pH change. The resolution (δpH) is calculated as pH change giving a signal-to-noise ratio SNR = 3:

$$SNR = \frac{\Delta I_{DS}/\Delta pH}{\sqrt{\int S_{I_D} df}} = 3 \tag{4.7}$$

Since in fig. 4.29 we see that $\Delta I_{DS}/\Delta pH = g_m \Delta V_T/\Delta pH$, we can also compute

$$SNR = g_m \frac{\Delta V_T/\Delta pH}{\sqrt{\int S_{I_D} df}} = \frac{\Delta V_T/\Delta pH}{\sqrt{\int S_V df}} \tag{4.8}$$

where $S_V = S_{I_D}/g_m^2$ is the voltage power spectral density. The noise-equivalent pH value is obtained by dividing the noise level (square root of the integral of the current noise spectra over the measurement frequency bandwidth) by the current sensitivity

($\Delta I_D/\Delta$pH). A resolution of $\sim$ 0.8 ‰ of pH change is achieved in a 1 Hz bandwidth, centered at 1 Hz, by a 4-fingers device occupying approximately 1.16 μm^2. In terms of the lowest detectable change of electron surface density at the gate interface, the achieved pH resolution corresponds to $1.78{\cdot}10^{17}$ C/μm^2.

This result is close to the lowest reported value obtained with tri-gate nanowires (0.5 ‰ of a pH shift in a 1 Hz bandwidth centered at 10 Hz) employing a device with a 7 μm^2 footprint [17]. Nevertheless, in the context of ever increasing array density of integrated pH sensors, the most indicative parameter is the resolution that can be achieved in a unit of occupied footprint area on the chip. In this regard, our results outperform the previous works (0.0008 pH vs. $0.0005{\cdot}\sqrt{7} = 0.0013$ pH change with 1 μm^2 footprint device)[17], despite our more conservative choice of the SNR level to define the resolution (SNR = 3) and of a lower central frequency (f_C) for the bandwidth (1 Hz vs. 10 Hz). When evaluated under the same conditions (SNR = 1, f_C = 10 Hz), our system outperforms the state-of-the-art by two orders of magnitude.

In order to compare the performance of multi-wire designs to single nanoribbon devices, the SNR data for NRs of equivalent area (A*, B*, C* and D*) has been reported in fig. 4.30c ($\diamond$ in the "signal"). The signal values have been derived from fig. 4.29, with the error bars taking into account the interpolation error of the fitted trend. The noise values ($\diamond$ in the "noise" plot fig. 4.30c) are evaluated on the basis of the noise characterization of single ribbon devices (fig. 4.27b, V_{DS} = 1.5 V) and the corresponding error bars take into account the interpolation error. The results suggest that the SNR of multi-wire devices increases with the area with a steeper trend than for single nanoribbons and, in particular, a device occupying 1.16 μm^2 is characterized by a SNR that is 15 times higher than the one of a single nanoribbon of identical footprint. The resolution can be further improved by increasing the density of interconnected nanowires per device, and by sampling at higher frequencies [133]. Moreover, using an high-k gate dielectric such as Al_2O_3 and HfO_2 [134, 35] would induce a larger change of surface potential upon a pH change, leading to a higher signal transduced by the sensor.

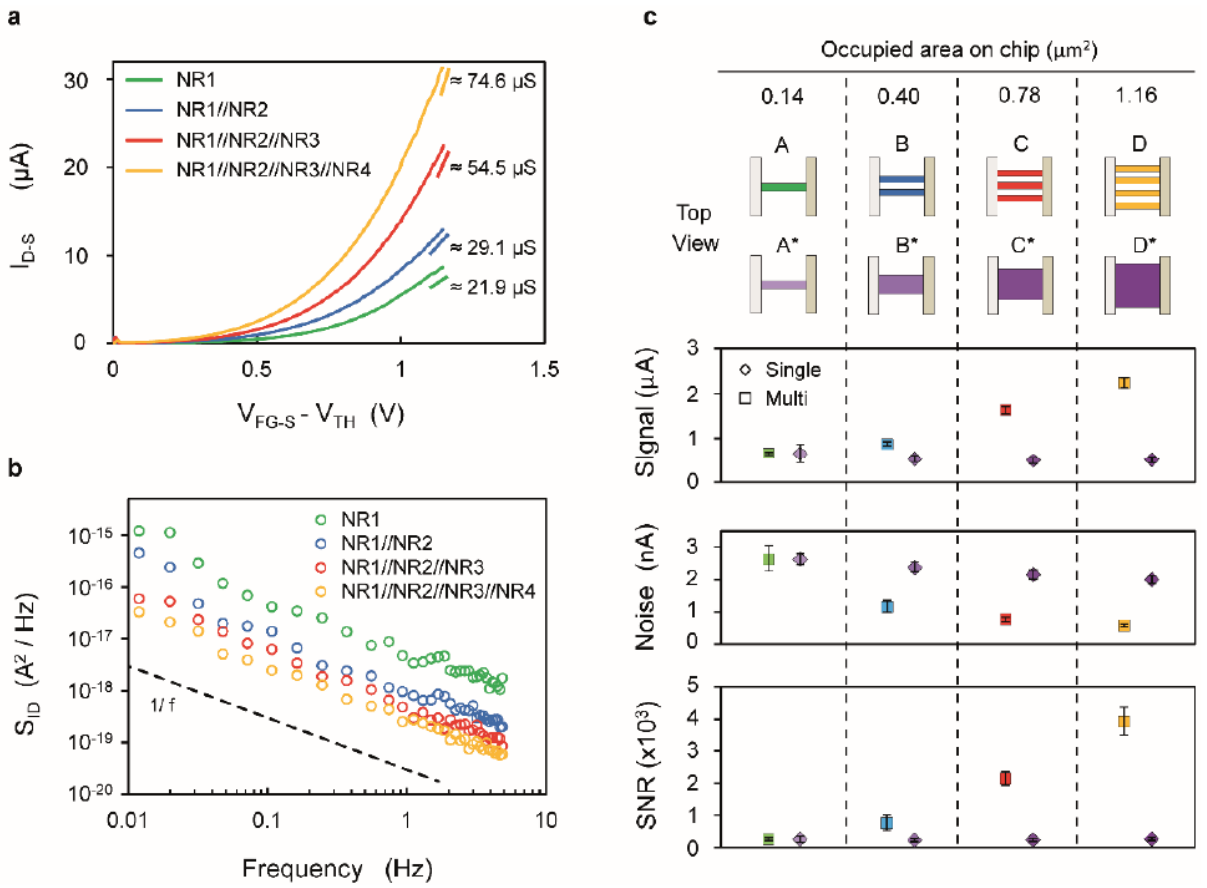

Figure 4.30: *a) Drain current (I_D vs. overdrive voltage ($V_{FG} - V_T$) characteristics; the value of the transconductance extracted at $V_{FG} - V_T = 1.1$ V is indicated on the right; b) Low-frequency current noise spectral density (S_{I_D}) characteristics; c) Signal, rms noise (as obtained by integrating the S_{I_D} over 1 Hz bandwidth centered around 1 Hz) and NR values for multi-finger devices (□) and for single NR occupying the same area on chip (◇) with color-coded cartoon representation of the devices with the indication of the occupied area, considering a distance of 50 nm between fingers. The NRs have dimensions as follows: $W_{NR1,2} = 60$ nm, $W_{NR3,4} = 110$ nm and $L_{NR1-4} = 2375$ nm.*

4.6 Summary

This chapter presented a comprehensive study of NR devices (and, marginally, also on FinFETs) operating in dry and liquid environments, combining measurements and simulations.

- The characterization in dry environment highlights some interesting results that were useful when compared to that in liquid. Firstly, biasing the devices from the back gate contact was complicated by the large back gate capacitance, intrinsic in SOI wafers. Furthermore, the measurements in dry have shown high instability, long transients and limited repeatability probably due to trapping, moisture or humidity which could be partially overcome by pulsing the applied voltages, instead of using the conventional linear sweep. The source/drain series resistances were characterized

(by using a technique based on two distinct $I_D - V_{FG}$ measurements at low V_{DS}) for devices featuring S/D connection and pads with and without silicidation.

- Such series resistance turned out to be a major limitation of the device operating in liquid environment and especially on wafers without silicided S/D connections. Only a proper de-embedding of their effects reveal a consistent scaling of the current with the device channel dimensions (W and L). Reducing dramatically the parasitic resistance and capacitance is the key to extend the frequency range of meaningful impedance spectroscopy measurements and to take advantage of high frequency characterization beyond the Debye screening limit. To this end integrated detection circuits appears a must.

- The static $I-V$ curves of NR and FinFET in both wet and dry environments could be accurately reproduced only by accounting for a non negligible concentration of traps and changes, whose energy and density were tuned to the measures. However all other parameters could be kept at their nominal or extracted values, confirming the correctness of the extraction methodology.

- By comparing measurements and simulations in both dry and wet environments we revealed remarkably different current density distributions inside the nanoribbon. In back-gated NRs in dry, the current density concentrates on the bottom corners of the ribbon, resulting in an effective width smaller than W. Instead, when the device works in liquid the electrolyte solution acts as a metal gate, the current density concentrates on the top and the sides of the NR channel, resulting in a much larger W. Differently from conventional (the MOSFET case) measures in dry are thus of limited usefulness when trying to identify the device geometry and doping parameters of the intrinsic device.

- Once all the parasitics where duly characterized and modelled, we carried out a pH sensitivity analysis on NRs with different layouts and connections. The experimental results suggest the choice of nanoribbons with a thin (25 nm instead of 50 nm) and low-doped (10^{16} cm^{-3} instead of $5 \cdot 10^{18}$ cm^{-3}) channel, and also with a sufficiently thick gate-oxide (8.5 nm instead of 3 nm) for a better stability.

- Once simulations in liquid environment were calibrated at a given pH we run calculations of the $I_D - V_{FG}$ and differential pH-sensitivity at a fixed voltage and at a fixed current. The results are in good agreement with the measures, both below and above threshold, elucidating the relation between S_V and S_I and proving the validity of the developed models and characterizations.

- Noise measurements on NRs biased in different working regimes suggest that working above threshold (i.e. with large currents) leads to higher SNR. Furthermore, we have shown that devices consisting of multiple NRs connected in parallel exceed the performance of single devices occupying the same footprint. With 4 nanoribbons

occupying approximately 1.16 μm^2 we reached a resolution of ~ 0.8 ‰ of pH change in a bandwidth of 1 Hz, centered at 1 Hz; value that can be converted in a charge resolution of $1.78{\cdot}10^{-17}$ C/μm^2 ($\approx$ 100 electrons μm^{-2}). This result exceeds the performance of previously reported studies on NRs by approximately two orders of magnitude.

Chapter 5

Microparticle and biomolecule detection

This chapter is focused on electrochemical impedance spectroscopy as a tool to detect microparticles and biomolecules in solutions.

Section 5.1 presents the results obtained by performing impedance spectroscopy with NRs [135, 136, 137, 138, 8]. The section starts with a brief introduction comparing the measurement setups alternatives, by discussing pros and cons. Consequently, we present a quasi-3D model that we used to study the impedimetric response of bare NRs first, and then to analyze the sensitivity to dielectric microparticles in solution.

Section 5.2 shows electrochemical impedance spectroscopy measurements on Electrolyte-Insulator-Semiconductor (EIS) samples [139, 140, 141, 142]. EIS samples, in contrast to NRs, are simple structure with a 1-D geometry. We firstly present a comprehensive characterization of the bare sensor (that is composed by a stack of p-type semiconductor, native oxide and electrolyte) based on an accurate compact electrical model. Secondly, we validate the compact model analyzing measurements performed using, as electrolyte, three buffers with different characteristics. Thirdly, EIS samples were functionalized for the detection of PNA/DNA hybridizations, and we used a modified version of the compact model to analyze the experimental findings.

Both sections end with a summary of the main achievements and present perspectives future applications employing NRs and EIS-based devices as biological sensors.

5.1 Impedance spectroscopy at nanoribbons

We characterized the NRs in AC conditions in two configurations, depicted in fig. 5.1. The idea is to bias the device at constant V_{FGS} and V_{DS} in a specific region of operation (subthreshold, inversion) and to apply the small-signal perturbation either at the drain ($\tilde{V}_{DS}$ fig. 5.1a) or at the reference electrode ($\tilde{V}_{FGS}$, fig. 5.1b). We measure the small-signal current, $\tilde{I}_S$, at the source contact by using a lock-in amplifier. The indefinite admittance matrix of the four terminal ISFET is given by

$$\begin{bmatrix} \tilde{I}_{FG} \\ \tilde{I}_S \\ \tilde{I}_D \\ \tilde{I}_B \end{bmatrix} = \begin{bmatrix} Y_{FGFG} & Y_{FGS} & Y_{FGD} & Y_{FGB} \\ Y_{SFG} & Y_{SS} & Y_{SD} & Y_{SB} \\ Y_{DFG} & Y_{DS} & Y_{DD} & Y_{DB} \\ Y_{BFG} & Y_{BS} & Y_{BD} & Y_{IZ} \end{bmatrix} \begin{bmatrix} \tilde{V}_{FG} \\ \tilde{V}_S \\ \tilde{V}_D \\ \tilde{V}_B \end{bmatrix} \tag{5.1}$$

Since the back gate bias is used as reference electrode, the matrix becomes

$$\begin{bmatrix} \tilde{I}_{FG} \\ \tilde{I}_S \\ \tilde{I}_D \end{bmatrix} = \begin{bmatrix} Y_{FGFG} & Y_{FGS} & Y_{FGD} \\ Y_{SFG} & Y_{SS} & Y_{SD} \\ Y_{DFG} & Y_{DS} & Y_{DD} \end{bmatrix} \begin{bmatrix} \tilde{V}_{FG} \\ \tilde{V}_S \\ \tilde{V}_D \end{bmatrix} \tag{5.2}$$

therefore we can extract the following admittances of the device under test

$$Y_{DS} = \frac{\tilde{I}_S}{\tilde{V}_{DS}}, \qquad Y_{FGS} = \frac{\tilde{I}_S}{\tilde{V}_{FGS}} \tag{5.3}$$

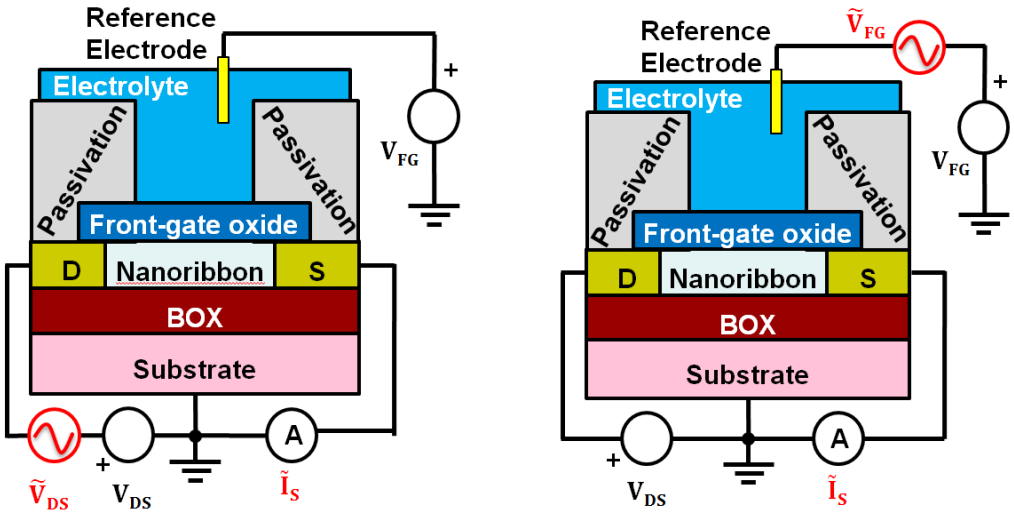

Figure 5.1: *AC measurement set-up. Measurement of the device current while applying the small-signal perturbation at the drain contact (a) or at the reference electrode (b).*

All the measurements presented in this section were performed using KCl as electrolyte (pH=7 independently of the molar concentration). We start by presenting the measurements of Y_{DS}. Fig. 5.2 shows the AC response of a NR (W = 170 nm, L = 2375 nm, wafer p07), biased at V_{DS} = 100 mV and V_{FG} such that the DC current is approximately

10 nA, subject to different solution ionic strengths. This bias correspond to an operation in the subthreshold region. The results show almost no sensitivity of the admittance Y_{DS} to the ionic strength, meaning that there is no effect of electrolyte on the NR drain-source admittance.

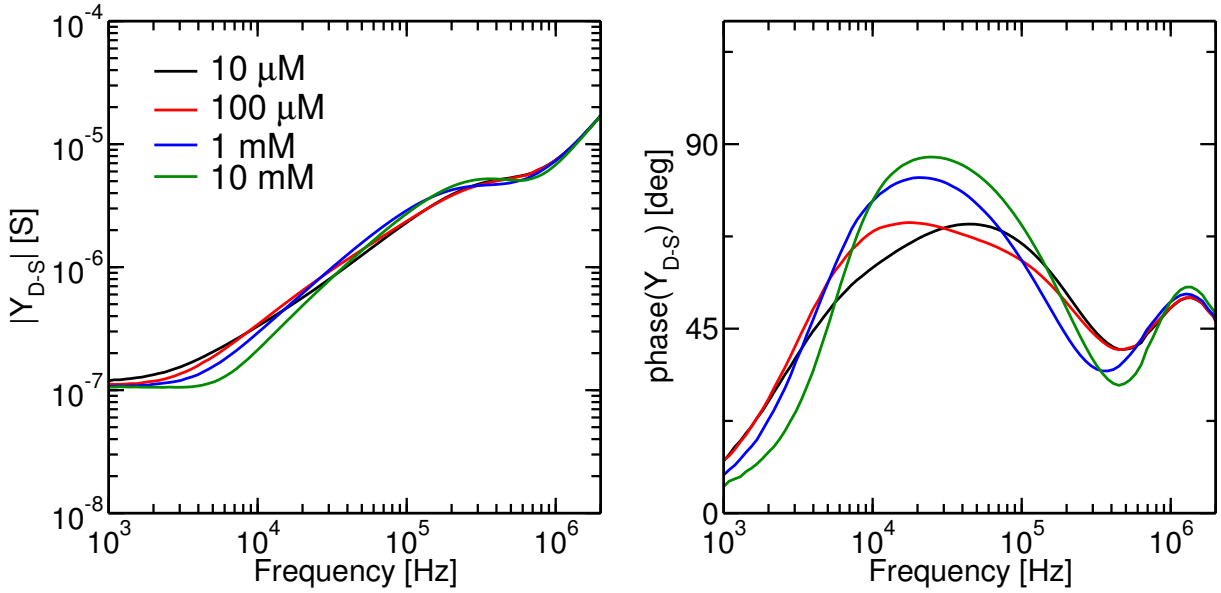

Figure 5.2: *Magnitude (left) and phase (right) of Y_{DS} for four different electrolyte concentrations, I_S fixed at 10 nA.*

Fig. 5.3 shows the Y_{DS} of the same device biased in three different regions while keeping the solution concentration at 10 mM. V_{DS} was fixed at 100 mV and V_{FG} sets I_S to 0 A (device off, $I_S < 1$ nA), 10 nA (subthreshold) and 100 nA (weak inversion). The results show different behaviours at low frequency, due to the three different DC current levels and channel conductance; in fact, the conductance at low frequencies is the $g_{DS} = V_{DS}/I_{DS}$. Instead, at high frequency, the AC response is independent of the bias point.

Fig. 5.4 shows the Y_{FGS}, obtained with a $V_{DS} = 100$ mV and a $V_{FG} = 0$ V. The same NR was measured by applying the small-signal perturbation at the reference electrode. In contrast with the previous configuration, the results show a large dependence on the ionic strength.

The results obtained with the two measurement configurations can be explained by examining the path followed by the AC signals across the device and a single lumped element circuit model. In configuration a) the small-signal perturbation is applied at the drain contact, it crosses the conductance of the NR channel and it is then measured as a current at the source contact. The channel conductance is the main contribution to the Y_{DS} at low frequency. Its value is mostly affected by the inversion charge density in the channel and by the parasitic capacitance through the substrate, while it its only slightly affected by the double layer capacitance (C_{DL}) since it is connected in parallel. Therefore, Y_{DS} does not change much with the ionic strength of the liquid environment.

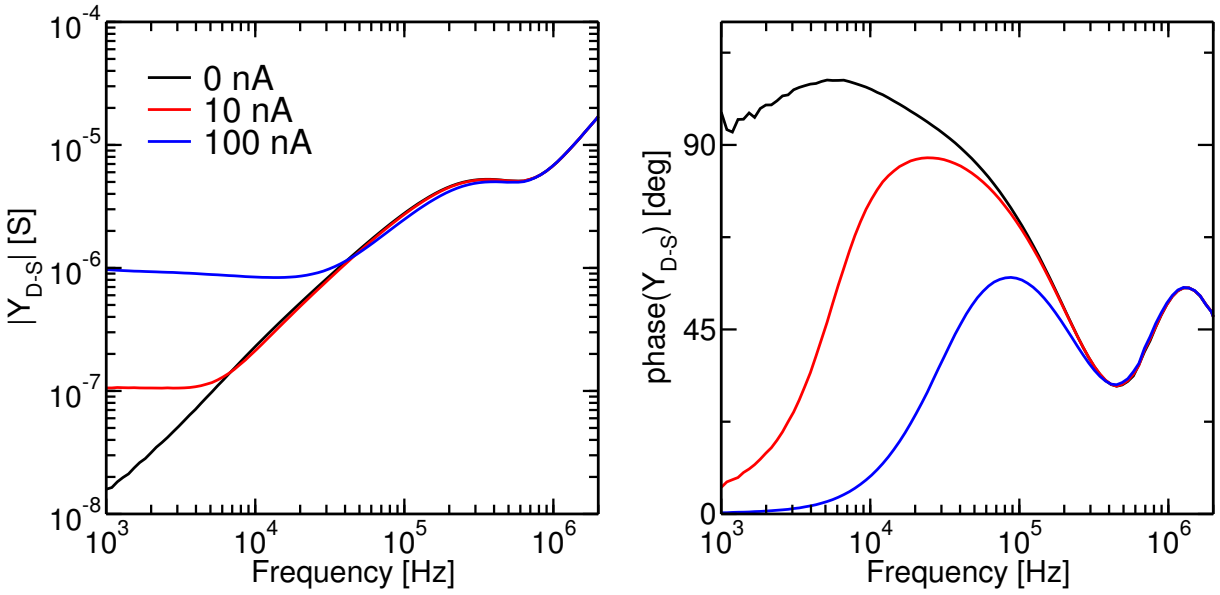

Figure 5.3: *Magnitude (left) and phase (right) of Y_{DS} in three different bias points, $I_S = 0$ nA (device off), 10 nA (subthreshold) and 100 nA (weak inversion).*

Instead, in configuration b), the signal path starts from the reference electrode, crosses the electrolyte and the double layer capacitance and then couples to the source contact passing through the NR channel. The admittance Y_{FGS} is thus affected by both the ionic strength (via C_{DL}) and the gate bias (via the channel conductance).

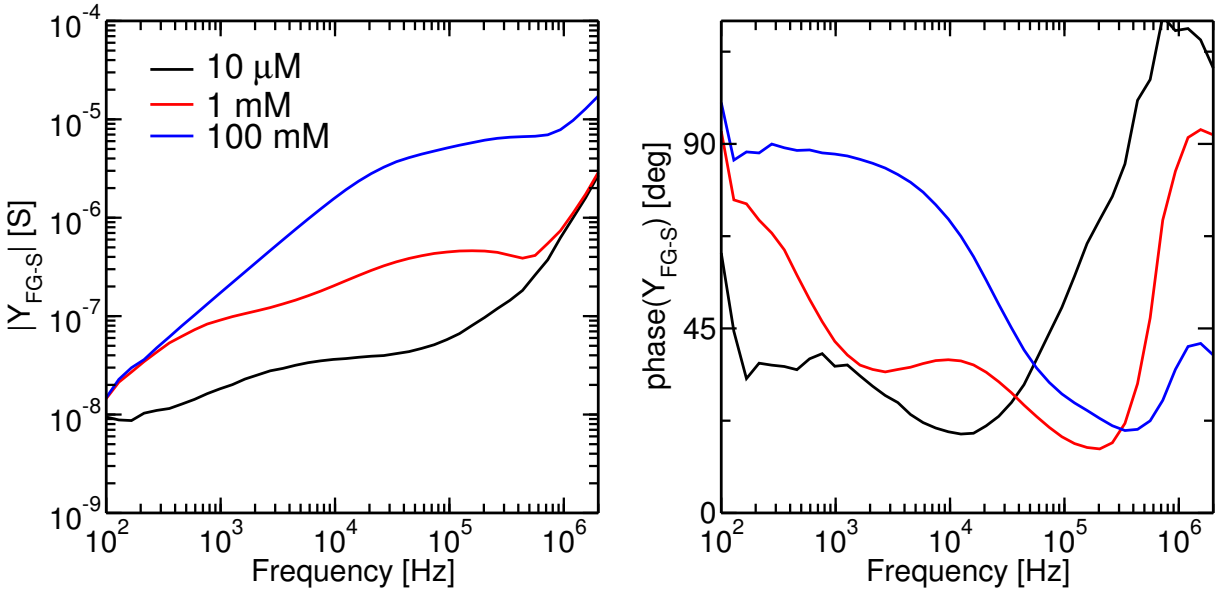

Figure 5.4: *Magnitude (left) and phase (right) of Y_{FGS} measured for three different electrolyte concentrations. $V_{DS} = 100$ mV, $V_{FG} = 0$ V, small-signal perturbation applied at the reference electrode.*

As a first step to understand the measurement results reported in fig. 5.4, we simulated a 1D structure (electrolyte-insulator-semiconductor) by using the simulator presented in

3.3.1. Left picture in fig. 5.5 reports the simulation results normalized by the area of the measured device. Firstly, the AC site-binding model was disabled and then activated to analyze its effect on the admittance response. The DC site-binding model, instead, is always active, since at pH=7 on SiO_2, the insulator/electrolyte interface is highly charged ($\approx 10^{14}$ C/cm^2). As we can see from fig. 5.5, the qualitative features of the AC spectra, at different concentrations, are replicated by the simulations, but there are still substantial quantitative discrepancies. In particular the $|Y_{FGS}|$ cut off frequencies are larger in simulation than in measurements.

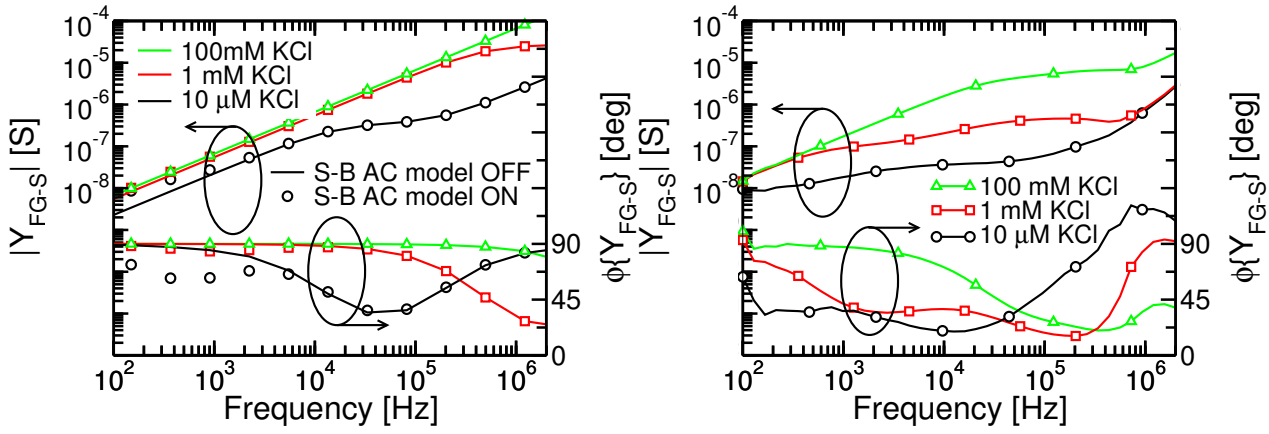

Figure 5.5: *Magnitude and phase of Y_{FGS}. Left: 1D simulations, with and without the AC site-binding (S-B AC) model; right: measurements.*

The simple 1D structure is clearly not sufficient to predict the measurements of the real complex geometry. However, reproducing the main features of the data without analytes is a mandatory first step prior to attempting the interpretation of the data with analytes. It is thus necessary to develop a more sophisticated model. In principle ENBIOS would allow to simulate the whole 3D system but, for the sake of computational efficiency we embraced a different approach. Fig. 5.6 shows a schematic representation of the developed model, which is based on a combination of 2D simulations and compact circuit elements.

This is a quasi-3D model representing the system as the parallel connection of two parts: the vertical area over the NR and the one over the S/D interconnects. Each part is represented as a quasi-3D domain with rectangular cross-section of thickness T (typically 2 nm in order to reduce at minimum the number of mesh points) containing the insulator and the very first micrometers of the electrolyte solution (∼15 µm). We used ENBIOS to simulate the domain $W \times T \times H_1$ and derive its admittance (Y_{NR} and $Y_{S/D}$), while we modelled the bulk electrolyte in the chamber ($W \times T \times H_2$) as a lumped G-C element ($Y'_E = G'_E + j\omega C'_E$ per unit area) with G'_E and C'_E computed according to the bulk electrolyte conductivity and dielectric constant. From the simulations we get the admittances Y_{NR} and $Y_{S/D}$, of nanoribbon and interconnections respectively, that we normalized by the simulated area ($W \times T$) to obtain Y'_{NR} and $Y'_{S/D}$, in S/m^2. For consistency with the real system the admittances in each branch were then multiplied by the areas of the

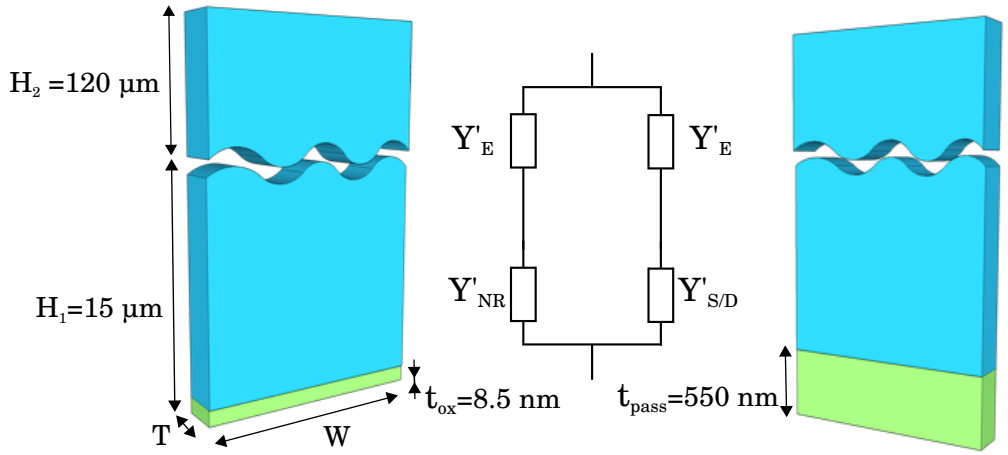

Figure 5.6: *Sketch of the simulated systems. Insulator (green) and electrolyte (cyan).* Y'_{NR} *and* $Y'_{S/D}$ *are the ENBIOS simulated admittances in* S/m^2. Y'_E *is the bulk electrolyte admittance per unit area (analytically calculated).*

respective regions, as defined by the layout (A_{NR}=100×10 µm^2, $A_{S/D}$ ≈550×100 µm^2). This equivalent model allows us to compute separately the contribution of the NR ($Y_{NR,E}$) and the interconnections ($Y_{S/D,E}$) as:

$$Y_{NR,E} = \left(\frac{1}{A_{NR}Y'_{NR}} + \frac{1}{A_{NR}Y'_E}\right)^{-1}, \qquad Y_{S/D,E} = \left(\frac{1}{A_{S/D}Y'_{S/D}} + \frac{1}{A_{S/D}Y'_E}\right)^{-1} \tag{5.4}$$

The total admittance is simply given by the sum of the two contributions: $Y_{TOT} = Y_{NR,E} + Y_{S/D,E}$.

Fig.5.7 compares the measurements with the results obtained with the model. The contributions of $Y_{NR,E}$ and $Y_{S/D,E}$ are shown separately. We clearly see that above 1 kHz the spectrum is dominated by the interconnects (compare measures, □, with $Y_{S/D,E}$, red line). The NR limits the conductance at low frequency; also, the large capacitance of its thin oxide emerges at low frequencies above the S/D interconnect capacitance (as it is visible around 100 Hz). The parallel model, Y_{TOT}, is in good agreement with the experimental data only if the contribution of the bulk electrolyte (Y'_E) is considered (solid black line). In fact the sum Y_{NR}+$Y_{S/D}$ only qualitatively reproduces the measures (dashed black line).

Once the model was verified and simulations were accurately fitted to the experiments on bare NRs, we performed experiments and calculations with dielectric beads in solution, that we reported in the following section.

5.1.1 Microparticles detection and data analysis

For the experiments with polystyrene beads (from SIGMA-ALDRICH, with a diameter of 8 µm, ε_r=2.6) we consider W=100 µm and L=10 µm to make sure that the beads can enter the opening in the passivation above the channel and touch the device active area.

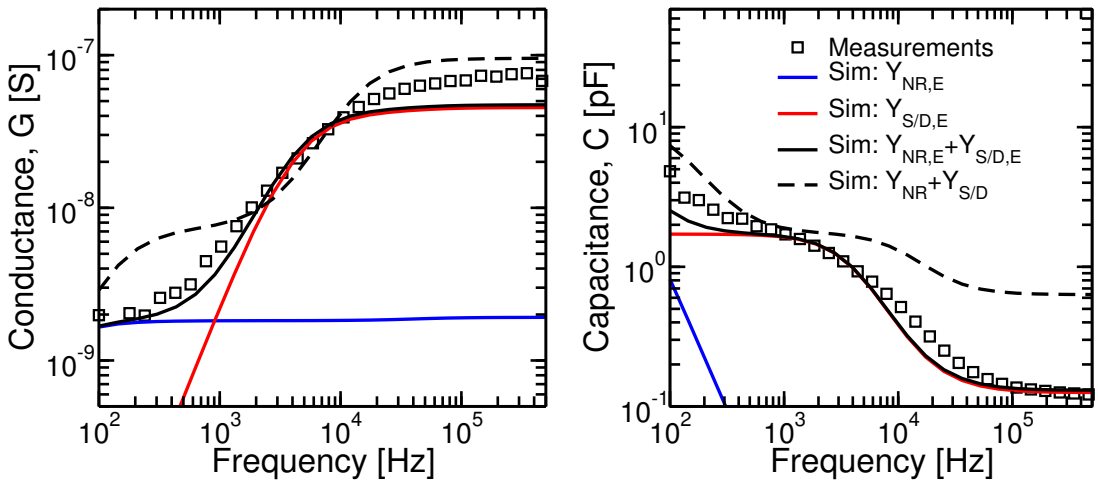

Figure 5.7: *Comparison between measurements and simulations, in terms of conductance (left) and capacitance (right). Solid blue: simulation of nanoribbon only; solid red: simulation of interconnects only; dashed black: parallel connection of NR and interconnect (without the electrolyte contribution); solid black: parallel connection of NR and interconnect (with the contribution of the electrolyte in the chamber).*

Since the microfluidic chamber is much larger than the active area, beads sediment on the interconnects and surrounding area as well. We opted to use a solution of 10 µM KCl, in order to analyze the AC NR response both below and above the electrolyte cut-off frequency, i.e. ≈10 kHz.

The admittance of the system was recorded by applying a small signal voltage (100 mV) at the reference electrode and measuring the current at the drain contact of the device under test, as depicted in fig. 5.8. Source and back gate terminals were kept at 0 V.

Before each experiment, the devices were flushed and equilibrated for approximately 30 minutes in a 10 µM KCl solution. Then, the beads were injected inside the microfluidic channel and verified by optical microscope inspection that the beads homogeneously cover both the device and the surrounding area. Fig. 5.9a shows image of the ribbons with a moderate concentration of beads, covering the NR and the interconnections. A larger concentration, corresponding to a rather uniform layer of beads was typically observed prior to the experiments, as shown in fig. 5.9b. The NR, in this case $L = W = 100$ µm, is highlighted by the light blue square. The beads were then flushed away by injecting the same KCl solution. Measurements were performed several times to identify the repeatable features of the data with and without beads.

In order to interpret the results and asses the ability of the NR to act as a microparticle sensor we resorted to simulations. However, the direct numerical simulation of the whole system homogeneously covered by the beads is a daunting computational effort, because meshing many spherical beads demands a very large number of grid points. To tackle the problem we used the quasi-3D model presented in the previous section. We consider now the case reported in fig. 5.10, where the spherical beads are modelled as cylindrical

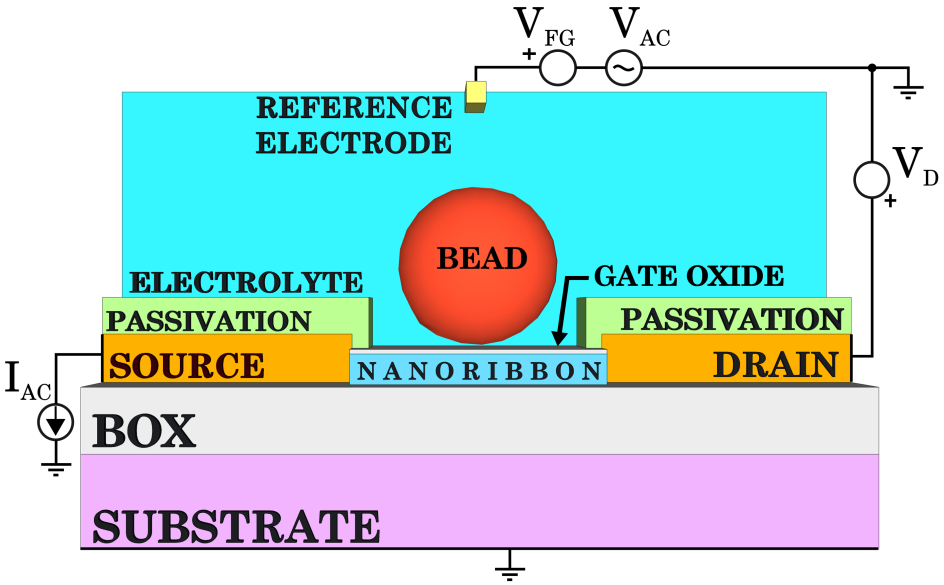

Figure 5.8: *Sketch of the NR cross-section, with a dielectric bead touching the NR gate oxide. In a real experiments the beads cover also the passivations of the source and drain leads. The measurement set-up is also depicted. The admittance of the system is calculated by applying the small-signal perturbation, V_{AC}, at the reference electrode, while measuring the AC current, I_{AC}, at the source terminal.*

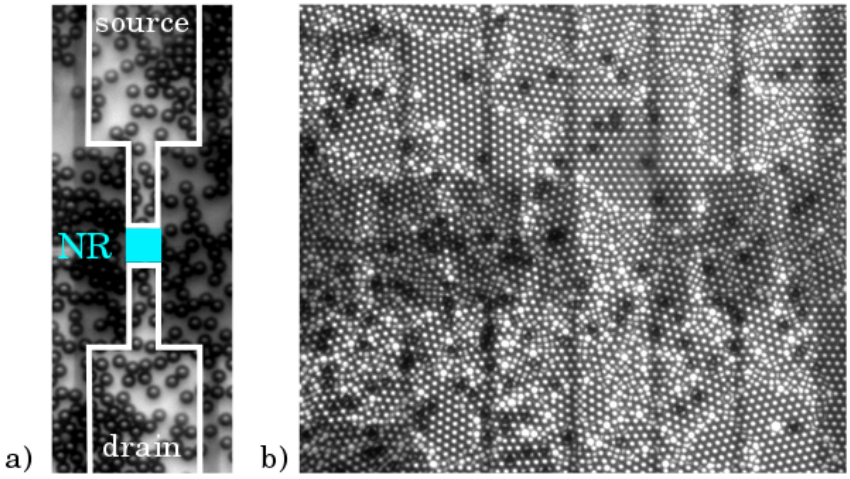

Figure 5.9: *Optical image of NR in liquid with dielectric beads in solution. a) Moderate concentration of beads. b) Layer of closely packed beads.*

entities in contact with the underling insulators. Simulations with and without the beads have been run using the same mesh and simply changing the dielectric properties of the bead region to avoid spurious numerical errors. Since the beads diameter is 8 µm, we chose $W = 8.1$ µm that corresponds to the assumption of a layer of closely packed cylindrical particles (as opposed to the actual spherical ones), consistently with the optical images taken before impedance measurements (fig. 5.9b). By changing the width, W, of the simulation domain, one can simulate different bead densities. Considering $W = 8.1$

µm, i.e. a bead average distance of 100 nm, is consistent with the close packing of the beads observed in the experiments and furthermore, essentially represents the maximum observable density and signal.

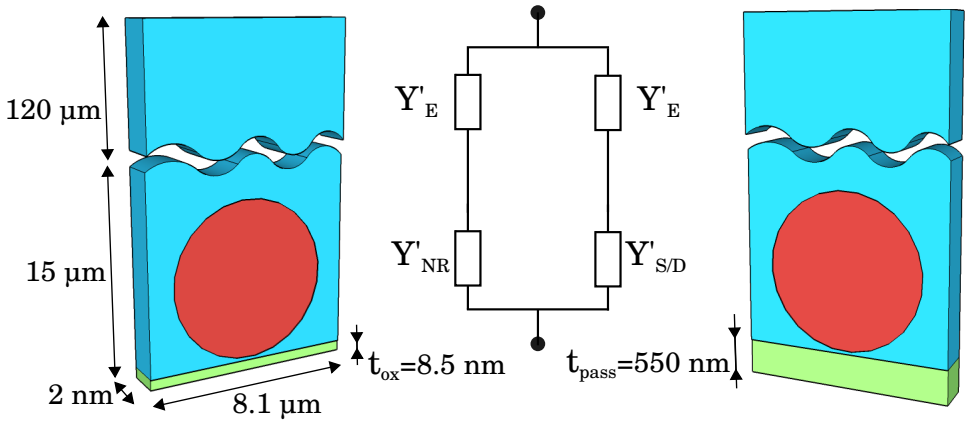

Figure 5.10: *Sketch of the simulated systems. Insulator (green), electrolyte solution (cyan) and dielectric beads (red).* Y'_{NR} *and* $Y'_{S/D}$ *are the ENBIOS simulated admittances in* S/m^2. Y'_E *is the bulk electrolyte admittance per unit area (analytically calculated).*

Fig. 5.11 shows the results computed with the quasi-3D model. We have simulated four different configurations: without beads, with uncharged beads and with positively and negatively charged beads. We considered a charge of 30 mC/m^2 [143]. These different configurations were firstly simulated with the site-binding AC model disabled (top figures) and then by enabling it (bottom figures) at the NR gate-oxide/electrolyte interface.

By comparing the results in fig. 5.11 we clearly see that the site-binding AC model has a detectable effect at low frequencies. The site-binding AC charge screens the detection of the bead at low frequencies; in fact, the AC spectra of conductance and capacitance are essentially the same, for the four configurations, till a few kHz. With the site-binding AC model disabled, the response is highly sensitive to the three bead charge, but unfortunately, this is not representative of the real situation. At frequencies above a few kHz, the screening effect of the site-binding AC charge vanishes, due to its considerably slow time constants.

Fig. 5.12 shows the conductance and capacitance change (as would be measured by the FET device), i.e.: $(X_{w/o} - X_w)/X_{w/o}$ with $X \in \{G, C\}$. By considering neutral beads (red curve), both sign and shape of the curves have opposite trends with respect to the measurements. To reconcile this remarkable discrepancy, we have then considered the possible existence of a residual DC surface charge of 20 or 70 mC/m^2 that alters the local electrolyte conductivity and shifts the electrolyte cut-off frequency. The blue and black curves in fig. 5.12 suggest that the surface charge is essential to explain the qualitative features of the measurements, especially at low frequency. This effect appears to be much more important than the presence of the AC site-binding charge.

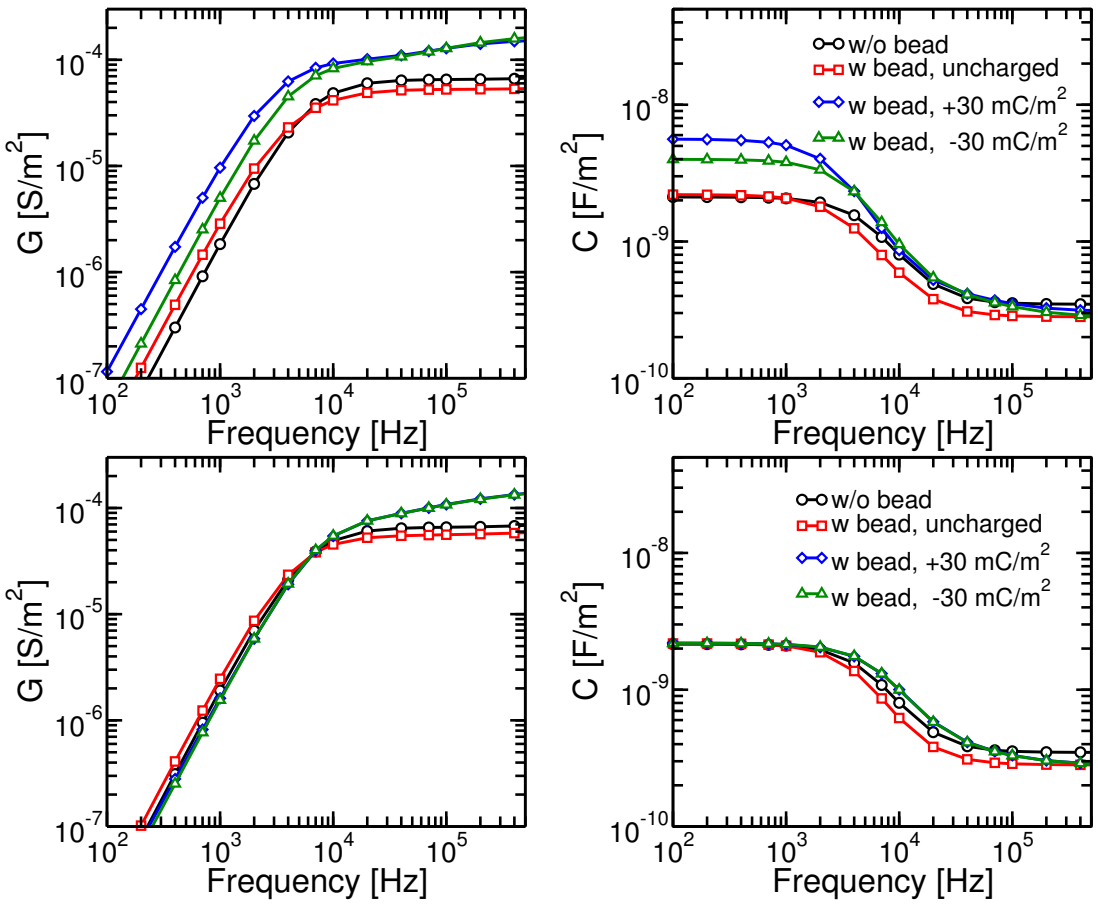

Figure 5.11: *Top graphs: AC site-binding model disabled. Bottom graphs: AC site-binding model enabled. Results presented in terms of normalized conductance (left) and capacitance (right). Simulation results of (black) unperturbed system, (red) system with uncharged beads, (green) system with negatively charged beads and (blue) system with positively charged beads.*

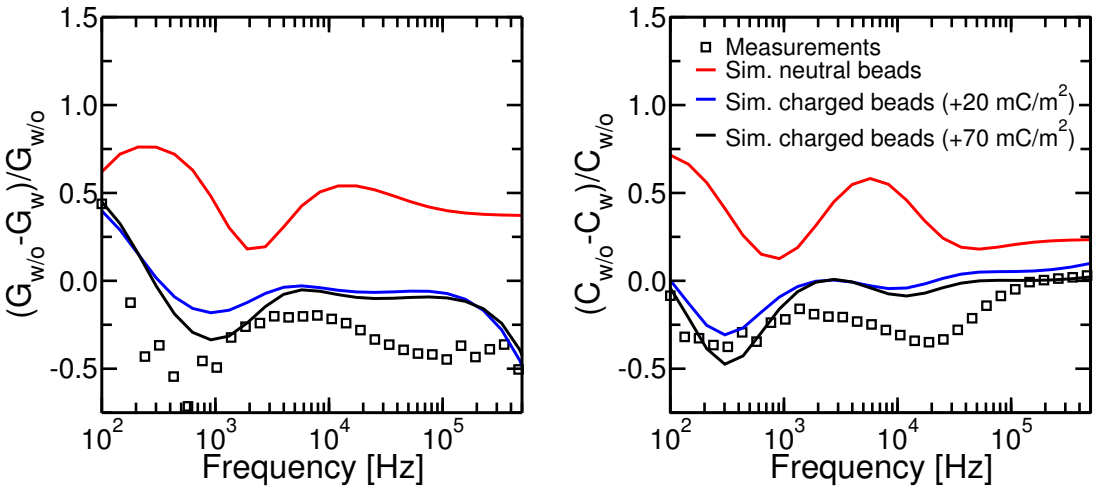

Figure 5.12: *Comparison between measurements (□) and simulations (solid lines), in terms of conductance (left) and capacitance (right) sensitivities. Simulations performed with neutral and charged beads (+20 and +70 mC/m^2).*

5.1.2 Summary

Experiments of bead detection at nanoribbon devices have been carried out and interpreted with the aid of a quasi-3D model based on numerical simulations and compact circuit models.

For the case without beads, the quasi-3D model shows excellent match with impedance measurements in the 100 Hz-500 kHz range. Careful analysis of the results indicates that the portion of interconnect in contact to the electrolyte, as opposed to the NR area, dominates the response at moderately high frequency, in spite of the top oxide being much thicker than the NR gate oxide. This result highlights the need to reduce the interconnects area wetted by the liquid or to largely increase the thickness of the passivation in order to achieve high sensitivity.

Furthermore we observe that our measurements of the NR admittance response to micron-sized beads can be qualitatively (sign) and quantitatively (magnitude) reproduced only by accounting for a residual surface charge of the beads. The simulation results clearly indicate that we can discriminate between neutral and charged beads, since they have an opposite response compared to the unperturbed case, both in conductance and in capacitance over the whole range of measured frequencies. These results underline the usefulness and need of accurate models for quantitative understanding of sensing experiments with NR devices.

5.2 Impedance spectroscopy at EIS capacitors

In this paragraph we will examine in detail the measures on EIS capacitors that we have described in sec. 2.2, with the objective to develop a modular equivalent circuit for the admittance (impedance) where each layer (semiconductor, insulator, electrolyte) is represented by a separate cell and all cells are connected in series.

Our purpose is to find an equivalent circuit model for the systems described in fig. 5.27, thus we start by considering the measurements of the reference system structure (fig. 5.27a), composed by p-doped semiconductor (Boron-doped, $4{\cdot}10^{18}$ cm^{-3}, resistivity $\sim$0.0175 $\Omega{\cdot}$m), native silicon dioxide (SiO_2) and electrolyte (100 mM NaCl plus 50 mM TRIS HCl, pH at 7.2). Our approach is to start from a simple electrical circuit, possibly with the minimum number of cells that is able to reproduce the main features of the frequency measured response, that is one cell for the electrolyte, one for the oxide and one for the semiconductor. We start by modelling the electrolyte which is usually well represented by the parallel connection of a capacitance and a conductance, $C_E||G_E$ [81, 22].

We calculate their values analytically as initial guess for a fitting procedure. Knowing the composition of the electrolyte, the area of the sample ($A_s = 0.189$ cm^2) and the distance between the surface of the sample (solid/liquid interface) and the reference electrode ($t_{elyte} \sim 20$ mm) we can roughly calculate their values: $C_E = 78\varepsilon_0/t_{elyte} \cong 345$

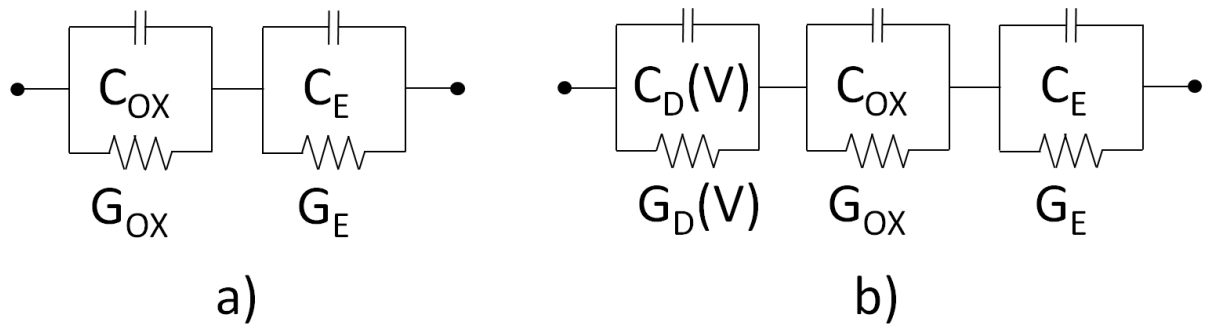

Figure 5.13: *Circuit model 1: a) accumulation/inversion, b) depletion.*

pF/cm^2 and $G_E = (2q^2\mu_{eq}n_\infty/t_{elyte}) \cong 0.0098 \cdot 10^{-3}$ S/cm^2 [1]. The impedance of the parallel connection of C_E and G_E has a pole at $(2\pi C_E/G_E)^{-1} \sim 4$ MHz. Regarding the SiO_2 layer, since it is native, we expect it to be very thin ($t_{OX} \sim 1$ nm, $\varepsilon_{SiO2} = 3.9$) and leaky. Thus, we can model it as $C_{OX}||G_{OX}$, where $C_{OX} = \varepsilon_{SiO2}\varepsilon_0/t_{OX} \cong 3.45$ μF/cm^2. Our first circuit model for the oxide-electrolyte system is thus the one reported in figure 5.13a. For the oxide conductance should be described as the slope of the static I-V curve at the bias point chosen for AC analysis. We start with a guess for G_{OX} and after tuning of the circuit elements, we were able to finely reproduce the measured impedances in fig. 5.14, for $V_{BG} = 0$ V and $V_{BG} = +0.5$ V. The results of the tuning procedure are reported in tab. 5.1 and suggest that the semiconductor part of the sample is not essential to reproduce the main frequency dependence of the spectra.

V_{BG}	C_{OX}	G_{OX}	C_E	G_E	C_D	G_D
V	μF/cm^2	μS/cm^2	pF/cm^2	S/cm^2	μF/cm^2	S/cm^2
+0.5	3.00	4.00	250	0.024	-	-
+0.0	3.00	0.25	250	0.024	-	-
-0.5	3.00	0.50	250	0.024	0.60	0.01

Table 5.1: Model 1, circuit elements values obtained by a manual fitting, starting from the analytical calculated values.

Let's consider the blue curve for $V_{BG} = +0.5$ V in fig. 5.14. There are two plateaus in the magnitude graph, one at low frequencies around 0.1 Hz and one at high frequencies. The former is given by the insulator conductance. In fact, if we set $R_{OX} = (G_{OX} \cdot A_s)^{-1} =$ 1.3 MΩ, we obtain exactly the plateau at 0.1 Hz. The latter is simply given by the electrolyte conductance G_E.

This equivalent circuit, with only 4 passive elements, is not able to reproduce the response for the case of $V_{BG} = -0.5$ V. Looking at the phase of the red curve in fig. 5.14, it is clear that there is an additional zero-pole pair around 3 kHz, that we model as an

[1] μ_{eq} is the average mobility among all the mobilities of the ions in the electrolyte, weighted on by the molar concentration, see sec.3.3.3.

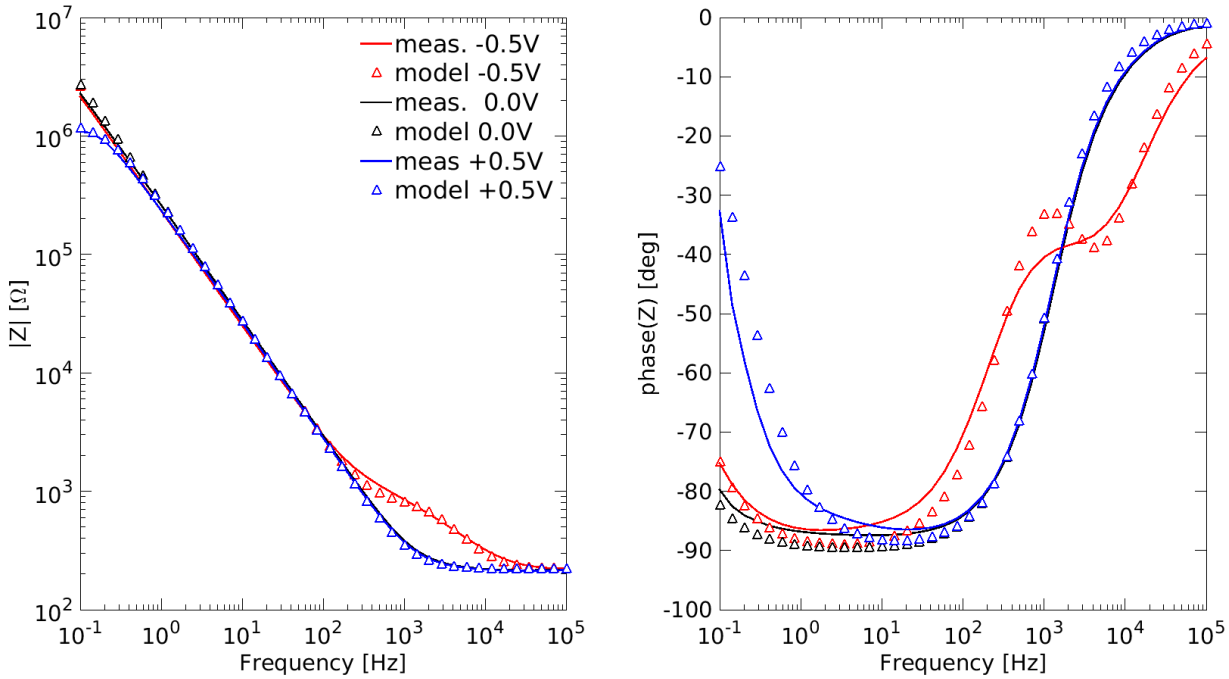

Figure 5.14: *Comparison between measurement on EIS capacitor and simulations with circuit model 1. Magnitude (left) and phase (right) of the impedance as a function of frequency.*

additional parallel $C_D||G_D$, corresponding to the bias dependent semiconductor behaviour.

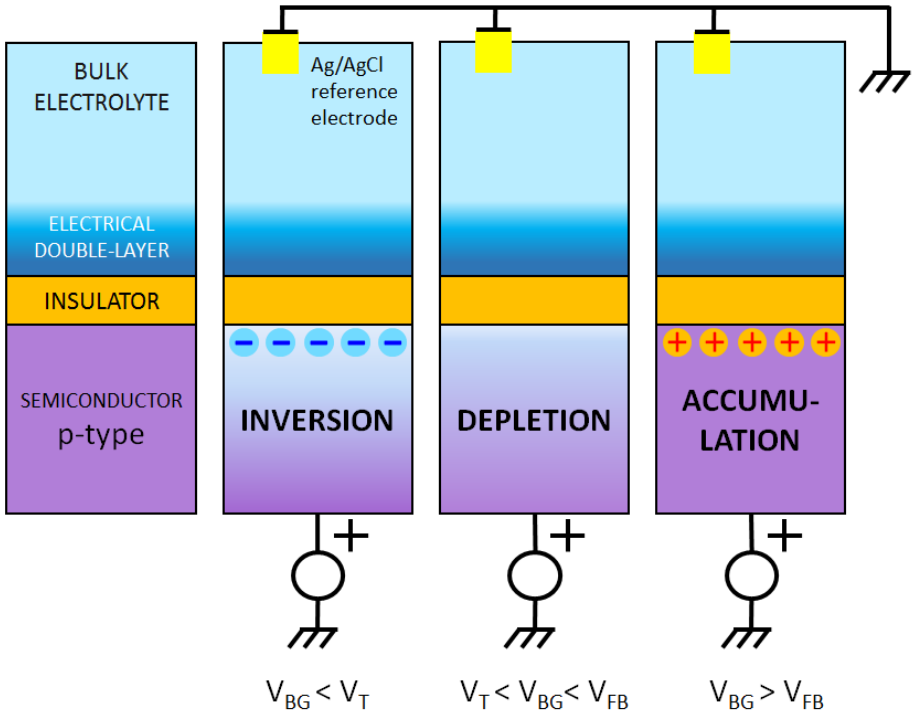

Figure 5.15: *Device structure and working regions.*

Fig. 5.15 shows a sketch of the measured system (on the left) and the three working conditions (three right pictures). Depending on the bias applied to the structure, between the back gate and the Ag/AgCl reference electrode (V_{BG}), the EIS capacitor can be in inversion, depletion or accumulation. In the case of a p-type substrate, accumulation occurs for positive V_{BG}, where the positive charge on the back-gate repels the holes from the substrate to the semiconductor-insulator interface. Depletion occurs decreasing the voltage applied to the back-gate. The positive charge at the interface decreases and the semiconductor, near the interface, starts to be depleted of mobile carriers. Consequently, a negative charge, due to the ionized acceptor ions, is left in the space charge region. The voltage separating the accumulation and depletion regime is referred to as the flatband voltage, V_{FB}. Inversion occurs when decreasing even more the back-gate voltage, to negative values. The voltage that separates depletion and inversion is called threshold voltage, V_T. The depletion layer is still present and in addition to it an inversion layer of negative charges is formed. This inversion layer is due to the minority carriers that are attracted to the interface by the negative back-gate voltage. Accumulation, depletion and inversion layers are essentially capacitances, that must be taken into account in order to accurately model the semiconductor response to the change of bias conditions.

The depletion layer thickness is given by:

$$x_{d,max} = \sqrt{\frac{2\varepsilon_0\varepsilon_{Si}\phi_s}{qN_{A,D}}} \tag{5.5}$$

The depletion layer will reach it's maximum extension when the potential at the semiconductor/insulator interface, ϕ_s, is equal to $2\phi_F$; where $\phi_F = k_BT/q \cdot ln(N_{A,D}/n_i)$. In our case we have $\phi_F = 510$ mV. The depletion capacitance can then be written as:

$$C_{dep} = \varepsilon_0\varepsilon_{Si} \cdot \sqrt{\frac{qN_{A,D}}{2\varepsilon_0\varepsilon_{Si}\phi_s}} = \sqrt{\frac{qN_{A,D}\varepsilon_0\varepsilon_{Si}}{2\phi_s}} \tag{5.6}$$

By substituting for the maximum depletion layer thickness, we get a depletion capacitance $C_{dep} = 0.577\ \mu\text{F/cm}^2$, in agreement with the value of the semiconductor capacitance C_D (tab. 5.1) obtained from the fitting of the impedance measurements in fig. 5.14. This confirms that we need to include a C/G parallel in order to account for the semiconductor when it approaches the depletion/inversion working regions.

Having added this block we can have a look at the real and imaginary components of the admittance reported in fig. 5.16. Although the imaginary part of the admittance is well fitted by the model, it is evident from the real part of the admittance that the model fails to reproduce the measurements at low frequency.

To understand the low frequency response we started looking at different quantities, as reported in fig. 5.17. From the real part of the admittance multiplied by ω it is even more clear that the model is missing some component. In fact the measurements are smoother than the spectrum calculated from the circuit model.

By looking at fig. 5.16 and 5.17 we can see that the spectra covers from 4 to 6 orders

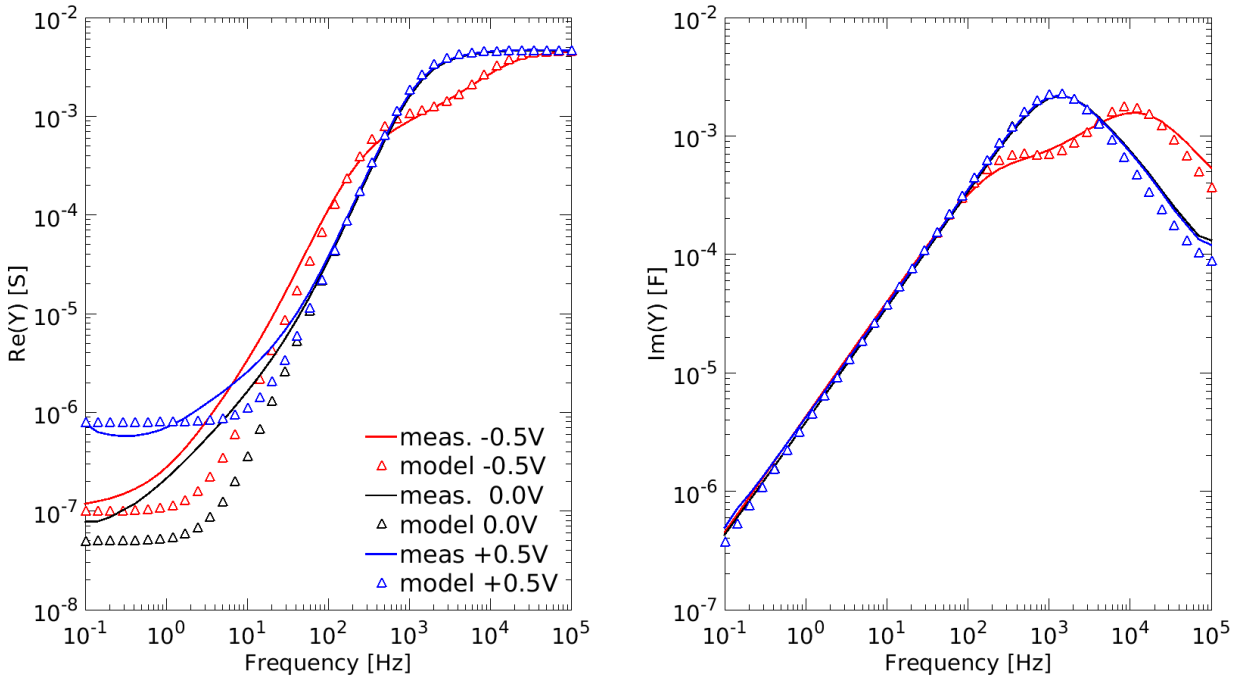

Figure 5.16: *Comparison between measurement on EIS capacitor and simulations with circuit model 1. Real (left) and imaginary (right) part of the admittance as a function of frequency.*

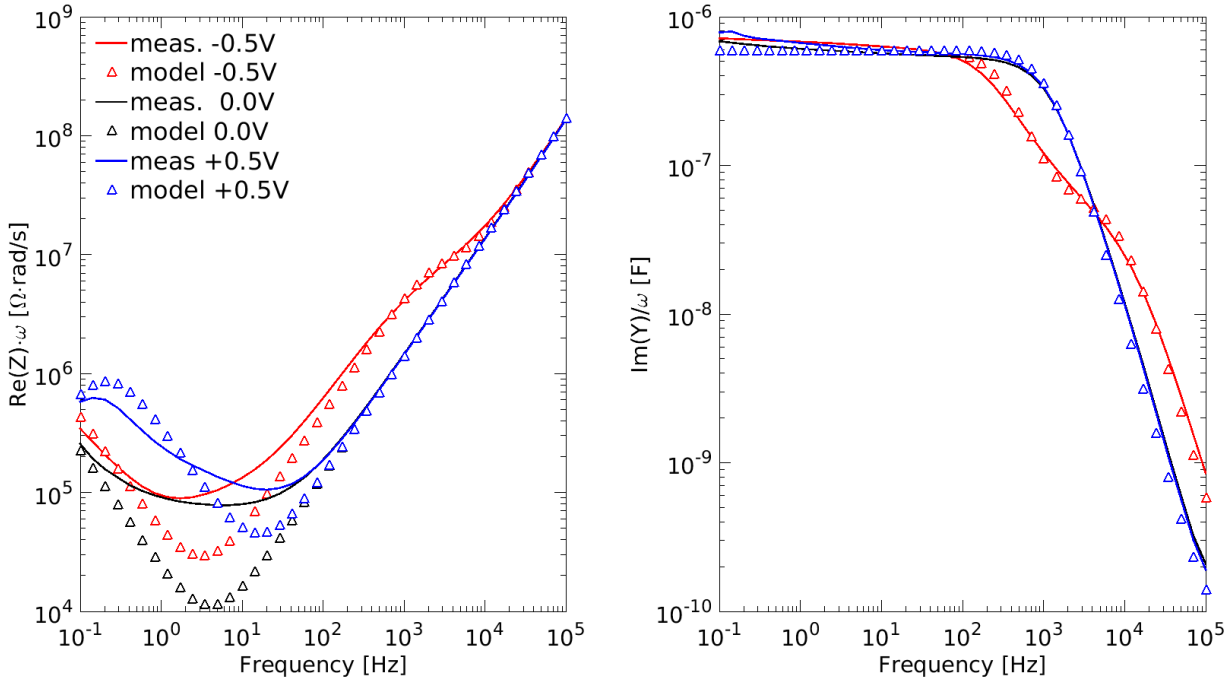

Figure 5.17: *Measurement fitting with circuit model 1. Real part of the impedance multiplied by ω (left) and imaginary part of the admittance divided by ω (right) as a function of frequency.*

of magnitude. In amplitude with such a large range we do not have the same view over the whole range of frequencies. For this reason we decided to reduce the range of the quantity plotted on the y-axis by considering two new quantities: the real part of the admittance divided by ω ($RY(\omega)$) and the imaginary part of the impedance multiplied by ω, with a minus sign ($IZ(\omega)$) to have always positive values, see fig. 5.18. Namely:

$$RY(\omega) = Re\{Y\}/\omega \tag{5.7}$$

$$IZ(\omega) = -Im\{Z\} \cdot \omega \tag{5.8}$$

These new quantities have unusual measurement units, but restrict the range of amplitude, and help gaining a better view of all the features of the spectrum and ultimately allows us to visualize the quality of the fitting at all frequencies with comparable degree of detail.

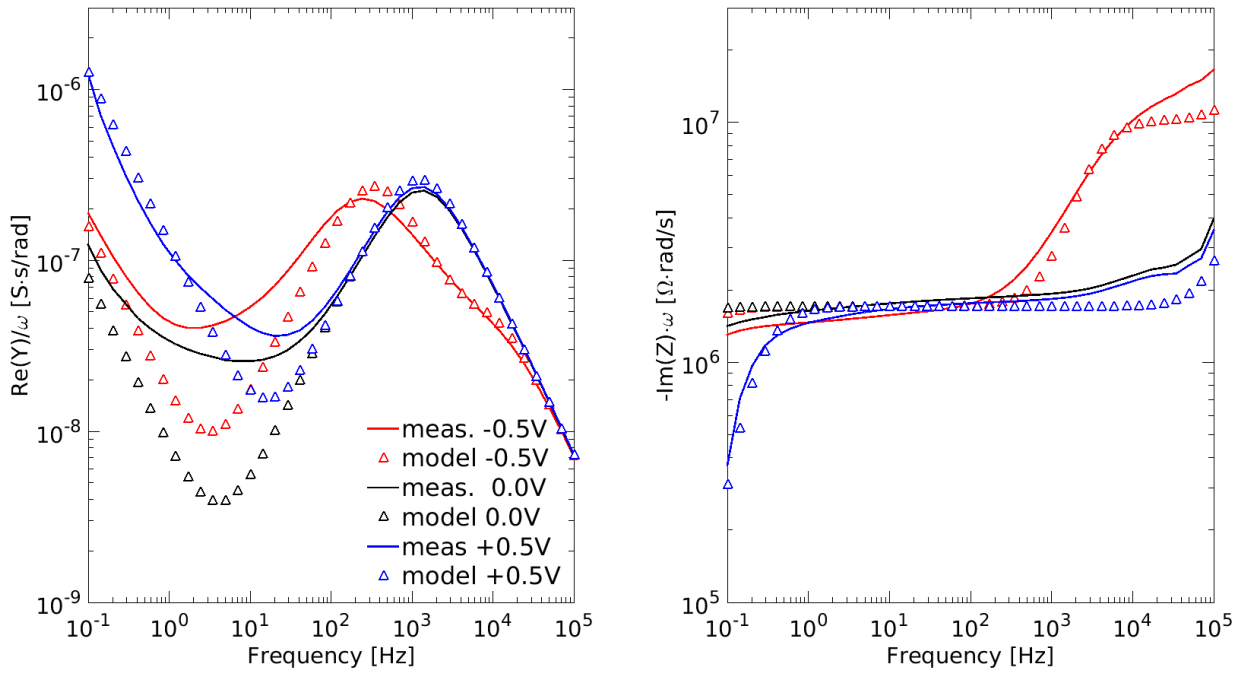

Figure 5.18: *Comparison between measurements and optimized circuit model 1. Real part of the admittance divided by ω (left) and imaginary part of the impedance multiplied by ω (right) as a function of frequency.*

By combining these two new quantities in a single plot (fig. 5.19), we get a very compact representation showing in a few order of magnitude all the features of the frequency response. From this last plot it is even more clear that the equivalent circuit model used so far must be improved (see fig. 5.19).

Looking into the electrochemistry literature [81, 22], one can easily find that it is of utmost importance to have a dedicated equivalent circuit element to describe the solid/liquid

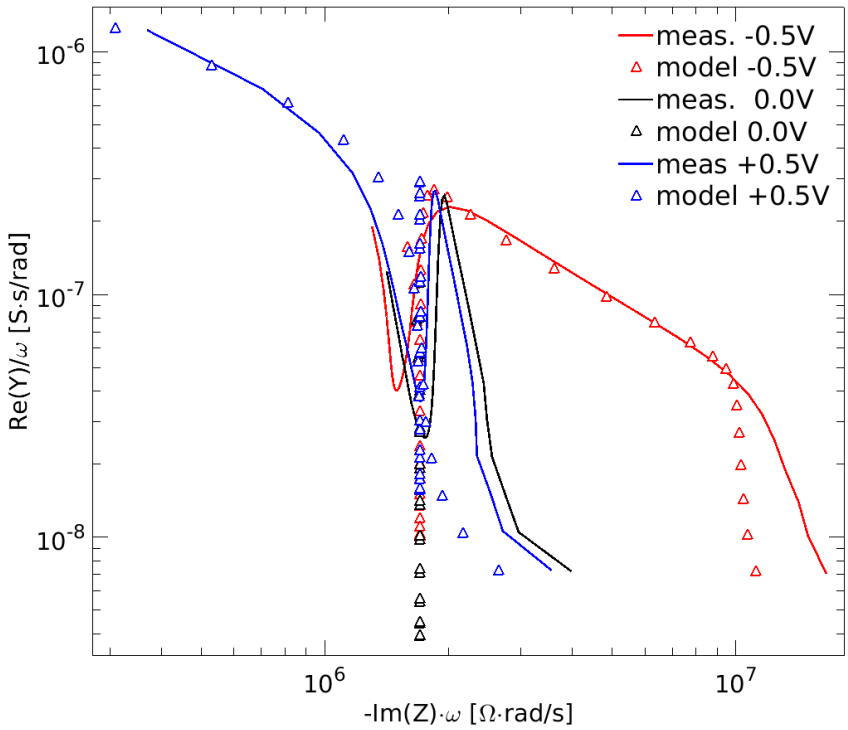

Figure 5.19: *Comparison between measurements and optimized circuit model 1. Real part of the admittance divided by ω (y-axis) as a function of the imaginary part of the impedance multiplied by ω (x-axis). Results obtained with the parameters in tab. 5.2.*

interface. We thus consider the extended circuit model in fig. 5.20, where the solid/liquid interface is represented with the parallel of a double layer capacitance (C_{DL}) and a dispersive constant phase element (Warburg admittance, Y_W)[26]

$$Y_W = Q_W \cdot (j\omega)^{1/2} = \frac{Q_W}{\sqrt{2}} \cdot (1+j)\sqrt{\omega} \tag{5.9}$$

where we used the fact that $(j)^{1/2} = e^{j\frac{\pi}{4}} = cos(\frac{\pi}{4}) + j \cdot sin(\frac{\pi}{4}) = \frac{\sqrt{2}}{2}(1+j)$. This element has a constant phase of $\pi/4$ at all frequencies and it is typically interpreted as the result of distributed diffusive processes next to the interface.

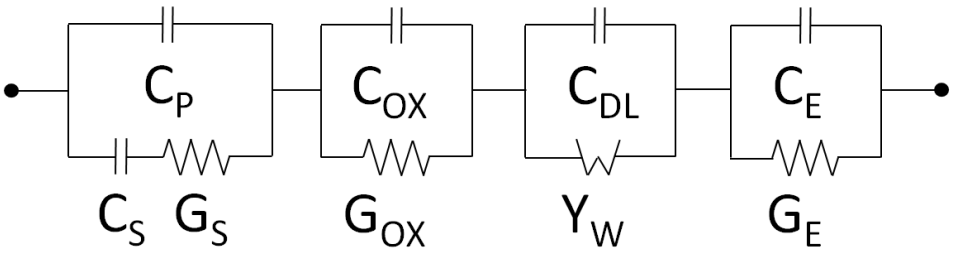

Figure 5.20: *Equivalent circuit model A.*

Considering that we now have six unknown elements, plus C_E and R_E (that we keep fixed), we decided to speed up the fitting procedure with the help of a dedicated Matlab script. To optimize the values of the six elements, representing the semiconductor, the insulator and the insulator/electrolyte interface, we consider the two following cost functions to be minimized:

$$f_{re} = 1 - \frac{RY_{cm}}{RY_{meas}}; \quad f_{im} = 1 - \frac{IZ_{cm}}{IZ_{meas}} \tag{5.10}$$

where the subscript *cm* stands for *circuit model*. We optimize, for each bias point separately, the error between the compact model and the measurements, considering both RY and IZ over the whole range of frequencies.

By implementing this minimization problem we get the optimized values for the six non-fixed circuit elements, reported in tab. 5.2. We remind that the electrolyte capacitance and conductance are left unchanged because the chamber is much thicker than the diffuse layer, thus they are considered as constants in the optimization process. We will initially neglect the substrate capacitance C_S that represents the inversion/accumulation capacitance, but we will show later that in some cases it is necessary to take it into account. C_P and G_S are respectively C_D and G_D of model 1 (5.13).

V_{BG}	C_{OX}	G_{OX}	C_{DL}	Q_W	C_P	G_S	C_E	G_E
V	μF/cm^2	μS/cm^2	μF/cm^2	$S \cdot \sqrt{s}$	μF/cm^2	S/cm^2	pF/cm^2	S/cm^2
+0.5	3.63	3.57	13.9	80.1	11.1	0.477	250	0.0244
+0.0	3.42	0.39	15.8	75.0	8.35	0.340	250	0.0244
-0.5	3.73	0.62	12.3	10.4	0.57	0.009	250	0.0244

Table 5.2: Model A, circuit elements values that minimize the functions in eq. 5.10 for all the frequency points. C_E and G_E are optimized for the TRIS electrolyte considered in this case.

The results of the optimization procedure, in terms of RY and IZ spectra, are reported in figures 5.21 and 5.22. It is clear that the introduction of the parallel $C_{DL}||Y_W$ and the minimization of the fitting functions, yield important results. Firstly because the spectra at the three different biases are very well reproduced by a unique equivalent circuit model topology at all bias points, considering the physically based origin of the circuit. Secondly, the optimized parameters are consistent with the analytical calculation presented before. In fact the insulator thickness varies between 0.93 nm ($C_{OX} = 3.73$ μF/cm^2) and 1.01 nm ($C_{OX} = 3.42$ μF/cm^2) compatible with the expected thickness of a native silicon dioxide ($t_{OX} \approx 1$ nm). C_P tends to the analytical value of maximum depletion capacitance calculated with eq. 5.6 when approaching the inversion region ($V_{BG} = +0.5$ V). C_{DL} is compatible with the range 10-40 μF/cm^2 double layer capacitance reported in literature [21, 81].

As a last example, we report in fig. 5.23 the impact of including C_S in the equivalent circuit model of the semiconductor. As expected, the effect of C_S is relevant around zero

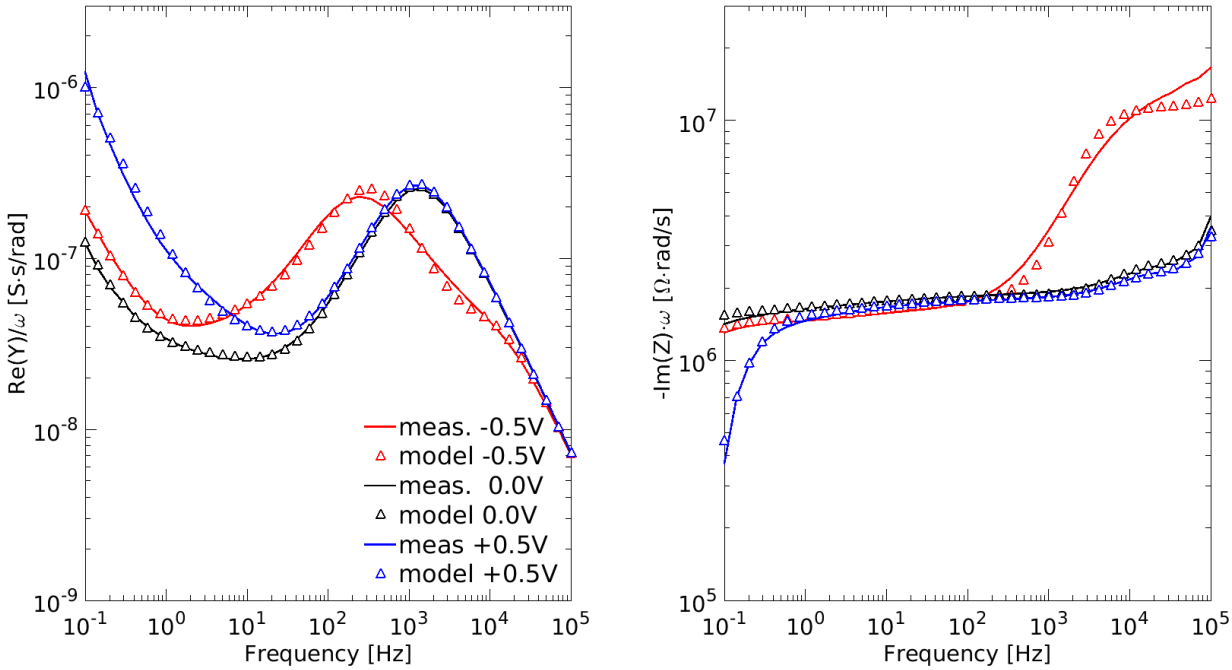

Figure 5.21: *Results of the optimization of model A elements expressed in terms of spectra of the RY and IZ functions defined in eqs 5.7, 5.7.*

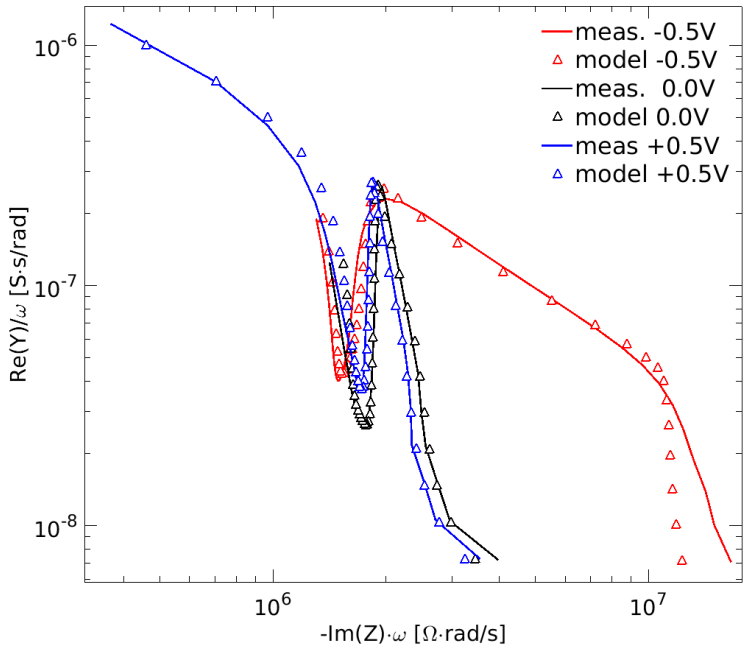

Figure 5.22: *Results of the optimization of model A elements expressed in terms of spectra of the RY and IZ functions defined in eqs 5.7, 5.7.*

bias, when the inversion/accumulation capacitance (C_S) is comparable with the depletion capacitance (C_P).

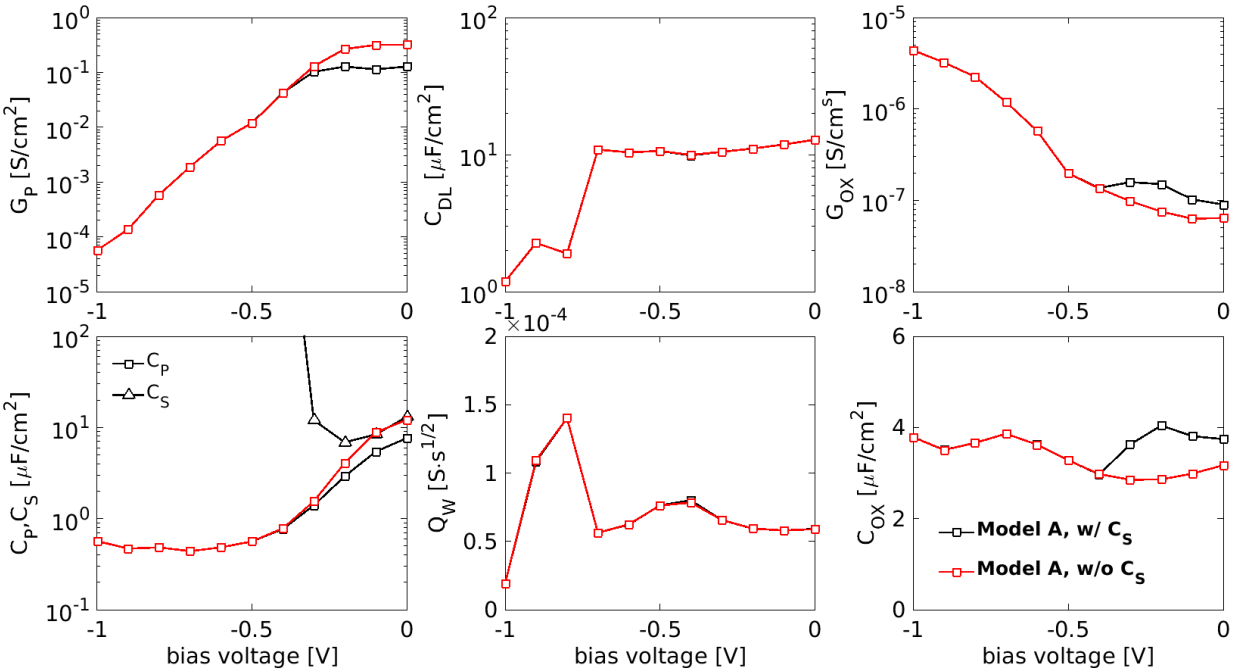

Figure 5.23: *Impact of C_S on the extracted values of the equivalent circuit model A parameters as a function of the bias.*

5.2.1 System response to TRIS, PBS and CH_3CN electrolytes

Now that an accurate circuit model and parameter extraction methodology has been established, we can proceed with the examination of the system response to a few electrolytes of common use during hybridization experiments. In particular, here we used the spectra measured with three different electrolyte solution as a test to verify and consolidate the equivalent circuit model presented in the previous section. The three electrolyte solutions are:

- *TRIS*: pH=7.55 @ 26.3 °C, 100 mM NaCl
- *PBS*: pH=7.2 @ 25.6 °C, 100 mM NaCl
- *CH_3CN*: pH=6.81 @ 21.9 °C, 100 mM Bu_4ClO_4

where Bu_4ClO_4 is composed by the tetrabutylammonium cation $(CH_3CH_2CH_2CH_2)_4N^+$ and the perchlorate anion ClO_4^-. Acetonitrile (CH_3CN) is typically used for electrochemical measurements, and since NaCl does not dissolve in it, the Bu_4ClO_4 has been used to reproduce physiological conditions (an high ionic strength of the buffer).

Fig. 5.24 shows the comparison between the measurements and the model predictions obtained with the equivalent circuit model A, for the three different buffered solutions. The fitting results are very good over the whole range of frequencies, meaning that model A is fully adequate to reproduce the experiments. Looking at these results we can make some useful considerations.

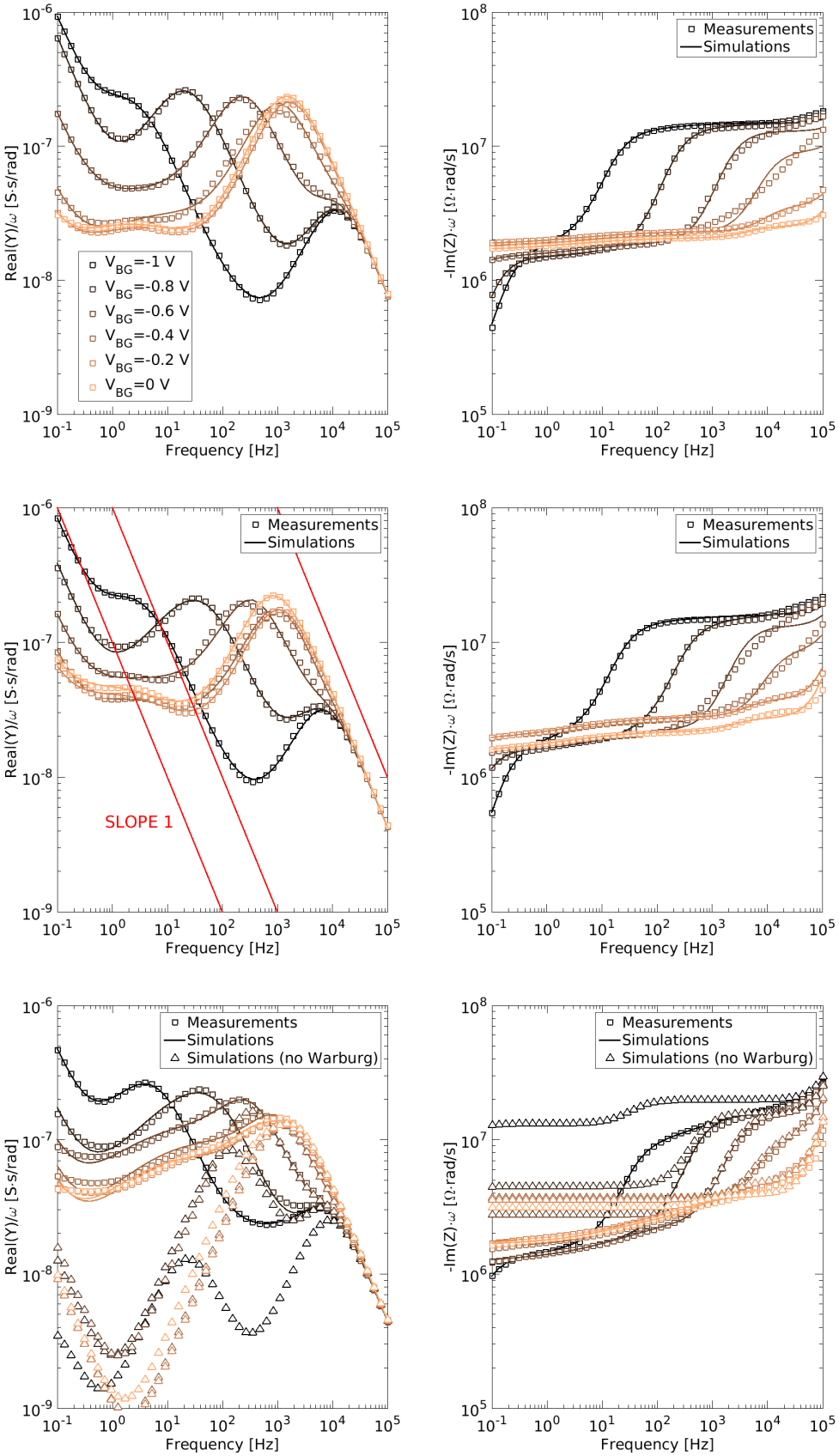

Figure 5.24: *Comparison between the three different buffers in terms of the RY and IZ function spectra, fitted with model A (including C_S). TRIS, PBS and CH_3CN from top to bottom.*

Let's consider an equivalent circuit model made the series connection of only capacitors/resistors blocks. In this case, the function IZ would have been flat with a number of amplitude levels given by the number of capacitors in the circuit model. In fact, in fig. 5.24 (CH_3CN buffer), we reported both the IZ and the RY functions, calculated without the dispersive Warburg element.

Concerning the function IZ, a non-flat behaviour is an indication of the presence of a dispersive element, frequency dependent capacitance in this case (compare triangles and squares in fig. 5.24, bottom right). Similarly, trends different from the slope 1 in the function RY (see fig. 5.24), indicate a dispersive conductance.

These frequency dependent behaviours, clearly visible in the RY and IZ functions of the CH_3CN buffer, reveal the presence of a dispersive Warburg element, typically indicating distributed or diffusion processes.

Fig. 5.25 reports the extracted model parameters as a function of bias. Several interesting observation can be made on these results. Firstly, it is confirmed that C_S has an impact only when $V_{BG} \approx 0$ V, i.e. close to inversion conditions. Secondly, C_{OX} is rather constant and independent of the electrolyte, as expected. Similarly, G_{OX}, C_P, G_P and Q_W show consistent results independently of the buffer composition. The double layer capacitance instead needs a separate analysis. By comparing the values of the double layer capacitance we see that the extracted C_{DL} values are similar for TRIS and PBS solvents, while C_{DL} is lower by a factor of $2 \div 3$ for the CH_3CN solvent.

This observation con be explained reminding that the three solutions have approximately the same salt concentration but the permittivities of TRIS and PBS are close the permittivity of water, $\approx$80 [83, 82], the permittivity of CH_3CN is $\approx$37 [144]. Furthermore this permittivity is presumably lowered by the presence of the Bu_4ClO_4 [145], confirming the extracted C_{DL} values reported in fig. 5.25.

These results suggest that the developed model is adequate to represent the physical system over a brad range of conditions and that no considered cross-coupling between the extracted parameters values is present when the electrolyte composition is changed.

5.2.2 Comparison between native and piranha treated SiO_2

In this section are compared two reference systems, one is SiO_2 native and the other has been cleaned with a Piranha treatment. The comparison is based on the analysis of the fitted parameters as a function of the applied bias voltage, fig. 5.26, in order to analyze the impact of the Piranha treatment on the native oxide electrical characteristics. Curves with square symbols (black and red curves) show the results of the extraction procedure obtained by optimizing all circuit components. Curves with triangle symbols (green and blue curves) show the results of the fitting procedure obtained by optimizing all circuit components, except C_{OX}, C_E and G_E that are kept fixed.

The first result that stands out regards the insulator characteristics. The oxide capacitance in the case of native oxide is $\sim$2.3 μF/cm^2 that corresponds to 1.50 nm, while the

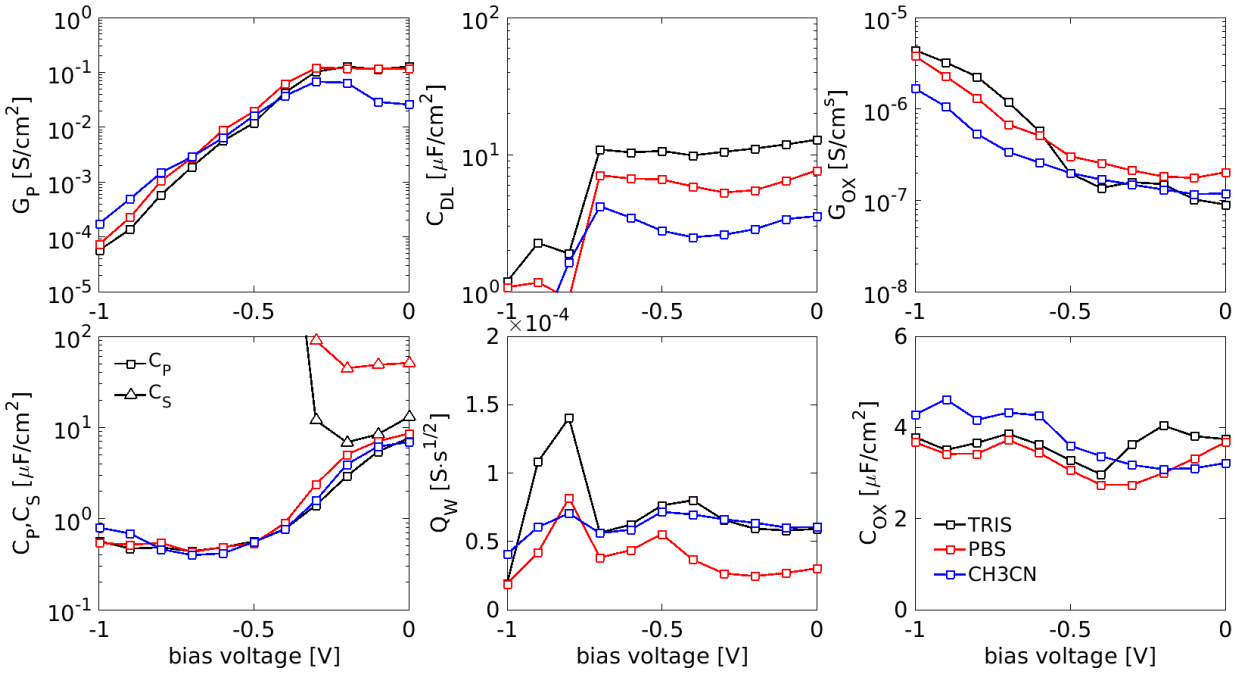

Figure 5.25: *Extracted values of the equivalent circuit model A parameters as a function of the bias.*

after the Piranha treatment the capacitance increase to ∼4.2 μF/cm^2 that corresponds to a thinner oxide of about 0.82 nm. The oxide conductance is compatible with the decrease in the oxide thickness, in fact the Piranha treated oxide is more conductive, meaning an increase in the leakage current.

The interface elements, C_{DL} and Q_W, are similar in all the four cases, meaning that the interface features are only slightly affected by the different treatments.

Finally, the semiconductor shows a shift towards positive voltages of the depletion capacitance (C_P) after the Piranha treatment. This can be interpreted as a positive shift of the flat band voltage V_{FB}, compatible with the decrease of the oxide layer thickness ($V_{FB} \propto -Q_i/C_{OX}$, where Q_i is the charge located at the silicon/insulator interface)

These results confirm the ability of the proposed model to highlight physically meaningful changes of the properties of the system under study without undesired cross interference between the model parameters.

5.2.3 DNA and PNA binding and detection

Having demonstrated the robustness and solid physical basis of the proposed model, this paragraph we explore the impact of two PNA configurations on the impedance spectroscopy response. A self-assembled-monolayer of organophosphonate (SAMP) [141] is initially deposited on the native oxide surface. The SAMP is consequently modified with a apposite maleimido-linkers [7] that have specific properties for the immobilization of

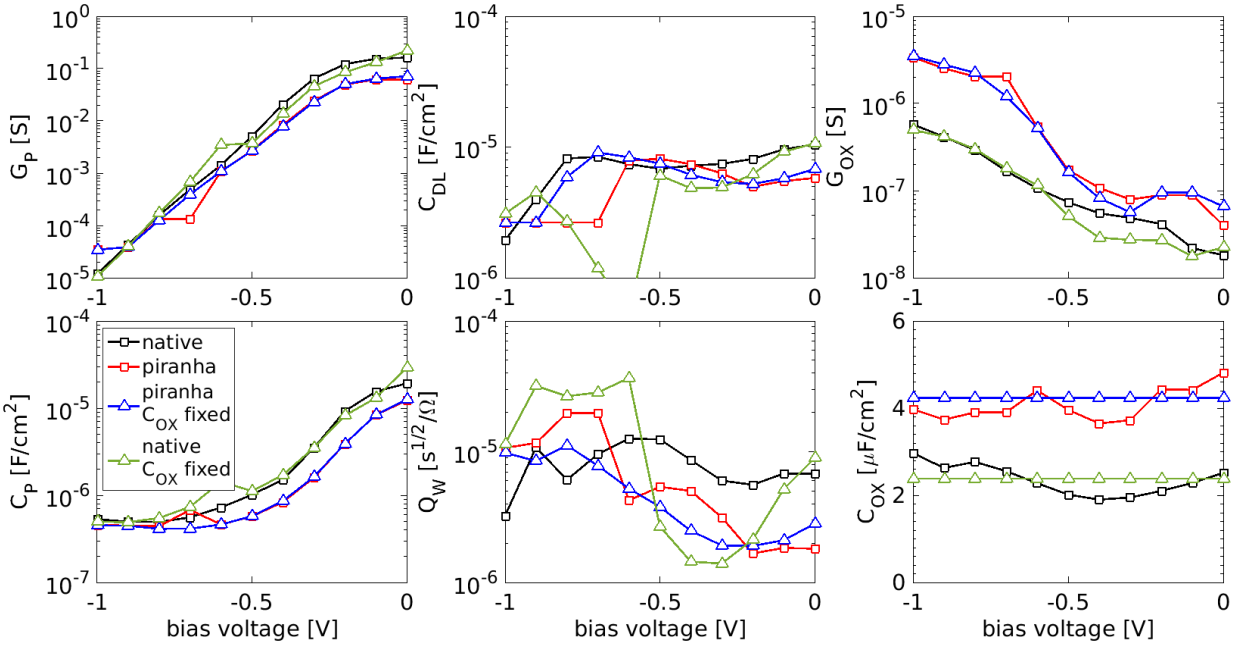

Figure 5.26: *Extracted values of the equivalent circuit model A parameters as a function of the bias. Square symbols (black and red curves) show the results of the fitting procedure obtained by optimizing all circuit components. Triangle symbols (green and blue curves) show the results of the fitting procedure obtained by optimizing all circuit components, except C_{OX}.*

PNA molecules. After these functionalization steps, two types of PNAs have been used as binding sites for DNA strands, in two separate experiments. The first, PNA1, is covalently bounded to the linker at three specific points while the second, PNA2, is only connected at the end of the backbone. Thus the PNA1 lies on the surface in an horizontal position, while PNA2 is in vertical position. This was unambiguously proven by the TU Munich group with physico-chemical analysis and characterizations.

We extracted equivalent circuit elements with the same optimization procedure adopted in the previous sections. We fixed the value of C_{OX} since we expect no changes in the oxide layer capacitance. Fig. 5.28 shows the extracted values of the equivalent circuit parameters as a function of the bias. The figure allows us to compare two different situations: PNA immobilized on the surface without the presence of DNA strands (labelled as PNA1 and PNA2) and PNA/DNA hybridized on the surface (labelled as PNA1+DNA and PNA2+DNA). For each situation, both PNA1 and PNA2 configuration examined, we compare these four curves with the reference system (native SiO_2).

For all the systems we used the same equivalent circuit model topology and consistently with previous results in sec. 5.2.2 we kept C_{OX}, C_E and G_E fixed. Therefore any differences in the physico-chemical status of the system, if there exist, will be reflected on the appropriate circuit elements. Thus enabling the identification of the part of the system affected by the PNA/DNA strands.

We start by comparing the reference and the systems with functionalization. The

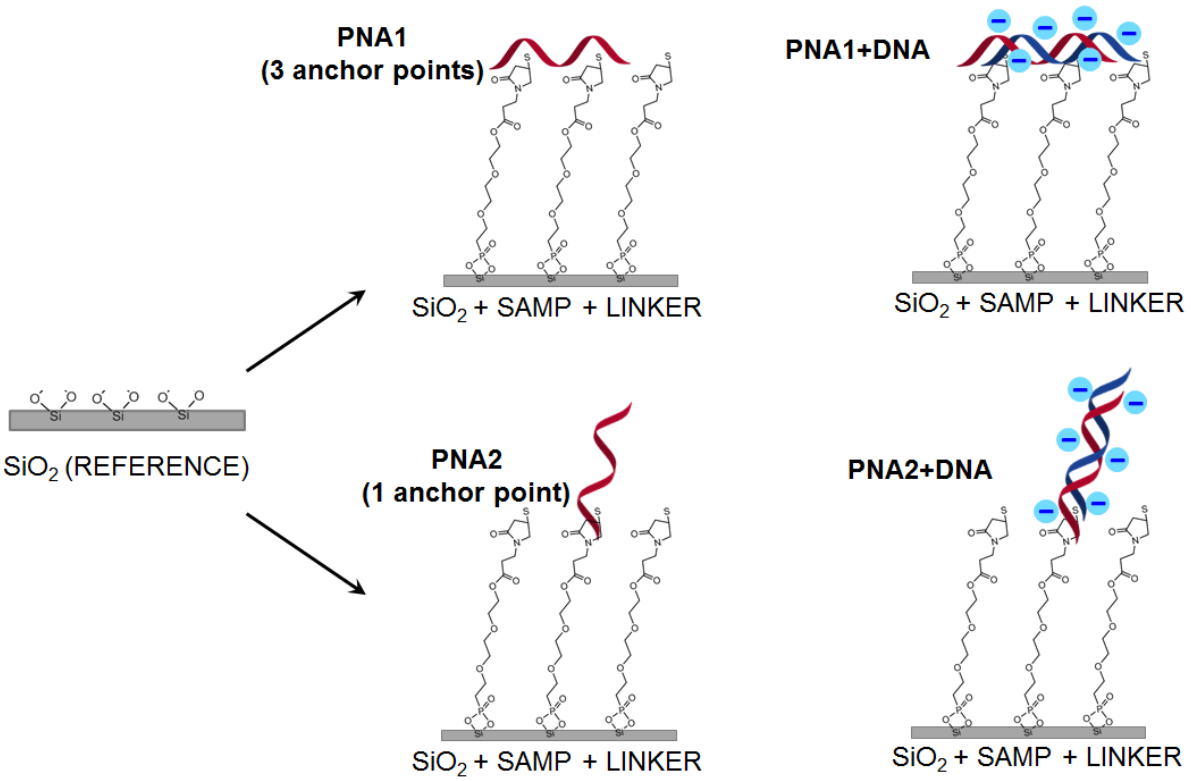

Figure 5.27: *Sketch of the five analyzed systems. The reference system is functionalized with maleimdo-linker terminated self assembled monolayer of organophosphonates (SAMP) for the immobilization of PNA molecules. Two types of PNA have been studied: PNA1 (top) has three anchor points to bind to the linker, while PNA2 (bottom) one has only one anchor point. DNA is finally injected in solution for PNA/DNA hybridization measurements.*

functionalizations (SAMP, maleimdo-linkers) combined with the immobilized PNA, have interesting and relatively large effects on both the semiconductor ($C_P||G_P$) and the interface ($Q_W||C_{DL}$). The oxide conductance is also affected. It is larger at low biases and lower at negative biases, with respect to the reference case. Thus, the oxide insulating properties in DC are enhanced at large negative biases but reduced in the other range, which suggest a modification of the energy levels that assist the tunneling through the oxide [146].

We now consider the systems with the hybridized DNA, namely: PNA1+cDNA, PNA2+cDNA, PNA1 and PNA2. On the semiconductor side, the conductance is remarkably affected by the PNA configurations being either horizontal or vertical, while the presence of the DNA has no effect. These results suggest the fabrication of a transistor structure in the semiconductor substrate, in order to monitor the surface conductance and sense the hybridization process, may not yield the desired results, at least at low substrate potential. The most interesting results are concentrated on the interface elements C_{DL} and Q_W. Measurements on PNA2 show smaller values of double layer capacitance and Warburg admittance, with respect to PNA1, compatible with an increase of the double layer thickness due to the vertical position of the PNA strands. A small but non negligible

sensitivity to the presence of the DNA is also visible. These results are also compatible with the the results of 3D simulations presented in [113] that compares the capacitive response of a nanoelectrode at 500 kHz to PNA/DNA strands with different orientations in physiological solution. The study, in fact, reports a larger capacitive response for a vertical configuration compared to horizontally immobilized strands.

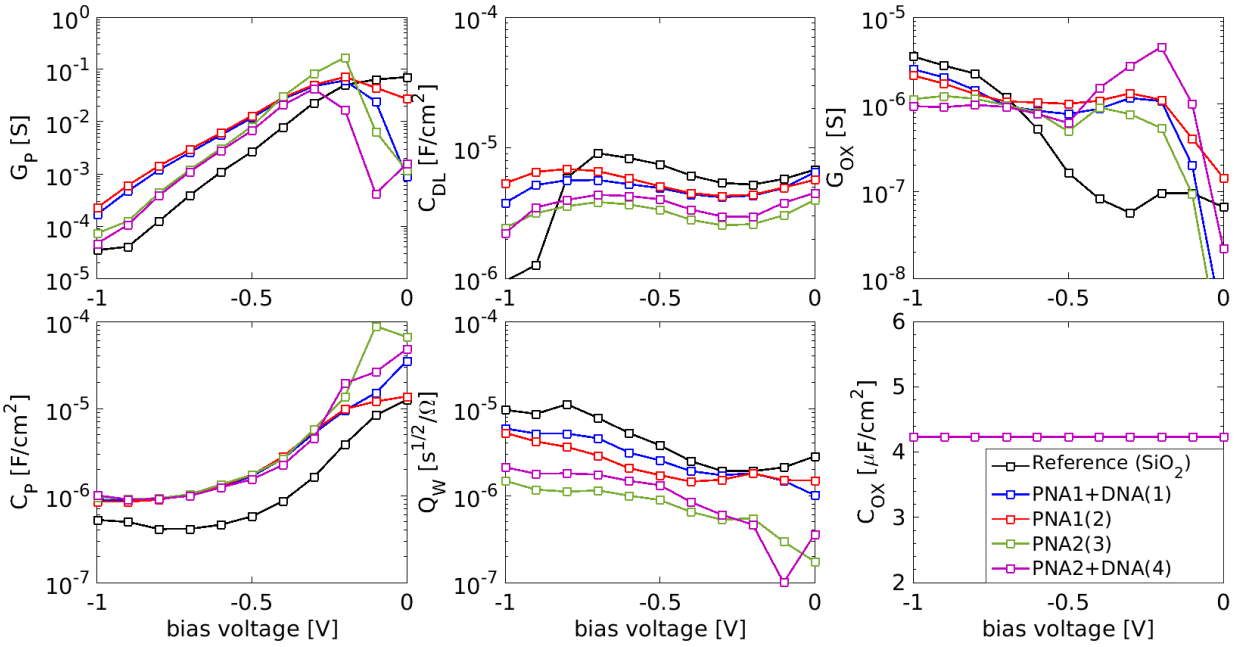

Figure 5.28: *Extracted values of the equivalent circuit model A parameters as a function of the bias.*

In view of the realization of a full sensor circuit it is interesting to consider in more detail the changes of the semiconductor equivalent circuit parameters induced by the different linkers, PNA and hybridization configurations. Consequently, we focus our attention on the C_P and G_P dependence on configuration and bias reported in fig. 5.28. The data proves a sensitivity of G_P to the PNA configuration when the bias voltage is in depletion or accumulation regardless of the PNA being hybridized with a complementary DNA strand or not. Both PNA configurations leads to an increase of the conductance with respect to the reference SiO_2 case, but the increase is larger if the PNA as an horizontal configuration (PNA1). Such increase is up to a factor of C_{OX} at low V_{BG} and suggests the necessity to explore the parameters also for positive bias voltages. The capacitance C_P is instead only sensitive to the presence of the PNA and not its orientation or hybridization state.

5.2.4 Summary

Section 5.2 is fully devoted to the analysis of impedimetric measurements performed on EIS samples. It is a useful model system to study the effect of functionalization layers on

the impedimetric response. The measurements cover a broad range of frequencies (from 0.1 Hz to 100 kHz) and a wide range of applied back gate voltages (mostly depletion and accumulation of the substrate).

We developed a modular and compact electrical model that accurately reproduces the frequency response of the EIS reference system composed by semiconductor, native oxide and electrolyte, over the whole range of applied voltages (from accumulation to inversion). The model is composed by parallel $G||C$ cells that describe separately the semiconductor, the native oxide and the electrolyte and an additional double layer capacitance C_{DL} and the Warburg admittance Y_W cell to describe the solid/liquid interface. We developed the compact model starting from analytical and physical considerations and we then completed the tuning of each circuit element by implementing an optimization process that minimizes the error function between the model and the measurements. The model has a sound physical basis, validated on measurements with three different buffer solutions and two oxide preparation treatments. Therefore it could support the analysis of impedance measurements of PNA/DNA hybridization performed with the EIS samples.

We analyzed the impact of the PNA orientation on the extracted circuit elements. A large impact was observed on the circuit elements describing the interface and to a smaller extent on those representing the semiconductor.

The results suggest that vertically immobilized PNAs produce a larger signal, in terms of capacitance variation, with respect to horizontally immobilized PNA. This result is perfectly consistent with full 3D numerical simulations based on the PB-PNP modeling framework as reported in [113] and indirectly confirm the usefulness and adequacy of such models for the interpretation of experiments.

Chapter 6

Conclusions

In this thesis we have scrutinized the use of a variety of nanoscale devices for pH and microparticle sensing via conductivity measures (nanoribbon and FinFETs) and impedance spectroscopy in the frequency range $0.1 \div 10^6$ Hz (nanoribbons and EIS capacitors). The experimental activity has been conducted in part at University of Udine and during a stage at EPFL Lausanne (NR [37], FinFETs[20]). Additional data on capacitors was provided by prof. Cattani-Scholz (TU Munich). The analysis and interpretation of the experimental results share the need to develop numerical models including pH dependent charges at the interfaces between the electrolyte and the sensor or the analyte; in particular, the build-up of site-binding charge at various dielectric/electrolyte interfaces has been considered in DC, AC and transient conditions.

The research activity focused on three main independent areas.

- the modeling and characterization of nanoribbon-based ion-sensitive field-effect-transistors (ISFETs) in the DC, transient and AC domains with experiments performed in dry and liquid electrolyte environments, and corresponding simulations performed with commercial TCAD and in-house developed tools. NRs were also used as microparticle detectors in AC small-signal impedance spectroscopy measurements and an original quasi-3D model was developed to understand the measured results.

- the analysis of AC measurements performed with EIS capacitors, with the aim of interpreting the response to PNA/DNA hybridization data via numerical simulations and the development of a robust physically-based modular an electrical compact model;

- the development of a new 1D simulation tool and the enhancement of general purpose 3D ones (ENBIOS and TCAD) to include surface electrochemistry reactions in DC, AC and transient conditions and the porting of those tools on the nanoHUB platform.

The measurements on the NRs were made at the University of Udine (dry environment) and during a stage at the CLSE laboratory at EPFL (Lausanne, CH, liquid environment).

The measurements on EIS samples were performed by Prof. Cattani-Scholz group at the Walter Schottky Institute in Munich (TUM).

As regards the first and third activity, the new 1D model of the pH-sensitivity in DC conditions and the extension of the TCAD[102] (with surface reactions specifically implemented [96]) allowed us to finely reproduce the experimental voltage (at fixed drain-source current) and current (at fixed fluid gate voltage) pH sensitivities of samples with SiO_2 dielectric, gain insight on the NR operation in dry and wet environments, explore the impact of t_{OX} on the stability of the measures and highlight improvements of the pH sensitivity with the use of high-k dielectrics [19].

In particular, measurements on nanoribbon ISFETs in air and liquid environments have been used to calibrate and verify a TCAD model for nanoribbon pH sensors. The simulations revealed remarkably different current density distributions and width scaling properties of these devices in the two environments and provide new insight on the bias, width and pH-dependence of the pH sensitivity of nanoribbons.

Combined with a comprehensive analysis of noise measures in NRs operating in liquid environment, the sensitivity studies allowed us to evaluate the smallest detectable pH change of the NR devices which was estimated in an outstanding 0.8 ‰ pH resolution per micron square footprint.

As regards transient and AC operations, we also developed a quasi-3D model for the AC response of NRs in liquid environment which consists in a combination of 2D simulations and compact circuit elements (R and C). The model is able to finely reproduce the response of bare NRs, and to study the sensitivity of NRs to dielectric microparticles in solution [97, 112] (sedimented on the device surface area), which represent an useful model system for the detection of various analytes.

A careful analysis of the experimental results obtained with the quasi-3D model indicates that the portion of interconnects in contact to the electrolyte, as opposed to the NR area, dominates the response at moderately high frequency, in spite of the top oxide being much thicker than the NR gate oxide. This result highlights the need to optimize the device design and reduce the interconnects area wetted by the liquid. Alternatively to largely increase the thickness of the passivation in order to achieve good sensitivity. Furthermore we observe that the NR admittance response to micron-sized beads can be qualitatively (sign) and quantitatively (magnitude) reproduced only by accounting for a residual surface charge on the oxide and even more important on the beads. These results underline the usefulness and need of accurate models for quantitative understanding of sensing experiments with NR devices.

As regards the second area of investigation, we developed a modular electrical compact model of the EIS structure by representing each of its layers as a separate cell, composed by a G-C parallel. An additional cell with a dispersive Warburg element turned out to be necessary to represent the insulator/electrolyte interface. A dedicated parameter

extraction procedure was developed to identify all circuit element values and their dependence on bias. The accuracy of the model was tested first against measures in different electrolyte environments and with different sample fabrication techniques. The compact model allowed us to analyze the electrical properties of each cell and to find out useful indications for a realization of a full sensor for the detection of DNA/PNA. The results put in evidence the ability of the studied system to induce a small but measurable changes of the substrate conductance induced by different PNA orientations and hybridization processes. These results confirmed previous analysis based on 3D simulations in the PB-PNP formalism.

As regards specifically the third area of investigation, besides model development, we invested efforts in making the results of our research available to the academic education and scientific community worldwide. To this end we published two simulation tools on the nanoHUB.org website, by using the Rappture GUI provided by the nanoHUB platform. The tools are based on ENBIOS, and include the surface reaction models which proved useful for the interpretation of the experiments during our research. These tools, named ENBIOS-1D Lab [109] and ENBIOS-2D Lab [110], are a useful platform for students to familiarize with practical examples on EIS and ISFET devices, respectively. They already received widespread appreciation with more than 50 users and 500 simulation runs worldwide.

Author publications

- S. Rigante, P. Scarbolo, D. Bouvet, M. Wipf, A. Tarasov, K. Bedner and A.M. Ionescu, "High-k dielectric FinFETs towards sensing integrated circuits," ULIS 2013, doi: 10.1109/ULIS.2013.6523494
- F. Pittino, P. Palestri, P. Scarbolo, D. Esseni and L. Selmi, "Models for the use of commercial TCAD in the analysis of silicon-based integrated biosensors," SSE, 2014, doi: 10.1016/j.sse.2014.04.011
- S. Rigante, P. Scarbolo, D. Bouvet, M. Wipf, K. Bedner, A.M. Ionescu, "Technological development of high-k dielectric FinFETs for liquid environment," SSE, 2014, doi: 10.1016/j.sse.2014.04.012
- F. Pittino, P. Scarbolo, F. Widdershoven and L. Selmi, "Derivation and Numerical Verification of a Compact Analytical Model for the AC Admittance Response of Nanoelectrodes, Suitable for the Analysis and Optimization of Impedance Biosensors," IEEE TNANO, 2015, doi: 10.1109/TNANO.2015.2434106
- S. Rigante, P. Scarbolo, M. Wipf, R.L. Stoop, K. Bedner, E. Buitrago, A. Bazigos, D. Bouvet, M. Calame, C. Schönenberger, and A.M. Ionescu, "Sensing with Advanced Computing Technology: Fin Field-Effect Transistors with High-k Gate Stack on Bulk Silicon," ACS Nano, 2015, doi: 10.1021/nn5064216
- P. Scarbolo, E. Accastelli, F. Pittino, T. Ernst, C. Guiducci and L. Selmi, "Characterization and modelling of differential sensitivity of nanoribbon-based pH-sensors," Solid-State Sensors, Actuators and Microsystems, 2015, doi: 10.1109/TRANSDUCERS.2015.7181394
- E. Accastelli, P. Scarbolo, T. Ernst, P. Palestri, L. Selmi and C. Guiducci, "Multi-Wire Tri-Gate Silicon Nanowires Reaching Milli-pH Unit Resolution in One Micron Square Footprint," Biosensors, 2016, doi: 10.3390/bios6010009
- P. Scarbolo, E. Accastelli, T. Ernst, C. Guiducci and L. Selmi, "Analysis of Dielectric Microbead Detection by Impedance Spectroscopy with Nanoribbons," IEEE NANO, 2016, doi: 10.1109/NANO.2016.7751538
- F. Pittino, P. Scarbolo, M. Dalla Longa, A. Cossettini, and L. Selmi, "ENBIOS-1D Lab," April 2016, doi: 10.4231/D3GX44W13
- A. Hoxha, P. Scarbolo, A. Cossettini, F. Pittino, and L. Selmi, "ENBIOS-2D Lab," October 2016, doi: 10.4231/D3V11VM7D

Bibliography

[1] "Global health expenditure."

[2] J. K. Rosenstein, S. G. Lemay, and K. L. Shepard, "Single-molecule bioelectronics," *Wiley Interdisciplinary Reviews: Nanomedicine and Nanobiotechnology*, vol. 7, no. 4, pp. 475–493, 2015.

[3] L. Su, W. Jia, C. Hou, and Y. Lei, "Microbial biosensors: a review," *Biosensors and Bioelectronics*, vol. 26, no. 5, pp. 1788–1799, 2011.

[4] C. Berggren, B. Bjarnason, and G. Johansson, "Capacitive biosensors," *Electroanalysis*, vol. 13, no. 3, pp. 173–180, 2001.

[5] C. Menzel, T. Lerch, T. Scheper, and K. Schügerl, "Development of biosensors based on an electrolyte isolator semiconductor (eis)-capacitor structure and their application for process monitoring. part i. development of the biosensors and their characterization," *Analytica chimica acta*, vol. 317, no. 1-3, pp. 259–264, 1995.

[6] C. Ziegler, "Cell-based biosensors," *Fresenius' journal of analytical chemistry*, vol. 366, no. 6-7, pp. 552–559, 2000.

[7] Cattani-Scholz, A. and Pedone, D. and Dubey, M. and Neppl, S. and Nickel, B. and Feulner, P. and Schwartz, J. and Abstreiter, G. and Tornow, M., "Organophosphonate-based PNA-functionalization of silicon nanowires for label-free DNA detection," *ACS nano*, vol. 2, no. 8, pp. 1653–1660, 2008.

[8] Abouzar, M. H. and Moritz, W. and Schöning, M. J. and Poghossian, A., "Capacitance–voltage and impedance-spectroscopy characteristics of nanoplate EISOI capacitors," *Physica Status Solidi (a)*, vol. 208, no. 6, pp. 1327–1332, 2011.

[9] N. Lago, A. Cester, N. Wrachien, M. Natali, S. D. Quiroga, S. Bonetti, M. Barbato, A. Rizzo, E. Benvenuti, V. Benfenati, *et al.*, "A physical-based equivalent circuit model for an organic/electrolyte interface," *Organic Electronics*, vol. 35, pp. 176–185, 2016.

[10] F. Widdershoven, D. V. Steenwinckel, J. Überfeld, T. Merelle, H. Suy, F. Jedema, R. Hoofman, C. Tak, A. Sedzin, B. Cobelens, E. Sterckx, R. van der Werf, K. Verheyden, M. Kengen, F. Swartjes, and F. Frederix, "CMOS Biosensor Platform," *Proceedings IEDM*, pp. 816–819, 2010.

[11] C. Laborde, F. Pittino, H. A. Verhoeven, S. G. Lemay, L. Selmi, M. A. Jongsma, and F. P. Widdershoven, "Real-time imaging of microparticles and living cells with CMOS nanocapacitor arrays," *Nature Nanotechnology*, vol. 10, pp. 791–795, 2015.

[12] A. Aghaei, M. R. M. Hosseini, and M. Najafi, "A novel capacitive biosensor for cholesterol assay that uses an electropolymerized molecularly imprinted polymer," *Electrochimica acta*, vol. 55, no. 5, pp. 1503–1508, 2010.

[13] A. Qureshi, J. H. Niazi, S. Kallempudi, and Y. Gurbuz, "Label-free capacitive biosensor for sensitive detection of multiple biomarkers using gold interdigitated capacitor arrays," *Biosensors and Bioelectronics*, vol. 25, no. 10, pp. 2318–2323, 2010.

[14] N. Couniot, A. Afzalian, N. Van Overstraeten-Schlögel, L. Francis, and D. Flandre, "Capacitive biosensing of bacterial cells: analytical model and numerical simulations," *Sensors and Actuators B: Chemical*, vol. 211, pp. 428–438, 2015.

[15] P. Bergveld, "Development of an Ion-Sensitive Solid-State Device for Neurophysiological Measurements," *Biomedical Engineering, IEEE Transactions on*, vol. 17, pp. 70–71, Jan 1970.

[16] F. Patolsky and C. M. Lieber, "Nanowire nanosensors," *Materials today*, vol. 8, no. 4, pp. 20–28, 2005.

[17] A. Tarasov, W. Fu, O. Knopfmacher, J. Brunner, M. Calame, and C. Schönenberger, "Signal-to-noise ratio in dual-gated silicon nanoribbon field-effect sensors," *arXiv preprint arXiv:1010.3169*, 2010.

[18] E. Accastelli, G. Cappi, J. Buckley, T. Ernst, and C. Guiducci, "Comparison between front- and back-gating of Silicon Nanoribbons in real-time sensing experiments," in *Proceedings IEEE Nanotechnology Conference (IEEE-NANO)*, pp. 517–520, 2013.

[19] P. Scarbolo, E. Accastelli, F. Pittino, T. Ernst, C. Guiducci, and L. Selmi, "Characterization and modelling of differential sensitivity of nanoribbon-based pH-sensors," in *Solid-State Sensors, Actuators and Microsystems (TRANSDUCERS)*, pp. 2188–2191, 2015.

[20] Rigante, S. and Scarbolo, P. and Wipf, M. and Stoop, R. L and Bedner, K. and Buitrago, E. and Bazigos, A. and Bouvet, D. and Calame, M. and Schönenberger, C. and others, "Sensing with Advanced Computing Technology: Fin Field-Effect Transistors with High-k Gate Stack on Bulk Silicon," *ACS nano*, vol. 9, no. 5, pp. 4872–4881, 2015.

[21] Bousse, L. and Bergveld, P., "On the impedance of the silicon dioxide/electrolyte interface," *Journal of Electroanalytical Chemistry and Interfacial Electrochemistry*, vol. 152, no. 1, pp. 25–39, 1983.

[22] Lasia, A., "Electrochemical impedance spectroscopy and its applications," in *Modern aspects of electrochemistry*, pp. 143–248, Springer, 2002.

[23] E. Katz and I. Willner, "Probing biomolecular interactions at conductive and semiconductive surfaces by impedance spectroscopy: routes to impedimetric immunosensors, DNA-sensors, and enzyme biosensors," *Electroanalysis*, vol. 15, no. 11, pp. 913–947, 2003.

[24] N. Couniot and T. Vanzieleghem and J. Rasson and N. Van Overstraeten-Schlögel and O. Poncelet and J. Mahillon and L. Francis and D. Flandre, "Lytic enzymes as selectivity means for label-free, microfluidic and impedimetric detection of whole-cell bacteria using ALD-Al_2O_3 passivated microelectrodes," *Biosensors & bioelectronics*, 2014.

[25] F. Pittino and L. Selmi, "A technique to model the AC response of diffuse layers at electrode/electrolyte interfaces and to efficiently simulate impedimetric biosensor arrays for many analyte configurations," in *Proc. SISPAD*, pp. 353–356, 2014.

[26] Carminati, M. and Ferrari, G. and Bianchi, D. and Sampietro, M., "Impedance Spectroscopy for Biosensing: Circuits and Applications," 2015.

[27] K. B. Oldham, "A Gouy–Chapman–Stern model of the double layer at a (metal)/(ionic liquid) interface," *Journal of Electroanalytical Chemistry*, vol. 613, no. 2, pp. 131–138, 2008.

[28] P. A. Hammond, D. Ali, and D. R. S. Cumming, "Design of a single-chip pH sensor using a conventional 0.6-μm CMOS process," *IEEE Sensors Journal*, vol. 4, no. 6, pp. 706–712, 2004.

[29] L. Shepherd and C. Toumazou, "Weak inversion ISFETs for ultra-low power biochemical sensing and real-time analysis," *Sensors and Actuators B: Chemical*, vol. 107, no. 1, pp. 468–473, 2005.

[30] Jieun L. and Bongsik C. and Seonwook H. and Jung H. L. and Byung-Gook P. and Tae J. P. and Dong M. K. and Dae H. K. and Sung-Jin C., "Investigation of Sensor Performance in Accumulation- and Inversion-Mode Silicon Nanowire pH Sensors," *IEEE TED*, vol. 61, pp. 1607–1610, May 2014.

[31] X. P. Gao, G. Zheng, and C. M. Lieber, "Subthreshold regime has the optimal sensitivity for nanowire FET biosensors," *Nano letters*, vol. 10, no. 2, pp. 547–552, 2009.

[32] S. Kim, T. Rim, K. Kim, U. Lee, E. Baek, H. Lee, C.-K. Baek, M. Meyyappan, M. J. Deen, and J.-S. Lee, "Silicon nanowire ion sensitive field effect transistor with integrated ag/agcl electrode: ph sensing and noise characteristics," *Analyst*, vol. 136, no. 23, pp. 5012–5016, 2011.

[33] C. Toumazou and S. Purushothaman, "Use of a pH sensor comprising an ion-sensitive field effect transistor (ISFET) to perform real time detection/quantification of nucleic acid amplification," 2012. US Patent 8,114,591.

[34] J. Go, P. R. Nair, and M. A. Alam, "Theory of signal and noise in double-gated nanoscale electronic pH sensors," *Journal of applied physics*, vol. 112, no. 3, p. 034516, 2012.

[35] K. Bedner, V. A. Guzenko, A. Tarasov, M. Wipf, R. L. Stoop, D. Just, S. Rigante, W. Fu, R. A. Minamisawa, C. David, M. Calame, J. Gobrecht, and C. Schönenberger, "pH Response of Silicon Nanowire Sensors: Impact of Nanowire Width and Gate Oxide," *Sensors and Materials*, no. 8, pp. 567–576, 2010.

[36] C. Toumazou *et al.*, "Simultaneous DNA amplification and detection using a pH-sensing semiconductor system," *Nature Methods*, pp. 641–646, 2013.

[37] E. Accastelli, P. Scarbolo, T. Ernst, P. Palestri, L. Selmi, and C. Guiducci, "Multi-wire tri-gate silicon nanowires reaching milli-ph unit resolution in one micron square footprint," *Biosensors*, vol. 6, p. 9, 2016.

[38] Harame, D. L. and Bousse, L. J. and Shott, J. D. and Meindl, J. D., "Ion-sensing devices with silicon nitride and borosilicate glass insulators," *IEEE Transactions on Electron Devices*, vol. 34, no. 8, pp. 1700–1707, 1987.

[39] Sudhölter, E. J. R. and Van der Wal, P. D. and Skowronska-Ptasinska, M. and Van den Berg, A. and Reinhoudt, D. N., "Ion-sensing using chemically-modified ISFETs," *Sensors and Actuators*, vol. 17, no. 1-2, pp. 189–194, 1989.

[40] Van Den Vlekkert, H. H. and De Rooij, N. F. and Van Den Berg, A. and Grisel, A., "Multi-ion sensing system based on glass-encapsulated pH-ISFETs and a pseudo-REFET," *Sensors and Actuators B: Chemical*, vol. 1, no. 1, pp. 395–400, 1990.

[41] Lee, C.-S. and Kim, S. K. and Kim, M., "Ion-sensitive field-effect transistor for biological sensing," *Sensors*, vol. 9, no. 9, pp. 7111–7131, 2009.

[42] Wipf, M. and Stoop, R. L. and Tarasov, A. and Bedner, K. and Fu, W. and Wright, I. A and Martin, C. J. and Constable, E. C. and Calame, M. and Schönenberger, C., "Selective sodium sensing with gold-coated silicon nanowire field-effect transistors in a differential setup," *ACS nano*, vol. 7, no. 7, pp. 5978–5983, 2013.

[43] C. Guiducci and C. Stagni and A. Fischetti and U. Mastromatteo and L. Benini and B. Riccó, "Microelectrodes on a Silicon Chip for Label Free Capacitive DNA Sensing," *IEEE Sensors Jou.*, vol. 6, no. 5, pp. 1084–1093, 2006.

[44] Y. Chen and Elling and Y.-l. Lee and S.-c. Chong, "A Fast, Sensitive and Label Free Electrochemical DNA Sensor," *Journal of Physics: Conference Series*, vol. 34, no. 1, p. 204, 2006.

[45] Stern, E. and Klemic, J. F. and Routenberg, D. A. and Wyrembak, P. N. and Turner-Evans, D. B., and LaVan, D. A. and Fahmy, T. M. and Reed, M. A., "Label-free immunodetection with CMOS-compatible semiconducting nanowires," *Nature*, vol. 445, pp. 519–522, 2007.

[46] M. Curreli and R. Zhang and F. N. Ishikawa and H-K. Chang and R. J. Cote and C. Zhou and M. E. Thompson, "Real-Time, Label-Free Detection of Biological Entities Using Nanowire-Based FETs," *IEEE Transactions on Nanotechnology*, vol. 7, pp. 651–667, November 2008.

[47] G. Wenga and E. Jacques and A-C. Salaün and R. Rogel and L. Pichon and F. Geneste, "Step-gate polysilicon nanowires field effect transistor compatible with CMOS technology for label-free DNA biosensor," *Biosens. and Bioel.*, vol. 40, no. 1, pp. 141 – 146, 2013.

[48] Matsumoto, A. and Miyahara, Y., "Current and emerging challenges of field effect transistor based bio-sensing," *Nanoscale*, vol. 5, pp. 10702 – 10718, 2013.

[49] Esfandyarpour, R. and Javanmard, M. and Koochak, Z. and Esfandyarpour, H. and Harris, J. S. and Davis, R. W., "Label-free electronic probing of nucleic acids and proteins at the nanoscale using the nanoneedle biosensor," *Biomicrofluidics*, vol. 7, no. 4, p. 044114, 2013.

[50] F. Pittino, L. Selmi, and F. Widdershoven, "Numerical and analytical models to investigate the AC high-frequency response of nanoelectrode/SAM/electrolyte capacitive sensing elements," *Solid-State Electronics*, pp. 82–88, 2013.

[51] Rajan, N. K. and Duan, X. and Reed, M. A., "Performance limitations for nanowire/nanoribbon biosensors," *Wiley Interdisciplinary Reviews: Nanomedicine and Nanobiotechnology*, vol. 5, no. 6, pp. 629–645, 2013.

[52] Simoen, Eddy and Claeys, Cor, "On the flicker noise in submicron silicon MOSFETs," *Solid-State Electronics*, vol. 43, no. 5, pp. 865–882, 1999.

[53] Crescentini, M. and Bennati, M. and Carminati, M. and Tartagni, M., "Noise limits of CMOS current interfaces for biosensors: A review," *IEEE transactions on biomedical circuits and systems*, vol. 8, no. 2, pp. 278–292, 2014.

[54] G. Ferrari, M. Farina, F. Guagliardo, M. Carminati, and M. Sampietro, "Ultra-low-noise CMOS current preamplifier from DC to 1 MHz," *Electronics letters*, vol. 45, no. 25, pp. 1278–1280, 2009.

[55] C. Halté, G. Delapierre, T. Fournier, J. Buckley, M. Gely, B. De Salvo, T. Baron, and F. Vinet, "Rapid Top-down Fabrication of Si Nanowire and Fully Automated Test Platform: Application to pH," in *Proceedings of the International Conference on Wearable Micro and Nano Technologies for Personalized Health, Valencia, Spain*, pp. 21–23, 2008.

[56] E. Accastelli, *Tri-gate silicon nanowire transistors for ultra-low pH resolution and improved scalability*. Ph.D. Thesis, doi:10.5075/epfl-thesis-6468, EPFL, École Polytechnique Fédérale de Lausanne, 2015.

[57] Hanson, E. L. and Schwartz, J. and Nickel, B. and Koch, N. and Danisman, M. F., "Bonding self-assembled, compact organophosphonate monolayers to the native oxide surface of silicon," *Journal of the American Chemical Society*, vol. 125, no. 51, pp. 16074–16080, 2003.

[58] Midwood, K. S. and Carolus, M. D. and Danahy, M. P. and Schwarzbauer, J. E. and Schwartz, J., "Easy and efficient bonding of biomolecules to an oxide surface of silicon," *Langmuir*, vol. 20, no. 13, pp. 5501–5505, 2004.

[59] Pylant, E. D. and Hoener, C. F. and Arendt, M. F. and Witowski, B., "Characterization of thin Chemical/Native Oxides on Si (100) by Auger and Angle-Resolved XPS," in *MRS Proceedings*, vol. 318, p. 99, Cambridge Univ Press, 1993.

[60] S. Rigante, *High-K Dielectric FinFETs on Si-Bulk for Ionic and Biological Sensing Intergrated Circuits* . Ph.D. Thesis, EPFL, École Polytechnique Fédérale de Lausanne, 2014.

[61] M. Green, M.-Y. Ho, B. Busch, G. Wilk, T. Sorsch, T. Conard, B. Brijs, W. Vandervorst, P. Räisänen, D. Muller, *et al.*, "Nucleation and growth of atomic layer deposited HfO2 gate dielectric layers on chemical oxide (Si-OH) and thermal oxide (SiO2 or Si-ON) underlayers," *Journal of Applied Physics*, vol. 92, pp. 7168–7174, 2002.

[62] S. Rigante, P. Scarbolo, D. Bouvet, M. Wipf, K. Bedner, and A. Ionescu, "Technological development of high-k dielectric FinFETs for liquid environment," *Solid-State Electronics*, pp. 81–87, 2014.

[63] Y. Wang and G. Li, "Performance investigation for a silicon nanowire fet biosensor using numerical simulation," in *Proc. IEEE Nanotechnology Materials and Devices Conference*, pp. 81–86, 2010.

[64] X. Yang, W. Frensley, D. Zhou, and W. Hu, "Performance Analysis of Si Nanowire Biosensor by Numerical Modeling for Charge Sensing," *IEEE Trans. on Nanotechnology*, vol. 11, no. 3, pp. 501–512, 2012.

[65] F. Pittino and L. Selmi, "Use and comparative assessment of the CVFEM method for Poisson-Boltzmann and Poisson-Nernst-Planck three dimensional simulations of impedimetric nano-biosensors operated in the DC and AC small signal regimes," *Computational Methods in Applied Mechanics and Engineering*, pp. 902–923, 2014.

[66] Flavell, A. and Machen, M. and Eisenberg, B. and Kabre, J. and Liu, C. and Li, X., "A conservative finite difference scheme for Poisson-Nernst-Planck equations," *Journal of Computational Electronics*, pp. 1–15, 2013.

[67] I.-Y. Chung, H. Jang, J. Lee, H. Moon, S. M. Seo, and D. H. Kim, "Simulation study on discrete charge effects of SiNW biosensors according to bound target position using a 3D TCAD simulator," *Nanotechnology*, 2012. 065202.

[68] Nair, P. R. and Alam, M. A., "Screening-Limited Response of NanoBiosensors," *Nano Letters*, vol. 8, no. 5, pp. 1281–1285, 2008.

[69] Y. Liu and R. W. Dutton, "Effects of charge screening and surface properties on signal transduction in field effect nanowire biosensors," *Journal of Applied Physics*, vol. 106, no. 1, pp. –, 2009.

[70] S. Baumgartner, M. Vasicek, A. Bulyha, and C. Heitzinger, "Optimization of nanowire dna sensor sensitivity using self-consistent simulation," *Nanotechnology*, vol. 22, no. 42, p. 425503, 2011.

[71] F. Fogolari and A. Brigo and H. Molinari, "The Poisson-Boltzmann equation for biomolecular electrostatics: a tool for structural biology," *Jou. of Molecular Recognition*, vol. 15, pp. 377–392, 2002.

[72] Levine, S and Smith, AL, "Theory of the differential capacity of the oxide/aqueous electrolyte interface," *Discussions of the Faraday Society*, vol. 52, pp. 290–301, 1971.

[73] Ninham, B. W. and Parsegian, V. A., "Electrostatic potential between surfaces bearing ionizable groups in ionic equilibrium with physiologic saline solution," *Journal of theoretical biology*, vol. 31, no. 3, pp. 405–428, 1971.

[74] D. E. Yates, S. Levine, and T. W. Healy, "Site-binding model of the electrical double layer at the oxide/water interface," *Journal of the Chemical Society, Faraday Transaction 1*, vol. 70, pp. 1807–1818, 1974.

[75] Davis, J. A. and James, R. O. and Leckie, J. O., "Surface ionization and complexation at the oxide/water interface: I. Computation of electrical double layer properties in simple electrolytes," *Journal of colloid and interface science*, vol. 63, no. 3, pp. 480–499, 1978.

[76] J. Bustillo *et al.*, "Development of the ion torrent cmos chip for dna sequencing," in *Proc. IEDM*, pp. 196–199, 2013.

[77] N. Rusk, "Torrents of sequence," *Nature Methods*, vol. 8, 2011.

[78] von Helmholtz, H, "The Double Layer," *Wied. Ann*, vol. 7, p. 337, 1879.

[79] M. Gouy, "Sur la constitution de la charge electrique a la surface d'un electrolyte," *J. Phys. Theor. Appl.*, vol. 9, no. 1, pp. 457–468, 1910.

[80] D. L. Chapman, "LI. A contribution to the theory of electrocapillarity," *The London, Edinburgh, and Dublin philosophical magazine and journal of science*, vol. 25, no. 148, pp. 475–481, 1913.

[81] A. J. Bard and L. R. Faulkner, *Electrochemical Methods: Fundamentals and Applications*. John Wiley & Sons, second ed., 2001.

[82] R. Somaraju and J. Trumpf, "Frequency, temperature and salinity variation of the permittivity of seawater," *IEEE Transactions on Antennas and Propagation*, vol. 54, pp. 3441–3448, nov. 2006.

[83] T. Meissner and F. Wentz, "The complex dielectric constant of pure and sea water from microwave satellite observations," *Geoscience and Remote Sensing, IEEE Transactions on*, vol. 42, pp. 1836–1849, Sept 2004.

[84] A. P. Stogryn, H. T. Bull, K. Rubayi, and S. Iravanchy, "The microwave dielectric properties of sea and fresh water," in *GenCorp Aerojet, Tech. Rep.*, 1995.

[85] Iwasaki, I. and de Bruyn, P. L. , "The Electrochemical Double Layer on Silver Sulfide at pH 4.7. I. In the Absence of Specific Adsorption," *The Journal of Physical Chemistry*, vol. 62, no. 5, pp. 594–599, 1958.

[86] O. Stern, "Zur theorie der elektrolytischen doppelschicht," *Zeitschrift für Elektrochemie und angewandte physikalische Chemie*, pp. 508–516, 1924.

[87] Wilk, G. D. and Wallace, R. M. and Anthony, J. M., "High-κ gate dielectrics: Current status and materials properties considerations," *Journal of applied physics*, vol. 89, no. 10, pp. 5243–5275, 2001.

[88] Robertson, J., "High dielectric constant gate oxides for metal oxide Si transistors," *Reports on Progress in Physics*, vol. 69, no. 2, p. 327, 2005.

[89] D. E. Yates, *The structure of the oxide/aqueous electrolyte interface*. Ph.D. Thesis, University of Melbourne, 1975.

[90] R. van Hal, J. Eijkel, and P. Bergveld, "A general model to describe the electrostatic potential at electrolyte oxide interfaces," *Advances in Colloid and Interface Science*, vol. 69, no. 1-3, pp. 31 – 62, 1996.

[91] A. Van den Berg, P. Bergveld, D. Reinhoudt, and E. Sudhölter, "Sensitivity control of ISFETs by chemical surface modification," *Sensors and Actuators*, vol. 8, no. 2, pp. 129–148, 1985.

[92] S. Martinoia, G. Massobrio, and M. Grattarola, "An ISFET model for CAD applications," *Sensors and Actuators B: Chemical*, vol. 8, no. 3, pp. 261 – 265, 1992.

[93] A. Tarasov, M. Wipf, R. L. Stoop, and K. Bedner, "Understanding the electrolyte background for biochemical sensing with ion-sensitive field-effect transistors," *ACS Nano*, pp. 9291–9298, 2012.

[94] P. Woias, L. Meixner, D. Amandi, and M. Schönberger, "Modelling the short-time response of ISFET sensors," *Sensors and Actuators B: Chemical*, vol. 24, no. 1-3, pp. 211 – 217, 1995.

[95] Bousse, L. and De Rooij, N. F. and Bergveld, P., "The influence of counter-ion adsorption on the ψ 0/pH characteristics of insulator surfaces," *Surface Science*, vol. 135, no. 1, pp. 479–496, 1983.

[96] Bandiziol, A. and Palestri, P. and Pittino, F. and Esseni, D. and Selmi, L., "A TCAD-Based Methodology to Model the Site-Binding Charge at ISFET/Electrolyte Interfaces," *IEEE Transactions on Electron Devices*, vol. 62, no. 10, pp. 3379–3386, 2015.

[97] P. Scarbolo, E. Accastelli, T. Ernst, C. Guiducci, and L. Selmi, "Analysis of Dielectric Microbead Detection by Impedance Spectroscopy with Nanoribbons," in *Proceedings IEEE Nanotechnology Conference (IEEENANO)*, 2016.

[98] F. Pittino and L. Selmi, "Improved sensitivity of nanowire Bio-FETs operated at high-frequency: A simulation study," in *Nanotechnology (IEEE-NANO)*, pp. 792–795, 2015.

[99] F. Pittino, F. Passerini, P. Palestri, L. Selmi, and F. Widdershoven, "On the response of nanoelectrode capacitive biosensors to DNA and PNA strands," in *Proc. Int. Workshop on Advances in Sensors and Interfaces*, pp. 40–45, 2013.

[100] J. Schöberl, *Netgen documentation*, 4.3 ed., 3 2003.

[101] F. Pittino, *Prospects of nanoelectronic biosensing with high-frequency impedance spectroscopy*. Ph.D. Thesis, Università degli Studi di Udine, 2015.

[102] F. Pittino, P. Palestri, P. Scarbolo, D. Esseni, and L. Selmi, "Models for the use of commercial TCAD in the analysis of silicon-based integrated biosensors," *Solid-State Electronics*, pp. 63–69, 2014.

[103] Synopsis Inc., *Synopsys Sentaurus Device simulator user manual*, 2013.

[104] A. Hassibi, Y. Liu, and R. Dutton, "Progress in biosensor and bioelectronics simulations: New applications for TCAD," in *Proc. SISPAD*, pp. 1–4, 2008.

[105] A. Hassibi, Y. Liu, and R. Dutton, "Electrical modulation of ion concentration in dual-gated nanochannels," in *Proc. IEDM*, pp. 374–377, 2010.

[106] J. Speight, ed., *Lange's Handbook of Chemistry*. McGraw-Hill, 15th ed., 1999.

[107] I. Borukhov, D. Andelman, and H. Orland, "Adsorption of large ions from an electrolyte solution: a modified poisson-boltzmann equation," *Electrochimica Acta*, vol. 46, no. 2-3, pp. 221–229, 2000.

[108] M. M. Kohonen, M. E. Karaman, and R. M. Pashley, "Debye length in multivalent electrolyte solutions," *Langmuir*, vol. 16, no. 13, pp. 5749–5753, 2000.

[109] Pittino, F. and Scarbolo, P. and Dalla Longa, M. and Cossettini, A. and Selmi, L., "ENBIOS-1D Lab," Apr 2016, doi:10.4231/D3GX44W13.

[110] Hoxha, A. and Scarbolo, P. and Cossettini, A. and Pittino, F. and Selmi, L., "ENBIOS-2D Lab," Oct 2016, doi:10.4231/D3V11VM7D.

[111] H. P. Erickson, "Size and shape of protein molecules at the nanometer level determined by sedimentation, gel filtration, and electron microscopy," *Biological Procedures Online*, vol. 11, no. 1, pp. 32–51, 2009.

[112] F. Pittino, P. Scarbolo, F. Widdershoven, and L. Selmi, "Derivation and numerical verification of a compact analytical model for the AC admittance response of nanoelectrodes, suitable for optimization of electronic nanobiosensors," submitted.

[113] Pittino, F. and Passerini, F. and Selmi, L. and Widdershoven, F., "Numerical simulation of the position and orientation effects on the impedance response of nanoelectrode array biosensors to DNA and PNA strands," *Microelectronics Journal*, vol. 45, no. 12, pp. 1695–1700, 2014.

[114] W. Hale, *The HarperCollins Dictionary Of Biology*. HarperCollins, 1991.

[115] E. Gongadze, U. van Rienen, and A. Iglic, "Generalized stern models of the electric double layer considering the spatial variation of permittvity and finite size of ions in saturation regime," *Cellular and Molecular Biology Letters*, vol. 16, pp. 576–594, 2011.

[116] Van Gerwen, P. and Laureyn, W. and Laureys, W. and Huyberechts, G. and De Beeck, M. O. and Baert, K. and Suls, J. and Sansen, W. and Jacobs, P. and Hermans, L. and others, "Nanoscaled interdigitated electrode arrays for biochemical sensors," *Sensors and Actuators B: Chemical*, vol. 49, no. 1, pp. 73–80, 1998.

[117] Bedner, K. and Guzenko, V. A and Tarasov, A. and Wipf, M. and Stoop, R. L. and Rigante, S. and Brunner, J. and Fu, W. and David, C. and Calame, M. and others, "Investigation of the dominant 1/f noise source in silicon nanowire sensors," *Sensors and Actuators B: Chemical*, vol. 191, pp. 270–275, 2014.

[118] L. De Michielis, K. Moselund, L. Selmi, and A. Ionescu, "Corner Effect and Local Volume Inversion in SiNW FETs," *IEEE Trans. on Nanotechnology*, pp. 810–816, 2011.

[119] Raider, S. I. and Gregor, L. V. and Flitsch, R., "Transfer of Mobile Ions from Aqueous Solutions to the Silicon Dioxide Surface," *Journal of the Electrochemical Society*, vol. 120, no. 3, pp. 425–431, 1973.

[120] S. Pud, F. Gasparyan, M. Petrychuk, J. Li, A. Offenhäusser, and S. Vitusevich, "Single trap dynamics in electrolyte-gated Si-nanowire field effect transistors," *Journal of applied physics*, vol. 115, no. 23, p. 233705, 2014.

[121] N. K. Rajan, K. Brower, X. Duan, and M. A. Reed, "Limit of detection of field effect transistor biosensors: Effects of surface modification and size dependence," *Applied Physics Letters*, 2014. 084106.

[122] Zhuge, J. and Wang, R. and Huang, R. and Tian, Y. and Zhang, L. and Kim, D.-W. and Park, D. and Wang, Y., "Investigation of low-frequency noise in silicon nanowire MOSFETs," *IEEE Electron Device Letters*, vol. 30, no. 1, pp. 57–60, 2009.

[123] Ghibaudo, G. and Roux, O. and Nguyen-Duc, C. and Balestra, F. and Brini, J., "Improved analysis of low frequency noise in Field-Effect MOS transistors," *physica status solidi (a)*, vol. 124, no. 2, pp. 571–581, 1991.

[124] Harris, F. J., "On the use of windows for harmonic analysis with the discrete Fourier transform," *Proceedings of the IEEE*, vol. 66, no. 1, pp. 51–83, 1978.

[125] Kirchner, J. W., "Aliasing in 1/ f α noise spectra: Origins, consequences, and remedies," *Physical Review E*, vol. 71, no. 6, p. 066110, 2005.

[126] Caloyannides, M. A., "Microcycle spectral estimates of 1/f noise in semiconductors," *Journal of Applied Physics*, vol. 45, no. 1, pp. 307–316, 1974.

[127] Foster, S. and Cranch, G. A and Tikhomirov, A., "Experimental evidence for the thermal origin of 1/f frequency noise in erbium-doped fiber lasers," *Physical Review A*, vol. 79, no. 5, p. 053802, 2009.

[128] Kasdin, N. J., "Discrete simulation of colored noise and stochastic processes and 1/f α power law noise generation," *Proceedings of the IEEE*, vol. 83, no. 5, pp. 802–827, 1995.

[129] Rajan, N. K. and Routenberg, D. A. and Reed, M. A., "Optimal signal-to-noise ratio for silicon nanowire biochemical sensors," *Applied physics letters*, vol. 98, no. 26, p. 264107, 2011.

[130] S. Pud, J. Li, V. Sibiliev, M. Petrychuk, V. Kovalenko, A. Offenhäusser, and S. Vitusevich, "Liquid and back gate coupling effect: toward biosensing with lowest detection limit," *Nano letters*, vol. 14, no. 2, pp. 578–584, 2014.

[131] Clément, N. and Han, X. L. and Larrieu, G., "Electronic transport mechanisms in scaled gate-all-around silicon nanowire transistor arrays," *Applied Physics Letters*, vol. 103, no. 26, p. 263504, 2013.

[132] Regonda, S. and Tian, R. and Gao, J. and Greene, S. and Ding, J. and Hu, W., "Silicon multi-nanochannel FETs to improve device uniformity/stability and femtomolar detection of insulin in serum," *Biosensors and Bioelectronics*, vol. 45, pp. 245–251, 2013.

[133] Tartagni, M. and Crescentini, M. and Rossi, M. and Morgan, H. and Sangiorgi, E., "An AC and phase nanowire sensing for site-binding detection," in *2014 IEEE International Electron Devices Meeting*, pp. 31–2, IEEE, 2014.

[134] O. Knopfmacher, A. Tarasov, W. Fu, M. Wipf, B. Niesen, M. Calame, and C. Schonenberger, "Nernst limit in dual-gated Si-nanowire FET sensors," *Nano letters*, vol. 10, no. 6, pp. 2268–2274, 2010.

[135] M. Rossi *et al.*, "Hybrid system for complex ac sensing of nanowires," in *Proc. ULIS*, 2014.

[136] M. Tartagni, M. Crescentini, M. Rossi, H. Morgan, and E. Sangiorgi, "An AC and phase nanowire sensing for site-binding detection," in *Electron Devices Meeting (IEDM)*, pp. 31.2.1–31.2.4, 2014.

[137] A. Susloparova, D. Koppenhofer, J. K. Y. Law, X. T. Vu, and S. Ingebrandt, "Electrical cell-substrate impedance sensing with field-effect transistors is able to unravel cellular adhesion and detachment processes on a single cell level," *Lab on a Chip"*, vol. 15, pp. 668–679, 2015.

[138] Susloparova, A. and Koppenhöfer, D. and Vu, X. T. and Weil, M. and Ingebrandt, S., "Impedance spectroscopy with field-effect transistor arrays for the analysis of anti-cancer drug action on individual cells," *Biosensors and Bioelectronics*, vol. 40, no. 1, pp. 50–56, 2013.

[139] A. Manickam, A. Chevalier, M. McDermott, A. Ellington, and A. Hassibi, "A CMOS Electrochemical Impedance Spectroscopy (EIS) Biosensor Array," *IEEE Trans. on Biomedical Circuits and Systems*, no. 6, pp. 379–390, 2010.

[140] A. G. Cherstvy, "Detection of dna hybridization by field-effect dna-based biosensors: mechanisms of signal generation and open questions," *Biosensors and Bioelectronics*, vol. 46, pp. 162–170, 2013.

[141] Cattani-Scholz, A. and Liao, K.-C. and Bora, A. and Pathak, A. and Hundschell, C. and Nickel, B. and Schwartz, J. and Abstreiter, G. and Tornow, M., "Molecular architecture: construction of self-assembled organophosphonate duplexes and their electrochemical characterization," *Langmuir*, vol. 28, no. 20, pp. 7889–7896, 2012.

[142] A. Poghossian, M. H. Abouzar, F. Amberger, D. Mayer, Y. Han, S. Ingebrandt, A. Offenhäusser, and M. J. Schöning, "Field-effect sensors with charged macromolecules: Characterisation by capacitance–voltage, constant-capacitance, impedance spectroscopy and atomic-force microscopy methods," *Biosensors and bioelectronics*, vol. 22, no. 9, pp. 2100–2107, 2007.

[143] Schwarz, G., "A theory of the low-frequency dielectric dispersion of colloidal particles in electrolyte solution1, 2," *The Journal of Physical Chemistry*, vol. 66, no. 12, pp. 2636–2642, 1962.

[144] Wohlfarth, C., "Dielectric constant of acetonitrile," in *Supplement to IV/6*, pp. 117–121, Springer, 2008.

[145] Wang, P. and Anderko, A., "Computation of dielectric constants of solvent mixtures and electrolyte solutions," *Fluid Phase Equilibria*, vol. 186, no. 1, pp. 103–122, 2001.

[146] Bora, A. and Pathak, A. and Liao, K.-C. and Vexler, M. I. and Kuligk, A. and Cattani-Scholz, A. and Meinerzhagen, B. and Abstreiter, G. and Schwartz, J. and Tornow, M., "Organophosphonates as model system for studying electronic transport through monolayers on SiO2/Si surfaces," *Applied Physics Letters*, vol. 102, no. 24, p. 241602, 2013.